TOWARDS TARGETED THERAPY FOR PEDIATRIC SARCOMAS

by

Yaniv Kazansky

A Dissertation

Presented to the Faculty of the Louis V. Gerstner, Jr.

Graduate School of Biomedical Sciences,

Memorial Sloan Kettering Cancer Center

In Partial Fulfillment of the Requirements for the Degree of

Doctor of Philosophy

New York, NY

September, 2023

Alex Kentsis, MD-PhD Dissertation Mentor	Date

DEDICATION

I would like to dedicate this thesis to my parents, and to my wife, Cheyanne Slocum. Without your incredible love, support, sacrifice, and good humor, this work would never have been possible.

ABSTRACT

Pediatric sarcomas, solid tumors that mainly strike children and young people, are characterized by a relative paucity of mutations. Indeed, some tumor types are driven by just a single mutation, which is nonetheless sufficient to profoundly dysregulate gene expression and transform cells. Yet although the causative mutations in many pediatric sarcomas are well-known, targeted therapeutic strategies are lacking, and the prognosis for patients who do not respond to aggressive chemotherapy, radiation, and surgery is dismal. The mutations that cause these tumors often involve non-enzymatic proteins, such as epigenetic regulators and transcription factor fusions. Thus, these oncogenic proteins have long been considered undruggable. Furthermore, our understanding of the molecular mechanisms that allow these mutations to transform cells is incomplete, hampering the development of targeted therapies. In this work, I study two strategies for targeting pediatric sarcomas which leverage specific epigenetic dependencies and aberrant protein-protein interactions as starting points for novel therapeutic approaches.

A subset of pediatric sarcomas, including malignant rhabdoid tumors and epithelioid sarcomas, are caused by a loss of the BAF/SWI/SNF subunit *SMARCB1*. While re-activation of the mutated gene is not a currently available therapeutic option, work over the past decade has shown that these tumors are dependent on the activity of the PRC2 chromatin repressor complex, and its methyltransferase subunit, EZH2. This is thought to be due to epigenetic antagonism between BAF and PRC2 and has led to the development of clinical inhibitors of EZH2. Recently, the most advanced of these inhibitors, tazemetostat (TAZ), was approved by the FDA as the first targeted therapy for these tumors. However, patient response rates to TAZ are low, and there is a critical need to better understand the principles of tumor response and resistance to epigenetic therapy in general and TAZ in particular. Using functional genomics of patient tumors and diverse

experimental models, I here define molecular mechanisms of TAZ resistance. I identify distinct classes of acquired mutations that converge on the RB1/E2F axis, decoupling EZH2-dependent differentiation and cell cycle control. This allows tumor cells to escape TAZ-induced G1 arrest despite EZH2 inhibition and suggests a general mechanism for effective EZH2 therapy. Thus, I propose and test combination strategies to circumvent TAZ resistance using cell cycle bypass and synthetic lethal targeting, and provide prospective biomarkers for therapy stratification. This offers a paradigm for rational epigenetic combination therapy suitable for immediate translation to clinical trials.

I also investigate Ewing sarcoma, a tumor of bone and soft tissue driven by a canonical EWS-FLI1 fusion and other chromosomal translocations involving *EWSR1*. While EWS-FLI1 is known to act as an aberrant transcription factor at neomorphic enhancers genome-wide, the precise molecular mechanism by which the fusion protein drives oncogenic gene expression is unknown. Here, I define the interactome of the fusion protein using mass spectrometry proteomics and use a genetic dependency analysis to nominate key protein cofactors of EWS-FLI1. This analysis yields both novel EWS-FLI1 cofactors and suggests a mechanism for oncogenic activity of previously known cofactors. Then, using a peptide interference approach, I found that the junction of this fusion protein is critical for its function. By incorporating a peptide spanning the fusion junction into a stable protein scaffold, I was able to reduce the expression of EWS-FLI1 target genes in a Ewing sarcoma cell line. I therefore hypothesize that the fusion junction creates a neomorphic interaction interface that recruits key protein cofactors. Thus, this peptide interference approach should serve as both a tool to probe the EWS-FLI1 oncogenic complex and may form the basis of a new therapeutic approach to combat this devastating disease.

ACKNOWLEDGMENTS

This thesis, and the years of work that it represents, would not have been possible without the help of a great number of individuals.

First, I want to thank my thesis mentor, Alex Kentsis. Alex was my first rotation mentor at Tri-I, and the Kentsis lab was my first introduction to cancer biology. Having started in the Kentsis lab with little cell/molecular biology experience, I found Alex's strong desire and ability to teach to be invaluable. Alex is a role model in many ways: his depth of knowledge and attention to detail have defined how I approach my experiments, while his wide-ranging curiosity has nurtured in me the confidence to ask important questions and to pursue projects with diverse topics. I will always be deeply indebted to him for supporting my career as a scientist and for being an incredible researcher to emulate.

I also want to thank all the members of the Kentsis research group, past and present, both for their scientific mentorship and their personal support. Although there are too many to name, I must especially acknowledge the following: Technicians Isaac Krasnopolsky, Phil Demarest, and more recently Daniel Cameron and Victor Morell, for their friendship, steady supply of good-natured ribbing, and of course for their constant hard work in support of all the science in our lab, including all of my projects- there would be no science without you; Helen Mueller, for her constant mentorship, daily support and encouragement, and instant friendship, as well as helpful feedback on this thesis- you are truly our lab mom and role model through all the daily struggles of lab, and our intrepid conference chaperone through all the shenanigans of crazy meetings, not to mention the best whiskey buddy; Shuyuan Cheng, for being the best lab neighbor ever- you've not only put up with me for three years (no matter how many times I've stolen your aspirator), but you've become a great friend and beloved kitty aunt; Anna Antonova, for being a constant source of much-needed coffee breaks and for dealing with my habit of answering

questions with more questions- you're an awesome friend, a true mensch, and I wish you the best of luck. I hope to have lots more drinks at Hunterian with all of you!

As my projects have evolved, my thesis committee has evolved as well, and I would like to acknowledge and thank all the members for their consistent support over the years: Mike Rout, Ari Melnick, David Scheinberg, and Scott Lowe, as well as my thesis proposal chair Omar Abdel-Wahab, my thesis defense chair Ping Chi, and my external advisor Sohail Tavazoie.

My projects would not have been possible without the support of many scientific collaborators and core facilities across the Tri-Institutional campus. Although there are too many to acknowledge specifically, I would like to especially thank Richard Koche for his help with our RNA-seq analysis, and the Rockefeller and MSK Proteomics cores for help with mass spectrometry.

I also want to thank my two best friends, Emily DeBoy and Gary Soroosh. Without you two, I would never have started on this crazy MD-PhD journey, and I am infinitely lucky to have met you both in LaPlata Hall. Thank you for a decade of friendship, support, and camaraderie through years of navigating and surviving academia, and for the steady two-way stream of wildly inappropriate jokes.

Above all, I would like to thank my family, which has grown over the course of my PhD studies. First, I would like to thank our two beautiful cats, Sansa and Daenerys, for the constant floofs, nuzzles, and headbutts (despite their hobby of walking across the keyboard while I write, a hobby they are indulging in as I write this section). I would also like to thank my in-laws, Janine and Jon, for their love and support, their words of encouragement before every lab meeting and conference, and for welcoming me into the family.

I cannot offer enough words of thanks to my parents. I would not be here if it were not for you, and the list of things I'm grateful for would be its own thesis. But just to mention

some highlights: Coming to the US with little more than a suitcase, a third language to learn, and me; mom driving me between skating practice and weekend math classes before even getting her morning coffee; building and fixing things with dad in the garage, from bows to model ships (with the added bonus of an impromptu education in Russian swearing); and supporting every step of my education in every way. I won the parent lottery, and every one of my accomplishments, past, present, and future, belong to you.

Finally, I would like to thank my incredible, loving, beautiful, and brilliant wife, Cheyanne. The past few years have been a long and tough road, but they've also been the best of my life because of you. A lot of life happened while I've gone through grad school- we got through a pandemic, became cat parents, got engaged and married, and became family. You started training as a resident physician, and somehow still found time to support me through the long days and many uncertainties of grad school. Throughout these years, you've been my greatest support and strongest inspiration. You keep me grounded and inspire me to be better. I love you, and I can't wait for the adventures to come.

TABLE OF CONTENTS

LIST OF TABLES

LIST OF FIGURES

LIST OF ABBREVIATIONS

MRT: Malignant rhabdoid tumor

ES: Epithelioid sarcoma

ATRT: Atypical teratoid/rhabdoid tumor

SWI/SNF: Switch/Sucrose Non-Fermenting

SMARCB1: SWI/SNF-related matrix-associated actin-dependent regulator of chromatin subfamily B member 1

INI1: Integrase Interactor 1

BAF: Brg/Brahma-associated factors

cBAF: Canonical BAF

PBAF: Polybromo-associated BAF

ncBAF: Noncanonical BAF

RB1: Retinoblastoma 1

PcG: Polycomb group

PRC1/2: Polycomb repressive complex 1/2

EZH1/2: Enhancer of Zeste Homolog 1/2

SAM: *S*-adenosyl methionine

CDK4/6: Cyclin-dependent kinase 4/6

CDKN1/2A: CDK inhibitor 1/2A

TAZ: Tazemetostat

EwS: Ewing sarcoma

EWSR1: Ewing sarcoma breakpoint region 1

FLI1: Friend leukemia integration 1

FET: FUS, EWSR1, and TAF15

IDR: Intrinsically disordered region

PrLD: Prion-like domain

LLPS: Liquid-liquid phase separation

TF: Transcription factor

CHAPTER I

1.1 Genetics of pediatric cancers- themes and opportunities

Cancer has traditionally been thought of as a disease of adults and the elderly, one whose incidence increases with age (1). This matches our understanding of cancer as a genetic disease, as exposure to environmental mutagens and the somatic acquisition of mutations increases with time. However, roughly 300,000 children worldwide are diagnosed with cancer every year (2, 3), and many cancer types occur most commonly or exclusively in children and young people. Recent reports indicate that between 8-10% (4, 5) of these cancers can be attributed to germline predisposition- inherited or acquired mutations in known tumor suppressors and oncogenes (6). However, for the majority of pediatric cancers, the mechanisms underlying their development are still being defined, and likely depend on a complex interplay between constitutional predisposition, environmental exposures, and developmental mutators (7).

Several themes have emerged from studies of pediatric cancers that distinguish them from cancers of aging adults. First, pediatric cancers generally harbor a smaller number of somatic mutations in comparison to adult cancers (8). The exception to this is in cancers driven by mutations of DNA repair genes (9). Second, many pediatric cancers harbor genomic alterations that are rarely seen in adult cancers (10, 11), suggesting distinct mechanisms of oncogenesis. Third, a substantial fraction of these pediatric-specific alterations are gene fusions. Some fusions are recurrent, involve known cancer-related genes, and are pathognomonic for specific cancer types. Other fusions are very rare and have yet to be functionally validated (3, 12), with the discovery of new gene fusions having accelerated since the advent of next-generation sequencing (NGS) (12). Finally, a large proportion of pediatric cancers are caused by mutations in epigenetic regulators. This includes genes encoding components of chromatin remodeling

complexes, regulatory histones, and epigenetic modifiers such as histone acetylases and DNA methylases (3).

The unique features of pediatric cancers present both challenges and opportunities for the development of targeted therapeutics. Over the past several decades, survival for many pediatric cancers has improved due to the refinement of multimodal therapy that includes cytotoxic chemotherapy, radiation, surgery, and supportive care. However, survival for other tumor types, particularly for solid tumors including metastatic and refractory sarcomas, has remained static. This is despite intensification of conventional chemotherapy, which often leads to significant long-term sequelae (13), and molecularly targeted therapies for most pediatric cancers are lacking. For example, gene fusions remain difficult to target pharmacologically. Apart from inhibitors of catalytically active fusion products such as *BCR-ABL*, direct targeting of non-catalytic fusions is not yet possible. Recently, the promise of therapeutic opportunities has arisen for some tumors caused by mutations in epigenetic regulators thanks to the discovery of synthetic lethal vulnerabilities conferred by these mutations, as will be discussed below.

In both cancers caused by recurrent gene fusions and mutations in epigenetic regulators, the relative paucity of mutations in pediatric cancers can be thought of as an opportunity. All cancers must overcome a set of evolved cell-intrinsic and cell-extrinsic mechanisms for their suppression and must manifest several phenotypes in order to grow and spread (14). In a tumor driven by very few mutations, and particularly by a single driver mutation, a very small number of genetic events must perturb the biochemistry of a cell so profoundly as to dysregulate many processes. Indeed, as will be discussed in the following sections, the expression of oncogenic fusions and the disruption of epigenetic regulators is often sufficient to substantially reprogram the epigenetic and transcriptional state of a cell. The logical corollary that follows from this is that the therapeutic disruption of even a single target may be sufficient to handicap a cancer cell just as profoundly.

In this thesis, I explore two tumor types that may be considered prototypical of two of the broad mechanisms by which young people get cancer. In Chapter 2, I focus on a class of tumors caused by mutation of an epigenetic regulator, *hSNF5/INI1/SMARCB1*. In particular, I explore a recently developed therapy that targets an epigenetic dependency in these tumors, how cancer cells develop resistance to this therapy, and how this resistance can be overcome. In Chapter 3, I focus on Ewing sarcoma, a tumor type caused by an oncogenic fusion protein that recruits a diverse array of cofactors to dysregulate the epigenetic landscape of the normal cell to cause cancer. Using a peptide interference approach, I demonstrate the feasibility of directly targeting such non-catalytic gene fusions.

1.2 Treatment of BAF-deficient cancers by targeting an epigenetic dependency

Loss of *hSNF5*/*INI1*/*SMARCB1* drives a subset of rare pediatric sarcomas

Rhabdoid tumor, a very rare and deadly tumor that typically strikes infants, has emerged as a prototypical epigenetically driven malignancy. This tumor was first described in 1978 as a variant of Wilms' tumor, a renal tumor of infants and young children (15), with a "monophasic sarcomatous" histology and an unfavorable prognosis (16). By 1981, rhabdoid tumor of the kidney, or malignant rhabdoid tumor (MRT) was recognized as a distinct entity, gaining its name from its microscopic similarity to rhabdomyosarcoma (17). MRT was distinguished from Wilms' tumors not only by a distinct histology but also by a highly aggressive and malignant character, with a poor response to therapy and a high propensity to metastasize. Children with metastases had an almost universally lethal outcome (17-19).

Further work revealed that rhabdoid tumors can occur in extra-renal tissues, including the liver (20), various soft tissue sites (21, 22), and the central nervous system

(CNS) (23, 24), where they are typically referred to as atypical teratoid/rhabdoid tumors (ATRT) (25). Cytogenetic analyses of cases of MRT and extrarenal rhabdoid tumors in the early and mid-1990s found that these tumors frequently harbor loss of chromosome 22 or deletions in the long arm of chromosome 22, region 11.2 (22q11.2) (24, 26-32). The specific region of chromosome 22 deleted or mutated in MRT was identified by Olivier Delattre et al in 1998 and found to contain the *hSNF5/INI1* gene (33), which encodes a core subunit of the BAF/SWI/SNF chromatin remodeling complex (discussed below). Indeed, in both rhabdoid tumor cell lines and renal and extra-renal rhabdoid tumor samples, biallelic inactivating mutations of *hSNF5/INI1* appeared to be an almost universal feature (33, 34).

In many cases of MRT and ATRT, children have germline loss-of-function mutations of one allele of this gene, with loss or mutation of the second allele in the tumor (34, 35). This pattern reflects the two-hit model of oncogenesis first observed by Alfred Knudson in retinoblastoma (36) and strongly indicates that the *hSNF5/INI1* gene is a classic tumor suppressor. The causative role of *hSNF5/INI1* inactivation in MRT was confirmed after numerous attempts to create a mouse rhabdoid tumor model: While constitutive *Snf5* deletion causes embryonic lethality in mice, conditional *Snf5* deletion using *Mx1-Cre* was shown by Charles Roberts, Stuart Orkin, and colleagues to induce some rhabdoid tumors, though predominantly lymphomas (37). Finally, work by Bourdeaut and colleagues showed that a mouse model with tamoxifen-inducible, *Cre*-mediated *Snf5* knockout induced between embryonic days E6.5 and E10.5 resulted in tumors resembling human rhabdoid tumors, with an exceptionally short latency (~3 months) (38). This both confirmed the role of the *SNF5* gene in rhabdoid tumorigenesis and demonstrated the unique vulnerability of cells at a specific stage of development to transformation by *SNF5* loss.

The SWI/SNF/BAF complex and its dysfunction in cancer

hSNF5/INI1 was the first SWI/SNF member found to function as a tumor suppressor (33). This gene was first identified by a yeast two-hybrid screen as an interactor of HIV-1 integrase (hence “integrase interactor 1” or *INI1*) (39) and found to contain significant sequence homology with the yeast SWI/SNF component *SNF5* (39, 40).

The SWI/SNF complex, of which *hSNF5/INI1* is a member, was originally described in yeast. The first SWI/SNF genes (*SWI1, SWI2, SWI3, SNF5,* and *SNF6*) were found in independent screens which identified them as being essential for mating type switching (hence “Switch” or “SWI”) (41) and for sucrose fermentation (hence “sucrose nonfermenting” or “SNF”) (42). A link between SWI/SNF and transcription regulation was made early, as SWI/SNF genes were found to be necessary for the transcription of specific genes (41, 42), and loss of SWI/SNF genes including *SNF5* reduced the transcription of many genes, all controlled by diverse regulatory mechanisms (43, 44). The SWI/SNF genes were therefore hypothesized to function together as general coactivators of transcription, possibly through the formation of a large complex (43). Additional genetic evidence for the transcriptional role of SWI/SNF came from yeast studies showing that the transcriptional defects caused by SWI/SNF mutations could be partially rescued by mutation of histone genes, indicating that SWI/SNF may act upon histones to regulate chromatin structure and relieve chromatin-mediated repression (45-48). This was perhaps the first example of the SWI/SNF complex antagonizing a repressive epigenetic process and raises the possibility of its therapeutic modulation.

SWI/SNF homologues were later found in multicellular organisms (49-51), with the *Drosophila brahma* or *brm* gene, a homologue of yeast *SWI2*, the first to be identified (52, 53). Fractionation of yeast extracts confirmed the predictions of earlier genetic studies that the SWI/SNF genes formed a large protein complex (54-56). Similarly sized complexes

with homologous subunits were also purified from HeLa cells (49). Biochemical studies of purified SWI/SNF found that the complex promoted the accessibility of nucleosomal DNA to transcription factors in an ATP-dependent manner *in vitro* (49, 55, 57). This function relies on the ATPase activity of *SWI2* in yeast (49, 58) and its human homologues *SMARCA4* (also known as *BRG1*) and *SMARCA2* (or *BRM*) (51), and is stimulated by double-stranded DNA (dsDNA).

The SWI/SNF complex is now known to be a ~2 MDa assembly whose ATP-dependent chromatin remodeling function has been conserved through evolution from yeast to metazoans, but has nonetheless evolved its architecture and subunit composition as transcriptional regulation has become more complex (59). The human SWI/SNF complex consists of three known subtypes, with each type of complex containing one ATPase subunit, either BRG1 or BRM, hence the more recent name for the mammalian SWI/SNF complex, “Brg/Brahma-associated factors”, or BAF (59, 60), which I will use in this work. The known BAF complex subtypes are canonical BAF (cBAF), polybromo-associated BAF (PBAF), and noncanonical BAF (ncBAF), all of which are formed through combinatorial assembly of protein subunits encoded by 29 genes. Some BAF subunits are shared across complex subtypes, while others are subtype specific. For example, *SNF5*, the tumor suppressor mutated in rhabdoid tumors and more frequently known in humans as *SMARCB1*, is now known to be a core component of the BAF and PBAF subtypes. The contributions of noncatalytic subunits of BAF are still under investigation (60).

An early link between BAF and cell cycle control was made through yeast two-hybrid experiments showing interactions between the tumor suppressor retinoblastoma protein 1 (*RB1*) and SWI/SNF components BRG1 and BRM (61, 62). These interactions confer tumor suppressor activity in human carcinoma cell lines (61) and appear to help RB1 repress E2F-mediated transcription (62). More recent work has found that different forms of the BAF complex play roles in cell cycle control during development. For example,

BAF subunit switching regulates cell cycle exit during neuronal development by antagonizing Polycomb repressive complexes at cell cycle genes (discussed in the next section) (63). Beyond cell cycle control, the BAF complex plays many diverse and critical roles in development (64), with the subunits of BAF complexes changing in different tissues at specific developmental stages.

In the two and a half decades since the initial discovery by Delattre et al of *SMARCB1* loss in MRT (33), sequencing efforts have revealed that many additional members of the SWI/SNF complex are mutated in cancer, and seminal work from Cigall Kadoch, Gerald Crabtree, and colleagues revealed that roughly 20% of human malignancies harbor mutations in this complex (59, 65). For example, in addition to MRT and ATRT, *SMARCB1* loss has also been observed in 90% of epithelioid sarcomas, soft tissue tumors that can arise in almost any anatomic site and which primarily affect young adults (66, 67). It should be noted here that other BAF subunit mutations tend to occur in cancers affecting older people, rather than children, and most often affect only one allele. Thus, the role of BAF complex mutations in other subunits likely involves somewhat distinct mechanisms, with these mutations acting as haploinsufficient tumor suppressors or possibly dominant oncogenes rather than recessive tumor suppressors (59).

Recent work has shed more light on the mechanism by which *SMARCB1* mutation impairs BAF function. Structural work has shown that the C-terminal domain of SMARCB1 directly contacts the nucleosome acidic patch, and that this is necessary for the nucleosome remodeling activity of cBAF (68, 69). While *SMARCB1* loss does not affect BAF complex assembly or stability, it does prevent the binding of BAF complexes to chromatin (70). Instead *SMARCB1*-deleted tumors rely and are dependent on the ncBAF complex, which incorporates unique subunits BRD9 and GLTSCR1/1L and not SMARCB1 (71, 72). This has led to recent exploration of BRD9 as a potential therapeutic target in

MRT. However, the first described molecular dependency found in *SMARCB1*-deleted tumors is the histone methyltransferase EZH2, as will be discussed in the next section.

Polycomb repressive complexes and their opposition by BAF

The first metazoan BAF homolog, the *Drosophila* gene *brm*, was identified in screens for suppressors of the Polycomb phenotype. Polycomb refers to the presence of developmentally abnormal sex combs (normally confined to the first pair of legs in male flies) of *Drosophila*, caused by both ectopic expression of homeotic (Hox) genes and mutation of a set of genes collectively called the Polycomb group (PcG) (52, 73). These observations eventually led to the hypothesis by Ed Lewis that the PcG genes were repressors of Hox genes (74). Work by Tamkun and others later identified a set of positive regulators of Hox genes, collectively called the Trithorax group (TrxG) that antagonized the PcG phenotype, with *brm* among them (52, 73). Thus, the field of BAF biology has been intimately tied to Polycomb almost since the former's inception, with BAF and Polycomb seemingly having antagonistic functions in the regulation of Hox gene expression.

In mammals, Polycomb complexes are now known to fall into two main groups- Polycomb Repressive Complex 1 and 2, or PRC1 and PRC2, respectively. The PRC1 complex has E3 ubiquitin ligase activity, ubiquitinating Lys119 of histone H2A. The PRC2 complex, which will be the focus of Chapter 2 of this thesis, is a lysine methyltransferase. PRC2 consists of four core proteins- Enhancer of Zeste Homolog 2 (EZH2) or its paralogue EZH1, embryonic ectoderm development (EED), Suppressor of Zeste 12 (SUZ12) and retinoblastoma-binding protein 4 and 7 (RBBP4/7). Human PRC2 also includes various accessory subunits that define multiple PRC2 subtypes (75).

The main enzymatic activity of PRC2 is the addition of one to three methyl groups to lysine 27 of histone H3, depositing H3K27me1, H3K27me2, and H3K27me3 histone

marks (76). This activity is catalyzed by the methyltransferase activity of the SET domain of *EZH2*, one of over 60 histone methyltransferases (HMTs) in the human genome, which include both histone lysine methyltransferases (HKMTs) and protein/histone arginine methyltransferases (PRMTs) (77). Nearly all HKMTs share a common catalytic mechanism that involves the formation of a ternary complex between the enzyme, its substrate, and the universal methyl donor *S*-adenosylmethionine (SAM) (77, 78). This results in a transfer of a methyl group from SAM to the side chain amino group, producing *S*-adenosylhomocysteine (SAH) as a byproduct (77). In the PRC2 complex, this activity requires association of EZH2 with other PRC2 subunits (76, 79) in order to relieve the autoinhibitory conformation of EZH2 (80).

PRC2 components often colocalize with both PRC1 and H3K27me3 on chromatin, creating Polycomb chromatin domains (80). Polycomb complexes are enriched at gene promoters and other gene regulatory elements (81) and CpG islands (82), although mammalian Polycomb complexes themselves do not have any sequence-specific binding activity (80). The functional output of the H3K27me3 mark is gene repression, which may occur at least in part through recruitment of PRC1 and H2AK1119 ubiquitination (83) and/or through direct recruitment of effector proteins containing Bromo Adjacent Homology (BAH) domains that bind H3K27me3 (84). The recruitment of PRC1 and PRC2 to specific chromatin regions, the interplay between the two complexes, and the mechanisms by which their respective histone marks mediate gene repression are still being elucidated.

Mutation of *EZH2* has been linked to cancer, which is discussed in greater detail in the next section. Of particular interest here, however, is the role played by *EZH2* in cancers caused by BAF dysfunction. An early clue to this role came from biochemical studies showing that purified *Drosophila* PRC1 could block remodeling of nucleosomes by BAF *in vitro* (85, 86). In addition, re-expression of *SMARCB1* in MRT causes eviction of

Polycomb proteins from tumor suppressor loci, in particular the cyclin-dependent kinase (CDK) inhibitor *CDKN2A*, which codes for the $p16^{INK4A}$ protein. (87). This is particularly compelling given the known role of *CDKN2A* in MRT; studies had previously shown that *CDKN2A* upregulation is a key mediator of *SMARCB1*-induced cell cycle arrest and senescence in MRT cells (88). This line of investigation culminated in seminal work by Charles Roberts and colleagues in 2010 that demonstrated that *EZH2* is overexpressed in MRT, and its expression is induced by *Snf5* deletion in mouse embryonic fibroblasts. Roberts et al further confirmed that *Snf5* loss in mice caused loss of BAF occupancy at the $p16^{INK4A}$ locus and its H3K27me3-mediated repression by EZH2, and that this pattern could be generalized to other PRC2 targets. Finally, they showed that inactivation of *EZH2* blocked formation of MRT *in vivo* with minimal effect on normal tissues, suggesting that *EZH2* constitutes a synthetic lethal dependency in *SMARCB1*-deleted tumors. These observations led to a model of epigenetic antagonism between BAF and PRC2 in MRT, in which BAF dysfunction allows for inappropriate PRC2-mediated silencing of tumor suppressors and pro-differentiation genes (89).

EZH2 and cancer

EZH2 has also been broadly linked to cancer in non-MRT contexts. Studies in lymphoma were the first to find elevated *EZH2* expression in cancer (90), followed by observations that linked high *EZH2* expression to poor prognosis in metastatic prostate cancer (91). Since then, high *EZH2* expression has been found in many other cancer types (92, 93). Indeed, work by Helin et al found that *EZH2*, along with *EED* and *SUZ12* are targets of regulation by the RB1/E2F pathway, which is often dysregulated in cancer, and suggested that *EZH2* is an oncogene (92). Further support of its oncogenic function emerged with the discovery of heterozygous *EZH2* point mutations at Tyr641 (Y641) in several types of lymphomas, including 7-25% of diffuse large B-cell lymphomas (DLBCL)

and follicular lymphomas (FLs) (94, 95). Biochemical experiments with reconstituted PRC2 complexes demonstrated that this mutation conferred a gain-of-function on the ability of EZH2 to convert H3K27me2 to H3K27me3, despite reducing its mono-methylation activity (93, 96). Additional gain-of-function mutations at A677 and A687 were also found in non-Hodgkin lymphomas (97, 98).

An antagonistic relationship between *EZH2* and the BAF complex has also been observed beyond *SMARCB1*-mutant tumors. For example, cancer cell lines harboring mutations in BAF subunits *ARID1A*, *PBRM1*, and *SMARCA4* are sensitive to *EZH2* inhibition, although this is only partially due to inhibition of the enzymatic activity of *EZH2*, and is partly due to destabilization of PRC2, indicating a non-enzymatic oncogenic function of *EZH2* (99). *EZH2* is also both highly expressed and a potential therapeutic target in small cell carcinoma of the ovary, hypercalcemic type, which is caused by mutation of BAF subunit *SMARCA4* (100).

Non-*EZH2* perturbations of PRC2 signaling have also been found in cancer. For example, loss-of-function mutations of *KDM6A* (*UTX*), a histone demethylase that antagonizes EZH2 activity, have been found in medulloblastoma (101), bladder cancer (102), pancreatic cancer (103), and several other cancer types (104). The oncogenic function of these mutations may be due at least in part to increased levels of H3K27me3 (105). A complex role for PRC2 is also found in diffuse midline gliomas (DMGs), which are often caused by mutations of the *EZH2* histone substrate H2K27 (H3K27M). In these tumors, H3K27me3 deposition is globally reduced, although retention of H3K27 methylation at specific PRC2 targets is required for tumor cell survival (106). Thus, PRC2 and the activity of its methyltransferase subunit EZH2 play a critical oncogenic role across diverse human cancers.

It should be noted that genomic EZH2 targets differ across cell types, and it is unclear whether there is a universal set of targets responsible for the oncogenic activity of

EZH2 (93). This variation in target genes matches the diverse roles of PRC2 in normal development. While PRC2 is known to repress lineage-specific genes and block cell differentiation, thereby maintaining embryonic stem (ES) cell renewal (107), it is also involved in lineage specification into multiple lineages later in development, and represses ES cell markers during differentiation (108). The genes that PRC2 represses, and therefore the specific cell fate that is repressed depends on the cellular context (89, 109). Similarly, the cancer-relevant targets of *EZH2*-mediated repression seem to vary depending on the tumor type, with known, functionally-validated targets including CDK4/6 inhibitor *CDKN2A* in MRT (89), *CDKN1A* in lymphoma (110, 111), DNA damage repair gene *RAD51* (112) and pro-differentiation transcription factor *FOXC1* (113) in breast cancer, and the mediator of epithelial cell cohesion E-cadherin in breast and prostate cancer (114), among many other genes. Further complicating our understanding of the cancer-related function of *EZH2* is the finding that this gene appears to function in some contexts as a tumor suppressor. For example, *EZH2* has been found to have loss-of-function mutations in myelodysplastic syndromes (MDS) and myeloproliferative neoplasms (MPN) (115) as well as T-cell acute lymphoblastic leukemias (T-ALL) (116). Other PRC2 subunits, such as *EED* and *SUZ12* have loss-of-function mutations in several cancer types such as malignant peripheral nerve sheath tumors (MPNST) (93, 117). In summary, there is unlikely to be a universal set of key *EZH2*-regulated genes that can account for its oncogenic function in every cancer type.

EZH2 inhibition as a therapeutic strategy

The first EZH2 inhibitor used experimentally, 3-deazaneplanocin (DZNep), is in fact not a direct EZH2 inhibitor. Rather, it inhibits the enzyme SAH hydrolase, which normally converts the product of SAM-dependent methyltransferases, SAH, into homocysteine and adenosine. Treatment with DZNep results in a buildup of cellular SAH

levels, which in turn inhibit the activity of SAM-dependent methyltransferases (118). Thus, DZNep is not specific to EZH2, although it does inhibit H3K27me3 deposition in PRC2-dependent cancer cell lines (119).

The high expression of *EZH2* in multiple cancer types, together with its gain-of-function mutation in non-Hodgkin lymphomas prompted the search for more specific inhibitors of EZH2. The first compound, EPZ005687 was described by Epizyme in 2012 as an apparent SAM-competitive EZH2 inhibitor and showed specific activity in blocking deposition of the H3K27me3 mark in lymphoma cell lines (120). Another simultaneously developed SAM-competitive EZH2 inhibitor, GSK126 (GlaxoSmithKline), was found to inhibit the growth of *EZH2*-mutant lymphoma cells *in vivo* (121), although it is not orally bioavailable and showed little clinical benefit in its phase I clinical trial (122). A third SAM-competitive inhibitor, EI1 (Novartis), showed activity against *EZH2*-mutant lymphoma cell lines and reduced H3K27me3 in a rhabdoid tumor cell line (123). The first orally bioavailable EZH2 inhibitor, UNC199, was developed shortly afterward (124, 125), and was also the first dual EZH1/EZH2 inhibitor, showing only about a 10-fold lower potency for EZH1 vs EZH2. This allows for anti-tumor efficacy against cancers expressing mutually exclusive but compensatory PRC2 methyltransferases, as in *MLL*-rearranged leukemias in which EZH1 and EZH2 compensate one another (125).

Further development of EPZ005687 through medicinal chemistry yielded EPZ-6438, or tazemetostat (TAZ), which showed improved potency and oral bioavailability (126). This was also the first EZH2 inhibitor to show activity against MRT cell lines *in vitro* and MRT xenografts *in vivo* (126). These preclinical successes have since been followed by the publication and clinical testing of several additional EZH2 inhibitors, including GSK343, (127) GSK503 (110), CPI-1205/Lirametostat (Constellation Pharmaceuticals) (128), PF-06821497 (Pfizer) (129), and SHR2554 (Hengrui) (130), with this list constantly expanding. Another compound, DS-3201b/valemetostat (Daiichi Sankyo), is a dual

EZH1/2 inhibitor that was recently approved for relapsed or refractory adult T-cell leukemias and lymphomas (131). Most of these EZH2 inhibitors exert their effect at least in part by blocking the SAM binding site, utilizing a 2-pyridone moiety that anchors the inhibitor through reciprocal hydrogen bonds with a tryptophan residue backbone within the catalytic SET domain (132, 133). Finally, an emerging class of inhibitors do not target the enzymatic activity of EZH2, but either disrupt the stability of the EZH2-EED interaction or the H3K27me3 recognition site on EED (134, 135), with the most advanced compound being MAK683 (Novartis) (135), currently under clinical investigation.

Compound	**NCT ID**	**Phase**	**Cancer types**	**Dates**	**Published Outcome**
GSK126	NCT02082977	1	DLBCL, FL, NHL, MM, ST	2014-2017	MTD determined, insufficient evidence of clinical benefit (122)
EPZ-6438 (TAZ)*	NCT02601950	2	MRT, ATRT, ES, ST	2015-2023	Approved
CPI-1205	NCT02395601 NCT03525795 NCT03480646	1 1 1/2	BCL ST mCRPC	2015-2022 2018-2022 2018-2021	Well-tolerated N/A N/A
CPI-0209	NCT04104776	1/2	ST, CRPC, lymphoma	2019-2026	N/A
PF-06821497	NCT03460977	1	CRPC, SCLC, FL	2018-2023	N/A
SHR2554	NCT03603951 NCT03741712 NCT04407741 NCT05896046	1 1/2 1/2 1/2	Lymphoid cancers CRPC ST, lymphoma HL	2018-2023 2018-2020 2020-2023 2023-2025	Well-tolerated Terminated Well-tolerated N/A
Valemetostat	NCT02732275 NCT04842877	1 2	Lymphoma Lymphoma	2016-2023 2021-2024	Approved
MAK683	NCT02900651	1	DLBCL	2016-2024	Well-tolerated

Table 1.1: List of ongoing and completed clinical trials involving PRC2 inhibitors. List shows trials as of 2021. *All TAZ trials with the exception of the trial leading to FDA approval not included for brevity. ST = solid tumors, MM = multiple myeloma, mCRPCT = metastatic castration-resistance prostate cancer.

Prior to the development of EZH2 inhibitors, *SMARCB1*-deficient tumors had no targeted therapies available. Treatments for rhabdoid tumors generally combine surgery with intensive combination chemotherapy, with overall survival rates nonetheless remaining at only 20-25% as of 2005 (136). Epithelioid sarcomas are treated either with

complete surgical resection for localized disease (137) or systemic chemotherapy for cases not amenable to surgery (138). Reported 5-year survival for patients with epithelioid sarcoma ranges between 34% (137) and 53% (67), with reported median overall survival ranging from 11 to 21 months as of 2020 (139). Thus, *SMARCB1*-deficient tumors represent an urgent, unmet clinical need, and the development of effective, targeted therapies is desperately needed.

Recently, the most clinically advanced EZH2 inhibitor, tazemetostat (TAZ), became the first targeted therapy approved for *SMARCB1*-deficient tumors. This was the result of a clinical trial run in part at the Memorial Sloan Kettering Cancer Center, with 15% of patients having an objective response (139). Despite the relatively low response rate, these results represent an incredible advance for patients with these devastating tumors. These results also speak to the promise of epigenetic EZH2 inhibitor therapy; as of June 2023, there are currently 43 completed, ongoing, or planned clinical trials with TAZ (clinicaltrials.gov), with other PRC2 inhibitors in the pipeline as well (**Table 1.1**). A deeper understanding of how tumors respond to EZH2 inhibition, why so many patient tumors do not respond, and how to combine EZH2 inhibition with other treatments effectively, are the next logical steps in advancing this promising therapy and is the focus of Chapter 2.

1.3 Towards direct targeting of fusion-driven pediatric sarcomas

History and clinical features of Ewing sarcoma

Ewing sarcoma (EwS) is a malignant tumor that primarily strikes children and adolescents, with a mean age of diagnosis of ~15 years (140, 141). It is the second most common pediatric bone tumor following osteosarcoma, although it can also arise in soft tissue, and its cell of origin remains debated (140). The tumor affects males slightly more

commonly than females (with a roughly 3:2 ratio) (140) and most commonly affects individuals of European descent (142, 143).

This tumor was first recognized as a distinct entity in 1921 by pathologist James Ewing (144) (at Memorial Hospital, now Memorial Sloan Kettering Cancer Center), who described it as a "diffuse endothelioma of the bone," with a probable origin "in the blood vessels of the bone tissue." Over six decades later, Ewing sarcoma cell lines and tumors were found to harbor a t(11;22) translocation (145, 146). This mutation was first cloned after another decade by Olivier Delattre et al (147), who found that this translocation created a chimeric transcript that fused together what they termed the *Ewing Sarcoma Breakpoint Region 1 (EWSR1)* gene on chromosome 22 and the *EWSR2* gene (more commonly known as *FLI1*, a member of the ETS transcription factor family) on chromosome 11. Within a few years, several similar but distinct fusions were discovered in other cases of EwS, including a fusion between *EWSR1* and the ETS transcription factor *ERG* (148).

Despite decades of advances in both the clinical management of EwS and molecular studies of its pathogenesis, progress in treatment has mainly revolved around the optimization of multimodal therapy consisting of surgery, radiotherapy (as EwS has been known to be radiosensitive since its initial description (144)) and chemotherapy (149), regimens that often have debilitating long-term effects. While 5-year overall survival is 65-75%, for the 20-25% of patients who initially present with metastases, 5-year survival is less than 30% as of 2015 (140, 149). Furthermore, there are currently no targeted therapies available for this tumor, and new treatment approaches are greatly needed.

FET family fusions in pediatric cancers

EWSR1 is now recognized as a member of a family of three RNA- and DNA-binding proteins that are recurrently translocated in various solid tumors. These three

genes, *FUS*, *EWSR1*, and *TAF15* together comprise the “FET” protein family. The *FUS* gene was originally discovered as part of a fusion with the transcription factor *CHOP* in myxoid liposarcoma (150), hence its name of *FUS* (fused in sarcoma) or *TLS* (translocated in liposarcoma). It is also translocated to multiple other partner genes in EwS, low-grade fibromyxoid sarcoma, and angiomatoid fibrous histiocytoma (151). The *TAF15* gene (also known as *TAFII68*, *RBP56*, and *TAF2N*) is translocated in extra-skeletal myxoid chondrosarcoma (152). The *EWSR1* gene itself, besides being fused to *FLI1* has also been found to be fused in less common cases of EwS to other partner genes including *ERG, ETV1, ETV4*, and *FEV*. Intriguingly, other fusions involving *EWSR1* have been found in other sarcoma types (153, 154). This includes fusion partner gene *WT1* in desmoplastic small round cell tumors (DSRCT), as well as *ATF1* and *CREB1* in clear cell sarcomas (151). The FET proteins are ubiquitously expressed and play multiple roles in the regulation of transcription and mRNA processing (155).

The oncogenic potential of FET proteins in multiple contexts suggests common features that allow their translocated forms to transform cells. Perhaps the most apparent common feature of the FET proteins is the N-terminal intrinsically disordered region (IDR), which is the portion of the FET proteins that is preserved in oncogenic fusions. This region consists of a low complexity domain (LCD) of a relatively small set of amino acids, ordered in degenerate repeats of the sequence [G/S]Y[G/S]. This composition is similar to that of yeast prion domains, leading to the term prion-like domain (PrLD) to refer to such amino acid sequences. Such domains consist of polar, uncharged amino acids, can adopt many conformational states, and their biochemical behavior is at least as much a function of their amino acid composition as their specific sequence (156, 157).

Extensive *in vitro* work over the past decade has focused on how the FET proteins interact with each other and with partner proteins. A common theme is that their behavior is both complex and context-dependent. The FET proteins can oligomerize *in vitro* given

high concentrations of protein (i.e. tens of mg/mL), forming hydrogels that include β-amyloid-type structures, albeit ones soluble in SDS (158). Other work has shown that FET oligomers behave more as liquid-like, phase separated droplets that form through liquid-liquid phase separation (LLPS) rather than more static gels, displaying a more dynamic character in both cell-free solutions and cells. These droplet-like structures have features of a liquid phase: They are spherical, are able to coalesce with each other, and have fast internal dynamics as measured by FRAP microscopy (159). NMR studies of FUS showed that FUS retains its disorder even in droplet form (160), suggesting that the formation of higher-order assemblies is mediated by weak, transient, but multivalent interactions. Some work has proposed that the EWS-FLI1 fusion phase separates together with cofactors to effect its oncogenic function, with the tyrosine residues within the [S/G]Y[S/G] repeats playing a critical role in oligomerization and cofactor recruitment (161), as they do in wild-type EWSR1 oligomerization (162). However, the specific mechanisms of FET protein oligomerization remain controversial, with multiple studies refuting the claim of LLPS by FET proteins (and many other proteins) in cells, as recently reviewed by Robert Tjian and colleagues (163). It is clear, however, that a greater understanding of FET protein assembly is needed to define the biophysical properties of EWS-FLI1 in cells.

Mechanisms of EWS-FLI1 function

The domain structure of EWS-FLI1 resembles that of a typical transcription factor (TF): A structured DNA-binding domain- in this case the C-terminal ETS domain from FLI1- joined to an unstructured N-terminal domain from EWSR1, similar to an unstructured activation domain of a TF (164). Indeed, EWS-FLI1 has been shown to act as a dominant oncogenic transcription factor (165), with the EWS portion acting as an activation domain (166, 167) that stimulates the transcription of a plethora of EWS-FLI1 target genes necessary for transformation and survival (168). A curious neomorphic property of EWS-

FLI1 is its sequence specificity; in addition to binding canonical ETS targets containing a GGAA core motif flanked by other variable bases (169), as would be expected from the presence of the FLI1 ETS domain, the fusion protein also binds to microsatellites throughout the genome consisting of tandem GGAA repeats (169), converting them into neomorphic enhancers. The consequences of binding at these genomic sites depends on the underlying sequence; EWS-FLI1 mediates transcriptional repression at canonical ETS sites and activation at GGAA microsatellites (170). Interestingly, GGAA microsatellites are highly polymorphic in the human population, and the population-based variation of GGAA microsatellite repeat length may in part explain the demographic variability in the incidence of EwS (171).

The functional consequences of EWS-FLI1 DNA binding depend on interactions with specific cofactors. For example, previous co-immunoprecipitation experiments have found a direct interaction between EWS-FLI1 and the histone acetylase p300, which appears to be important for deposition of active enhancer marks at microsatellite-activated EWS-FLI1 targets (170). Recent work has found that EWS-FLI1 also interacts with the BAF complex through its PrLD, recruiting it to GGAA microsatellites and increasing chromatin accessibility at EWS-FLI1 targets (161). Indeed, this finding represents an expansion of the set of cancers in which BAF dysfunction plays a role, even in the absence of direct BAF subunit mutations. Numerous other interactors have been described in the past, such as transcriptional machinery components including RNA Polymerase II (172), proteins involved in mRNA splicing (173), and the NuRD co-repressor complex (174). EWS-FLI1 therefore appears to be part of a larger complex that interacts with multiple cofactors, many of them multi-subunit complexes themselves, to perform its oncogenic function.

However, many questions remain about the EWS-FLI1 oncogenic assembly, which I will probe in Chapters 3 and 4: First, what is the complete list of protein interactors

of the fusion protein, and what is the relative importance of each interactor in cell transformation and survival? Such cofactors would likely fall into two broad functional classes: 1) Those that directly take part in transcriptional activation, repression, or another oncogenic function as part of the EWS-FLI1 complex, and 2) Those that are sequestered away from their normal sites in the cell of origin, thereby preventing their tumor suppressive function at these normal sites. The first class may include transcriptional coactivators like p300, repressors like the NuRD complex, or TFs that co-regulate EWS-FLI1 target genes. The second class may include TFs that stimulate differentiation or transcription of tumor suppressors during normal development but are mis-recruited to the EWS-FLI1 complex, thus blocking their normal function. Some proteins might, in fact, belong to both classes of cofactors, for example by stimulating the transcription of pro-growth genes at EWS-FLI1-bound loci rather than tumor suppressive genes at their developmentally normal loci. This would be reminiscent of previous studies in acute myeloid leukemia (AML), in which peptidomimetic interference with an oncogenic complex caused both loss of a key coactivator at pro-survival genes and the redistribution of pro-differentiation transcription factors to their normal loci (175).

This question has both mechanistic and therapeutic relevance. The nature of the EWS-FLI1 interactome may shed light on what determines susceptibility to transformation by EWS-FLI1. The cell of origin of EwS is still unconfirmed, with leading candidates being mesenchymal stem cells (MSCs) and neural crest stem cells (176), and the ability of EWS-FLI1 to transform cells appears to be exquisitely context-specific. For example, ectopic expression of EWS-FLI1 is toxic to most primary cell types (177, 178), and attempts to generate a faithful mouse model of Ewing sarcoma using ectopic expression of the fusion have to date been unsuccessful (179). While it has been posited that EWS-FLI1-mediated transformation requires either a specific germline background (143), co-occurring somatic mutations (176) or a specific epigenetic state (180), it is also possible that the expression

of specific proteins and their interaction with EWS-FLI1 are necessary for oncogenic transformation by the fusion protein. Indeed, these explanations need not be mutually exclusive, as expression of specific proteins may be either a consequence or a cause of a permissive epigenetic state. If one or more EWS-FLI1 cofactors are restricted in their expression to a specific developmental cell type, corresponding to the EwS cell of origin, this would be a compelling explanation for the context specificity of EWS-FLI1-mediated transformation. From a therapeutic perspective, such a cofactor(s), particularly those that are either limited in expression to developing tissues or those that form aberrant assemblies in EwS, might represent Ewing-specific dependencies. Such cofactors would be compelling therapeutic targets.

Second, what is the molecular architecture of the complex of proteins formed by EWS-FLI1? It is clear that the LCD of EWSR1 mediates some of the interactions, such as with the BAF complex (161). However, despite many *in vitro* studies of FET protein assembly, the specific protein-protein interactions that EWS-FLI1 makes with cofactors and their role in tumor development remain largely unexplored. This is a challenging area of study, as the disordered and degenerate nature of EWS-FLI1 make it unamenable to conventional structural approaches, like X-ray crystallography or cryogenic electron microscopy.

Third, what mechanisms regulate the assembly of the oncogenic EWS-FLI1 complexes in EwS cells? Recent work has indicated that the protein levels and transcriptional output of EWS-FLI1 are tightly controlled and correspond to specific variations in cell phenotype. For example, the ubiquitin ligase TRIM8 is a regulator of EWS-FLI1 stability through degradation of EWS-FLI1 by the proteasome (181). Interestingly, knockdown of TRIM8 causes a toxic increase in EWS-FLI1 levels, indicating that despite being dependent on the fusion for growth and survival (182), EwS cells can only tolerate a very specific “Goldilocks” dosage of the fusion. A similar theme has

emerged from other studies, with work showing that tumor cells with lower EWS-FLI1 expression have a higher propensity to invade and metastasize, while those with higher expression are characterized by a higher cell proliferation rate (183, 184). This regulation is at least partly dependent on co-expression of proteins that either cooperate with or antagonize EWS-FLI1 activity, including HOXD13 and ETV6 (184-186).

In addition to control by competing transcription factors, do Ewing sarcoma cells regulate EWS-FLI1 output by controlling assembly of EWS-FLI1 with its interactors? If so, post-translational modifications (PTMs) would be a compelling regulatory mechanism. Apart from the recently uncovered role of TRIM8-mediated ubiquitination of EWS-FLI1, other PTMs have been found on EWS-FLI1 including threonine phosphorylation (187) and serine/threonine O-GlcNAcylation (188). In addition, the FET proteins are known to be modified by phosphorylation which regulates their ability to form hydrogels in vitro (189). It is therefore a compelling hypothesis that similar regulation may take place with EWS-FLI1. For example, the previously observed interaction between EWS-FLI1 and RNA Polymerase II is dependent on the phosphorylation state of the RNA Pol II C-terminal domain (190), similar to the interaction between wild-type FET proteins and RNA Pol II (162).

Finally, is it possible to perturb the assembly of the EWS-FLI1 protein complex, both to probe its function in cells, and to therapeutically disassemble it in tumors? My inspiration for this question comes from previous work in the Kentsis lab on AML: Knowledge of a protein-protein interaction interface that is a dependency in AML led to the design of a peptidomimetic inhibitor of this interaction with activity against AML cells, providing a probe for the development of clinical-grade pharmacologic inhibitors suitable for translation to human clinical trials for patients (191). More generally, peptidomimetic approaches have recently shown promise as specific inhibitors of protein-protein interactions previously considered “undruggable” (192). Given the dependence of EwS on

EWS-FLI1 expression, and hypothesizing the requirement of specific PPIs that involve EWS-FLI for cell survival, I propose that a peptidomimetic targeting a specific region of the fusion protein offers a promising approach for defining the molecular mechanisms of EWS-FLI1 function and ultimately directly therapeutically targeting EwS.

CHAPTER II

Overcoming clinical resistance to EZH2 inhibition using rational epigenetic combination therapy

2.1 Introduction

Unlike conventional cytotoxic chemotherapy, epigenetic therapy offers the ability to target cancer-specific dependencies with increased specificity and reduced toxicity. This is especially true for cancers caused by genetic mutations of transcriptional regulators, such as the chromatin remodeling BAF/SWI/SNF (Brg/Brahma-associated factors) complex that is mutated in more than 20% of human cancers (59). For example, malignant rhabdoid tumors (MRT) and epithelioid sarcomas (ES) are lethal tumors of children and young adults caused by inactivating mutations of *SMARCB1/SNF5/INI1/BAF47*, one of the core BAF/SWI/SNF complex subunits (99, 193, 194). Loss of normal BAF function can confer a dependency on the Polycomb Repressive Complex 2 (PRC2) and its methyltransferase EZH2. This dependency results from epigenetic antagonism between the two complexes, in which normal BAF activity evicts PRC2 from tumor suppressor loci (89, 195).

The prevalence of high *EZH2* expression in many cancer types and gain-of-function *EZH2* mutations in lymphoma (93, 96-98) has led to the development of multiple inhibitors of EZH2 (121, 124, 126), several of which have now entered clinical trials (133). This includes clinical trials for *SMARCB1*-deficient tumors without *EZH2* mutations (139). However, despite the potential of such targeted epigenetic therapies, the principles governing their effective application remain unknown. Intrinsic and acquired resistance limits their use as monotherapies (196, 197).

A recent clinical trial led to the FDA approval of the EZH2 methyltransferase inhibitor tazemetostat (TAZ) as the first targeted therapy for *SMARCB1*-deficient

epithelioid sarcomas (139). However, only 15% of patients showed objective clinical responses, with most epithelioid sarcomas being resistant to TAZ. Ongoing clinical trials in patients with rhabdoid tumors have shown similar results, with only a subset of brain rhabdoid tumor patients exhibiting objective responses to TAZ, while extracranial rhabdoid tumors appear to be uniformly resistant (198). Recent studies have nominated the histone methyltransferase NSD1 as a regulator of TAZ susceptibility in rhabdoid tumor cells, but the clinical relevance of this mechanism is currently not known (199). In all, the outcomes for most patients with MRT and ES remain dismal, and the mechanisms of clinical response and resistance to EZH2 inhibition remain unknown. This hinders our ability to stratify treatment using prospective biomarkers to identify patients who may benefit from TAZ and to develop effective combination therapies with improved and durable benefits for patients.

Here, we define the key requirements for effective epigenetic therapy in diverse *SMARCB1*-deficient epithelioid sarcomas and rhabdoid tumors *in vivo*. Using comparative genomic analyses of clinical trial patients treated with TAZ, we identify multiple acquired mutations that cause therapy resistance. Using functional genomic approaches, we show that resistance mechanisms converge on a common RB1/E2F axis that integrates control of tumor cell division and differentiation. This organizes patient resistance mutations into a general framework, allowing us to develop rational combination therapies to circumvent TAZ resistance. Using diverse patient-derived ES and MRT cell lines and mouse xenografts, we demonstrate cell cycle bypass and synthetic lethal treatment strategies suitable for immediate translation to combination clinical trials for patients.

2.2 Results

Patient tumor sequencing reveals diverse resistance mutations

To identify mutations associated with clinical resistance to TAZ, we performed targeted gene sequencing of patient tumors using MSK-IMPACT, which is based on a panel of over 500 genes recurrently mutated in diverse cancer types (200). We analyzed 33 tumor specimens from 20 patients treated as part of the recent TAZ clinical trial (139), and identified somatic tumor mutations in matched pre- and post-treatment specimens (**Supplementary Tables S1 and S2**). We found distinct sets of somatic mutations in responding and non-responding tumors, with nearly all mutations, apart from *SMARCB1* loss itself, being exclusive to either TAZ-responsive or TAZ-resistant tumors (**Figure 2.1A, top panel**). Strikingly, we observed two tumors which initially responded to TAZ based on radiographic imaging but later developed clinical resistance (**Figure 2.1A, bottom panel, 2.1B**). Targeted sequencing of the resistant tumors revealed two newly acquired somatic mutations: heterozygous missense mutation of *EZH2* (*EZH2*^{Y666N}) in the Patient 3 tumor specimen, and biallelic loss of function mutation of *RB1*, including a hemizygous deletion and a frame shift mutation (*RB1*^{del}) in the remaining allele, in the Patient 15 tumor specimen. We confirmed both mutations using RNA-seq of the respective tumor specimens (**Figure 2.2A-B**). Since one mutation affected *EZH2* directly, and the other involved the known EZH2 target *RB1* (92), we hypothesized that both mutations were responsible for TAZ resistance in their respective patients.

First, we investigated the *EZH2*^{Y666N} mutation. Past studies using forward genetic screens in lymphoma cell lines have identified putative resistance mutations within both the N-terminal D1 domain and the catalytic SET domain of EZH2, both of which are predicted to interact with S-adenosyl methionine (SAM)-competitive EZH2 inhibitors such as TAZ (201, 202). One such SET domain mutation previously identified in cell lines is *EZH2*^{Y661D}, with Y661 corresponding to Y666 in isoform 2 of *EZH2*, the isoform referred to

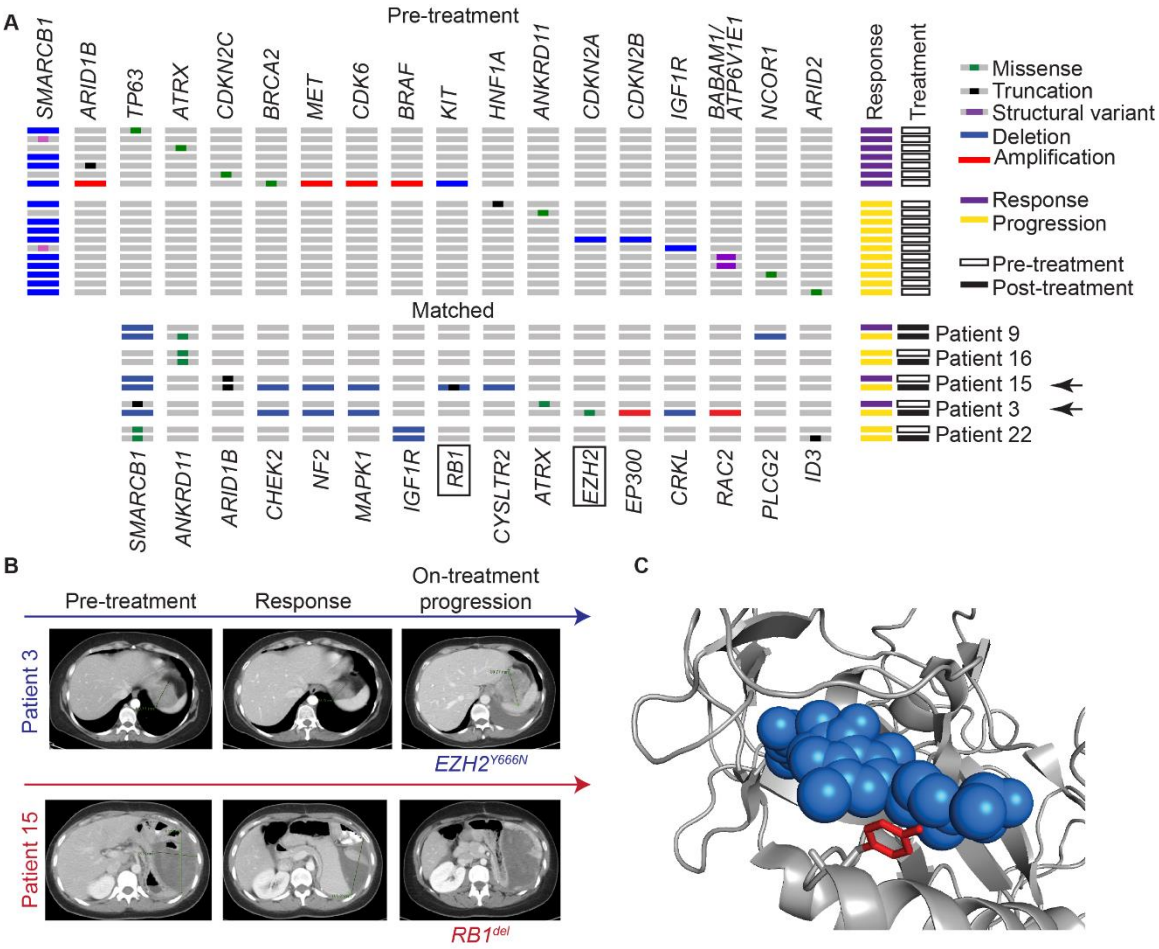

Figure 2.1: Patient tumor sequencing reveals diverse tazemetostat resistance mutations. (**A**) Abridged oncoprint of selected genes from MSK-IMPACT sequencing on patient tumor samples. Top panel: Tumor samples prior to TAZ treatment. Bottom panel: Matched samples pre- and post-TAZ or pre- and post-acquisition of resistance. (**B**) Pre- and post- treatment CT imaging of the indicated patient tumors which acquired *EZH2* and *RB1* mutations. (**C**) Atomic molecular model of the chimeric *Homo sapiens/Anolis carolinensis* EZH2 bound to pyridone-based EZH2 inhibitor I (blue), PDB: 5IJ7. Y666 is highlighted in red.

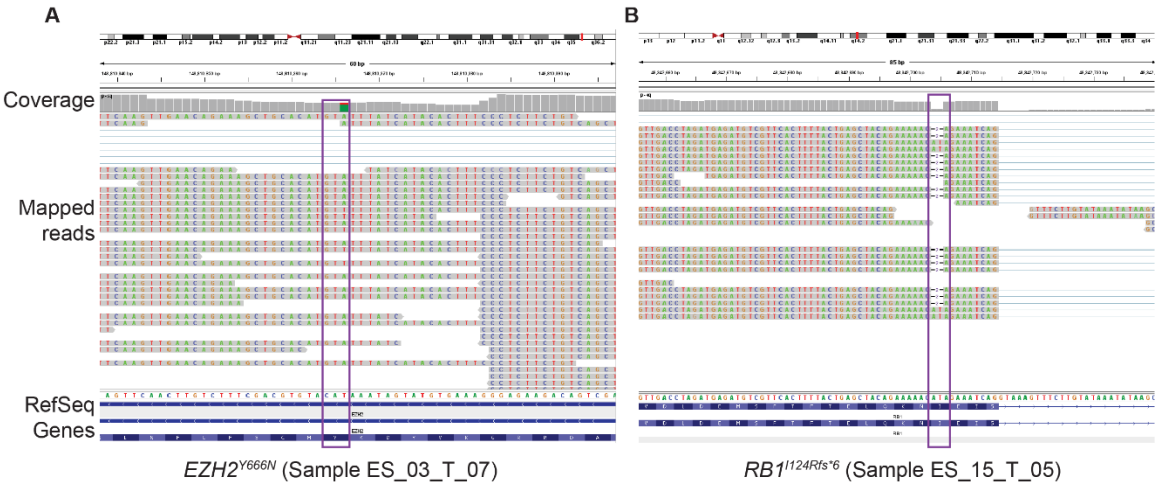

Figure 2.2: Validation of tumor resistance mutations: (**A-B**) Integrated Genome Viewer (IGV) tracks of RNA-seq data for post-treatment tumor samples from patients 3 and 15. Purple boxes indicate the mutation sites. (**A**) Aligned reads and coverage plot of exon 16 of *EZH2*, showing expression of mRNA with the T (red) → A (green) mutant allele. (**B**) Aligned reads and coverage plot of exon 3 of *RB1*, showing expression of mRNA with frame shift deletion at I124.

in this study, and thus concordant with the mutation we observed in the Patient 3 tumor (201).

Based on the atomic resolution structure of a pyridone-based EZH2 inhibitor bound to the *Anolis carolinensis* EZH2 (PDB 5IJ7) (132), we reasoned that residue Y666 in human EZH2 may form a critical part of the TAZ binding site and that its mutation can prevent TAZ from binding to the SET domain (**Figure 2.1C**). To test $EZH2^{Y666N}$ as a resistance allele, we expressed doxycycline-inducible $EZH2^{Y666N}$ in *SMARCB1*-deficient G401 rhabdoid tumor cells. We observed that $EZH2^{Y666N}$ expressing clones are resistant to TAZ as compared to cells expressing equal levels of wild-type *EZH2* by assessing both cell viability (**Figure 2.3A**) and cell morphology (**Figure 2.3B**). The resistance phenotype of $EZH2^{Y666N}$-expressing cells depends on the intact catalytic activity of the SET domain, as a compound mutant combining the catalytically inactive triple mutant $EZH2^{F672I,H694A,R732K}$ ($EZH2^{CatMut}$) with the Y666N mutation, termed $EZH2^{QuadMut}$, did not confer resistance to TAZ (**Figure 2.4A**). We also observed that $EZH2^{Y666N}$ confers resistance to the dual EZH1/2 inhibitor valemetostat (203), consistent with putative resistance to SAM-competitive, pyridone-based EZH2 inhibitors (**Figure 2.4B**). This also suggests that combined inhibition of EZH2 and EZH1 may not overcome this type of acquired EZH2 inhibitor resistance.

Previous studies found that lymphoma cells resistant to EZH2 inhibitors remained susceptible to the inhibition of the non-enzymatic PRC2 subunit EED (204), including those with mutations in the *EZH2* SET domain ($EZH2^{C663Y}$ and $EZH2^{Y726F}$) and the D1 domain (202, 205). We therefore hypothesized that TAZ resistance conferred by $EZH2^{Y666N}$ could be overcome by PRC2 inhibitors that do not bind to EZH2. Indeed, we found that the allosteric EED inhibitor MAK683 overcomes $EZH2^{Y666N}$-mediated resistance (134), demonstrating that these cells remain generally susceptible to PRC2 inhibition

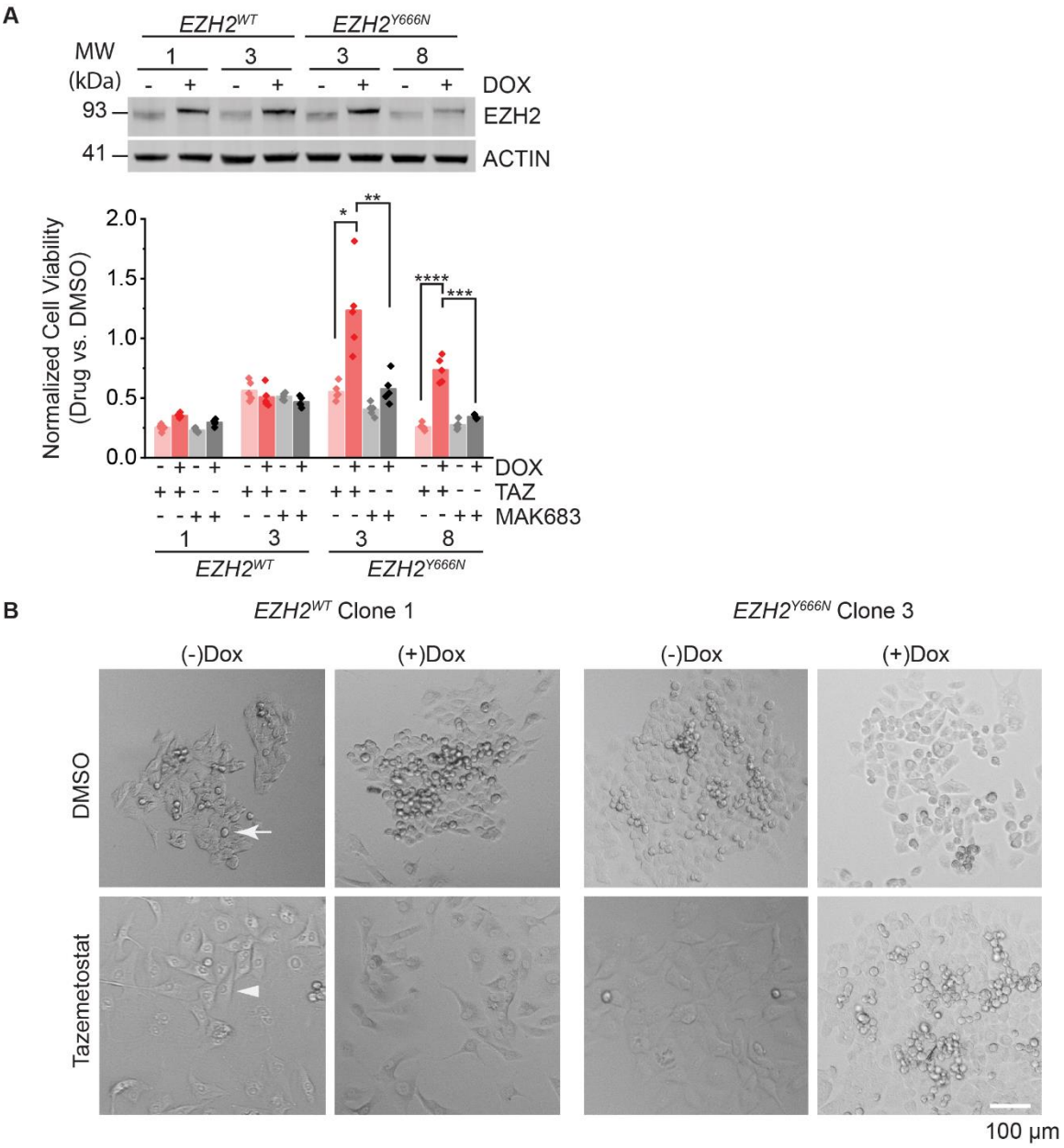

Figure 2.3: *EZH2^{Y666N}* confers resistance to TAZ in vitro: (**A**) Top panel: Doxycycline-inducible *EZH2* is expressed in single-cell G401 clones at near-physiological levels after 3 days treatment with doxycycline at 1 µg/mL. Numbers indicate clone ID. Bottom panel: Cell viability measured by CellTiter-Glo after 14 days of treatment with the indicated drug at 10 µM or equivalent volume of DMSO. n=5 biological replicates per condition. **p* = 3.5E-3, ***p* = 5.2E-3, ****p* = 3.8E-5, *****p* = 1.1E-5 by two-sided Student's t-test. (**B**) Phase-contrast microscopy of G401 single-cell clones expressing the indicated form of *EZH2*. Cells were treated with 10 µM tazemetostat or DMSO for 9 days and imaged with an Evos FL Auto 2 imager at 10X magnification. Arrow indicates a refractile, mitotic cell. Arrowhead indicates a post-treatment, morphologically altered cell.

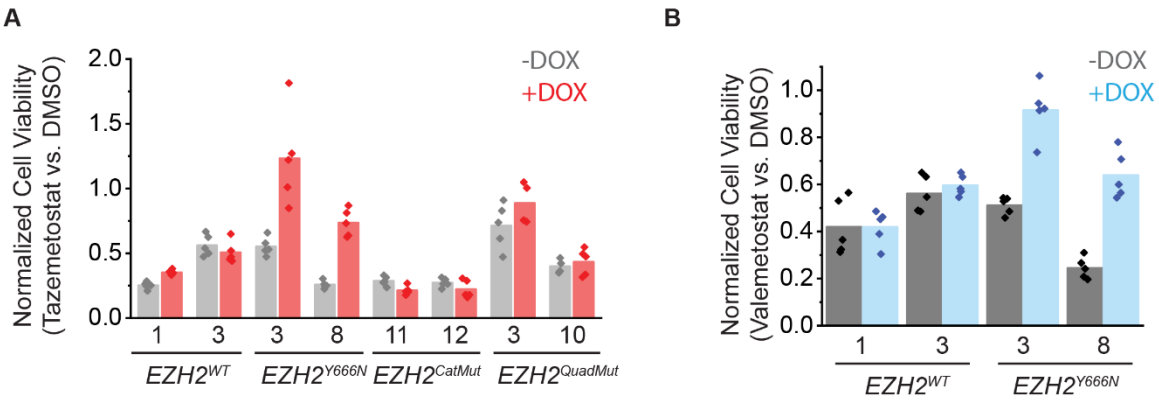

Figure 2.4: *EZH2*^{Y666N} retains catalytic activity: (**A**) Cell viability measured by CellTiter-Glo after 14 days of treatment with 10 µM tazemetostat or equivalent volume of DMSO. Data is the same as in Figure 1D with the addition of *EZH2*^{CatMut} and *EZH2*^{QuadMut} clones. *n*=5 replicates per condition. (**B**) Cell viability after treatment with 10 µM valemetostat or DMSO for 14 days. *n*=5 replicates per condition.

(**Figure 2.3A**). EED inhibition may thus be an effective strategy to overcome acquired TAZ resistance mutations in *EZH2*.

RB1 loss allows escape from cell cycle arrest despite effective EZH2 inhibition

Past work has shown that *EZH2* is a direct target of repression by RB1/E2F (92, 206). This suggests that acquired *RB1* loss may confer resistance to EZH2 inhibition by increasing EZH2 expression. To test $RB1^{del}$ as a TAZ resistance allele, we used CRISPR/Cas9 genome editing to generate biallelic $RB1^{del}$ mutations in G401 cells, as compared to isogenic *RB1*-wild type control cells produced by targeting the safe harbor locus *AAVS1*. We confirmed absence of RB1 protein expression in two independent clones using Western blotting, and found that $RB1^{del}$ cells were indeed resistant to TAZ (**Figure 2.5A**).

Despite *EZH2* being a known target gene of RB1/E2F, we were surprised to observe that $RB1^{del}$ G401 cells showed similar morphological changes upon TAZ treatment (**Figure 2.5B**) to those previously reported for TAZ-treated $RB1^{WT}$ G401 cells (126). To define the effects of TAZ on $RB1^{del}$ cells more precisely, we performed RNA-seq of isogenic G401 $RB1^{del}$ and wildtype *AAVS1*-control cells, treated with either 10 μM TAZ or DMSO control for 11 days, based on an established treatment regimen to model EZH2 inhibition *in vitro* (126). As predicted, we observed that *EZH2* mRNA and protein levels remained high in TAZ-treated $RB1^{del}$ cells, unlike in $RB1^{WT}$ cells (**Figure 2.6A-C, 2.7A**). However, EZH2 inhibition induced significant upregulation of hundreds of genes in both $RB1^{WT}$ and $RB1^{del}$ cells, including upregulation of known PRC2 target genes (**Figure 2.6A-F**).

Importantly, trimethylation of the EZH2 substrate H3K27 was substantially reduced by TAZ regardless of *RB1* status (**Figure 2.7A**). This indicates that despite persistent EZH2 expression, EZH2 methyltransferase activity is effectively inhibited by TAZ despite

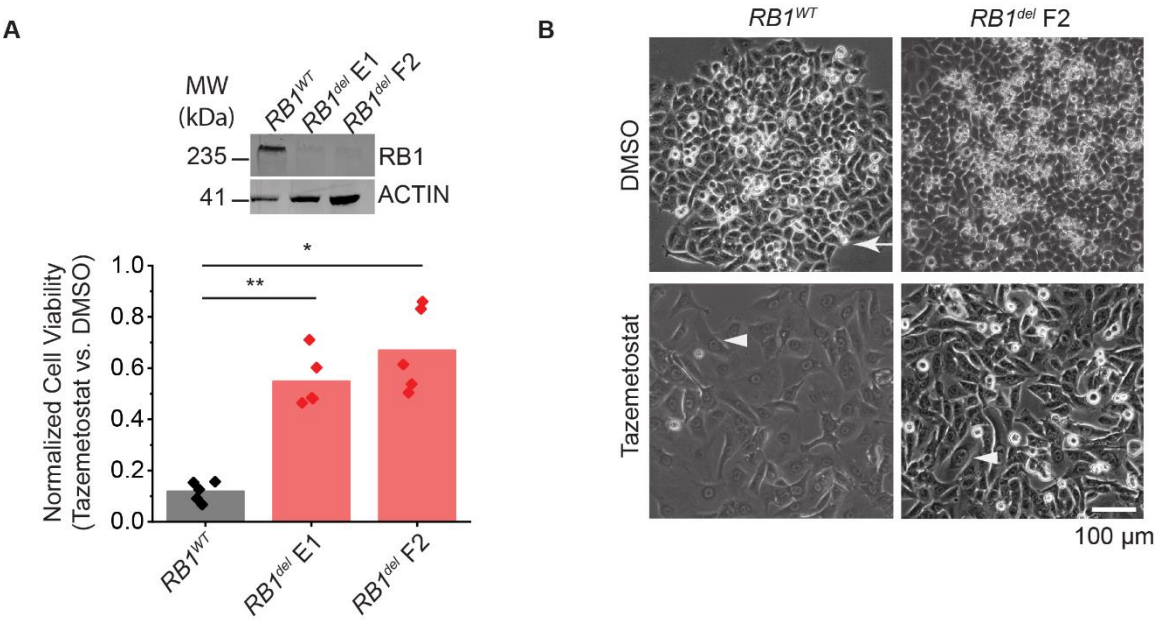

Figure 2.5: *RB1*^{del} confers resistance to TAZ in vitro: (**A**)Top panel: *RB1* knockout in two G401 clones (E1 and F2). Bottom panel: Cell viability measured by CellTiter-Glo after treatment with 10 µM tazemetostat or DMSO for 14 days. *n*=5 biological replicates per condition. **p* = 2.8E-5, ***p* = 9.0E-5 by two-sided Student's t-test. (**B**) Phase-contrast microscopy of G401 cells with or without *RB1* expression. Cells were treated with 10 µM tazemetostat or DMSO for 9 days and imaged with an Evos FL Auto 2 imager at 10X magnification. Arrow indicates a refractile, mitotic cell. Arrowhead indicates a post-treatment, morphologically altered cell.

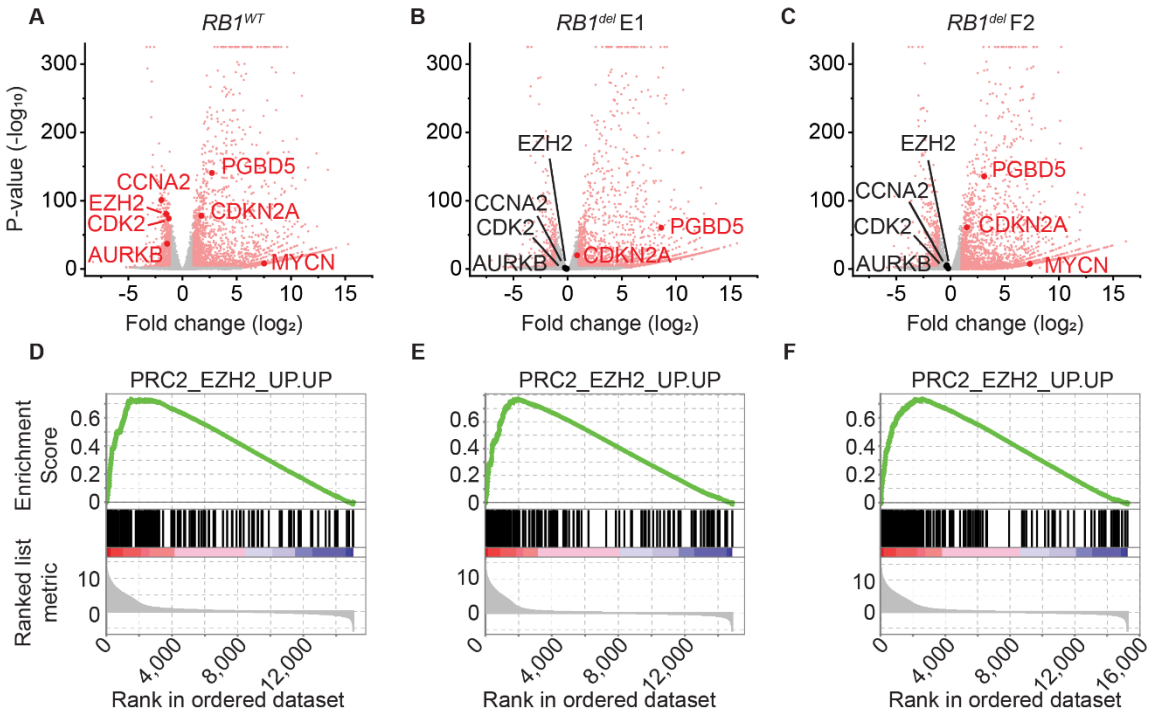

Figure 2.6: *RB1*^{del} show a transcriptional response to TAZ: (**A-C**) Volcano plots of RNA-seq data from TAZ-treated G401 *RB1*^{WT} (**A**), *RB1*^{del} *E1* (**B**), and *RB1*^{del} *F2* (**C**). Plots show gene expression changes of cells treated with 10 μM TAZ versus equivalent volume of DMSO for 11 days. n=3 biological replicates per condition. Dots in red show genes with expression changes of $\log_2$(fold change) > ±1 and *p*-value < 0.01. (**D-F**) GSEA plots showing the PRC2_EZH2_UP.UP gene set for G401 *RB1*^{WT} (**D**), *RB1*^{del} *E1* (**E**), and *RB1*^{del} *F2* (**F**) cells treated in A-C.

RB1 loss. Gene set enrichment analysis (GSEA) showed that all three clones significantly upregulated multiple gene sets upon TAZ treatment (**Figure 2.7B**). This included gene sets associated with cell differentiation such as epithelial-to-mesenchymal transition (EMT; **Figure 2.8A**), as well as specific markers of differentiation such as *MMP2* (**Figure 2.8B**), used previously as a mesenchymal marker induced by *SMARCB1* re-expression in rhabdoid tumor organoids (207). This is reminiscent of recent observations that re-expression of *SMARCB1* in G401 cells can lead to a mesenchymal chromatin state (208), and is consistent with the idea that PRC2 inhibition may allow BAF to re-activate a more developmentally normal gene expression state. We note that *MMP2* was not upregulated by TAZ at the protein level (**Figure 2.8C-D**). However, the induction of mesenchymal genes at the mRNA level does suggest that TAZ induces a transcriptional differentiation program regardless of *RB1* status, even though their protein-level expression is controlled by additional mechanisms. Taken together, these findings indicate that *RB1* loss-induced TAZ resistance is independent of EZH2.

In addition to *EZH2*, additional RB1/E2F target genes were also upregulated in TAZ-treated $RB1^{del}$ cells compared to TAZ-treated $RB1^{WT}$ control cells (**Figure 2.7C-D**). Given the function of RB1 in the regulation of the G1/S cell cycle checkpoint, we hypothesized that *RB1* loss could allow cells to escape TAZ-induced cell cycle arrest. Flow cytometry cell cycle analysis showed that G401 cells treated with 1 μM TAZ arrest at the G1/S checkpoint, as reported previously (126). However, $RB1^{del}$ cells exhibited a significant reduction in the proportion of cells in G1 phase upon TAZ treatment (50% of TAZ-treated $RB1^{WT}$ cells versus 31% and 28% for $RB1^{del}$ E1 and F2 clones, respectively), with a corresponding increase of the proportion of cells remaining in S and G2/M phases (**Figure 2.9A**). In agreement with this, we observed persistent mRNA expression of S/G2/M-phase-associated *CCNA2*, *CDK2*, and *AURKB* genes in $RB1^{del}$ cells upon TAZ treatment (**Figure 2.6A-C**). This is despite upregulation of the CDK4/6 inhibitor *CDKN2A*

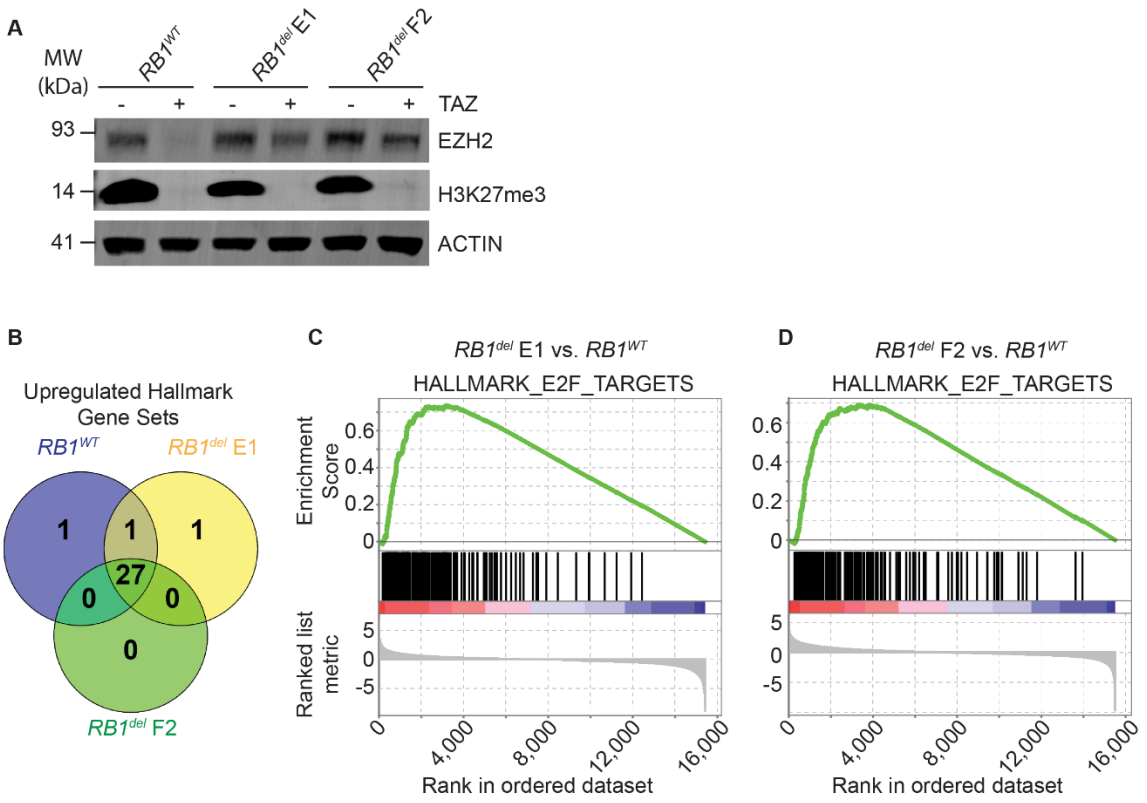

Figure 2.7: *RB1*^{del} show loss of H3K27me3 upon TAZ treatment: (**A**) Western blot of the indicated G401 cell clones treated with 10 µM TAZ vs. equivalent volume of DMSO for 11 days. Bulk H3K27me3 levels are reduced in all three clones despite persistent EZH2 expression in *RB1*^{del} clones. (**B**) Comparison of all Hallmark gene sets upregulated in G401 cells upon TAZ treatment with significance at FDR < 25%. (**C-D**) GSEA plots showing the Hallmark_E2F_Targets gene set comparing TAZ-treated *RB1*^{del} G401 cells with *RB1*^{WT} cells.

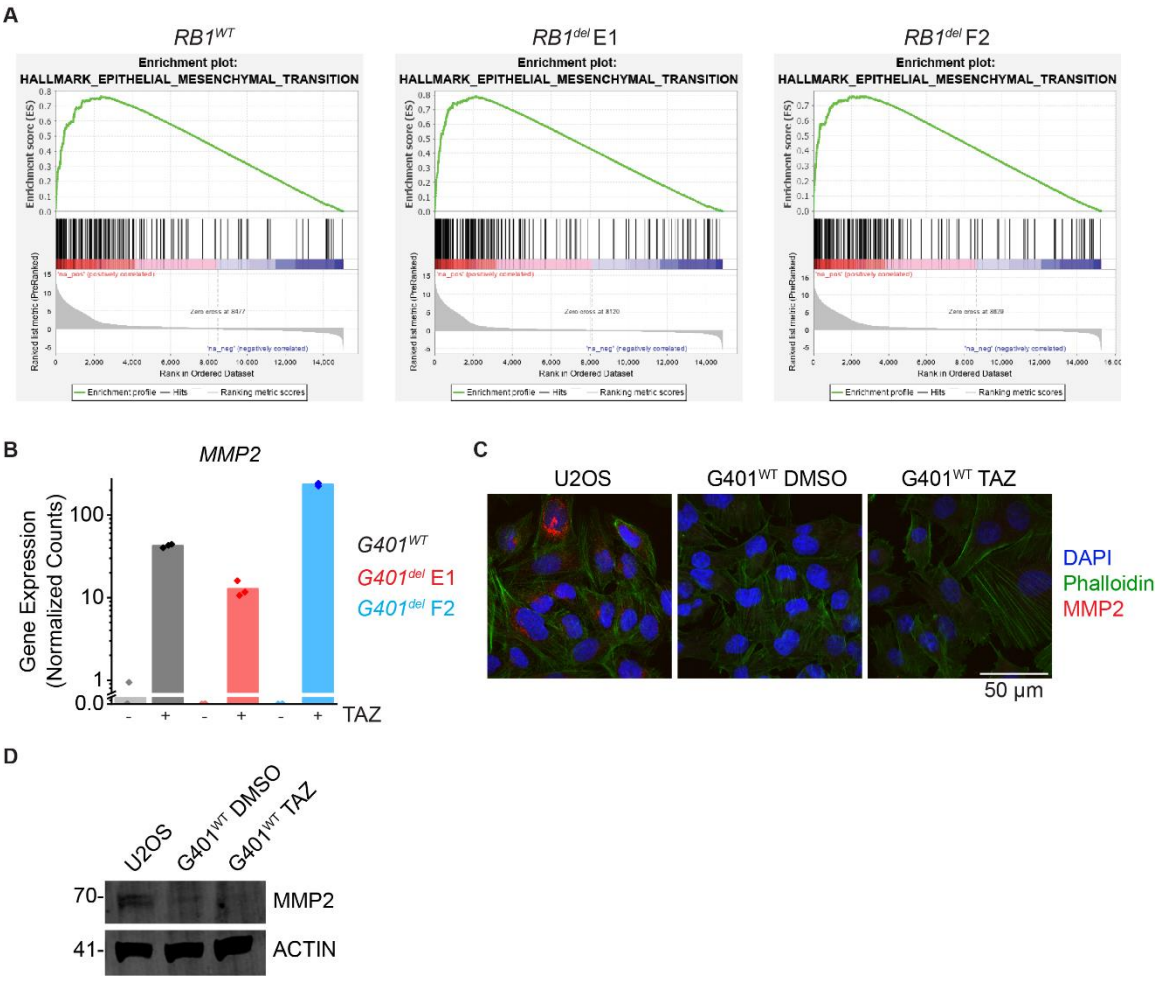

Figure 2.8: TAZ-treated *RB1*^{del} cells show evidence of differentiation at the transcript, but not protein level. (**A**) GSEA plots showing the Hallmark_Epithelial_Mesenchymal_Transition gene set for the indicated TAZ-treated G401 cells compared to DMSO. (**B**) RNA-seq data from cells in Figure 2.6A-F, showing normalized read counts for the *MMP2* gene. (**C**) Indicated cells treated with 1 µM TAZ for 11 days, stained with MMP2 antibody. U2OS cells are shown as a positive control. (**D**) MMP2 western blot on cells treated as in (B).

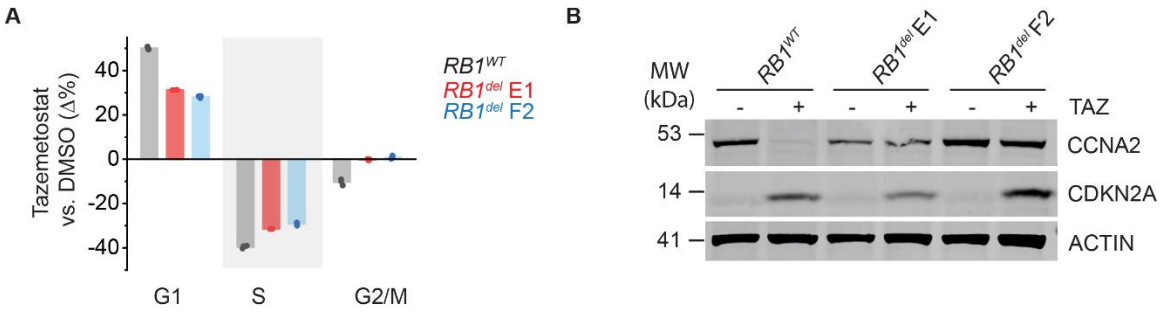

Figure 2.9: *RB1* loss allows escape from cell cycle arrest despite effective EZH2 inhibition: (**A**) Cell cycle analysis of the indicated G401 clone. Plot shows triplicate measurements of cells treated with 1 µM TAZ versus equivalent volume of DMSO for 11 days. Y-axis shows the percent difference of the TAZ-treated cells in each cell cycle phase compared to DMSO-treated cells. (**B**) Western blot of the indicated G401 cell clones treated with 10 µM TAZ versus equivalent volume of DMSO for 11 days. Actin serves as loading control.

(p16), a known PRC2 target in MRT (87, 89, 209), upon TAZ treatment in both *RB1*^{WT} and *RB1*^{del} cells (**Figure 2.6A-C**). We confirmed persistent maintenance of S-phase cyclin A2 (CCNA2) protein levels despite p16 upregulation using Western blotting (**Figure 2.9B**). Together, these results show that *RB1* loss is sufficient to evade TAZ-induced cell cycle arrest at the G1/S restriction point despite maintaining the expected global transcriptional response to EZH2 inhibition, including upregulation of cell cycle inhibitor genes.

Intact RB1/E2F axis is required for TAZ susceptibility

The requirement for *RB1* expression in the therapeutic response to TAZ suggests that an intact RB1/E2F axis may be a general requirement for effective EZH2 inhibitor therapy. This would predict that other genetic and epigenetic perturbations to the RB1/E2F axis, beyond *RB1* loss itself, would similarly confer escape from TAZ-induced cell cycle arrest. Analysis of our TAZ clinical trial treatment cohort revealed one patient tumor specimen with primary resistance to TAZ with intact *RB1* but inactivating mutations of both *CDKN2A* and *CDKN2B* (**Figure 2.1A**, **Supplementary Tables S1-2**), both of which are known to inhibit CDK4/6-mediated phosphorylation of RB1. Two additional specimens had missense mutations in *ANKRD11*: One tumor with primary resistance to TAZ and another which initially responded but later progressed on treatment, at which point a newly acquired *ANKRD11* mutation was detected (**Figure 2.1A**- Patients 9 and 16, respectively). *ANKRD11* is a known TP53 cofactor and putative tumor suppressor that contributes to TP53-mediated expression of pan-CDK inhibitor *CDKN1A* (210-212). *CDKN1A* itself is also known to be a PRC2 target in tumors (110, 213, 214), although its role in the response to EZH2 inhibition in *SMARCB1*-deficient sarcomas is currently unknown. These results converge on the dysregulation of the RB1/E2F axis as a mechanism of evasion of TAZ-induced cell cycle arrest.

To investigate the functional determinants of tumor cell response to TAZ, we first analyzed the response to TAZ of seven MRT and four ES cell lines in which we confirmed loss of SMARCB1 protein expression in all ES and MRT cell lines using Western blotting, as compared to SMARCB1-expressing HEK293T cells (**Figure 2.10A**). We classified each line as sensitive or resistant based on the area under the curve (AUC) of their TAZ dose responses (AUC > 0.3 for sensitive G401, KP-MRT-NS, TTC642, A204, TM8716, KP-MRT-RY cell lines and AUC ≤ 0.3 for resistant ES1, VAESBJ, ES2, EPI544, MP-MRT-AN cell lines; **Figure 2.10B**). Given that TAZ treatment requires at least 4 days for the cellular reduction of methylated EZH2 substrates and at least 7 days for apparent antiproliferative effects in the rapidly-dividing G401 cell line (126), we confirmed that the apparent TAZ susceptibilities of these MRT and ES cell lines are not correlated with their proliferation rates (Pearson's r = -0.073 and p = 0.81; **Figure 2.10C**). In agreement with somatic mutations affecting the RB1/E2F axis associated with TAZ resistance in clinical tumor specimens (**Figure 2.1A**), we found mutations of *CDKN2A* in 4 out of 5 TAZ-resistant cell lines, *CDKN2B* in 2 out of 5 resistant cell lines, *CDKN1A* in 1 out of 5, and *ANKRD11* in 3 out of 5, as compared to no such mutations in any TAZ-sensitive MRT and ES cell lines (**Figure 2.11A, Supplementary Table S3**). While our analysis detected reduction in copy number of *RB1* in TAZ-sensitive KP-MRT-RY cells, manual inspection of sequencing reads within the *RB1* gene revealed lack of homozygous deletion, with presumed retention of *RB1* expression (**Figure 2.11C**). Thus, mutations associated with the RB1/E2F axis are associated with resistance to TAZ in *SMARCB1*-deficient cell lines and patient tumors.

To assess whether the detected mutations were associated with changes in cell cycle proteins upon TAZ treatment, we tested 4 TAZ-sensitive and 4 TAZ-resistant cell lines. In all 4 sensitive cell lines, TAZ induced upregulation of p16, as well as reduction in CCNA2 and EZH2. However, p16 was induced in none of the TAZ-resistant lines, and we observed no change in CCNA2 and EZH2 protein expression (**Figure 2.11B**).

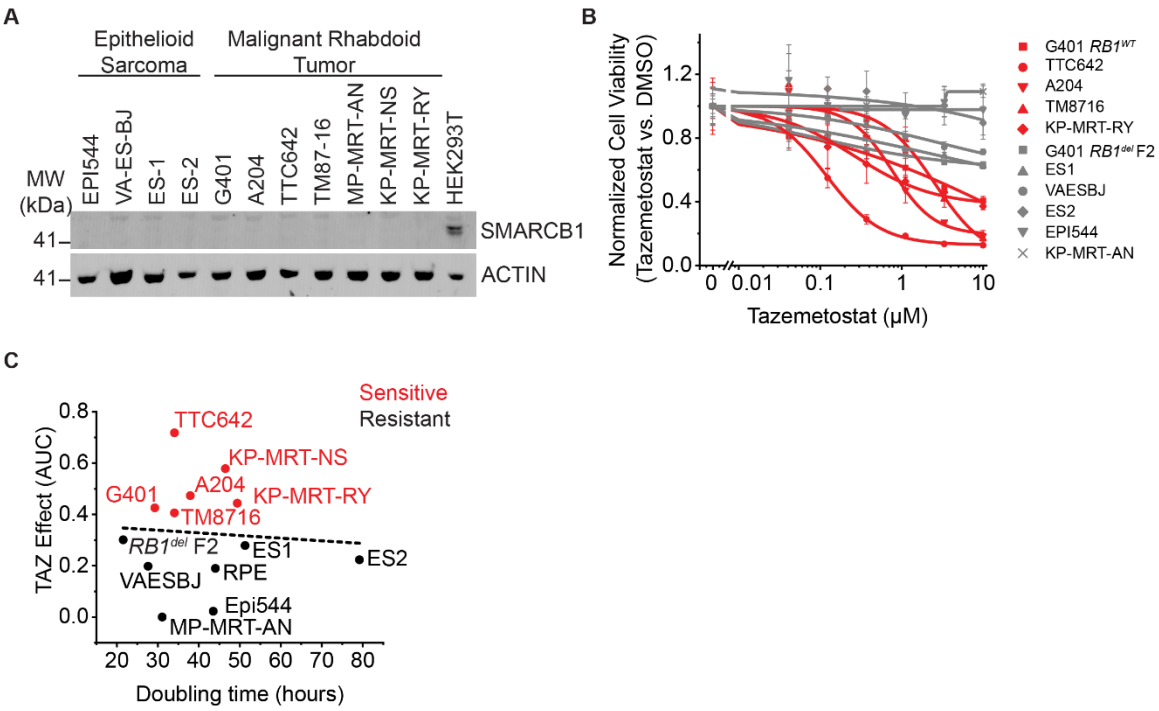

Figure 2.10: Characterization of MRT and ES cell lines: (**A**) Confirmed loss of SMARCB1 expression in all MRT and ES cell lines used. (**B**) Dose-response curves of a panel of MRT and ES cell lines treated with TAZ for 13 days. Curves in red correspond to TAZ-responsive cell lines, grey to TAZ-resistant cell lines. (**C**) Plot of area under the curve (AUC) of the dose-response curves from Figure 3A plotted against doubling time. AUC was integrated from 40 nM to 50 μM.

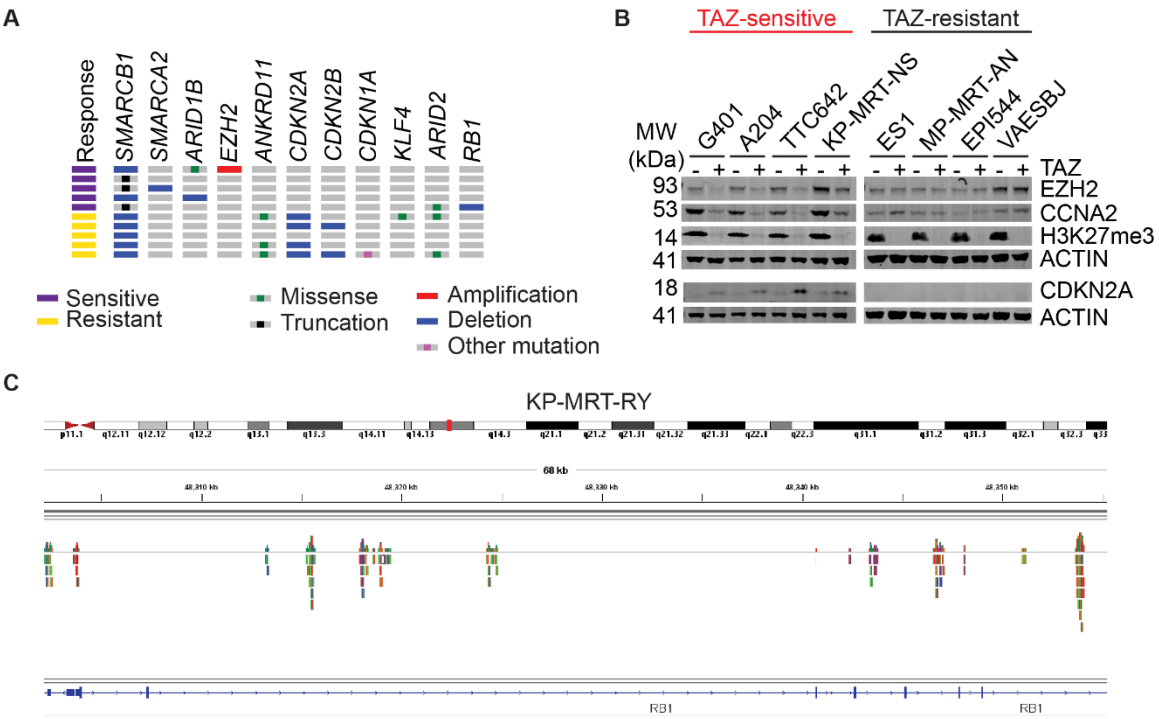

Figure 2.11: An intact RB1/E2F axis is a key requirement for response to TAZ: (**A**) Abridged oncoprint of MRT and ES cell lines. Genes included here are BAF subunits and CDK4/6/RB1/E2F axis genes. (**B**) Western blots of the indicated cell lines treated with 10 µM TAZ or equivalent volume of DMSO for 11 days. (**C**) IGV track of reads from MSK-IMPACT sequencing of KP-MRT-RY cells, focusing on the *RB1* gene, shows reads spanning segments across the full gene and indicates the presence of at least one allele.

We next assessed the apparent transcriptional activity of the RB1/E2F axis in patient tumors using quantitative gene expression analysis of TAZ responding and non-responding tumors biopsied before and after TAZ treatment using RNA-seq (**Supplementary Table S1**). Pre-treatment TAZ-resistant tumors exhibited significant enrichment of multiple Gene Ontology (GO) terms associated with the cell cycle and in particular with the S and G2/M phases (**Figure 2.12A**). Similarly, post-treatment tumors that progressed on TAZ showed increased gene expression of GO terms associated with mitosis, as compared to TAZ-responsive tumors (**Figure 2.12B**). Indeed, TAZ-resistant tumors exhibited consistently higher expression of S/G2/M-phase-associated genes prior to treatment (**Figure 2.12C-D**). These findings suggest that in addition to the mutations affecting the RB1/E2F axis associated with TAZ resistance, additional mutations not captured by MSK-IMPACT targeted gene sequencing and/or epigenetic dysregulation, such as putative silencing of tumor suppressor genes like *CDKN1A* or *CDKN2A*, likely contribute to TAZ resistance and the decoupling of RB1/E2F-mediated proliferation and PRC2-regulated differentiation.

Since TAZ-resistant MRT and ES cell lines and patient tumors show distinct mutations and gene expression changes that converge on the RB1/E2F axis, we inquired whether these perturbations would similarly converge on common prognostic biomarkers of TAZ resistance. Comparative gene expression analysis of untreated $RB1^{del}$ cells versus $RB1^{WT}$ G401 cells showed a small set of consistently and significantly up- and down-regulated genes in two independent clones (**Figure 2.13A**). The most substantially and significantly upregulated gene associated with *RB1* loss was *PRICKLE1* (**Figure 2.13B-C**), which we confirmed to be overexpressed at the protein level in both $RB1^{del}$ clones using Western blotting (**Figure 2.13D**).

In agreement with this, we also found that *PRICKLE1* was among the most differentially expressed genes between 10 pre-treatment patient tumors with response and

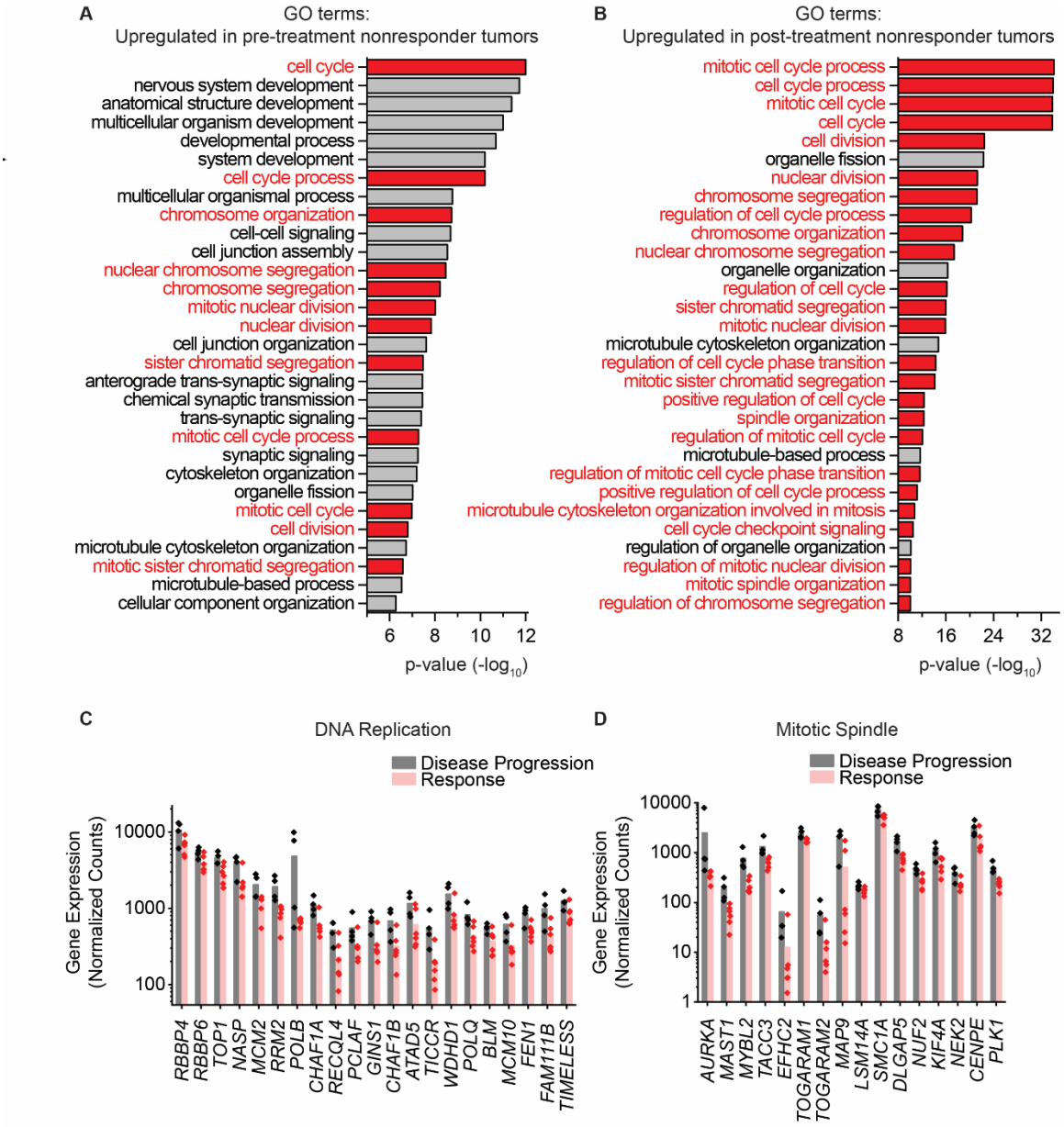

Figure 2.12: TAZ-resistant patient tumors show upregulation of cell cycle genes: Top 30 GO terms, sorted by p-value, enriched in pre-treatment (**A**) and post-treatment (**B**) patient tumor specimens that did not respond to TAZ, compared to those that did. (**C-D**) DESeq2-normalized read counts of genes from the indicated GO terms comparing pre-treatment TAZ-responding tumors to pre-treatment non-responding tumors.

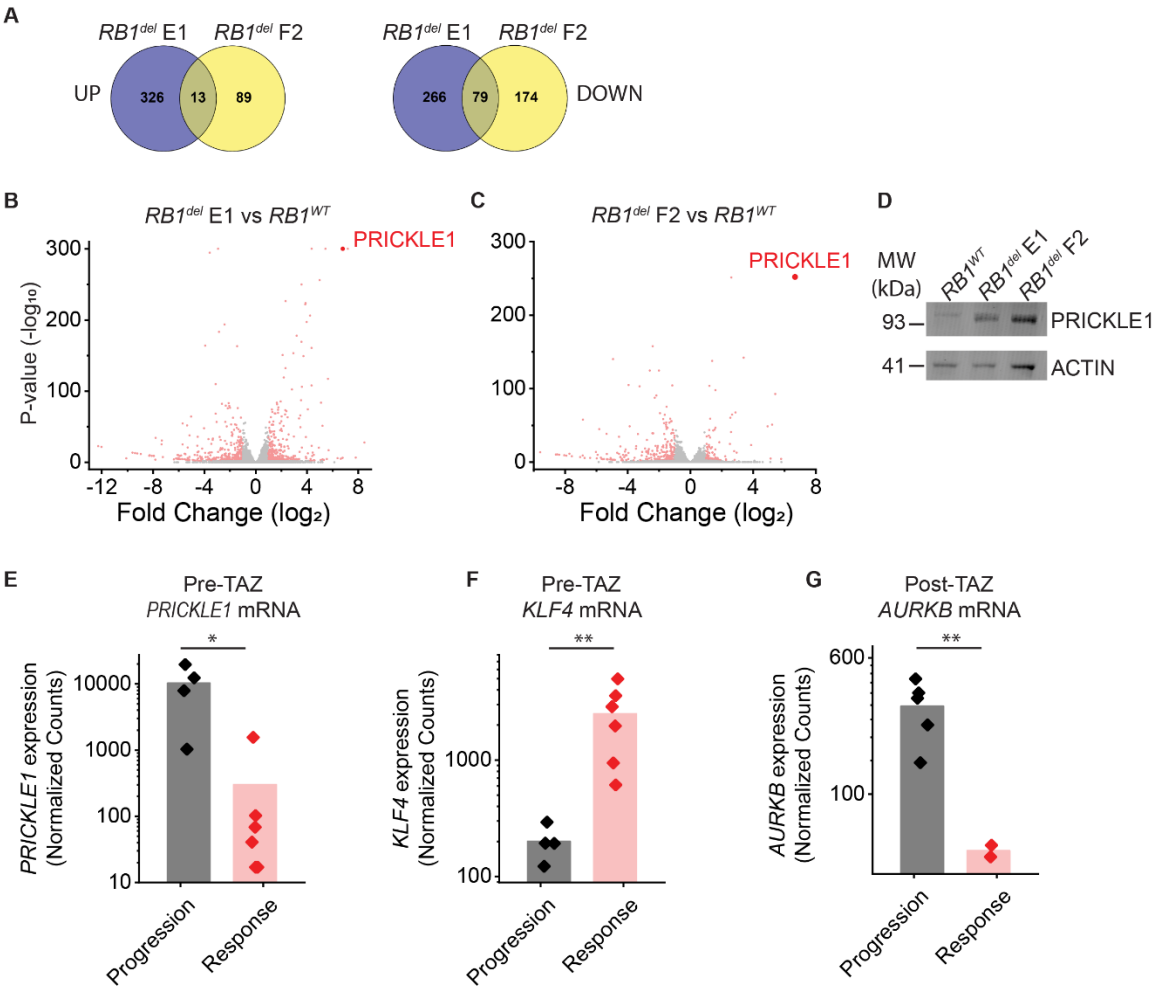

Figure 2.13: Potential biomarkers of TAZ response and resistance: (**A**) Venn diagrams of genes up- or down-regulated by *RB1* knockout in the indicated clone. Same data as in Figure 2.6. (**B-C**) Volcano plots of RNA-seq data comparing DMSO-treated G401 *RB1*^{del} E1 (**B**) and F2 (**C**) with *RB1*^{WT} cells. (**D**) Western blot for PRICKLE1 in untreated G401 cells. (**E-F**) Read counts for *PRICKLE1* (**E**) and *KLF4* (**F**) showing counts normalized by DESeq2 for patient tumor samples collected prior to TAZ treatment. (**G**) Read counts for *AURKB* for patient tumor samples collected after TAZ treatment. **p*=0.013, ***p*=0.03.

resistance to TAZ, with *PRICKLE1* expression being higher in TAZ-resistant tumors (mean normalized reads = 10,237 and 300 for resistant and responsive tumors, respectively; Student's t-test $p = 0.013$; **Figure 2.13E, 2.14A**). *PRICKLE1* can control planar cell polarity (PCP), a key cell differentiation pathway, and has previously been implicated as a prognostic biomarker of poor prognosis in breast cancer (215, 216), acute myeloid leukemia (217), and gastric cancer (218, 219). Several other genes encoding PCP pathway factors were also upregulated in TAZ-resistant tumors compared to TAZ-sensitive tumors (**Figure 2.14A**). We next looked for differentially expressed genes in TAZ-sensitive tumors as potential markers of sensitivity. These included the transcription factor *KLF4* which can control the G1/S transition by regulating *CDKN1A* expression (220, 221) (mean normalized reads = 200 and 2,489 for resistant and responsive tumors, respectively; Student's-test $p = 0.03$; **Figure 2.13F, 2.14B**). Thus, PRICKLE1 and additional factors controlling PCP and integration of RB1/E2F cell cycle and differentiation are potential prognostic pre-treatment biomarkers to identify clinical TAZ resistance and susceptibility of *SMARCB1*-deficient tumors.

Synthetic lethal and cell cycle bypass epigenetic combination strategies overcome tazemetostat resistance

Given that $RB1^{del}$ cells are able to bypass cell cycle arrest at the G1/S checkpoint, we reasoned that inhibiting cell cycle kinases downstream of this checkpoint could overcome TAZ resistance. In particular, cell cycle kinases *CDK2* and *AURKB*, which are downregulated by EZH2 inhibition in TAZ-sensitive cells but persistently expressed in TAZ-resistant cells, may offer especially compelling therapeutic targets to overcome TAZ resistance (**Figure 2.6A-C**). Indeed, we found that the CDK2 inhibitor seleciclib (222), as well as the mitotic kinase Aurora A inhibitor alisertib (223), and Aurora B inhibitor barasertib (224), were able to overcome TAZ resistance in $RB1^{del}$ G401 cells (**Figure**

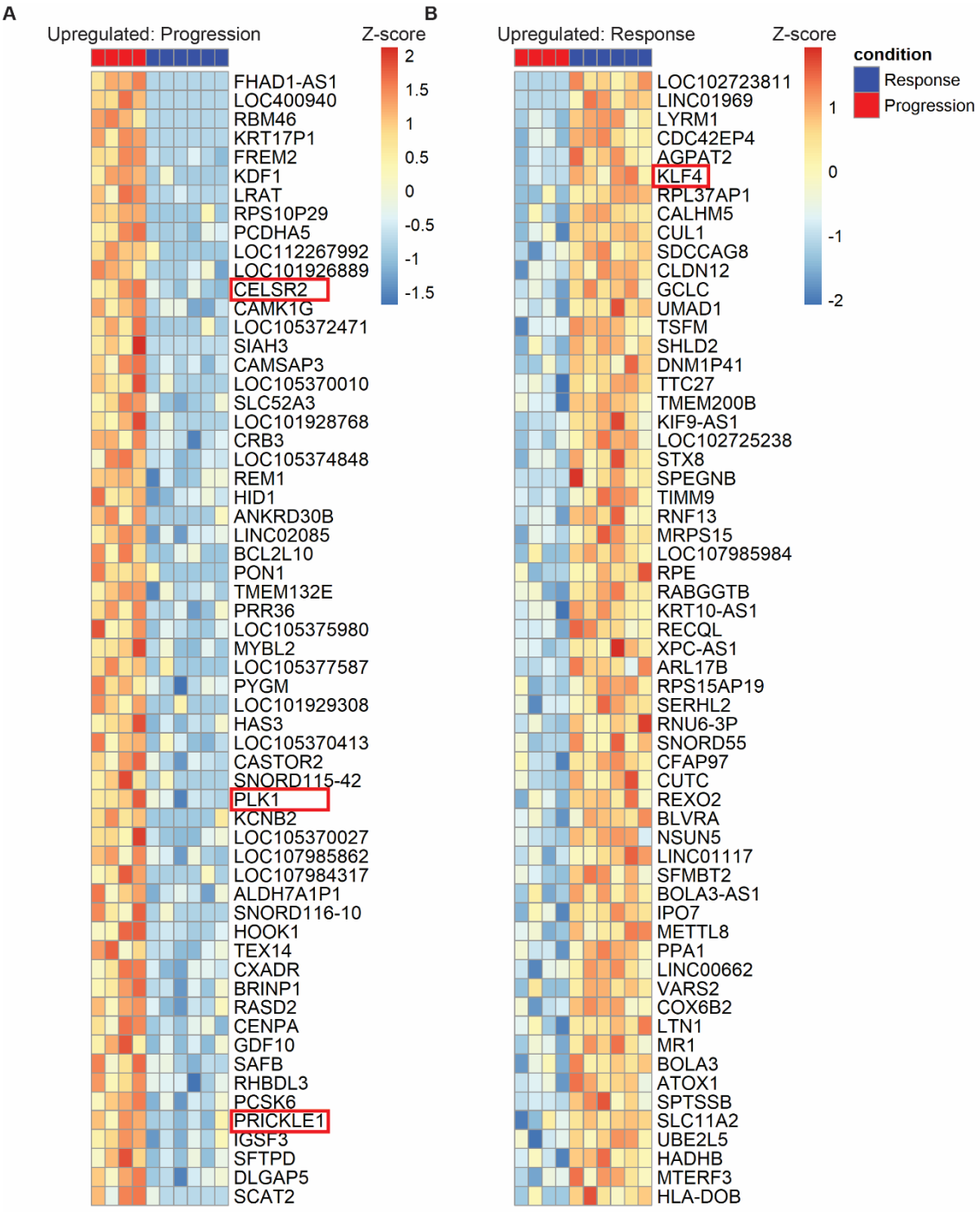

Figure 2.14: Transcriptomic analysis of patient tumors nominates putative biomarkers of TAZ sensitivity and resistance: (**A-B**) Heatmaps showing the top 60 upregulated (**A**) and downregulated (**B**) genes in patient tumors collected prior to TAZ-treatment. Each column indicates a separate tumor. Heatmaps are sorted by t-statistic calculated using a two-tailed Student's t-test, $p<0.05$. Red boxes indicate planar cell polarity genes *CELSR2*, *PLK1*, and *PRICKLE1* and *CDKN1A* regulator *KLF4*.

2.15A-B, Figure 2.16A). We term this combination strategy cell cycle bypass. Consistent with the function of CDK4/6 kinases upstream of RB1/E2F, sensitivity to CDK4/6 inhibitors palbociclib and abemaciclib was reduced by *RB1*^{del} mutation (**Figure 2.15C-D**). In support of the cell cycle bypass strategy for TAZ combination therapy, we observed that patient tumors which progressed on TAZ showed higher expression of *AURKB* mRNA as compared to those that responded (**Figure 2.13G**). Combined with the high sensitivity of G401 cells to barasertib (**Figure 2.16A**; half-maximal effective concentration of 6.5 ± 0.5 nM, 5.5 ± 0.6 nM, and 5.9 ± 0.9 nM for *RB1*^{WT}, *RB1*^{del} E1, and F2 clones, respectively), these findings suggest that the cell cycle bypass strategy may effectively overcome TAZ resistance.

We therefore asked whether the combination of TAZ and barasertib would have activity against both TAZ-responsive and TAZ-resistant *SMARCB1*-deficient MRT and ES cell lines, using RPE cells as a *SMARCB1*-proficient control. The effects of the combination of TAZ and barasertib on cell viability did not substantially exceed the effect of barasertib alone at the doses tested (**Figure 2.16B**; 200 nM TAZ, 8 nM barasertib). However, nearly all cell lines tested, including those resistant to TAZ monotherapy, showed substantial susceptibility to barasertib, with RPE cells displaying the lowest sensitivity (**Figure 2.16B**). Cell cycle analysis on G401 cells treated with this combination showed that the TAZ + barasertib caused a greater cell cycle arrest than either drug alone, as measured by EdU incorporation (**Figure 2.17A**). This was the case in both *RB1*^{WT} and *RB1*^{del} cells, consistent with our predictions that cell cycle inhibition downstream of the G1/S checkpoint would cause cell cycle arrest even in cells with *RB1* loss (**Figure 2.17A**). The reduced S phase incorporation was not a result of apoptosis as measured by cleaved caspase 3 staining (**Figure 2.17B-C**). In agreement with previous studies (225), barasertib induced polyploidy as evidenced by giant, multinucleated cells (**Figure 2.17C**), suggesting that cells exit mitosis and proceed into S-phase, leading to mitotic catastrophe.

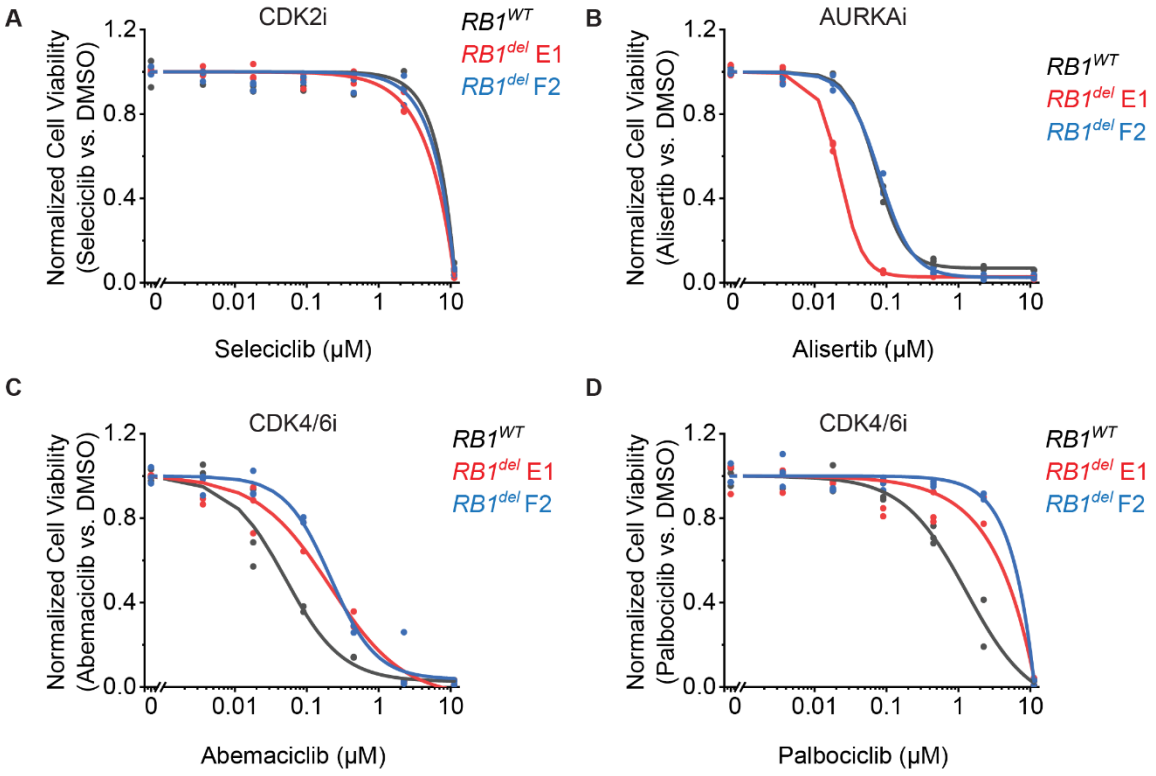

Figure 2.15: Downstream cell cycle inhibitors overcome resistance to TAZ: G401 cells treated with seleciclib (**A**), alisertib (**B**), abemaciclib (**C**), or palbociclib (**D**) 9 days.

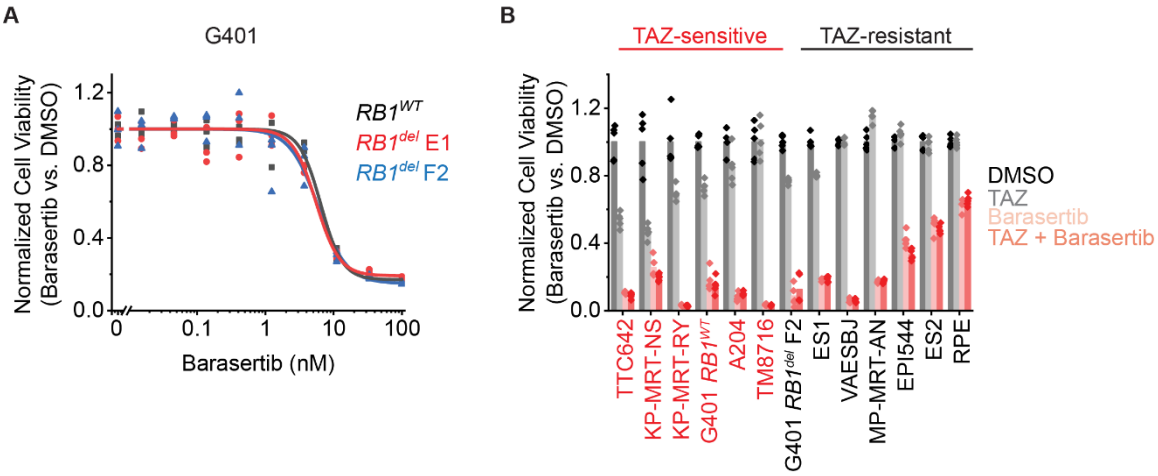

Figure 2.16: Cell cycle bypass combination strategy using AURKB inhibition overcomes TAZ resistance and improves response: (**A**) G401 cells treated with barasertib for 6 days (**A**). (**B**) Panel of MRT and ES cell lines ordered left to right by decreasing response to TAZ monotherapy. Cells were treated with the indicated monotherapy or combination for 11 days. Drug concentrations used were: TAZ: 200 nM, barasertib: 8 nM.

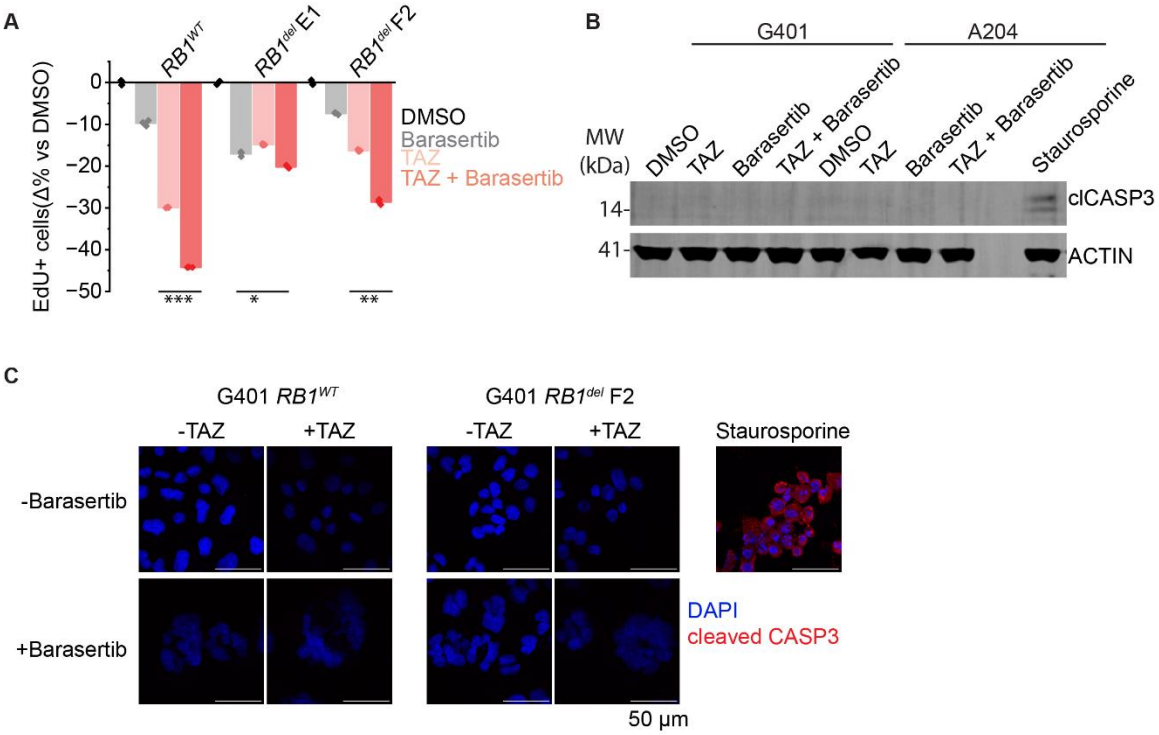

Figure 2.17: Cell cycle bypass combination strategy using AURKB inhibition causes cell cycle arrest and polyploidy: (**A**) Triplicate measurements of cells treated with 1 µM TAZ versus equivalent volume of DMSO for 8 days, followed by 3 days of combination treatment with 12 nM barasertib. Y-axis shows the percent change in EdU positive cells versus DMSO. **p*=1.4E-3, ***p*=5.3E-6, ****p*=2.2E-9. (**B-C**) Cleaved caspase 3 western blot (**B**) and immunofluorescence (**C**) in G401 and A204 cells treated as in (A). Staurosporine treatment for 0.5 µM staurosporine for 6 h was used as a positive control.

To test the effects of this combination *in vivo*, we treated a panel of five patient-derived rhabdoid tumor and epithelioid sarcoma xenografts (PDX) in immunodeficient mice (**Supplementary Table S4**), comparing TAZ and barasertib monotherapies with their combination. Importantly, in contrast to the modest reduction of tumor growth and extension of survival of mice with tumors <1,000 mm^3 with TAZ or barasertib alone, PDX mice treated with the combination of TAZ and barasertib showed significant reductions in tumor growth (Vardi *U*-test p = 4.0E-4 and 2.0E-4 for combination versus barasertib or TAZ, respectively; **Figure 2.18A**) (226). In two of the PDX models, this combination led to tumor regressions (**Figure 2.18C-E**). Consistent with this benefit, the combination was also found to significantly increase mean tumor-free animal survival from 65 days (95% confidence interval (CI) = 51-78 days) for barasertib and 67 days (95% CI = 53-81 days) for TAZ to 98 days (95% CI = 84-112 days) for the combination (log-rank test p = 3.3E-3 and 5.8E-3 for combination versus barasertib or TAZ, respectively; **Figure 2.18B**). These results indicate that the combination of TAZ with a downstream cell cycle inhibitor such as barasertib can improve response and overcome resistance to TAZ in diverse rhabdoid tumors and epithelioid sarcomas *in vivo*.

In addition to distinct cell cycle dynamics of TAZ resistance, we observed that regardless of *RB1* status, TAZ treatment also caused significant increase in expression of *PiggyBac transposable element derived 5* (*PGBD5)* (**Figure 2.6A-C**). *PGBD5* is a transposase-derived gene with retained nuclease activity in human cells, which has been implicated as a somatic mutator and inducer of double-strand DNA (dsDNA) breaks in childhood solid tumors (227-229). In rhabdoid tumors in particular, PGBD5 was observed to induce sequence-specific mutations and DNA rearrangements, including somatic deletions of *SMARCB1* itself (227). In turn, *PGBD5* expression was both necessary and sufficient to confer a cellular dependency on end-joining DNA repair and ATR kinase signaling (228).

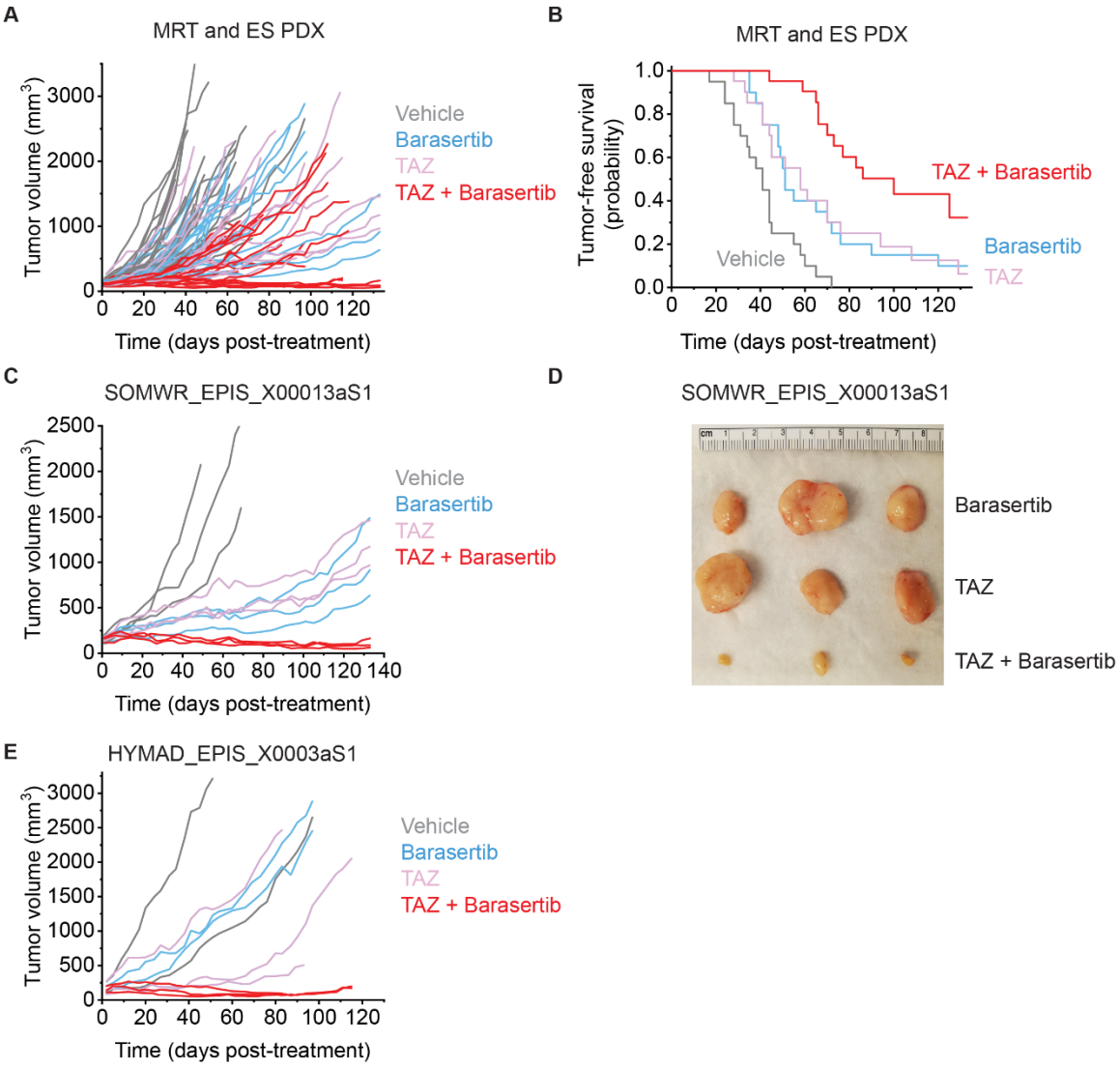

Figure 2.18: Cell cycle bypass combination strategy using AURKB inhibition *in vivo*: (**A**) Tumor growth curves showing volumes calculated from caliper measurements for 5 mouse PDXs treated with the indicated drug regimen. n = 20 mice for vehicle and barasertib-treated groups, n = 21 for TAZ and TAZ + barasertib-treated groups. Vardi *U*-test p = 4.0E-4 and 2.0E-4 for combination vs. barasertib or TAZ, respectively. (**B**) Kaplan-Meier curves showing tumor-free survival (defined as tumor volume ≤ 1,000 mm^3) for the PDXs in panel A. Mean survival is 65 days (95% CI: 51-78 days) for barasertib, 67 days (95% CI: 53-81 days) for TAZ, 98 days (95% CI: 84-112 days) for the combination. Log-rank test p = 3.3E-3 and 5.8E-3 for combination vs. barasertib or TAZ, respectively. (**C**) Tumor growth curves for the subset of mouse tumors in panel A from the SOMWR_EPIS_X00013aS1 PDX model. n = 3 mice per treatment group. Vardi *U*-test p = 0.10 and 9.4E-2 for combination vs. barasertib or TAZ, respectively. (**D**) Tumors from panel C harvested on Day 135 of treatment. (**E**) Tumor growth curves for the subset of mouse tumors in Figure 4C from the HYMAD_EPIS_X0003aS1 PDX model. n = 2 mice for vehicle and barasertib-treated groups, n = 3 mice for TAZ and TAZ + barasertib-treated groups.

TAZ-induced upregulation of *PGBD5* expression suggests that TAZ treatment may potentiate this synthetic lethal dependency. To test this idea, we used the ATR-selective kinase inhibitor elimusertib, which is currently undergoing clinical trials in patients with solid tumors, including patients with PGBD5-expressing tumors such as MRT and ES (Clinical Trials Identifier NCT05071209). We found that elimusertib exhibited low-nanomolar potency against *RB1*^{WT} and *RB1*^{del} G401 cells *in vitro* (half-maximal effective concentration of 17.6 ± 1.6 nM, 19.2 ± 3.8 nM, and 26.7 ± 3.2 nM for *RB1*^{WT}, *RB1*^{del} E1 and F2 clones, respectively; **Figure 2.19A**). We also found that the combination of TAZ and elimusertib exerted greater antitumor effects than either drug alone against diverse MRT and ES cell lines (**Figure 2.19B**), exhibiting synergy in a subset of the cell lines (**Figure 2.19C-D**). To determine whether the synergistic elimusertib and TAZ combination antitumor effects were due to increased DNA damage, we used confocal immunofluorescence microscopy to quantify γH2AX phosphorylation, a specific marker of dsDNA breaks (230). In agreement with prior studies (228), untreated G401 cells showed dsDNA breaks associated with baseline *PGBD5* expression (**Figure 2.20A**). Consistent with TAZ-mediated induction of *PGBD5* expression (**Figure 2.6A-C**), we found that TAZ treatment alone significantly increased nuclear γH2AX fluorescence (median normalized level = 0.061 versus 0.12, respectively; *t*-test *p* = 1.7E-8; **Figures 2.20B & 2.21**), and the combination of TAZ and elimusertib induced additional dose-dependent increases in dsDNA break levels than either drug alone (median normalized level = 0.079 versus 0.12 and 0.20, respectively; *t*-test *p* = 5.1E-3 and 6.5E-4 for 50 and 100 nM TAZ, respectively; **Figure 2.20C**). Targeting TAZ-potentiated and PGBD5-induced DNA damage using the ATR kinase-selective inhibitor elimusertib was specific, because combination of TAZ with the DNA replication repair CHK1 kinase-selective inhibitor SRA737 showed no increased activity as compared to either drug alone (**Figure 2.22A**). Indeed, TAZ treatment did not induce apparent replication stress, as measured by RPA phosphorylation (**Figure 2.22B**),

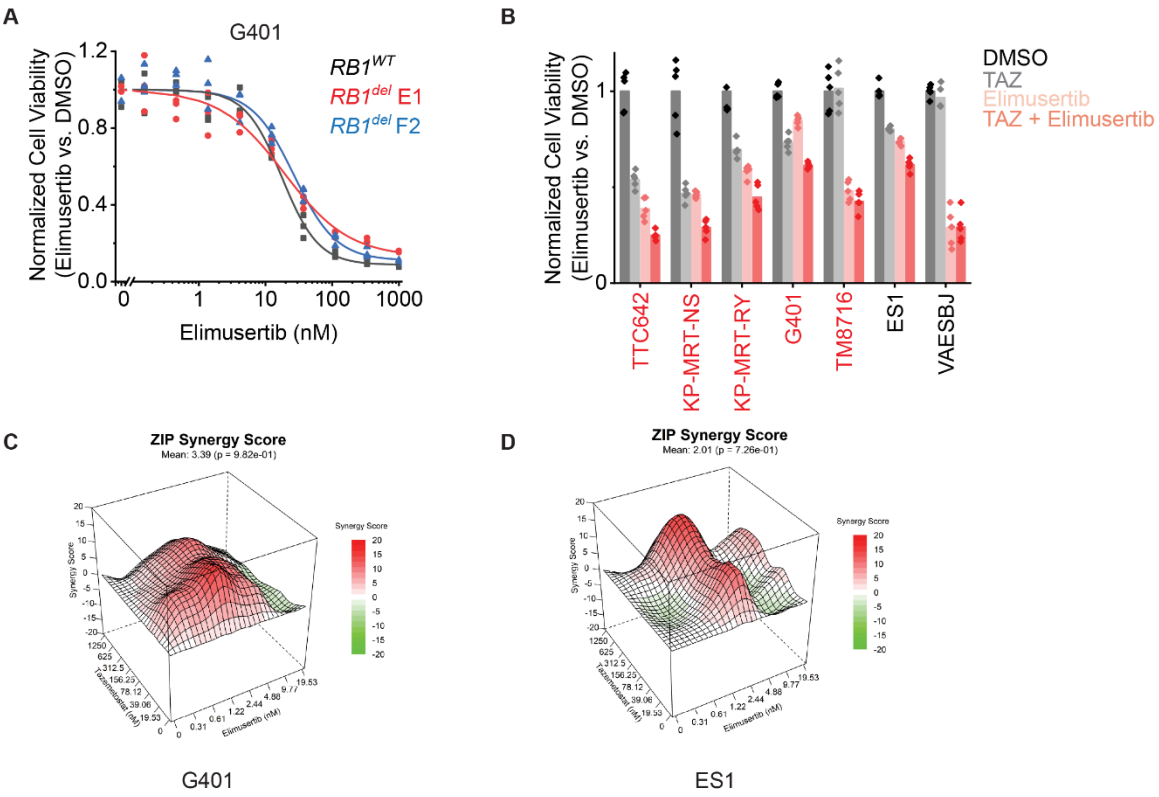

Figure 2.19: Synthetic lethal combination strategy using ATR inhibition overcomes TAZ resistance and improves response: (**A**) G401 cells treated with elimusertib for 4 days. (**B**) Panel of MRT and ES cell lines ordered left to right by decreasing response to TAZ monotherapy. Cells were treated with the indicated monotherapy or combination for 11 days. Drug concentrations used were: TAZ: 200 nM, elimusertib: 8 nM. We selected an elimusertib dose below its monotherapy IC_{50} (for G401 cells) in order to visualize any additive effects upon combination with TAZ. (**C-D**) Synergy plots for combination treatment with TAZ and elimusertib for (**C**) G401 and (**D**) ES1 cells. Cells were treated at the indicated doses for 9 days and analyzed for synergy using the Zero Interaction Potency (ZIP) model.

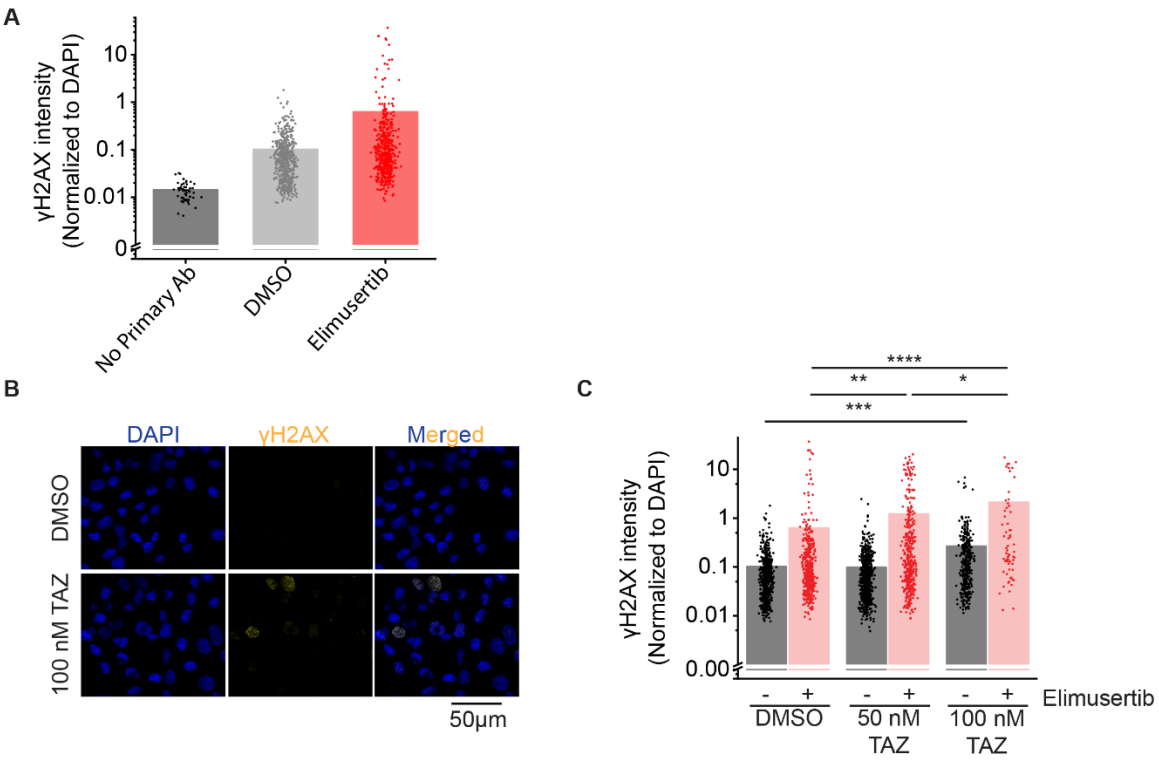

Figure 2.20: TAZ induces DNA damage in G401 cells: (**A**) Quantification of γH2AX fluorescence relative to DAPI fluorescence using CellProfiler. *n* = 53, 548, and 432 nuclei for negative control, DMSO, and elimusertib, respectively. (**B**) Representative images of G401 cells treated with the indicated treatment for 7 days. (**C**) Quantification of γH2AX fluorescence relative to DAPI fluorescence. **p* = 0.042, ***p* = 5.1E-3, ****p* = 1.7E-8, *****p* = 6.5E-4 by two-sided Student's t-test. n = 548 nuclei for DMSO, 432 for elimusertib, 696 for 50 nM TAZ, 401 for 50 nM TAZ + elimusertib, 373 for 100 nM TAZ, 63 for 100 nM TAZ + elimusertib.

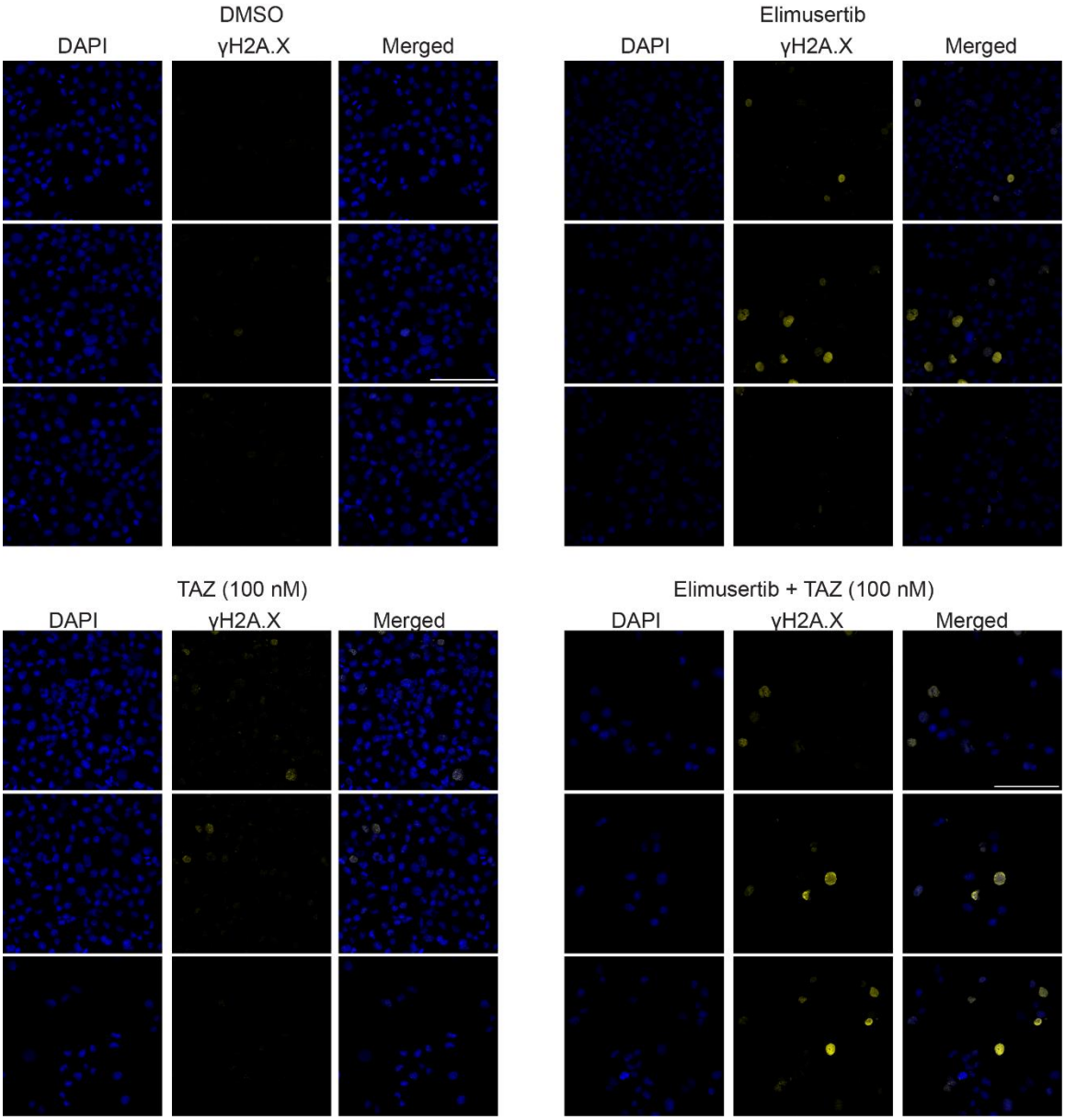

Figure 2.21: TAZ induces DNA damage in G401 cells as measured by γH2AX: (**A**) Quantification of γH2AX fluorescence relative to DAPI fluorescence using CellProfiler. *n* = 53, 548, and 432 nuclei for negative control, DMSO, and elimusertib, respectively. (**B**) Representative uncropped images of G401 cells treated as indicated (same images as in Figure 5C). 3 field are shown per condition. Scale bars are 50 µm.

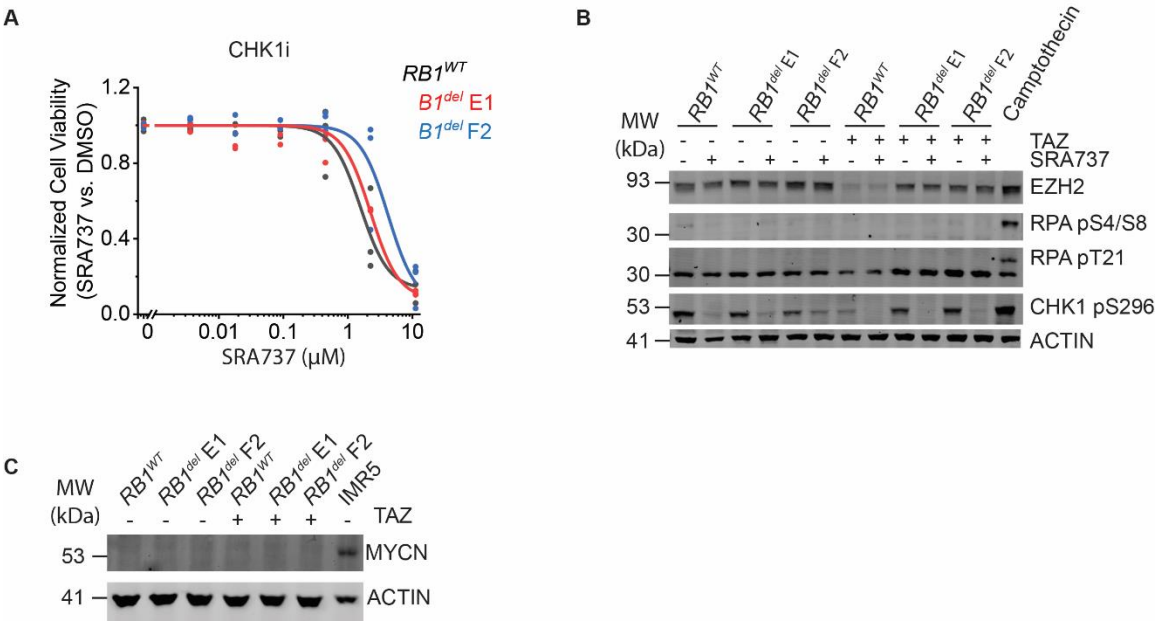

Figure 2.22: CHK1 inhibition does not induce replication stress or synergize with TAZ: (**A**) Dose-response curves of G401 cells treated with the CHK1 inhibitor SRA737 for 9 days. (**B**) Western blot assaying replication stress as measured by RPA phosphorylation at S4/8 and T21. Camptothecin treatment (1.5 μM) for 2 h was used as a positive control for replication stress. Autophosphorylation of CHK1 at S296 was used to confirm CHK1 inhibition. Cells were pre-treated with 10 μM TAZ or DMSO for 9 days. Cells were then split and additionally treated with SRA737 (3 μM) or equivalent volume of DMSO for 2 days. (**C**) Cells treated with 10 μM TAZ or DMSO for 11 days do not express MYCN protein. *MYCN*-amplified neuroblastoma cell line IMR5 was used as a positive control for MYCN expression.

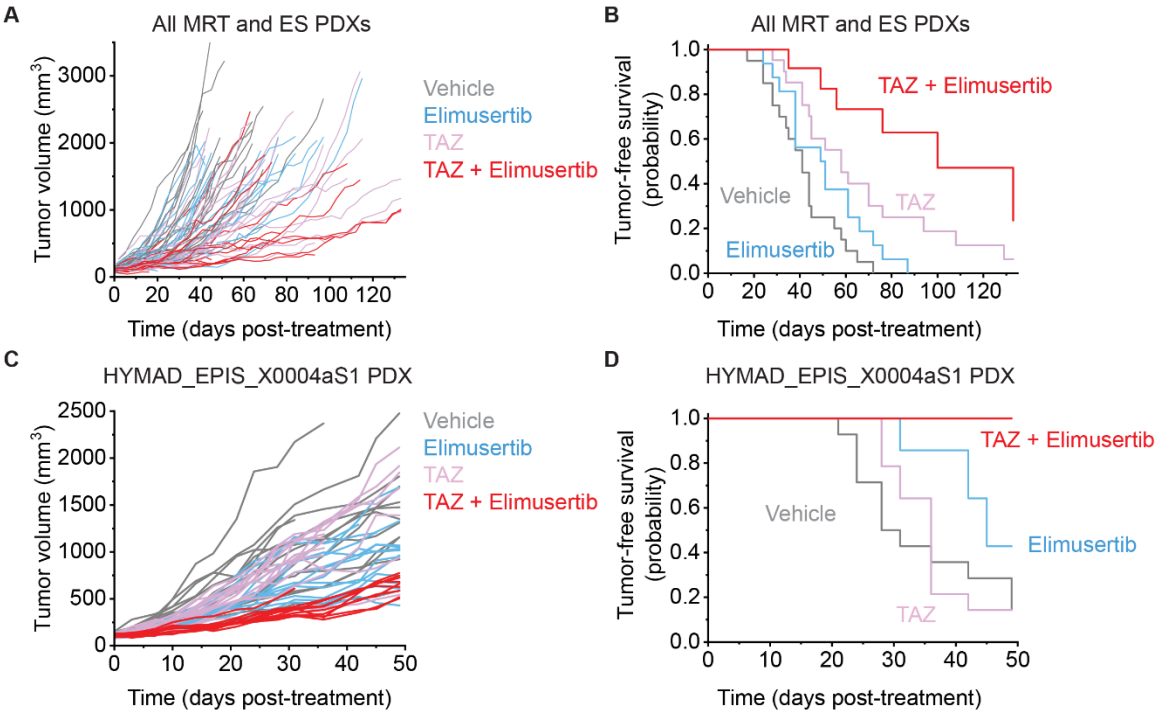

Figure 2.23: Synthetic lethal combination strategy using ATR inhibition overcomes TAZ resistance and improves response *in vivo*: (**A**) Tumor growth curves for 5 mouse PDXs treated with the indicated drug regimen. n = 20 mice for vehicle and elimusertib-treated groups, n = 21 for TAZ and TAZ + elimusertib-treated groups. Vardi *U*-test p = 3.2E-2 and 0.23 for combination vs. elimusertib or TAZ, respectively. (**B**) Kaplan-Meier curves showing tumor-free survival (defined as tumor volume ≤ 1,000 mm^3) for the PDXs in panel C. Mean survival is 51 days (95% CI: 42-60 days) for elimusertib, 67 days (95% CI: 53-81 days) for TAZ to 99 days (95% CI: 74-123 days) for the combination. Log-rank test p = 5.8E-4 and 3.9E-2 for combination versus elimusertib or TAZ, respectively. (**C**) Tumor growth curves for the HYMAD_EPIS_X0004aS1 PDX model treated with the indicated drug regimen. Vardi *U*-test p = 2.0E-4 for combination versus elimusertib or TAZ. n = 14 mice per treatment group. (**D**) Kaplan-Meier curves showing tumor-free survival (defined as tumor volume ≤ 1,000 mm^3) for the PDXs in panel E. Log-rank test p = 6.2E-3 and 6.3E-5 for combination versus elimusertib or TAZ, respectively.

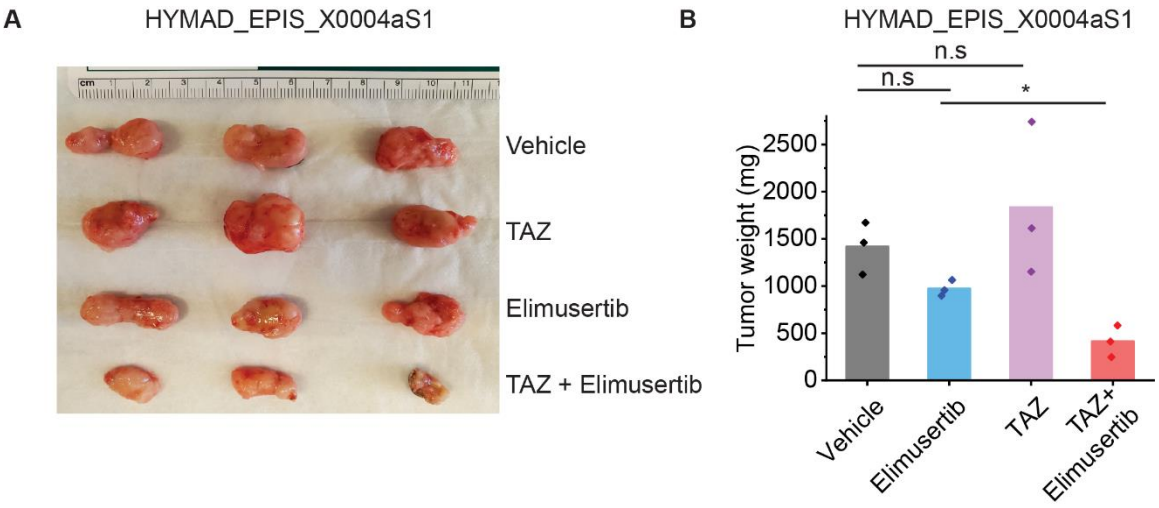

Figure 2.24: PDX tumor weights of mice treated with TAZ and elimusertib combination: (**A**) Image of representative tumors extracted from mice in Figure 2.23C and on Day 52 of treatment (**B**) their corresponding weights. *p = 6.7E-3 by two-sided Student's t-test.

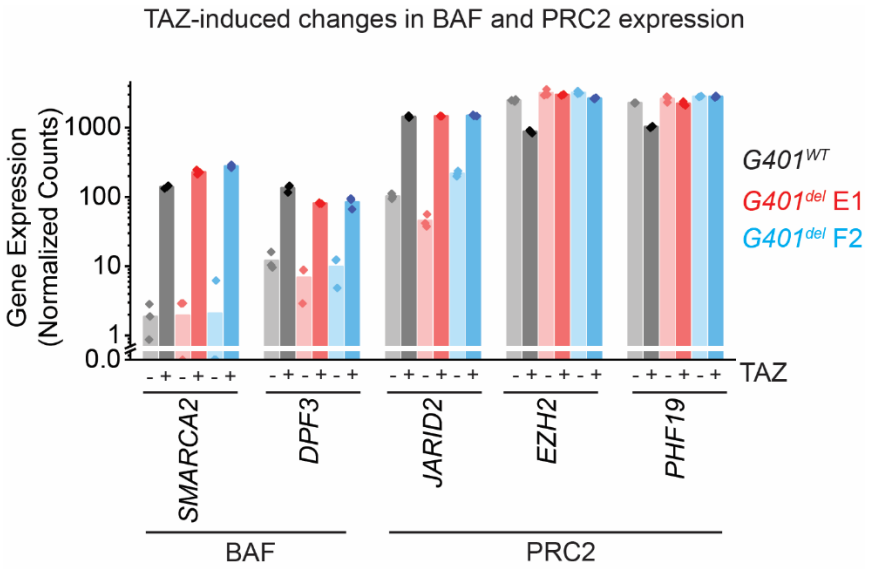

Figure 2.25: TAZ may remodel BAF and PRC2 composition by transcriptional regulation of their subunits: DESeq2-normalized read counts for all BAF and PRC2 subunits showing significantly altered gene expression between TAZ and DMSO-treated cells. Same data as in Figure 2.6A-C.

which was also not potentiated by combined CHK1 inhibition with SRA737, in spite of effective suppression of CHK1 auto-phosphorylation (**Figure 2.22B**). Unlike T-ALL, where EZH2 suppression induces MYCN protein expression and replication stress (231), TAZ treatment of G401 rhabdoid tumor cells failed to increase MYCN protein abundance (**Figure 2.22C**), in spite of significant upregulation of *MYCN* mRNA (**Figure 2.6A-C**).

Encouraged by the potent and specific antitumor activity of synthetic lethal combination TAZ therapy *in vitro*, we tested the antitumor activity of elimusertib and TAZ combination using a diverse cohort of MRT and ES PDX mice *in vivo* (**Supplementary Table S4**). The combination of TAZ and elimusertib exceeded the effect of treatment with either drug alone when assessed by tumor measurements (Vardi *U*-test p = 2.0E-2 and 0.19 for combination versus elimusertib or TAZ, respectively; **Figure 2.23A**) and significantly extended tumor-free survival from 51 days (95% CI = 42-60 days) for elimusertib and 67 days (95% CI = 53-81 days) for TAZ to 99 days (95% CI = 74-123 days) for the combination (log-rank test p = 5.8E-4 and 3.9E-2 for combination versus elimusertib or TAZ, respectively; **Figure 2.23B**). This was most pronounced for the HYMAD_EPIS_X0004aS1 tumor (**Figures 2.23C-D & 2.24A-B**), which exhibited a relatively poor response to TAZ monotherapy, when assessed by tumor growth measurements (Vardi *U*-test p = 2.0E-4 for combination versus elimusertib or TAZ; **Figure 2.23C**) and tumor-free survival (log-rank test p = 6.2E-3 and 6.3E-5 for combination versus elimusertib or TAZ, respectively; **Figure 2.23D**). Thus, the combination of EZH2 and ATR inhibition constitutes a synthetic lethal rational combination strategy to improve TAZ clinical response and overcome resistance.

2.3 Discussion

What defines effective epigenetic EZH2 inhibition therapy for *SMARCB1*-deficient epithelioid sarcomas and rhabdoid tumors? Our studies of ES patients treated with TAZ demonstrate that effective inhibition of PRC2 enzymatic activity is necessary but not sufficient for durable antitumor effects. Using clinical genomics and transcriptomics, combined with functional genetic studies of more than 15 diverse MRT and ES cell lines and patient-derived tumors *in vitro* and *in vivo*, we propose a general molecular model for effective epigenetic TAZ therapy (**Figure 2.26**). This model places validated *RB1* and *EZH2* TAZ resistance alleles within the context of a molecular sequence of events required for clinical TAZ response. This model also explains additional mutations associated with TAZ resistance based on the perturbation of each stage of this sequence and provides candidate prognostic biomarkers and therapeutic combination strategies. We discuss the evidence for this model below, and summarize its novel predictions and implications.

First, TAZ must be able to bind and enzymatically inhibit the EZH2 SET domain (**Figure 2.26; Step 1**). This inhibition can be blocked by gatekeeper mutations of the EZH2 drug binding site, as observed in lymphoma cell lines (201), and demonstrated for the first time here in an epithelioid sarcoma with clinically acquired $EZH2^{Y666N}$ mutation. Such resistance mutations can be overcome by targeting EED, a non-enzymatic PRC2 subunit.

For effective epigenetic TAZ therapy, chromatin remodeling complexes must act on tumor suppressor loci that were aberrantly repressed by PRC2 (**Figure 2.26; Step 2**). The canonical BAF complex is thought to oppose the activity of the Polycomb Repressive Complex (PRC), associated with its chromatin eviction (89, 195). However, the precise mechanism of eviction of TAZ-inhibited PRC2 in *SMARCB1*-deleted tumors is not fully defined. This may involve TAZ-induced remodeling of BAF and/or PRC2. For example, a recent study of *SMARCA4*-deficient cell lines found that upregulation of the expression of BAF helicase *SMARCA2*, which is under PRC2 control in these cells, is necessary for

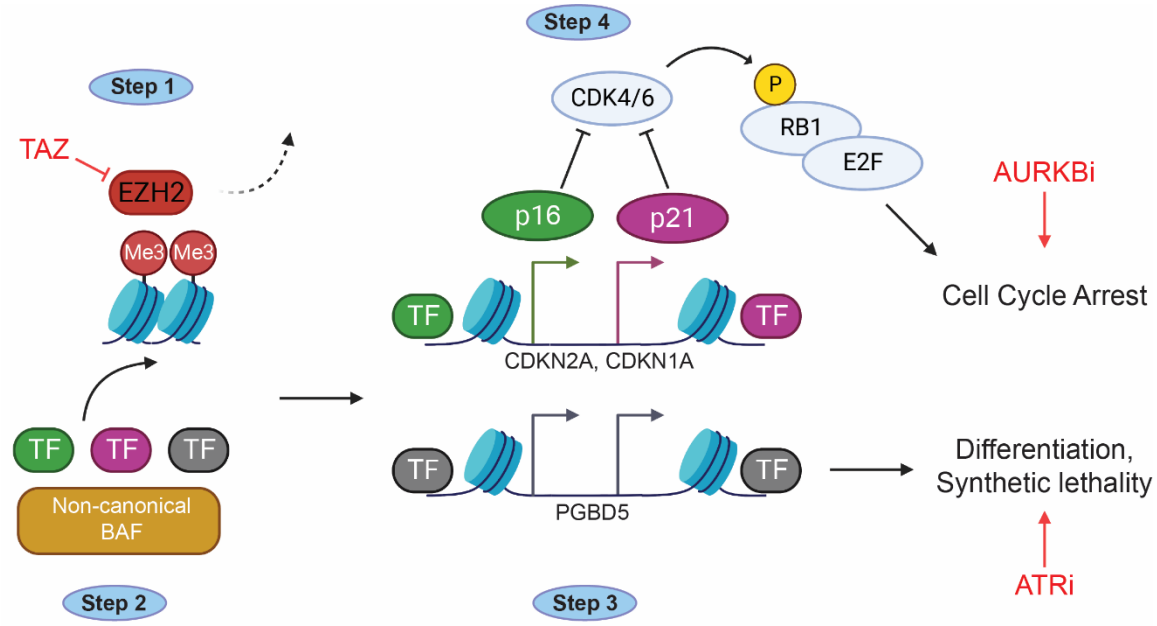

Figure 2.26: Mechanistic schematic for the response of BAF-deficient tumors to effective EZH2 therapy: Step 1: TAZ inhibits histone methylation activity of PRC2. **Step 2:** Activating chromatin-bound complexes, such as ncBAF bind to tumor suppressor loci. **Step 3:** Tumor suppressor loci are activated by their transcription factors and their coactivators. **Step 4:** Tumor suppressors inhibit cell cycle progression through their downstream effectors, such as RB1/E2F.

response to EZH2 inhibition (232). In our study, we observed *RB1*-independent upregulation of the expression of BAF subunits *SMARCA2* and *DPF3* upon TAZ treatment in G401 cells (**Figure 2.25**). This suggests that TAZ may impact BAF complex assembly as part of its therapeutic mechanism in *SMARCB1*-deficient tumor cells. However, this also indicates that *SMARCA2* re-expression upon EZH2 inhibition is not sufficient to induce cell cycle arrest in the absence of *RB1* expression. After assessing TAZ-induced gene expression changes in PRC2 subunits, we also observed *RB1*-independent TAZ-induced upregulation of PRC2 subunit *JARID2*, and *RB1*-dependent downregulation of *PHF19*, suggesting that PRC2 composition itself may be affected by TAZ treatment (**Figure 2.25**). Additionally, it is unknown whether PRC2 eviction in TAZ-treated cells requires a specific form of the BAF complex, such as the non-canonical *SMARCB1*-deficient ncBAF or GBAF complex described previously (71, 72).

If the activity of specific BAF subtypes is indeed needed to evict PRC2 from chromatin upon EZH2 inhibition, then genetic perturbation of specific BAF subunits may impact tumor response to TAZ. For example, in our patient cohort, we observed one TAZ-sensitive tumor with a truncation in the canonical BAF-specific subunit *ARID1B*, while a TAZ-resistant tumor had a missense mutation in PBAF-specific subunit *ARID2* (**Figure 2.1A**). We also found *ARID1B* to be mutated in 2 out of 5 TAZ-responsive cell lines (0 out of 5 TAZ-sensitive cell lines) and *ARID2* to be mutated in 2 out of 5 TAZ-resistant cell lines, though also in 1 out of 5 TAZ-sensitive lines (**Figure 2.11A**). It is not known whether these mutations affect tumor response to TAZ, and further work will be needed to elucidate the specific mechanism of chromatin de-repression in TAZ-treated tumor cells, and its requirement of specific BAF subunits and complexes.

Effective epigenetic TAZ therapy must also upregulate PRC2-repressed tumor suppressor loci (**Figure 2.26; Step 3**). In our patient cohort, one TAZ-resistant tumor had deletions of both *CDKN2A* and *CDKN2B* (**Figure 2.1A**), which can inhibit CDK4/6 from

phosphorylating RB1 and are known to be de-repressed by TAZ treatment (126). Our genomic analysis of MRT and ES cell lines also showed that 4 out of 5 TAZ-resistant cell lines tested had apparent loss of *CDKN2A*, with two also having loss of *CDKN2B*, and one having *CDKN1A* loss as well (**Figure 2.11A**). These mutations may phenocopy *RB1* loss, suggesting that upregulation of these cell cycle inhibitors may be necessary for effective TAZ therapy.

In addition to the preservation of these tumor suppressor loci, transcription factors and coactivators that upregulate their expression must also be intact and expressed for tumor cells to effectively respond to TAZ (**Figure 2.26; Step 3**). In our patient cohort, 2 TAZ-resistant patient tumors had missense mutations in *ANKRD11* (**Figure 2.1A**), as did 3 out of 5 TAZ-resistant cell lines. *ANKRD11* is a putative tumor suppressor that exhibits loss of heterozygosity in breast cancer (233), and is recurrently mutated in other cancers (234, 235). *ANRKD11* can cooperate with p53 to upregulate *CDKN1A*, and previous reports have suggested possible risk of cancer development in patients with a constitutional loss of *ANKRD11* (236, 237). While its importance in *SMARCB1*-deficient sarcomas is unknown, its association with TAZ resistance suggests potential causality. We note that its proposed tumor suppressor function would require all alleles to be lost or mutated. Consistent with potential functional significance, EPI544 cells harbor multiple mutations in *ANKRD11*, two with an apparent allele frequency of 1.0 and MP-MRT-AN cells harbor two mutations, both with 0.5 allele frequencies (**Supplementary Table S3**). Interestingly, a recent report described a patient with KBG syndrome, a developmental condition caused by mutation of *ANKRD11*, who also developed a rhabdoid tumor (237). The co-occurrence of these two exceedingly rare conditions in the same patient is consistent with potential functional involvement of *ANKRD11* in rhabdoid tumor development and susceptibility to EZH2 inhibition.

We also identified *KLF4* as a putative marker of susceptibility to TAZ in patient tumors (**Figure 2.13F**), and found *KLF4* to be mutated in 1 out of 5 TAZ-resistant cell lines (**Figure 2.11A**). Although KLF4 is a transcription factor with both an activating and repressing functions, its role in *SMARCB1*-deleted tumors is not known. Its expression has long been known to upregulate *CDKN1A*, causing cell cycle arrest at the G1/S checkpoint (220, 238). This suggests that KLF4 may regulate the induction of tumor suppressor genes in response to EZH2 inhibition, such as its bona fide target *CDKN1A*. This may occur through recruitment of BAF to tumor suppressor loci; KLF4 can recruit BAF to target genes to upregulate them (239). Like *ANKRD11*, *KLF4* may thus be a key activator of PRC2-repressed genes.

Finally, effective TAZ therapy also requires the function of downstream cell cycle effectors of the relevant tumor suppressor loci (**Figure 2.26; Step 4**). As we have demonstrated in this study, loss of *RB1* leads to the evasion of TAZ-induced cell cycle arrest, despite effective inhibition of EZH2 activity and sustained transcriptional response to TAZ. A recent genome-wide CRISPR screen also found *RB1* as a top mediator of TAZ resistance (199). This is reminiscent of the necessity of intact *RB1* for therapeutic response to clinical inhibitors of CDK4/6 (240-242). The transcriptional upregulation of hundreds of genes by TAZ in $RB1^{del}$ tumors, including EMT gene sets (**Figures 2.7B & 2.8A**), suggests that these cells are undergoing forced differentiation, even while maintaining proliferation (**Figure 2.9A-B**). This upregulation of mesenchymal gene sets is consistent with previous work that has shown that PRC2 inhibition, similar to *SMARCB1* re-expression, can drive *SMARCB1*-deficient tumors into a terminally differentiated, mesenchymal-like state (70, 126, 207), possibly recapitulating the normal developmental trajectory of their cells of origin (207). In this way, *RB1* loss and dysregulation of the RB1/E2F axis appear to decouple the regulation of cell fate and identity from its control of cell cycle progression.

In our search for predictive biomarkers of TAZ response, we identified increased expression of the PCP gene *PRICKLE1* to be associated with a deficient RB1/E2F axis and TAZ resistance (**Figure 2.13B-E**). The molecular mechanism connecting G1/S dysregulation and *PRICKLE1* expression is currently unknown, but the PCP pathway is known to be under cell cycle control (243, 244). This is mediated at least in part by PLK1, which we found to be one of the top upregulated genes in TAZ-resistant tumors (**Figure 2.14A**). Likewise, deletion of the *Drosophila RB1* homologue *Rbf1* results in the upregulation of several PCP genes, including the *PRICKLE1* homologue *pk* (245). This suggests that dysregulation of the RB1/E2F axis may lead to upregulation of *PRICKLE1* through dysregulation of normal cell cycle control of PCP. Further work will be needed to define this mechanism, as well as to investigate PRICKLE1 as a clinical biomarker for TAZ resistance.

Finally, our study developed two strategies to circumvent clinical TAZ resistance. First, since dysregulation of the RB1/E2F axis mediates escape from cell cycle arrest at the G1/S checkpoint, we reasoned that cell cycle kinases that function downstream of this checkpoint would remain viable therapeutic targets. This cell cycle bypass strategy is supported by previous work showing that loss of *RB1* can sensitize cancer cells to Aurora kinase inhibition through a primed spindle assembly checkpoint (246). As predicted, $RB1^{del}$ cells remain sensitive to CDK2, AURKA, and AURKB inhibition (**Figures 2.16A, 2.15A-B**). We found that MRT and ES cell lines resistant to TAZ, including those with *ANKRD11* and *CDKN1A/2A/2B* mutations were sensitive to barasertib. Most compellingly, we found that the combination of TAZ and barasertib exhibits improved antitumor activity *in vivo* compared to either drug alone.

This is reminiscent of the therapeutic combination mechanism proposed by Sorger and Palmer (247), in which inter-patient and inter-tumor variability in response to individual drugs rather than their pharmacological interactions lead to apparent combined effects.

We observed substantial benefit of TAZ and barasertib combination within individual PDX models. This suggests that the improved efficacy of this combination may also result from intra-tumor heterogeneity and tumor evolution *in vivo*, as proposed for combination therapy more than fifty years ago (248, 249). Dual targeting of two different parts of the cell cycle can prevent tumors from evading cell cycle arrest through the presence or acquisition of mutations in cell cycle control genes. For example, cells with a defective G1/S checkpoint that continue to transit through the cell cycle remain sensitive to AURKB inhibition. Further work will be needed to elucidate whether barasertib causes postmitotic endoreduplication due to its disruption of the spindle assembly and/or direct inhibition of the mitotic checkpoint (250, 251).

Our findings also advance synthetic lethal strategy for rational epigenetic TAZ combination therapy due to TAZ-induced expression of *PGBD5*, the putative developmental mutator in rhabdoid and other young-onset solid tumors, due to its induction of dsDNA breaks (227). We found that the DNA damage repair ATR kinase inhibitor elimusertib not only overcomes RB1/E2F axis-mediated resistance, but in combination with TAZ, also exerts synergistic anti-tumor effects *in vitro* and *in vivo*. TAZ-induced upregulation of PGBD5 is associated with the induction of DNA damage. It is possible that the enhanced sensitivity to ATR inhibition due to the increased requirements for DNA repair also depends on the intrinsic variation in DNA damage repair signaling among different tumor subtypes. This may also be due to the variation in the expression and activity of PGBD5 nuclease activity among tumors, both of which may be associated with the recently described molecular subtypes of ES and MRT tumors (228). Additional synthetic lethal strategies may also be developed based on the immunologic effects of EZH2 inhibitors, particularly as combined with epigenetic and synthetic lethal therapies, both of which can promote tumor immunogenicity. In all, this study develops a paradigm

for rational epigenetic combination therapy, including candidate prognostic biomarkers, all of which should be incorporated into future clinical trials for patients.

2.4 Materials and Methods

Cell culture

All cell lines were obtained from the American Type Culture Collection if not otherwise specified. ES1 and ES2 cells were generated and kindly provided by Nadia Zaffaroni. EPI544 cells were obtained from the MD Andersen Cancer Center Cytogenetics and Cell Authentication Core. Rhabdoid tumor cell lines KP-MRT-NS, KP-MRT-RY, and MP-MRT-AN were kindly provided by Yasumichi Kuwahara and Hajime Hosoi. The identity of all cell lines was verified by STR analysis. Absence of *Mycoplasma* contamination was determined using the MycoAlert kit according to manufacturer's instructions (Lonza). Cell lines were cultured in 5% CO_2 in a humidified atmosphere in 37°C. All media were obtained from Corning and supplemented with 10% fetal bovine serum (FBS), 1% L-glutamine, and 100 U/mL penicillin and 100 µg/mL streptomycin (Gibco). RPE, G401, A204, ES1, ES2, and VAESBJ cells were cultured in Dulbecco's Modified Eagle Medium (DMEM). TTC642, TM8716, MP-MRT-AN, KP-MRT-NS, and KP-MRT-RY cells were cultured in Roswell Park Memorial Institute (RPMI) medium. EPI544 cells were cultured in DMEM/F12 medium.

Western Blotting

To assess protein expression by Western immunoblotting, pellets of 1 million cells were prepared and washed once in cold PBS. Cells were resuspended in 100-130 µL of RIPA lysis buffer (50 mM Tris-HCl, pH 8.0, 150 mM NaCl, 1.0% NP-40, 0.5% sodium deoxycholate, 0.1% sodium dodecyl sulfate) and incubated on ice for 10 minutes. Cell

suspensions were then disrupted using a Covaris S220 adaptive focused sonicator for 5 minutes (peak incident power: 35W, duty factor: 10%, 200 cycles/burst) at 4 °C. Lysates were cleared by centrifugation at 18,000 g for 15 min at 4 °C. Protein concentration was assayed using the DC Protein Assay (Bio-Rad) and 15-35 µg whole cell extract was used per sample. Samples were boiled at 95 °C in Laemmli buffer (Bio-Rad) with 40 mM DTT and resolved using sodium dodecyl sulfate-polyacrylamide gel electrophoresis. Proteins were transferred to Immobilon FL PVDF membranes (Millipore), and membranes were blocked using Intercept Blocking buffer (Li-Cor). Primary antibodies used were: anti-EZH2 (Cell Signaling Technology, 5246) at 1:1,000, anti-RB1 (Cell Signaling Technology, 9309) at 1:250, anti-H3K27me3 (Cell Signaling Technology, 9733) at 1:500, anti-p16 (Abcam, ab108349) at 1:500, anti-CCNA2 (Santa Cruz, sc-271682) at 1:100, anti-PRICKLE1 (Santa Cruz, sc-393034) at 1:100, anti-SMARCB1 (BD Biosciences, 612110) at 1:500, anti-RPA32 pT21 (abcam, ab109394) at 1:2,000, anti-RPA32 pS4/pS8 (ThermoFisher, A300-245A) at 1:2,000, anti-pCHK1 S296 (Cell Signaling Technology, 90178) at 1:250, anti-MYCN (Cell Signaling Technology, 9405) at 1:250, anti-MMP2 (Cell Signaling Technology, 40994S) at 1:250, anti-cleaved Caspase 3 (Cell Signaling Technology, 9661S) at 1:500, anti-Actin (Cell Signaling Technology, 4970 and 3700) at 1:5,000. Blotted membranes were visualized using goat secondary antibodies conjugated to IRDye 680RD or IRDye 800CW (Li-Cor, 926-68071 and 926-32210) at 1:15,000 and the Odyssey CLx fluorescence scanner, according to manufacturer's instructions (Li-Cor). Image analysis was done using the Li-Cor Image Studio software (version 4).

Lentivirus production

Lentivirus production was carried out as described previously (252). Briefly, HEK293T cells were transfected using TransIT-LT1 using a 2:1:1 ratio of the lentiviral

vector and psPAX2 and pMD2.G packaging plasmids, according to manufacturer's instructions (Mirus). Viral supernatant was collected at 48 and 72 hours post-transfection, pooled, filtered and stored in aliquots at -80 °C. G401 cells were transduced at a multiplicity of infection (MOI) of 0.3. Transduced cells were selected for 7 days with G418 sulfate (ThermoFisher) at 1 mg/mL. Single-cell clones were then isolated and expanded. Inducible EZH2 expression was confirmed by Western blotting against EZH2.

Cell Viability Testing

Drugs used for *in vitro* treatment were supplied by Selleckchem (TAZ; S7128, Elimusertib; S9864, abemaciclib; LY2835219, palbociclib; S1116, seleciclib; S1153, alisertib; S1133, barasertib; S1147, camptothecin, S1288).

The effects of *RB1* loss or *EZH2* mutation on TAZ susceptibility was assessed over 14 days. Cells were plated in 96-well microplates at equal densities and treated with 10 µM TAZ or equivalent volume of DMSO on Day 0. Drug and media were replaced on Days 4, 7, and 11. CellTiter-Glo assays were performed on Day 14, with luminescence readings taken using an automated fluorescence plate reader (Tecan). CellTiter-Glo reagent was freshly reconstituted on the day of measurement and added in a 1:1 proportion to cell media. A similar protocol was used for all other cell viability experiments, with treatment times indicated in the relevant figure legends. Cell line doubling time was determined by measuring cell viability every 24 hours over the course of 4 days, and fitting the cell viability to a two-parameter exponential curve. For combination treatment with TAZ and elimusertib, we used a two-dimensional dose matrix design, treating the cells for 9 days. After the addition of cells, drugs were added using a pin tool (stainless steel pins with 50 nL slots, V&P Scientific) mounted onto a liquid handling robot (CyBio Well vario, Analytik Jena). For analysis of synergy, we used the synergyFinder package (253). Outliers due to pinning errors were excluded after manual examination.

Cell line RNA-sequencing

G401 cells with or without *RB1* loss were plated and treated with 10 μM TAZ or equivalent volume of DMSO on Day 0. Drug and media were replaced on Days 4 and 8. Cells were harvested on Day 11 and RNA was isolated using RNeasy Mini kit, according to manufacturer's instructions (Qiagen). After RiboGreen quantification and quality control by Agilent BioAnalyzer, 149-500ng of total RNA underwent Poly(A) selection and TruSeq library preparation according to instructions provided by Illumina (TruSeq Stranded mRNA LT Kit, catalog RS-122-2102), with 8 cycles of PCR. Samples were barcoded and sequenced using a HiSeq 4000 instrument using 50bp/50bp paired end mode, using the HiSeq 3000/4000 SBS Kit (Illumina). An average of 42 million paired reads was generated per sample. Ribosomal reads represented less than 0.03% of the total reads generated and proportion of mRNA bases averaged 74%.

Patient tumor samples

Patient tumor and matched normal blood samples were obtained from patients at Memorial Sloan Kettering Cancer Center (MSKCC) enrolled in the TAZ clinical trial (139). All patients provided informed consent for this study under the Institutional Review Board approved research protocol 12-245. Patient tumors were classified into "Response" or "Progression" groups based on RECIST 1.1 criteria (254). "Response" included tumors exhibiting a complete response, partial response, or stable disease. All other tumors were classified under the "Progression" group. The complete list of tumor samples used and corresponding clinical data may be found in **Supplementary Table S1**. This cohort includes both tumor samples that underwent targeted sequencing with MSK-IMPACT (200) as part of their clinical care at MSKCC as well as archived tumors that were analyzed for this study. For genomic analysis, DNA was extracted from either flash frozen tumor samples or formalin-fixed, paraffin-embedded (FFPE) blocks or slides and samples were

processed using the IMPACT468 or IMPACT505 panels depending on the time of their sequencing (200). The detected mutations and copy number alterations were obtained from cBioPortal (255, 256) and can be found in **Supplementary Table 2**. Oncoprints were generated using Oncoprinter (cBioPortal).

For transcriptomic analysis, archived frozen tumor samples were weighed and up to 20-30 mg were homogenized in RLT buffer, followed by extraction using the AllPrep DNA/RNA Mini Kit (QIAGEN catalog 80204) according to the manufacturer's instructions. RNA was eluted in 13 µL nuclease-free water. After RiboGreen quantification and quality control by Agilent BioAnalyzer, 1 µg of total RNA with DV200 percentages varying from 78% to 100% underwent ribosomal depletion and library preparation using the TruSeq Stranded Total RNA LT Kit (Illumina catalog RS-122-1202) according to instructions provided by the manufacturer with 8 cycles of PCR. Samples were barcoded and sequenced using NovaSeq 6000 in a PE150 mode, with the NovaSeq 6000 S4 Reagent Kit (Illumina). On average, 84 million paired reads were generated per sample and 70% of the data mapped to mRNA.

Targeted sequencing of cell lines

To assess for the presence of somatic mutations in MRT and ES cell lines, DNA was extracted using the PureLink Genomic DNA Minikit (Invitrogen) and processed using the IMPACT505 panel as above. Due to the lack of matched normal tissue for cell lines, copy number alterations were detected using a custom algorithm using circular binary segmentation (257) implemented by the MSK Bioinformatics core. Code is available on github at: https://github.com/kentsisresearchgroup/seqCNA_tazemetostat_resistance.

Analysis of RNA-seq data

For RNA-seq analysis of G401 cell lines, read adaptors were trimmed and quality filtered using 'trim_galore' (v0.4.4_dev) and mapped to GRCh38/hg19 reference genome using STAR v2.6.0a with default parameters (258). Read counts tables were generated using HTSeq (259). Normalization was performed using DESeq2 using the default parameters (260).

For RNA-seq analysis of patient tumor samples, read adaptors were trimmed and quality filtered using 'trim_galore' and mapped to GRCh38/hg19 reference genome using STAR v2.7.9 with default parameters (258). Read count tables were generated using HTSeq v0.11.3 (259). Bam files were sorted by name using 'samtools' and alignment quality was assessed using 'qualimap' v2.2.2. Normalization was performed using DESeq2 v1.34.0 using the default parameters (260). To assess gene expression changes between TAZ-sensitive and TAZ-resistant tumors, samples in both categories were compared by two-tailed Student's t-test using 'rowttests' in R v4.1.3. Genes were filtered by $p<0.05$ and sorted by t-statistic. Heatmaps were then generated using 'pheatmap.' Genome browser tracks were visualized from bam files using Integrated Genomics Viewer v2.13.1.

Gene ontology analysis

Genes significantly up- or down-regulated in TAZ-sensitive and TAZ-resistant tumors determined by two-tailed Student's t-test at p-value < 0.5 were searched against the Gene Ontology database (DOI: 10.5281/zenodo.5725227 Downloaded 2021-11-16).

Microscopy

Bright field microscopy was performed using an Evos FL Auto 2 imager at 10x magnification, with cells grown on plastic dishes. Immunofluorescence for γH2AX was

performed on cells plated on Millicell EZ Slide glass slides (EMD Millipore), coated for 45 minutes with bovine plasma fibronectin (Millipore Sigma). After drug treatment, cells were washed once with PBS and fixed in 4% formaldehyde for 10 minutes at room temperature. Slides were then washed three times in PBS for 5 minutes, permeabilized for 15 minutes in 0.3% Triton X-100, washed again in PBS three times, and blocked with 5% goat serum (Millipore Sigma, G9023) in PBS for 1 hour at room temperature. Slides were incubated with mouse anti-γH2A.X primary antibody (Sigma-Aldrich, 05-636) at 1:500 in blocking buffer for 1 hour, washed three times in PBS, and incubated with goat anti-mouse secondary antibody conjugated to AlexaFluor555 (Invitrogen, A-21422) at 1:1,000. Cells were then counterstained with DAPI at 1:1,000 for 10 minutes and treated with ProLong Diamond Antifade Mountant with DAPI (Invitrogen, P36962) for 48 hours. For MMP2 and cleaved caspase 3 immunofluorescence, cells were processed as above, using anti-MMP2 antibody (Cell Signaling Technology, 40994S) at 1:200 or anti-cleaved Caspase 3 antibody (Cell Signaling Technology, 9661S) at 1:300, and Phalloidin conjugated to AlexaFluor488 (ThermoFisher, A12379) at 1:400 added to the secondary antibody mix.

Images were acquired on a Leica SP5 confocal microscope in the upright configuration at 63x magnification. Images were then processed using a custom pipeline in CellProfiler (261). Per-cell integrated γH2A.X intensity was normalized against per-cell integrated DAPI intensity. Overlaid images in Figure 5 were prepared using Fiji (262).

Xenografts

All mouse experiments were carried out in accordance with institutionally approved animal use protocols. To generate PDXs, tumor specimens were collected under approved IRB protocol 14-091, immediately minced and mixed (50:50) with Matrigel (Corning, New York, NY) and implanted subcutaneously in the flank of 6-8 weeks-old female NOD.Cg-*Prkdc*^{scid} *Il2rg*^{tm1Wjl}*/Szj* (NSG) mice (Jackson Laboratory, Bar Harbor, ME),

as described previously (263). Mice were monitored daily and PDX samples were serially transplanted three times before being deemed established. PDX tumor histology was confirmed by review of H&E slides and direct comparison to the corresponding patient tumor slides. PDX identity was further confirmed by MSK-IMPACT sequencing analysis.

Therapeutic studies used female and male NSG mice obtained from the Jackson Laboratory. Xenografts were prepared as single-cell suspensions, resuspended in Matrigel, and implanted subcutaneously into the right flank of 6-10 week old mice. 100 µL of tumor cell suspension was used for each mouse. Tumors were allowed to grow until they reached a volume of 100 mm^3, at which point they were randomized into treatment groups without blinding. Drugs were prepared using the following formulations: Tazemetostat was dissolved at 25 mg/mL in 5% DMSO, 40% PEG 300, 5% Tween 80, and 50% water. Elimusertib was dissolved at 5 mg/mL in 10% DMSO, 40% PEG 300, 5% Tween 80, and 45% water using a sonicator. Barasertib was dissolved at 2.5 mg/mL in 5% DMSO, 40% PEG 300, 5% Tween 80, and 50% water. Drugs were reconstituted daily. The following drug doses and schedules were used: TAZ was dosed at 250 mg/kg twice daily by oral gavage, 7 days per week. Barasertib was dosed at 25 mg/kg once daily by intraperitoneal injection using 3 days on and 4 days off cycle. Elimusertib was dosed at 40 mg/kg twice daily by oral gavage using 2 days on and 12 days off cycle. Caliper tumor measurements were taken twice weekly. Tumor volumes were calculated using the formula Volume = $(\pi/6)$ x length x $width^2$. Tumor growth analysis was performed using the Vardi *U*-test (226), as implemented in the clinfun R package using the aucVardiTest function. Tumor-free survival analysis was calculated using OriginPro (Microcal) by the Kaplan-Meier method, using the log-rank test.

EZH2 mutant plasmids

The *EZH2*^{Y666N} mutation detected in the clinical trial patient refers to amino acid numbering in isoform 2 of the protein. For consistency of nomenclature, all engineered mutations use numbering referring to isoform 2 (Uniprot ID: Q15190-2), although isoform 1 was expressed in cells for this study. Plasmids containing wild-type EZH2 (*EZH2*^{WT}) and catalytically inactive triple mutant (F672I, H694A, R732K, referred to as *EZH2*^{CatMut}) plasmids were kindly provided by Alejandro Gutierrez in the doxycycline-inducible pINDUCER20 vector (264). The plasmids contain human *EZH2* tagged N-terminally with a FLAG-Avi tag.

The Y666N mutation was engineered in both the *EZH2*^{WT} and *EZH2*^{CatMut} plasmids to yield *EZH2*^{Y666N} and what we termed *EZH2*^{QuadMut}. The mutation was introduced by site-directed mutagenesis using the QuikChange Lightning Kit (Agilent) per manufacturer's instructions (mutagenesis primers: 5'-GCAAAGTGTACGACAAGAACATGTGCAGCTTTCTG-3' and 5'-CAGAAAGCTGCACATGTTCTTGTCGTACACTTTGC-3') to engineer a TAC to AAC codon change. After mutagenesis, PCR products were transformed into Stbl3 *E. coli* cells and expanded at 30°C. Correct plasmid sequences were confirmed by Sanger sequencing (Eton). The sequencing primers used are:

F1: 5'-GGACAGCAGAGATCCAGTTTG-3'

R1: 5'-GGTCCGTTCCAGGATCTTCT-3'

F2: 5'-TCCAGTGTGGTGGAATTCTG-3'

R2: 5'-TATCGCTGGGGAACTTTCTG-3'

F3: 5'-TGCTGCACAACATCCCTTAC-3'

R3: 5'-TGCTGGTTTCGTCCTTCTTT-3'

F4: 5'-CCTACAAGCGGAAGAACACC-3'

R4: 5'-GTTCTTGCTGTCCCAGTGGT-3'

F5: 5'-CTGAAGAAGGATGGCAGCTC-3'

R5: 5'-CTTGGGTGGGTTACTCCAGA-3'

RB1 Knockout

G401 cells with *RB1* mutations were engineered by Synthego. Briefly, a single guide RNA targeting exon 2 of *RB1* was used (AGAGAGAGCUUGGUUAACUU). Ribonucleprotein containing spCas9 and sgRNA was transfected into G401 cells by electroporation. The target site was then PCR-amplified and Sanger sequenced to ensure homozygous indels (PCR and sequencing primers: Forward-CACTGTGTGGTATCCTTATTTTGGA, Reverse- AGGTAAATTTCCTCTGGGTAATGGA, with the forward primer used for sequencing). The cells were then single-cell cloned and re-verified by Sanger sequencing. Loss of the RB1 protein was confirmed by Western blot.

Cell cycle analysis

G401 cells were plated on Day 0 and treated for 10 days with 1 μm tazemetostat or equivalent volume of DMSO, with drug and media replaced on Days 4 and 7. On Day 11, cells were pulsed with EdU for 1 hour. Cells were then harvested and processed for flow cytometry using the manufacturer's protocol (Click-iT, Invitrogen). Briefly, cells were washed with PBS with 1% BSA, permeabilized, and incubated with AlexaFluor647 for 30 minutes. DNA content was measured using propidium iodide (0.05 μg/μL). Cells were analyzed on a CytoFLEX LX (Beckman Coulter).

CHAPTER III

Defining the protein interactome of EWS-FLI1 using mass spectrometry proteomics and peptide interference

3.1 Introduction

Ewing sarcoma (EwS) is a pediatric tumor of the bone and soft tissue that primarily strikes children in their teens. Despite advances in multimodal treatment that includes surgery, chemotherapy, radiation, and supportive care, the survival of patients with refractory and metastatic disease is dismal, and no targeted therapies are currently available (140). The causative oncogenic gene fusion that drives this tumor, most commonly EWS-FLI1, was cloned three decades ago (265), yet despite extensive studies in that time on the molecular mechanisms of EWS-FLI1-mediated transformation, we still lack a complete molecular understanding of EWS-FLI1 function. This impedes the development of targeted therapeutics for this devastating tumor.

In this chapter, I use an unbiased proteomic approach to fully define the protein interactome of the EWS-FLI1 fusion protein. I integrate this with a genetic dependency analysis to nominate new putative cofactors with potential functional roles in EwS, ranking them against known cofactors. This analysis revealed specific subunits of known cofactor complexes, including the BAF complex, with high Ewing sarcoma-specific dependency scores, thus building on previous work in the field. In addition, this analysis revealed previously unknown cofactors that require further exploration. Finally, I use a peptide interference approach to begin defining the regions of EWS-FLI1 critical for its function. Based on a leading candidate peptide, I nominate the EWS-FLI1 fusion junction as a key dependency and potential therapeutic target in Ewing sarcoma.

3.2 Results

Proteomic analysis of the EWS-FLI1 complex

To comprehensively define the protein interactome of EWS-FLI1, I immunoprecipitated EWS-FLI1 from the TC-32 EwS cell line (**Figure 3.1A**) and analyzed the pulldown samples by high-resolution mass spectrometry (MS). I used an antibody specific to FLI1, as wild-type FLI1 is not expressed in EwS cells (266). I detected 1,396 unique proteins (at a protein FDR of 1%), of which 1,151 were enriched in the FLI1 pulldown compared with IgG control pulldown, based on a positive $\log_2$(fold-change) of MS1 spectral counts (or 1,082 based on a more stringent cut-off of $\log_2$(fold-change) ≥ 1).

To narrow down this list for functionally important cofactors, I calculated Ewing sarcoma-specific genetic dependency scores for each detected protein. This was accomplished by cross-referencing the list of detected proteins with CRISPR gene dependency data from the 769 cancer cell lines included in the DepMap Cancer Dependency Map, which included 13 EwS cell lines harboring EWS-FLI1 or EWS-ERG fusions, uniformly profiled using loss-of-function genome-wide CRISPR screens (**Figure 3.1B**). I hypothesized that proteins that scored highly by this metric would be relatively dispensable for most cell types, but important for EwS cell survival. Indeed, the highest-scoring gene by this metric is *EWSR1* itself. Using both this dependency score, which I refer to as ΔDepScore, and the $\log_2$(fold-change), I ranked the detected interactors to determine the proteins that were most strongly detected by MS based on a $\log_2$(fold-change) ≥ 1, and those likely to play significant functional roles in EwS cells (ΔDepScore > 0). I applied a further filter for nuclear proteins, as EWS-FLI1 localizes to the nucleus (267). Together, these three filters left 394 putative interactors (**Figure 3.1B, Supplementary Table S5**). Finally, I performed a network analysis by searching the detected proteins against the STRING protein interaction database (268) in order to group them into functional complexes (**Figure 3.2**).

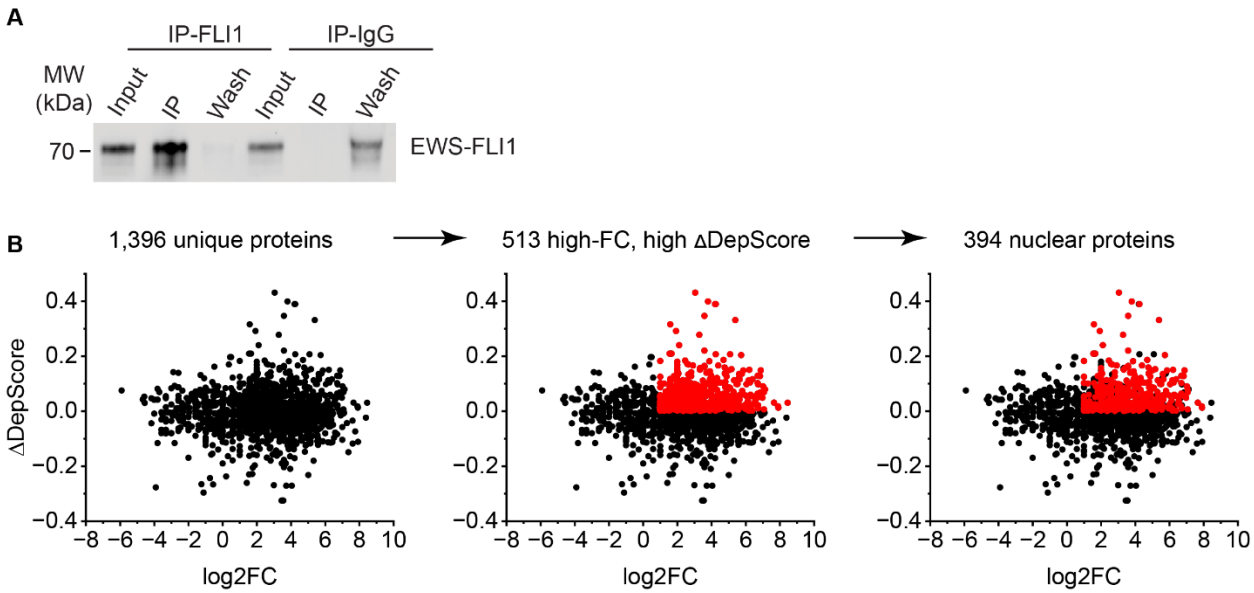

Figure 3.1: IP-MS of TC-32 nominates potential EwS-specific dependencies. (**A**) anti-FLI1 western blot showing efficient immunocapture of full-length EWS-FLI1 from TC-32 cells. (**B**) EwS-specific dependency score cross-refenced with detected IP-MS interactors, plotted against $\log_2$(fold-change), showing filtering of detected proteins.

The IP-MS data combined with the dependency and network analyses revealed several known interactors of EWS-FLI1. For example, 10 subunits of the BAF complex, previously found to interact with EWS-FLI1, were highly ranked (**Figure 3.2A, 3.3A**) (161), demonstrating the sensitivity of this approach in detecting known interacting complexes. Interestingly, despite the requirement of BAF for activation of EWS-FLI1 target genes (161), most BAF complex subunits score relatively low by the ΔDepScore metric (**Figure 3.2A, 3.3A**), showing that most subunits are not Ewing sarcoma-specific dependencies. The exceptions were the subunits BCL11B and ACTL6A, which scored near the top of detected interactors ranked by ΔDepScore. The NuRD complex, another known interactor, was also detected (**Figure 3.2B**). This included the NuRD histone deacetylase subunits HDAC1/2, although I did not detect the associated histone demethylase LSD1, in contrast to previous results (174), and NuRD components were not among the highest scoring EwS-specific dependencies (**Figure 3.3B**).

Other detected interactors have known functional roles in EwS but have not been previously explored as direct interactors of EWS-FLI1. For example, all core subunits of the PRC2 complex, including the histone methyltransferase EZH2 were detected (**Figure 3.2B**), although most scored poorly by ΔDepScore. In addition, I detected the transcription factors ZEB2 and NKX2-2, which play important roles in EwS but have not been previously studied as direct EWS-FLI1 interactors. Both scored near the top of the detected interactors by ΔDepScore.

Excitingly, several of the detected interactors do not have previously described roles in EwS. Several of the proteins cluster into two overlapping complexes in my network analysis (**Figure 3.2A**), one containing multiple TBP-associated factors (TAFs), proteins that associate with TATA box binding protein (TBP) as part of the TFIID basal transcription complex within the pre-initiation complex (PIC). TBP itself was detected along with 9 TAFs. In addition to TFIID, many of these subunits are shared among multiple coactivator

complexes, including the STAGA, PCAF, and TFTC complexes. In addition to multiple TAFs, these coactivators incorporate additional subunits that form a second, adjacent complex in my network analysis. One complex in particular that appears to merit further investigation, and which had a high overlap with detected proteins is the Tip60/EP400 chromatin remodeling complex, which uniquely contains the EP400 protein, together with RUVBL1/2, ACTL6A, and EPC2 (**Figure 3.3C**). This complex appears to be of particular interest due to the additional detection of the histone variant H2AFZ. Among the interactors detected, H2AFZ is one of the highest-scoring proteins by ΔDepScore in the IP-MS data, and indeed genome-wide. H2AFZ is incorporated into chromatin by one of two complexes, SRCAP or Tip60/EP400, the latter complex including both histone acetyltransferase and H2AFZ loading activity imparted by the EP400 subunit.

Another previously unknown interactor, and one with a surprisingly high ΔDepScore, is the mRNA-regulatory protein IGF2BP3, along with related protein IGF2BP1 (**Figure 3.3D**). Finally, multiple DNA repair proteins were also detected, showing some of highest coverage of all detected proteins. XRCC5 (KU80) in particular showed a high ΔDepScore (**Figure 3.3D**) and was pulled down together with other members of the non-homologous end-joining (NHEJ) pathway KRCC6 (KU70), PRKDC (DNA-PK), PNKP, and APTX, as well as single-strand break repair proteins XRCC1, LIG3, and PARP1 (**Figure 3.2C**).

To facilitate further exploration of the EWS-FLI1 interactome by the research community, we have made our complete proteomics dataset, together with the combined analysis incorporating DepMap data, publicly available with the Sarcoma Network Server App Combined Analysis Tool, or SaNSA CAT (https://kentsisresearchgroup.shinyapps.io/sansacat/).

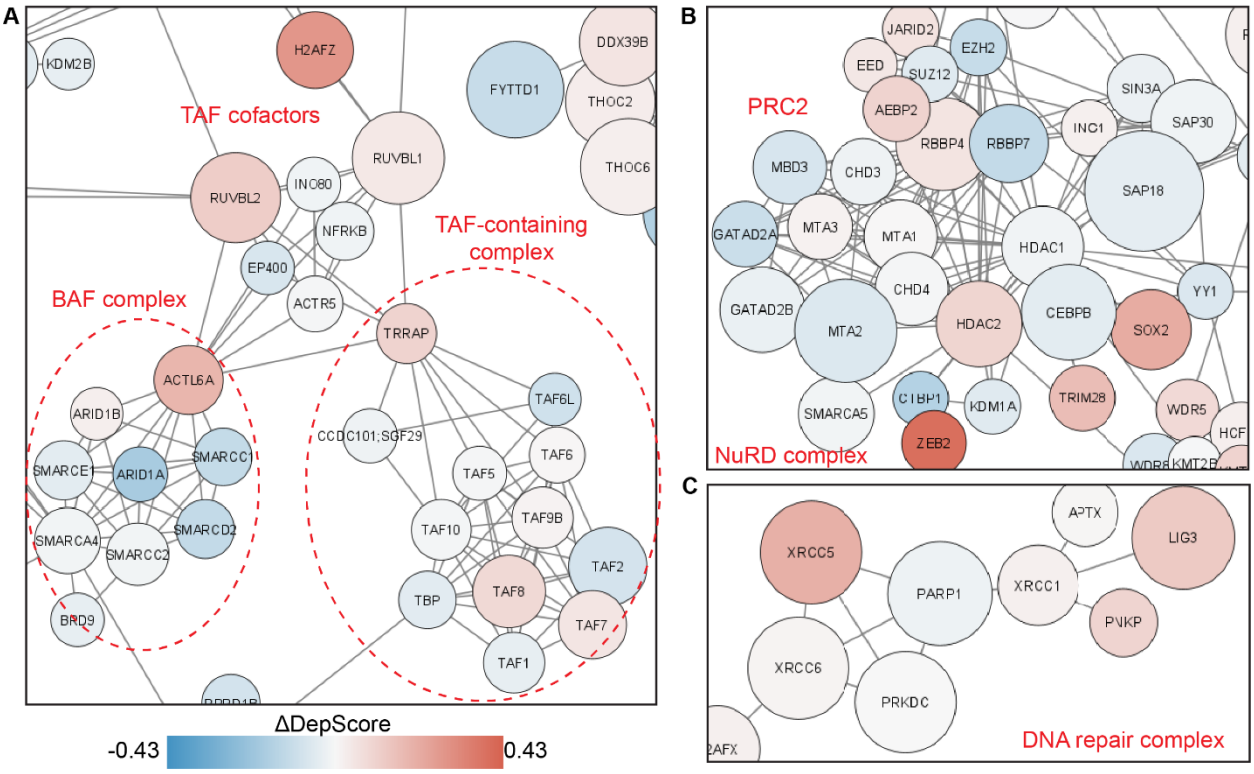

Figure 3.2: Network analysis of IP-MS data. EWS-FLI1 interactors cross-referenced with both DepMap dependency data and the STRING protein interaction database. The indicated snapshots show (**A**) the BAF complex, as well as the TAF containing complex and its cofactors, (**B**) the NuRD and PRC2 repressive complexes, and (**C**) the DNA repair complex detected. Color indicates ΔDepScore, while size is proportional to protein coverage.

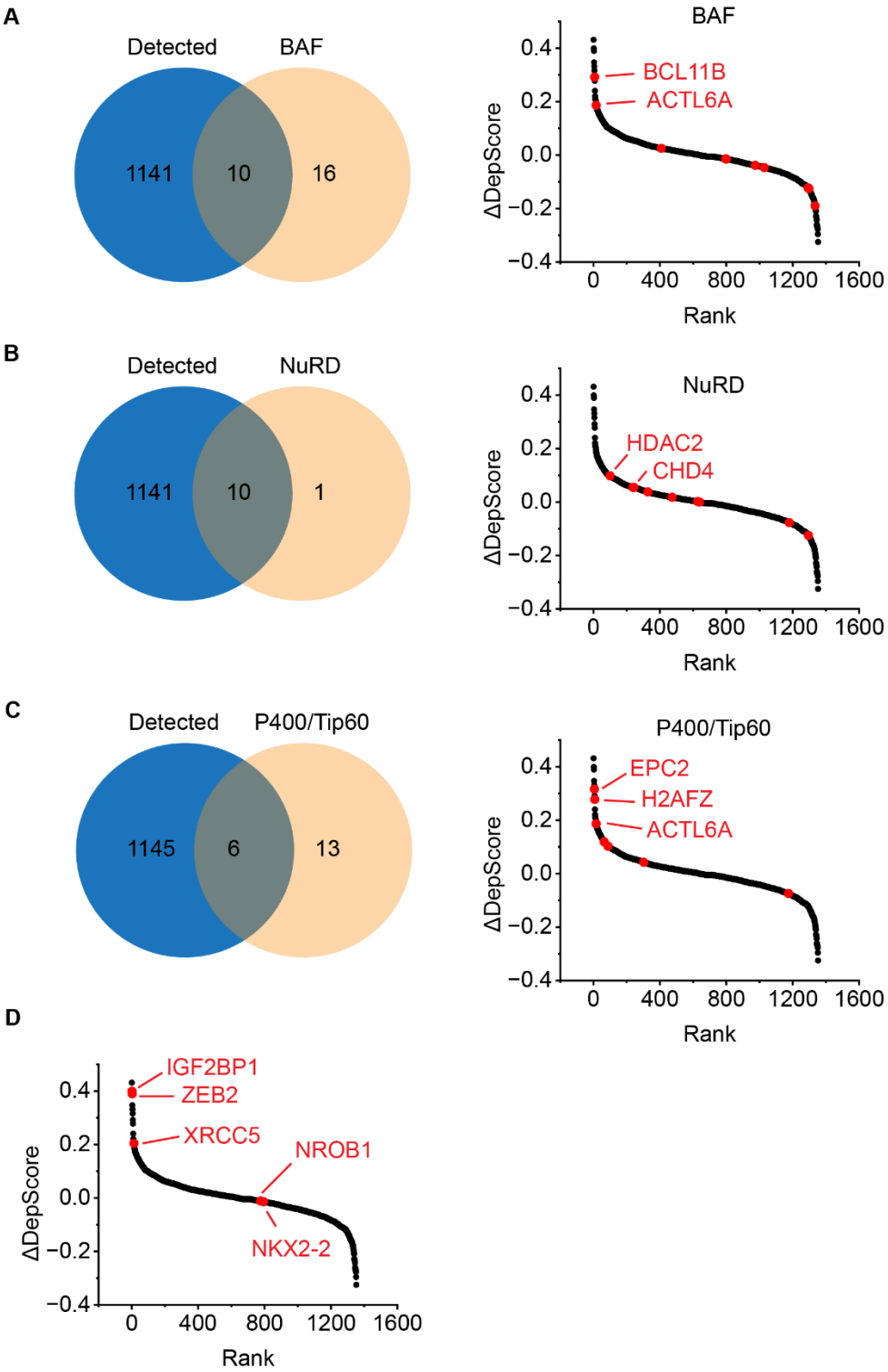

Figure 3.3: IP-MS data cross-referenced to known complexes and EwS interactors. (**A-C**) Venn diagrams showing the overlap of detected interactors with the indicated complexes, together with rank-order plots showing ΔDepScore for the indicated complexes. Red dots indicate detected members of each complex. (**D**) Other proteins of interest within the rank-order plot.

A peptide interference screen reveals that the fusion breakpoint is critical for EWS-FLI1 target gene expression in Ewing sarcoma cells

After identifying the list of putative cofactors of EWS-FLI1, I next attempted to address two parallel questions: 1) Do certain cofactors form direct protein-protein interactions with EWS-FLI1 that, if blocked, would interfere with EWS-FLI1 function? In other words, which of the proteins identified in the previous section are dependencies specifically by virtue of their interaction with EWS-FLI1? 2) Are there specific regions of the EWS-FLI1 protein that mediate its direct interaction with these key cofactors?

I hypothesized that different portions of the EWS-FLI1 protein might interact with distinct cofactors. Some of these cofactors, and the corresponding interaction domains on EWS-FLI1, may be dispensable for the fusion protein's oncogenic function, while others are likely critical for cancer cell survival. In surveying the sequence of EWS-FLI1, I hypothesized that the fusion breakpoint, being a pathogenic juxtaposition of the EWS LCD and FLI1 ETS domain, might function as a neomorphic interaction domain. This would thus constitute a truly synthetic dependency, being a domain that does not exist in the normal human proteome.

In order to define the regions of the EWS-FLI1 fusion protein critical for its function, I used a peptide interference approach, similar to that used recently for other dominant oncogenes (269). The advantages of this approach include: 1) The ability to perform a structure-function analysis of the fusion without the need for endogenous fusion knockdown and ectopic expression of truncated fusion proteins, 2) High temporal control of interference peptide expression, compared with genetic approaches targeting EWS-FLI1, thus avoiding secondary effects of gene editing, and 3) The potential for an immediately usable probe molecule that can be used for further exploration of key interaction domains and ultimate development of clinical-grade pharmacologic inhibitors. To this end, I designed a set of doxycycline (dox)-inducible genetic constructs encoding

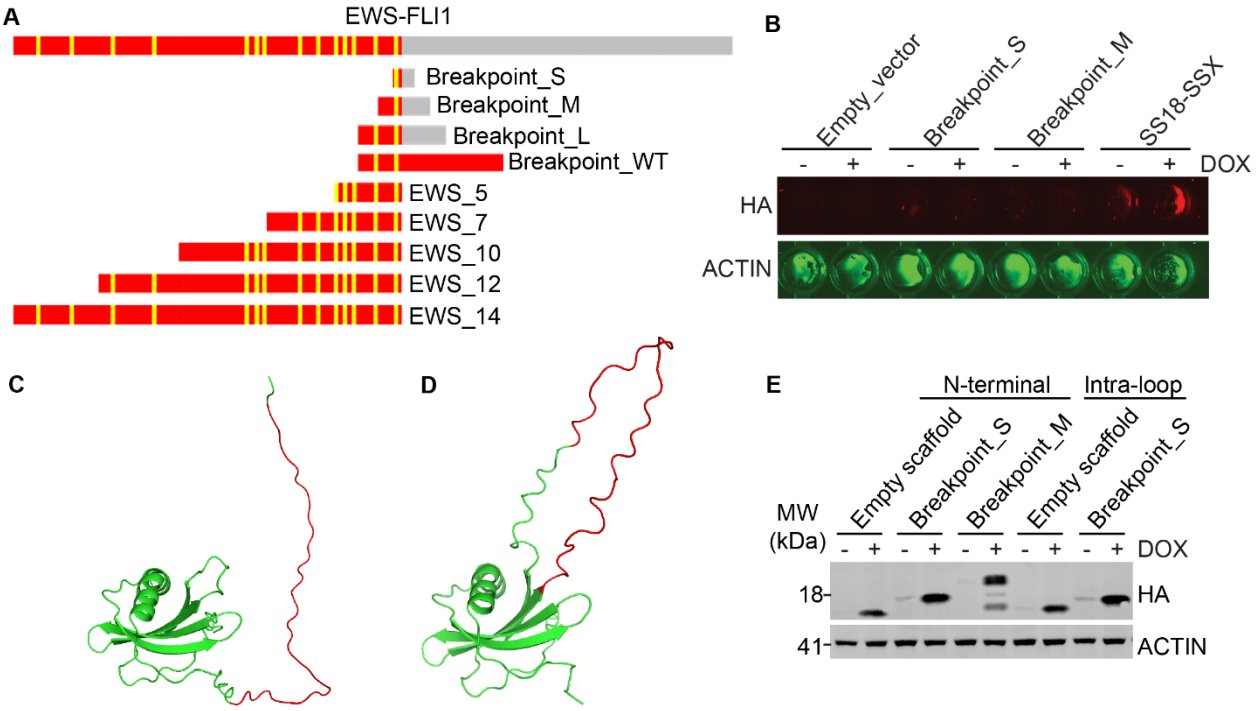

Figure 3.4: Schematic and initial test of Ewing peptides. (**A**) Schematic of designed peptides and their positions along the fusion protein. EWSR1 is in red, FLI1 is in grey, [S/G]Y[S/G] repeats are in yellow. (**B**) In-cell western/cytoblot of the unscaffolded peptides and SS18-SSX indicated in HEK293T cells. Samples were treated with Dox for 4 days at 1 µg/mL. (**C-D**) AlphaFold2 predictions of Affimer scaffolds containing Breakpoint_M inserted into the scaffold N-terminus (**C**) and a flexible display loop (**D**). (**E**) HEK293T cells transfected with the indicated construct and treated with Dox for 2 days at 1 µg/mL.

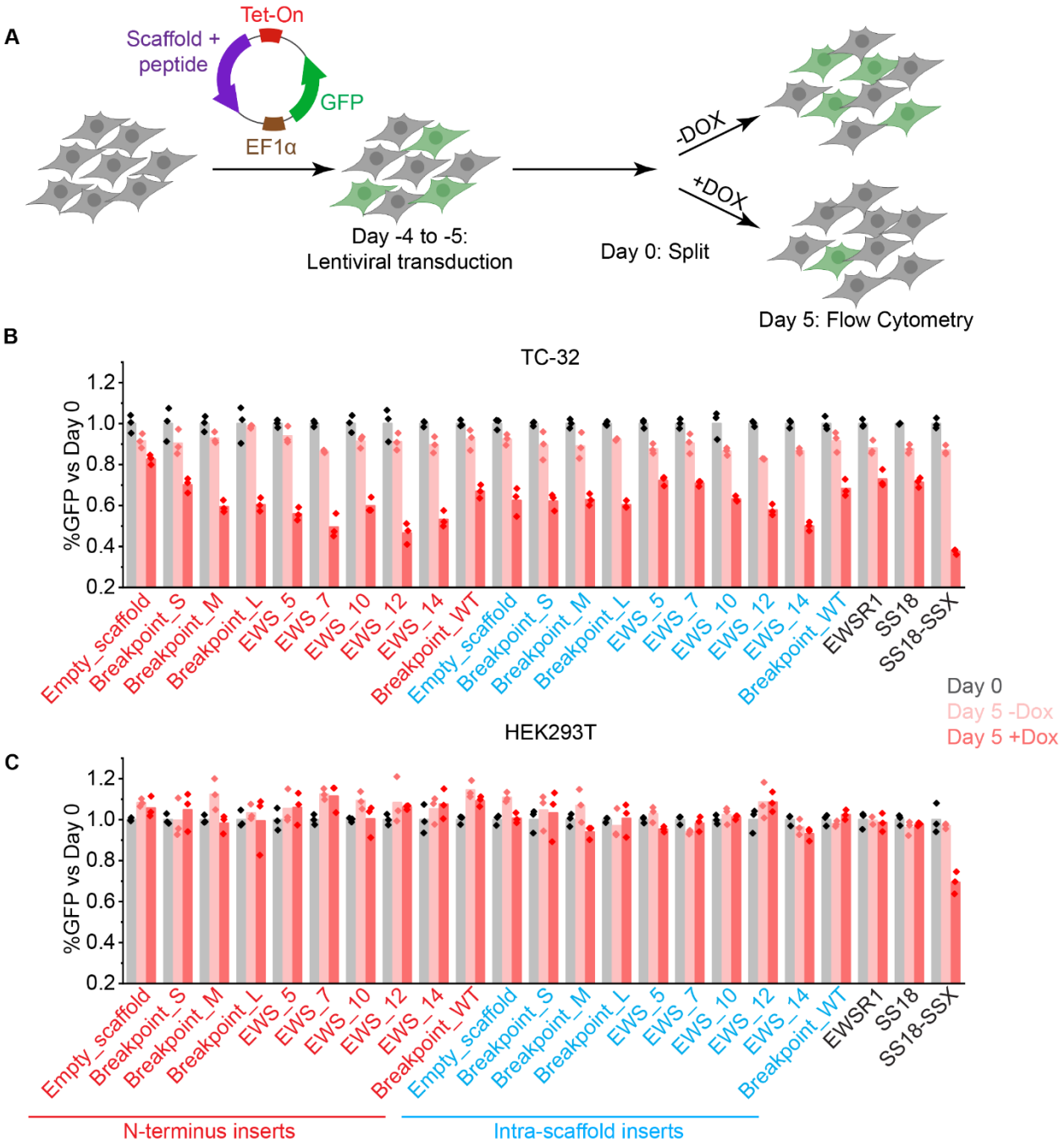

Figure 3.5: Screen of Affimer-scaffolded peptides reveals potential dependency on fusion breakpoint. (**A**) Schematic for flow cytometry screen of scaffolded peptides. (**B-C**) Plots of percent of GFP+ TC-32 (**B**) and HEK293T (**C**) cells in each treatment condition, normalized to Day 0. Cells were treated with Dox at 1 µg/mL.

peptides spanning different regions of the fusion protein. For expression in mammalian cells, I made use of the pINDUCER21 vector (264), which expresses the tetracycline transactivator protein (rTA) and GFP from the constitutive EF-1α promoter, and the peptides from the tetracycline response element (**Figure 3.5A**).

To probe the role of the breakpoint, I designed three peptides that spanned progressively larger segments centered on the fusion junction, which I designated Breakpoint_S (Small), Breakpoint_M (Medium), and Breakpoint_L (Large), as well as a control Breakpoint_WT (Wild-Type) peptide that includes a region of wild-type EWSR1 C-terminal to the breakpoint. I also designed expression constructs encoding peptides spanning progressively larger segments of the disordered EWS portion of the fusion, as the EWS portion is known to be necessary for EWS-FLI1 interaction with known cofactors. I designed these peptides to include increasing numbers of [G/S]Y[G/S] repeats, in order to define a threshold number of repeats sufficient to interfere with EWS-FLI1 assembly and function (**Figure 3.4A**). These peptides were named for the number of repeats contained within (i.e. EWS_5 contains 5 repeats). The complete list and sequence of peptides is found in **Supplementary Table S6**.

For a Dox-inducible positive control, I looked for a protein that would both impair the growth of most cells, and that would specifically disassemble a known component of the EWS-FLI1 complex key for Ewing sarcoma cell survival. I therefore chose to use the SS18-SSX fusion oncogene, which causes synovial sarcoma. Expression of this fusion protein, which contains the BAF subunit SS18, causes aberrant assembly and re-targeting of the BAF complex (270) which interacts with EWS-FLI1 and is necessary for some of its functions in Ewing sarcoma cells (161). I hypothesized that expression of SS18-SSX would be deleterious to Ewing sarcoma cells and would serve as a positive control for partial suppression of the EWS-FLI1 function.

To test the stability of these peptides, I transduced them into HEK293T cells conjugated only to a monopartite Simian Virus 40 (SV40) large T antigen NLS (nuclear localization sequence) and an HA-tag for detection. However, I found that expression of the first peptides tested, Breakpoint_S and Breakpoint_M, was undetectable by western blot or cytoblot, indicating that they are not stable within cells (**Figure 3.4B**). This was the case even with the relatively large (24.6 kDa) EWS_12 peptide (data not shown), suggesting that this lack of stability is a result of peptide disorder rather than the small size of the Breakpoint peptides. In order to improve peptide stability, I grafted them into a stable, well-folded protein scaffold, an approach frequently used for the display of small peptides to improve their stability and binding properties (271, 272). I selected the Affimer scaffold, based on the human protease inhibitor stefin A (also called cystatin A), as it has been shown to accommodate large inserts, is biorthogonal, and has been tested in mammalian cells with a nuclear localization sequence in previous work (273-275).

Each peptide was inserted either into the N-terminus of the scaffold or into a flexible loop within the middle of the scaffold (**Figure 3.4C-D**). In transfected HEK293T cells, this scaffold was able to stabilize the peptides, with expression being detectable by western blot (**Figure 3.4E**). I then transduced TC-32 cells and HEK293T cells (as a non-Ewing sarcoma control cell line) with each peptide. In total, this amounted to 10 peptides, each with 2 insertion sites, as well as SS18-SSX as positive control. As added controls, I also included full-length SS18 and EWSR1. After transduction, I screened cells expressing the peptides in a competition assay: I induced expression of the peptides/proteins with dox and measured the proportion of GFP+ cells after 3 days using FACS (**Figure 3.5A**). In TC-32 cells, the Empty_scaffold (i.e. only the NLS inserted into the N-terminus of the Affimer scaffold) induced only a small reduction in the percent of GFP+ cells, suggesting minimal toxicity of the scaffold alone (**Figure 3.5B**). However, all other N-terminally inserted peptides caused a dox-dependent reduction in GFP positivity, with the small,

medium, and large breakpoint peptides conferring progressively stronger effects. All of the EWS constructs appeared to have similar effect sizes to Breakpoint_L, with the Breakpoint_WT construct having a somewhat reduced effect size, suggesting a potentially higher potency for the peptide targeting the breakpoint junction compared to wild-type ESWR1. Indeed, the effect of full-length EWSR1 expression was milder than that for Breakpoint_M and Breakpoint_L (**Figure 3.5B**).

I also noted that all of the intra-scaffold peptides, including the empty scaffold (i.e. with the NLS inserted into the flexible loop) appeared to have roughly equal effects on GFP+ cells (**Figure 3.5B**). This suggested that the presence of the highly positively charged NLS within the loop conferred some non-specific toxicity in TC-32 cells. For future studies, I therefore chose to use the N-terminal insertion site, which in any case should maximize conformational flexibility. Encouragingly, none of the constructs showed any activity in HEK293T cells, with the exception of the SS18-SSX positive control (**Figure 3.5C**).

I next tested the effect of the N-terminal peptides on cell viability, including all N-terminally inserted peptides that demonstrated activity in the flow cytometry screen. To do this, I found it necessary to generate single-cell clones of each peptide, as protein expression was barely detectable by Western blot for many of the constructs in TC-32 cells when transduced at a low MOI of ~0.3, with only the Empty_scaffold and Breakpoint_M peptides showing clear bands in dox-treated samples (**Figure 3.6A**). The larger peptides showed only faint smears or were barely detectable by western blot (data not shown). This indicates that although the peptides are stable when expressed from transfected cells containing a high copy number of the peptides (**Figure 3.4E**), they are still expressed at low levels when present in a single copy within a polyclonal population (**Figure 3.6A**). I therefore generated single-cell clones for cells expressing each construct, selecting clones with high induction of each peptide as measured by anti-HA Western blot

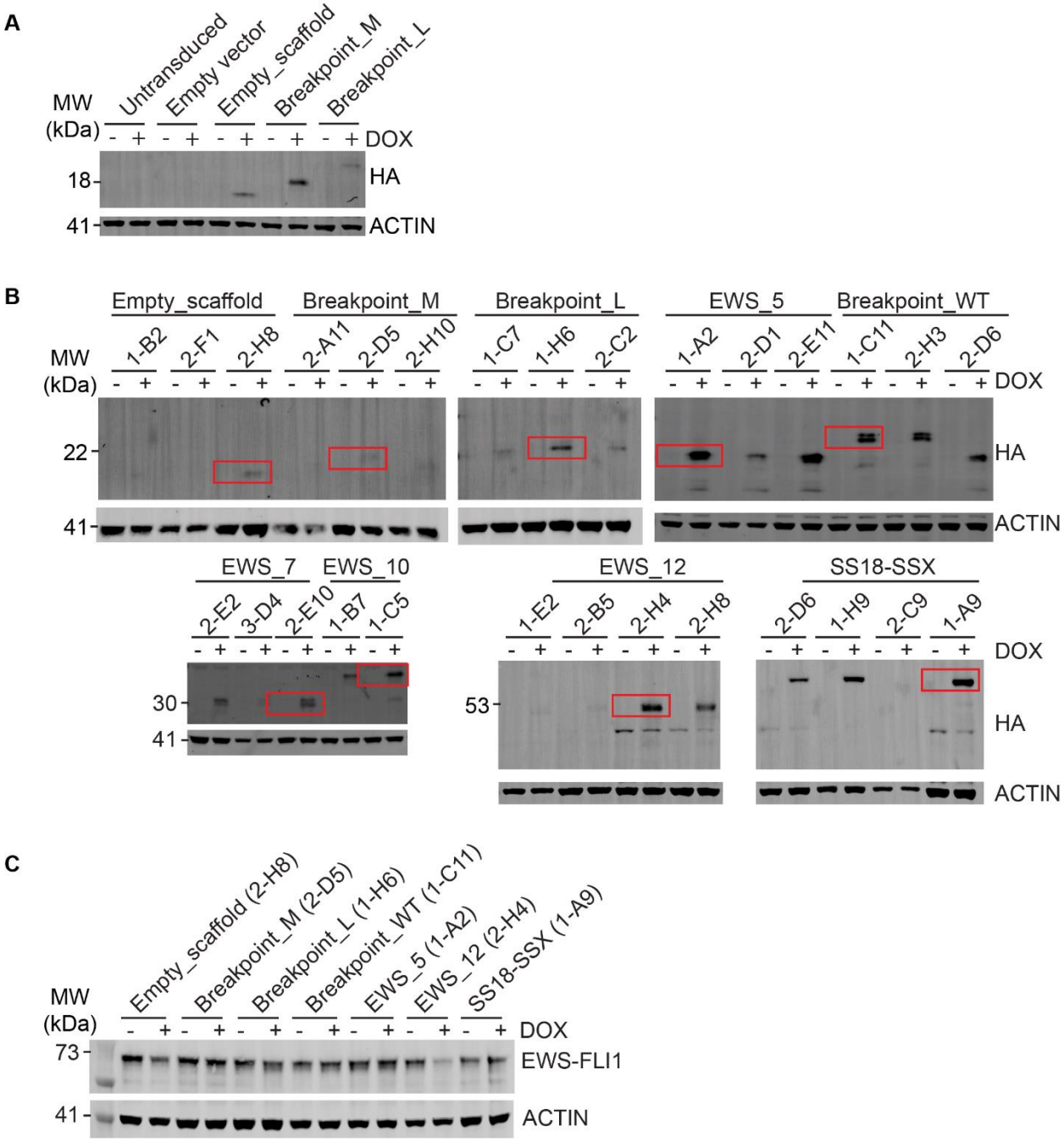

Figure 3.6: Single-cell cloning of Affimer-scaffolded peptides. (**A**) Polyclonal populations of TC-32 cells, transduced with the indicated constructs or empty pInducer21. (**B**) TC-32 single-cell clones of the indicated construct, showing selected clones with the highest expression levels of HA-containing constructs. Red boxes indicate clones selected for further experiments. (**C**) All cells were dox-treated for 4 days at 1 µg/mL.

(**Figure 3.6B**). Despite repeated attempts at cloning out these cells, I found that induction of Empty_scaffold, Breakpoint_M and Breakpoint_L constructs is relatively low compared to all other constructs (**Figure 3.6B**). I confirmed that all clones express equal levels of the EWS-FLI1 fusion protein (**Figure 3.6C**). Interestingly, I found that dox induction of the EWS_12 scaffolded peptide led to a clear reduction of EWS-FLI1 protein levels (**Figure 3.6C**).

I then tested the effect of each construct on cell viability, as measured by CellTiter-Glo. The effect of dox induction on most peptide clones was negligible, but Breakpoint_L showed a slightly reduced cell viability after 16 days of treatment (**Figure 3.7**). The Breakpoint_WT peptide actually showed a slight increase in viability with dox treatment. I also noted that the growth rates of each clone vary, indicating that despite equal EWS-FLI1 expression levels, some of the clones are more proliferative than others. Surprisingly, the EWS_12 peptide had no measurable effect despite reduction of EWS_12 levels. This data, together with the flow cytometry measurements of GFP expression as a surrogate of cell fitness, indicates that the Breakpoint_L peptide has a subtle, but significant negative effect on TC-32 growth. It should be noted, however, that the discrepancy between the effect sizes seen in the flow cytometry assay (**Figure 3.5B**) and the cell viability assay (**Figure 3.7**) will require clarification through future experiments.

To more fully define the effect of the peptides on EWS-FLI1 activity, I performed comparative gene expression analysis using RNA-seq, collecting samples after 6 days of dox treatment. Apart from the SS18-SSX positive control, Breakpoint_L and to a lesser extent Breakpoint_WT induced significant gene expression changes (**Figure 3.8**). Surprisingly, untransduced cells also showed a transcriptional response to dox induction. However, this is likely to be a nonspecific effect of high doxycycline concentration, as the differentially expressed genes (DEGs) in the untransduced cells are largely distinct from those in the Breakpoint_L and Breakpoint_WT groups (**Figure 3.9A**).

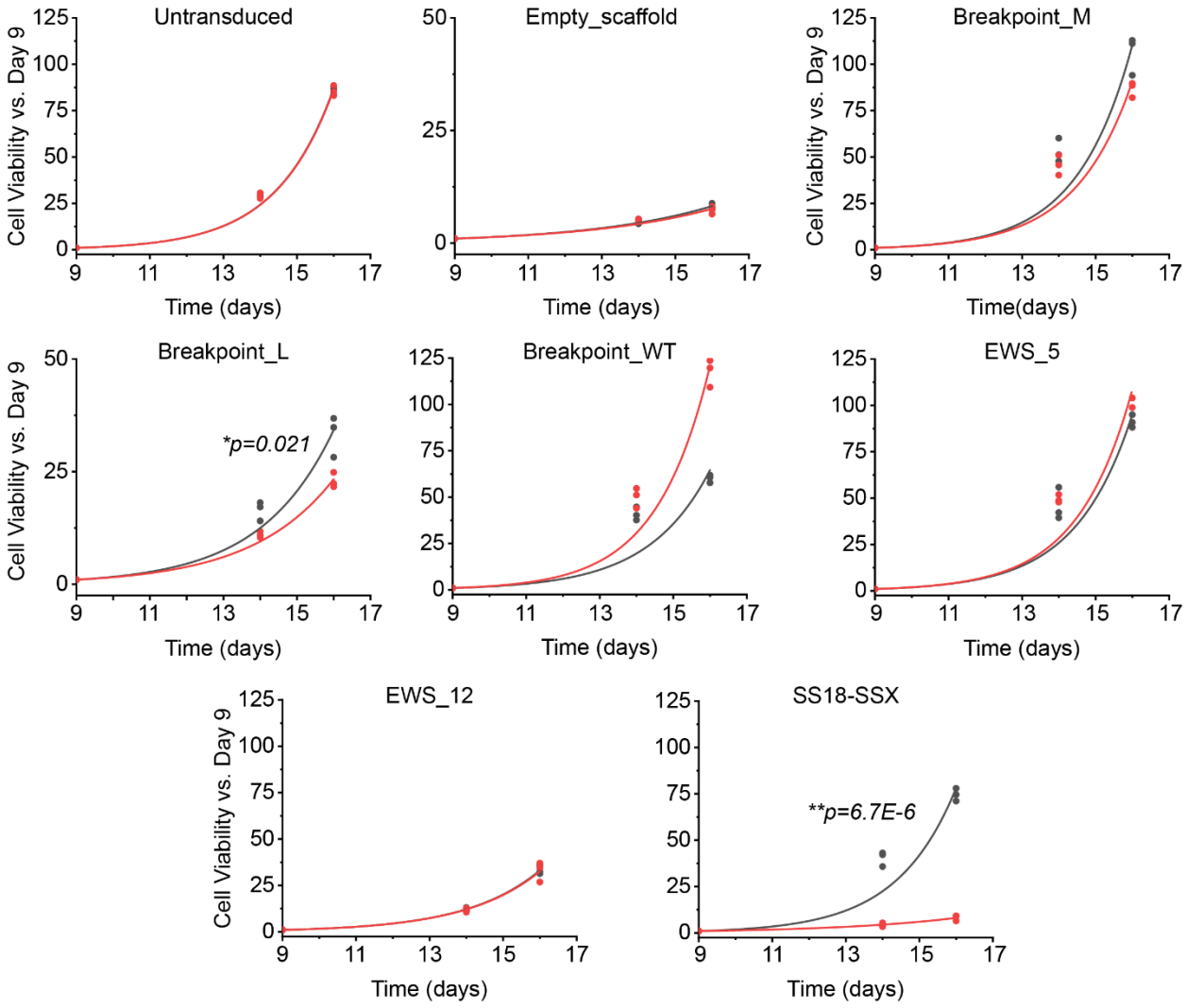

Figure 3.7: Effects of scaffolded peptides on cell viability. Plots of cell viability as measured by CellTiter-Glo for the indicated constructs in TC-32 cells. Cells were treated with dox at 1 µg/mL for 9 days, re-plated at equal seeding densities, and treated for an additional 7 days. Y-axes show cell viability normalized to Day 9. P-values are calculated by Student's two-tailed t-test on Day 16.

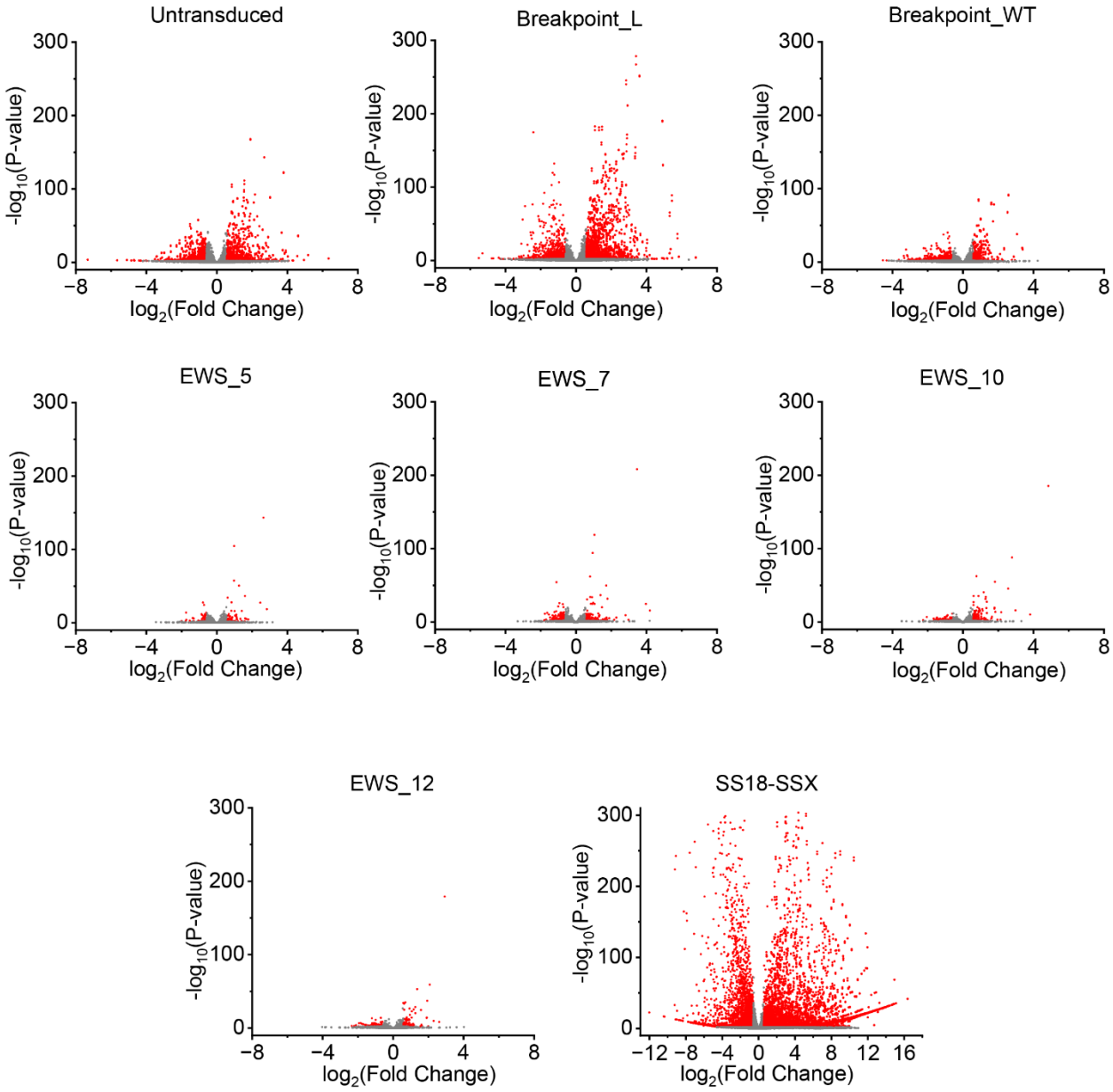

Figure 3.8: RNA-seq analysis of scaffolded peptides. Volcano plots of TC-32 single-cell clones indicated in Figure 3.6B treated with dox at 1 µg/mL for 6 days. Plots show a comparison of (+)dox samples with (-)dox, each in triplicate. Red dots indicate a fold-change > 1.5 and p<0.01.

Gene set enrichment analysis (GSEA) showed multiple Ewing sarcoma gene sets responded to Breakpoint_L induction as would be expected with a disruption of EWS-FLI1, but not by Breakpoint_WT (**Figure 3.9B**). In order to precisely assess the effect of interference with EWS-FLI1 on transcription, I performed RNA-seq on TC-32 cells containing a degron tag on EWS-FLI1 that allows for temporally controlled knockdown (KD) of the fusion upon danoprevir treatment (276), kindly provided by David McFadden's lab. Encouragingly, principal component analysis (PCA) of RNA-seq data indicated a shift in danoprevir-treated cells along the same PC as Breakpoint_L induction, suggesting a similar transcriptomic effect (**Figure 3.10A**). As expected, EWS-FLI1 KD caused perturbation of several EWS-FLI1-related gene sets (**Figure 3.10B**), as well as upregulation of epithelial-to-mesenchymal transition (EMT) gene sets (**Figure 3.10C**). This is in line with previous observations that Ewing cells with lower EWS-FLI1 expression exhibit a more mesenchymal phenotype compared to those with higher EWS-FLI1 expression (183, 184, 277). Using the RNA-seq data of danoprevir-treated EWS-FLI1 KD cells, I generated a custom gene set of EWS-FLI1-upregulated genes specific to TC-32 cells and found that Breakpoint_L expression causes a significant downregulation of this gene set (**Figure 3.10D**).

Finally, I examined the effect of Breakpoint_L on several validated EWS-FLI1 target genes (**Figure 3.11**). I found that only Breakpoint_L and EWS-FLI1 KD caused a downregulation of multiple target genes including *LOXHD1* (278), *NR0B1* (279, 280), and *NKX2-2* (266, 277), as well as *CCND1*, which shows uniquely high expression in Ewing compared to other sarcomas (281, 282). For all genes examined, the effect of Breakpoint_L was statistically significant but lower in magnitude than the effect of EWS-FLI1 KD (i.e. up to a 4-fold reduction with Breakpoint_L compared to a 10-fold reduction with KD). This matches my observations of the fairly mild cell viability defect observed with Breakpoint_L, and suggests that the effective dose of the peptide is not sufficient to fully

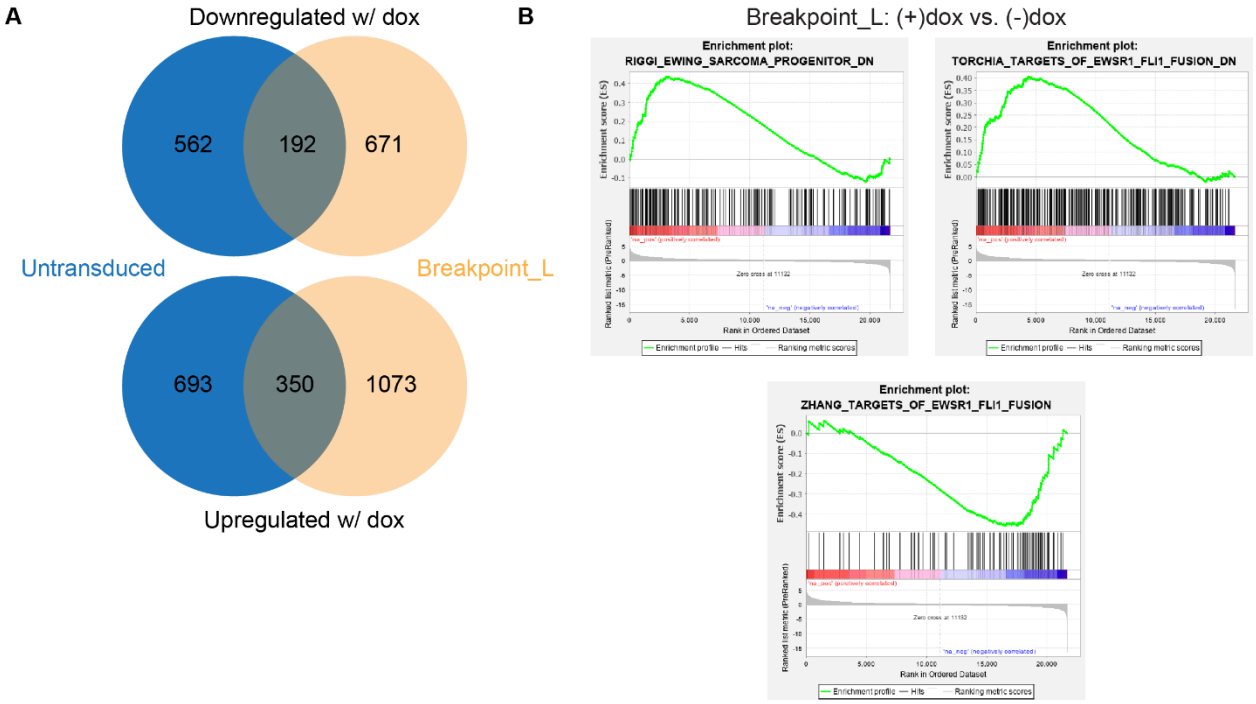

Figure 3.9: Breakpoint_L causes specific changes in gene expression. (**A**) Venn diagram showing differentially expressed genes in untransduced TC-32 cells compared with cells transduced with Breakpoint_L. (**B**) GSEA of RNA-seq data from Breakpoint_L induction.

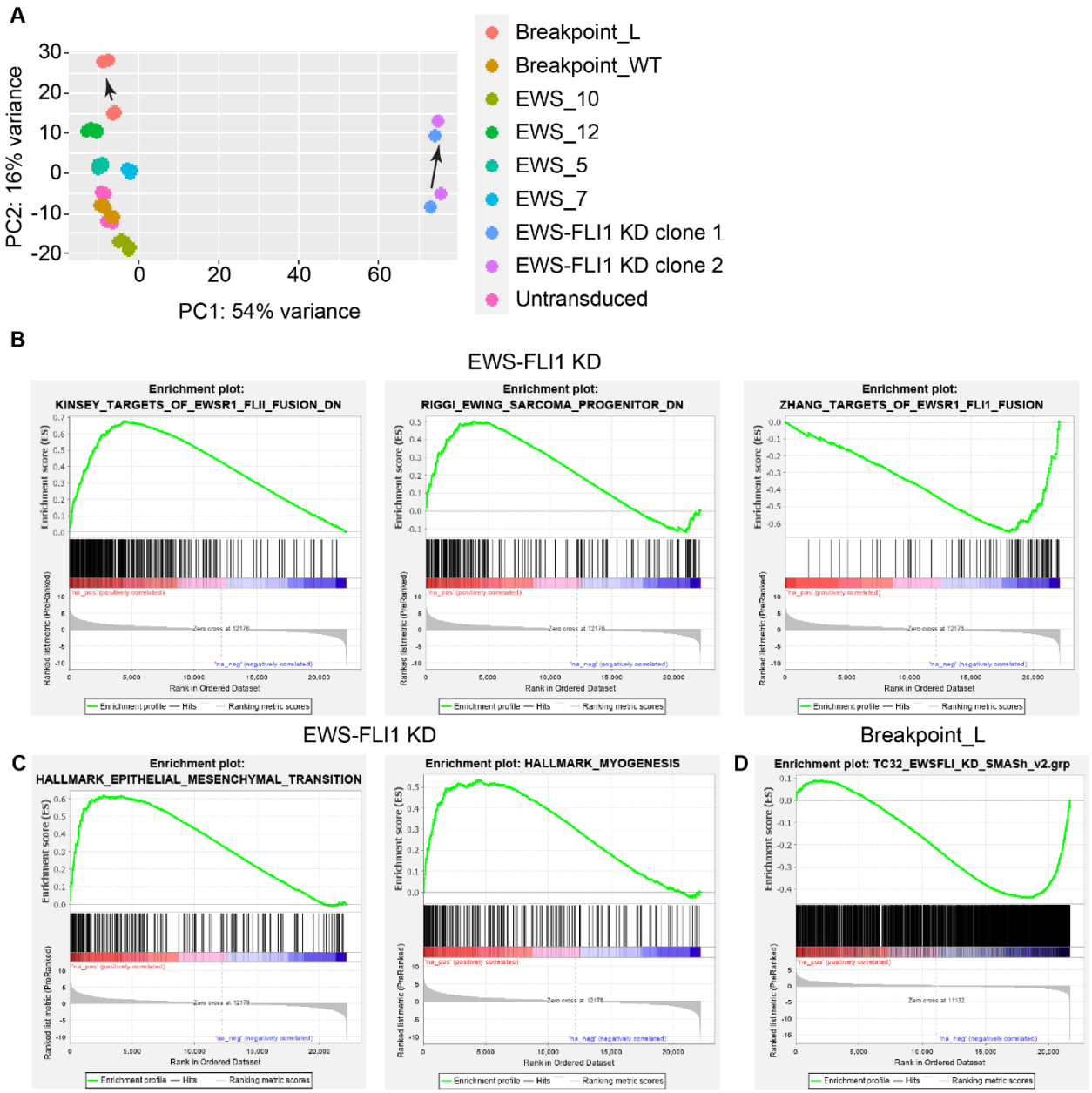

Figure 3.10: Breakpoint_L causes similar gene expression changes to EWS-FLI1 KD. (**A**) PCA of RNA-seq data. Arrows show the effect of dox treatment on Breakpoint_L-transduced TC-32 cells, or danoprevir on two EWS-FLI1 KD clones. (**B**) Selected EwS gene sets perturbed by EWS-FLI1 KD. (**C**) Selected gene sets showing mesenchymal differentiation upon EWS-FLI1 KD. (**D**) Custom TC-32-specific gene set derived from EWS-FLI1 KD cell, showing the effect of dox on Breakpoint_L-transduced cells.

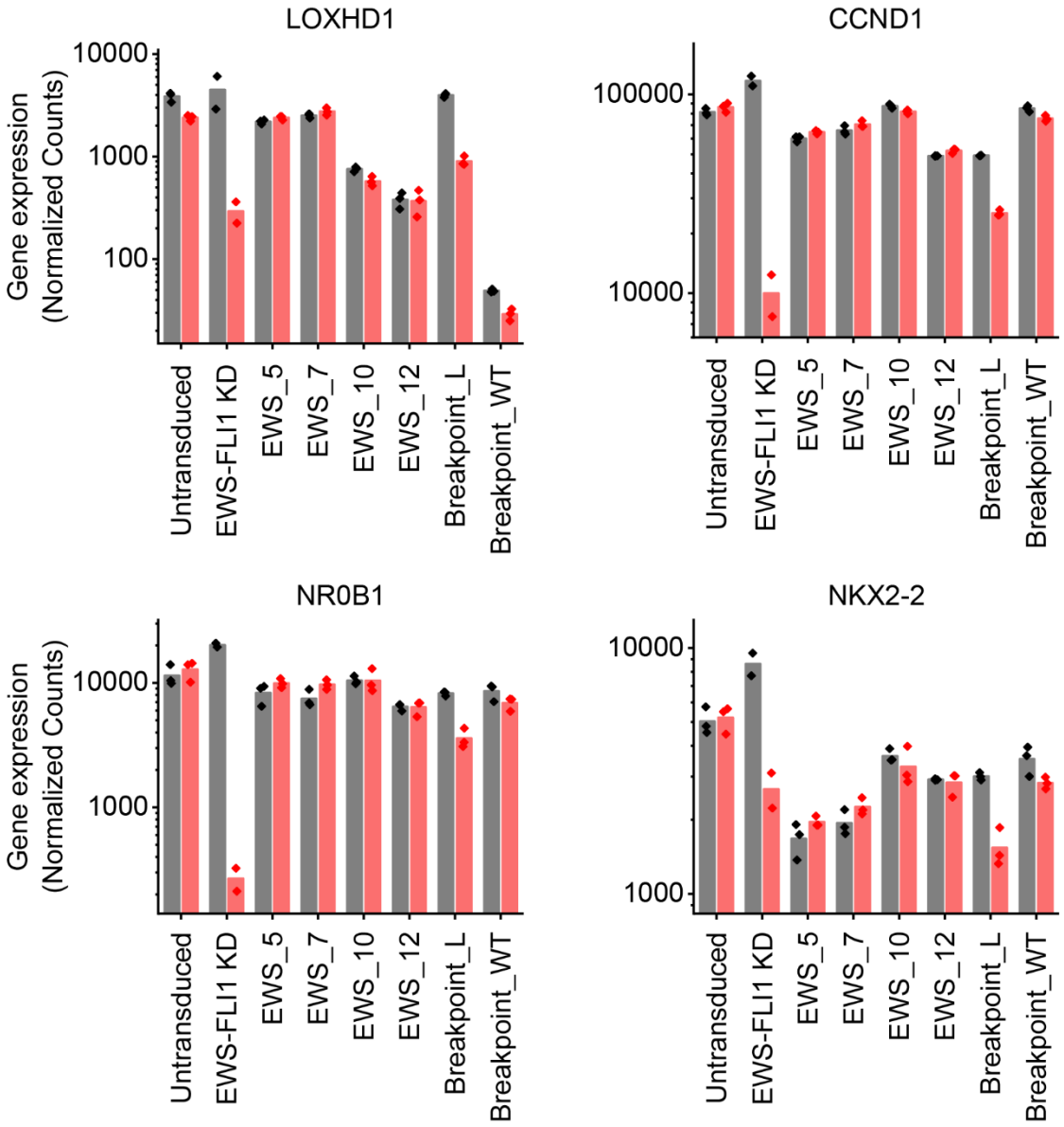

Figure 3.11: Breakpoint_L induces downregulation of EWS-FLI1 target genes. RNA-seq read counts normalized by DESeq2 showing changes in the indicated genes for each peptide.

interfere with EWS-FLI1 function. Nonetheless, the measurable effects of Breakpoint_L suggest that even at a low level of expression, its expression interferes with EWS-FLI1 function sufficiently to perturb EWS-FLI1 target gene expression.

3.3 Discussion

The set of proteins that EWS-FLI1 interacts with directly presents a daunting list, numbering in the hundreds. This is even more the case with the set of genes that EWS-FLI1 regulates, which numbers in the thousands and varies between experimental systems (283). In this work, I have attempted to both comprehensively define the list of EWS-FLI1 interactors, and then narrow it to those that are functionally important and potentially Ewing sarcoma-specific.

I chose to approach the EWS-FLI1 interactome through a two-part framework, positing that interacting proteins are either effectors of EWS-FLI1 or are sequestered away from their normal functions. The first category includes proteins and complexes that either repress or activate transcription of EWS-FLI1 target genes, with the BAF complex among them. Here, I have found that while most BAF subunits are not EwS-specific dependencies, the subunits ACTL6A and BCL11B do show high EwS-specific dependency scores. Tumor-specific roles for these subunits have been found in other cancers. Recent work on ACTL6A has found that it is a sub-stochiometric component of the BAF complex whose gene dosage varies in different stages of epithelial differentiation (284). Its overexpression in squamous cell carcinomas increases its occupancy within BAF and enhances the association of BAF with other transcriptional regulators, leading to expression of oncogenic genes (285). BCL11B is a transcription factor frequently mutated in hematological malignancies, and was found to be a BAF

complex subunit fairly recently (65). The role of these two BAF subunits within the EWS-FLI1-associated BAF complex thus merits further investigation.

In addition, I have found that a putative complex consisting of multiple TAF proteins and several additional cofactors co-immunoprecipitates with EWS-FLI1. This may constitute a specialized or aberrant transcriptional co-activation complex that is recruited by EWS-FLI1, which may in turn associate with the variant histone H2AFZ, which appears to be a potential EwS-specific dependency. Although the enzymes that mediate H2AFZ incorporation into chromatin do not have high ΔDepScore values, this may be a result of functional redundancy between the Tip60/EP400 and SRCAP complexes, both of which serve this function (286). In addition, the Tip60/EP400 subunits RUVBL2, EPC2, and ACTL6A (also a BAF subunit) score highly in my dependency analysis. H2AFZ itself is known to be aberrantly expressed in multiple cancer types (287), although its specific functions are still being elucidated. H2AFZ is associated with both gene activation and repression, depending on additional levels of regulation by PTMs of H2AFZ itself (286). Its high EwS-specific dependency score and association with EWS-FLI1 are compelling and require further investigation.

Other detected interactors may fall either within this first category or may be aberrantly sequestered away from their normal sites. One possible example of this second class of cofactors is ZEB2, another detected interactor with one of the highest dependency scores in my IP-MS data. ZEB2 is a master regulator of EMT (288) and is known to play an important role in EwS, antagonizing some of the functions of EWS-FLI1 to promote the transcription of mesenchymal genes (289). Concordant with recent findings, I found that EWS-FLI1 KD led to an upregulation of EMT gene signatures. One possible explanation is that loss of EWS-FLI1 from GGAA repeats liberates ZEB2, and potentially other lineage-specific transcription factors, to increase transcription of pro-EMT targets. Alternatively, ZEB2 may localize along with EWS-FLI1 to ETS-responsive

genes, playing a role in EWS-FLI1-mediated gene repression. In either case, the observation that ZEB2 associates with EWS-FLI1 warrants further investigation of its role in EwS.

Another potentially interesting cofactor found in this study is IGF2BP1, a protein expressed in many fetal tissues and several cancers, but rarely in adult tissues (290). IGF2BP1 is a post-transcriptional regulator, contributing to the stability and transport of multiple mRNAs important to proliferation and oncogenesis, including PTEN, MYC, and MKI67. The association of IGF2BP1 with EWS-FLI1, its high dependency score, and its restricted pattern of expression merit further investigation, although it is currently unclear which category of EWS-FLI1 interactors IGF2BP1 falls into.

Most importantly, the peptide interference experiments are encouraging and point to specific directions for further study. In the experiments described here, I have observed interesting effects of two peptides. Breakpoint_L expression slightly reduces TC-32 cell proliferation and causes mild but significant reduction in EWS-FLI1 target gene expression. This suggests a disruption of at least part of the oncogenic function of EWS-FLI1. EWS_12 significantly reduces EWS-FLI1 protein levels but does not affect either proliferation or transcription. The latter observation may be a result of remaining detectable EWS-FLI1 expression, and it is possible that the effect size produced by EWS_12 keeps EWS-FLI1 levels within the “Goldilocks zone” proposed by Stegmaier and colleagues (181).

Further study of these peptides will require overcoming several limitations of the current versions. One important challenge has been the relatively low expression levels of the peptides used here, with peptide stability apparently varying between peptides. While the Affimer scaffold offers improved peptide stability compared to unscaffolded peptides, ongoing studies indicate that alternative scaffolds may improve the activity of these peptides. For example, grafting the Breakpoint_L peptide onto other published

scaffolds resulted in readily detectable expression even in polyclonal transduced cells (**Figure 3.12A**), particularly with the designed ankyrin repeat protein (DARPin) scaffold (291) and a recently-developed scaffold based on the recombinase RadA from *Pyrococcus furiosus* (275). This is a clear improvement from the expression levels achieved with the Affimer scaffold (**Figure 3.6A**), and future experiments will make use of the RadA scaffold, which appears to have the highest expression levels.

Despite higher expression levels, however, the RadA-scaffolded Breakpoint_L peptide did not impair cell proliferation in preliminary studies, as measured by CellTiter-Glo (data not shown), suggesting that this scaffold requires further optimization. Immunofluorescence of the scaffolded peptide revealed that despite containing a single NLS, the RadA-scaffolded peptide did not specifically localize to the nucleus (**Figure 3.12B**). The addition of two additional NLS peptide sequences to the scaffold (termed RadA_3xNLS) was necessary to force nuclear localization (**Figure 3.12C**), as previously observed for other proteins including Cas9 (292). Finally, in order to test the effect of imposing some conformational constraint on the interference peptides, as was done with the first version of the RadA-scaffolded peptide, I engineered two versions of the RadA_3xNLS_Breakpoint_L construct- one inserted into the C-terminus of the scaffold in order to maximize conformational flexibility, and another inserted into a flexible loop within the scaffold.

Finally, even with the improvements in stability and presentation described above, it is unlikely that this peptide represents a true “magic bullet” against EWS-FLI1. One recent attempt at a structure-function analysis of EWS-FLI1 found for example, that the region of FLI1 just C-terminal to the fusion junction is dispensable for the transactivation activity of EWS-FLI1 (293). Other recent work using deletion mutants of EWS-FLI1 found that a mutant in which the pre-junction region of EWSR1 was replaced with an [G/S]Y[G/S]-rich motif from another portion of EWSR1 was able to bind to GGAA

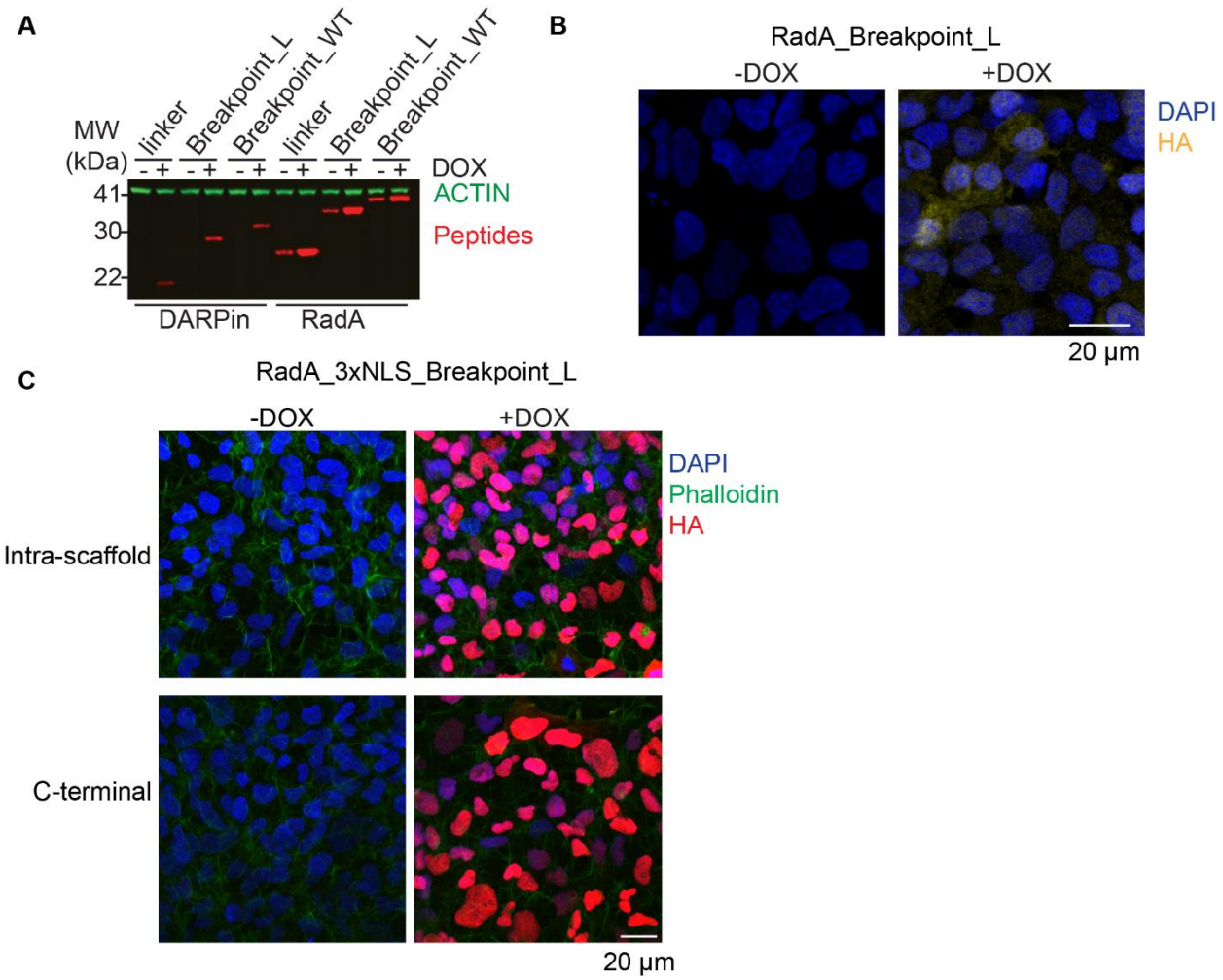

Figure 3.12: Alternative scaffolds increase expression of Breakpoint_L peptides. (**A**) Dox induction of HEK293T cells transduced with the indicated peptides grafted onto the DARPin or RadA scaffolds. Cells were treated with dox at 333 ng/µL for 3 days. (**B**) Anti-HA immunofluorescence of TC-32 cells transduced with the RadA-scaffolded Breakpoint_L peptide, inserted within the scaffold. Cells were treated as in (A). (**C**) Anti-HA immunofluorescence of TC-32 cells transduced with the indicated peptide. Cells were treated as in (A-B).

repeats in cells (161). These results suggest that at least some of the functions of EWS-FLI1 do not depend on the fusion junction or are sufficiently delocalized across the EWS-FLI1 sequence that fusion junction deletion does not abrogate them. Nonetheless, the improved versions of the scaffolded Breakpoint_L peptide should serve as valuable probe compounds in future studies of the EWS-FLI1 complex, and if sufficiently active, should represent leads for pharmacologic development.

3.4 Materials and Methods

Cell culture

Cell lines were obtained from the American Type Culture Collection. The identity of all cell lines was verified by STR analysis. Absence of Mycoplasma contamination was determined using the MycoAlert kit according to the manufacturer's instructions (Lonza). Cell lines were cultured in 5% CO_2 in a humidified atmosphere at 37°C. All media were obtained from Corning and supplemented with 10% fetal bovine serum (FBS), 1% L-glutamine, and 100 U/mL penicillin and 100 µg/mL streptomycin (Gibco). TC-32 cells were cultured in Roswell Park Memorial Institute (RPMI) medium. HEK293T cells were cultured in Dulbecco's Modified Eagle Medium (DMEM).

Western Blotting

To assess protein expression of EwS interference peptides by Western immunoblotting, pellets of 1 million cells were prepared and washed once in cold PBS. Cells were resuspended in 100 µL of RIPA lysis buffer (50 mM Tris-HCl, pH 8.0, 150 mM NaCl, 1.0% NP-40, 0.5% sodium deoxycholate, 0.1% sodium dodecyl sulfate) and incubated on ice for 10 minutes. Lysates were cleared by centrifugation at 18,000 g for 15 min at 4 °C. Protein concentration was assayed using the DC Protein Assay (Bio-Rad) and 15-35 µg whole cell extract was used per sample. Samples were boiled at 95 °C in

Laemmli buffer (Bio-Rad) with 40 mM DTT and resolved using sodium dodecyl sulfate-polyacrylamide gel electrophoresis. Proteins were transferred to Immobilon FL PVDF membranes (Millipore), and membranes were blocked using Intercept Blocking buffer (Li-Cor). Primary antibodies used were: anti-FLI1 (abcam, ab133485), anti-HA (Cell Signaling Technology, 3724S), and anti-Actin (Cell Signaling Technology, 4970 and 3700) at 1:5,000. Blotted membranes were visualized using goat secondary antibodies conjugated to IRDye 680RD or IRDye 800CW (Li-Cor, 926-68071 and 926-32210) at 1:15,000 and the Odyssey CLx fluorescence scanner, according to manufacturer's instructions (Li-Cor). Image analysis was done using the Li-Cor Image Studio software (version 4).

In-cell western blot/cytoblot

Single-cell clones were screened for inducible expression of HA-tagged peptides by in-cell western. Briefly, after growth in 96-well plates and treatment with dox at 1 µg/mL for 3 days, cells were fixed with ice-cold methanol for 10 min at -20°C. Cells were then washed three times with cold PBS and blocked with Intercept Blocking buffer (Li-Cor) with gentle shaking at room temperature for 1 h. Cells were stained with primary antibody at 1:1,000 in blocking buffer at 4°C overnight. Cells were then washed with TBST 5 times for 5 min and incubated with secondary antibodies conjugated to IRDye 680RD or IRDye 800CW (Li-Cor, 926-68071 and 926-32210) at 1:800. Cells were washed 4 additional times with TBST for 5 min and imaged on the Odyssey CLx fluorescence scanner, according to manufacturer's instructions (Li-Cor) and using a 3.5 mm offset. Image analysis was done using the Li-Cor Image Studio software (version 4).

Design of doxycycline-inducible peptide constructs

All constructs were synthesized by Atum (Newark, CA) in a modified pINDUCER21 backbone, which allows dox induction of transgene constructs and expressed GFP under the constitutive EF-1α promoter (264). The backbone was modified by Atum by removing the BsmBI restriction site in the CMV 5' UTR element. Unscaffolded and Affimer-scaffolded peptides contained an SV40 monopartite NLS directly C-terminal to the peptide. All peptide constructs incorporated the HA tag and triple stop codon present in the vector, with the cloning site introducing a Phe-Glu dipeptide just N-terminal to the HA tag. RadA-scaffolded peptides included an additional HA tag in tandem to the original tag.

For Affimer-scaffolded peptides, two insertion sites were used. N-terminally inserted peptides were placed starting at amino acid position 4, replacing Trp4. Intra-scaffold inserted peptides were inserted into the flexible loop beginning at Phe70 and replaced the following Lys-Ser-Leu motif within the loop.

For RadA-scaffolded peptides, two insertion sites were used. Intra-scaffold inserted peptides were inserted at position 181 and flanked by linkers comprised of "SGGGGS" in order to impart conformational flexibility to the insert. C-terminally inserted peptide were inserted C-terminal to the scaffold sequence and N-terminal to the HA and NLS sequences. The SV40 monopartite NLS and HA tag are located at the C-terminus. Constructs containing three NLS sequences additionally contained a c-Myc-like NLS at the N-terminus and a nucleoplasmin NLS between the SV40 NLS and the HA tag.

A complete list of plasmids and their peptide/scaffold amino acid sequences are listed in **Supplementary Table S7**.

Lentivirus production

Lentivirus production was performed as described previously (252). Briefly, HEK293T cells were transfected using TransIT-LT1 (Mirus) using a 2:1:1 ratio of lentiviral vector, psPAX2, and pMD2.G packaging plasmids. Viral supernatant was collected at 48

and 72 hours pos-transfection, pooled, filtered, and stored in aliquots at -80°C. TC-32 and HEK293T cells were transduced at a multiplicity of infection (MOI) of 0.3. Transduced cells were allowed to grow for 3 days and collected using fluorescence-activated cell sorting (FACS) for GFP+ cells.

Immunoprecipitation of EWS-FLI1

To prepare antibody-coupled beads, 3 mg of 1:1 Protein A:Protein G Dynabeads slurry (Invitrogen, 10002D and 10004D) was washed 3 times with 1 mL blocking solution containing PBS w/ 0.5% bovine serum albumin (BSA). Beads were then resuspended in 1 mL blocking solution with 12.5 µg antibody (anti-FLI1 from abcam, ab15289 or normal rabbit IgG control from EMD Millipore, 12-370) and incubated at room temperature for 1 h with end-over-end rotation. Beads were then washed again 3 times with blocking solution.

TC-32 cells were grown to a confluence of ~80% in 15-cm plates and harvested by trypsinization. Six total samples were prepared with ~130 million cells per sample. Cells were pelleted by centrifugation at 500 x g and washed once in cold PBS. Cells were incubated in 20 mL hypotonic lysis buffer per sample (10 mM HEPES, pH 7.9, 10 mM NaCl, 1 mM $MgCl_2$, 0.5 mM dithiothreitol/DTT, protease inhibitors) for 1 h on ice. Samples were Dounce homogenized on ice (15 strokes with a loose pestle), and nuclei were pelleted by centrifugation at 3,300 x g for 15 min at 4°C and resuspended in 3 mL per sample of low-sucrose buffer (10 mM HEPES, pH 7.9, 10 mM $MgCl_2$, 0.25 M sucrose). Nuclei were then layered on top of an equal volume of high-sucrose buffer (10 mM HEPES, pH 7.9, 10 mM $MgCl_2$, 0.88 M sucrose) and centrifuged at 1,200 g for 10 min at 4°C to isolate nuclei. Non-nuclear debris was carefully aspirated, and nuclei were resuspended in 1 mL nuclear lysis buffer (50 mM HEPES, pH 7.4, 150 mM NaCl, 0.25 mM EDTA, 0.5% Triton X-100, 10% glycerol, 1 mM DTT, protease inhibitors) per sample. Nuclei were incubated on ice for 20 min, and lysed by sonication using the Covaris S220

adaptive focused acoustic sonicator in millitubes at 80 W peak incident power level, 5% duty factor, 200 cycles/burst for 5 min at 4°C. This sonication step was included to disrupt indirect interactions with chromatin-dependent cofactors. Nuclear lysates were clarified by centrifugation at 18,000 x g for 15 min at 4°C. Clarified nuclear lysates were incubated with antibody-coupled Protein A/G beads in nuclear lysis buffer (4 mL per sample) overnight at 4°C with end-over-end rotation. Beads were then washed 3 times with nuclear lysis buffer and eluted in 40 µL glycine, pH 3.0. Eluted proteins were neutralized with 2 µL 1.0 M Tris, pH 11 and prepared for gel loading by addition of 8 µL of 5X western blot sample buffer (to a final concentration of 4.5 mM Tris-HCl, pH 6.8, 1%SDS, 2% beta-mercaptoethanol, 7% glycerol, 0.0002% Bromophenol Blue). Samples assessed for pulldown efficiency by western immunoblotting were boiled at 95°C for 5 min.

Mass spectrometry proteomics

Eluates prepared as described above were resolved by SDS-PAGE 10% polyacrylamide Bis-Tris gels (Invitrogen) at 100V for 10 min. To visualize proteins, gels were stained using the Silver Stain for Mass Spectrometry Kit (Pierce) according to manufacturer's instructions. Full lanes were excised and destained using 50 µL of 30 mM $K_3[Fe(CN)_6]$ in 100 mM aqueous $Na_2S_2O_3$ with incubation at room temperature for 30 min. Destained gel fragements were washed once in 500 µL of 25 mM NH_4HCO_3 with shaking at 650 rpm on a thermomixer for 5 min at room temperature. Solution was removed and gel pieces were washed in 500 µL 25 mM NH_4HCO_3 in 50% acetonitrile with shaking at 650 rpm for 10 min at room temperature. This wash step was repeated two additional times. Solution was removed and 100 µL of acetonitrile was added and incubated for 5 min with shaking at 650 rpm for 5 min at room temperature. Solution was removed and gel fragments were vacuum centrifuged and stored at -20°C.

To reduce disulfide bonds, gel fragments were rehydrated with 50 µL of 10 mM DTT in 100 mM aqueous NH_4HCO_3 and incubated at 56°C for 1 h. Samples were cooled to room temperature. Cysteines were alkylated by addition of 50 µL of 55 mM iodoacetamide in 100 mM aqueous NH_4HCO_3 and incubation at room temperature in the dark for 30 min. The alkylation was quenched by adding a further 50 µL of 100 mM DTT and incubating at room temperature for 5 min. Gel fragments were washed with 500 µL of 100 mM NH_4HCO_3 for 10 min. Solution was removed, and gel fragments were washed by adding 100 µL of acetonitrile and incubation for 5 min at room temperature, followed by addition of 500 µL of 100 mM NH_4HCO_3 and incubation for 10 min at room temperature. Solution was removed and this wash step was repeated once. Solution was removed and gel fragments were washed with 100 µL of acetonitrile for 10 min at room temperature. All solution was removed and gel fragments were vacuum centrifuged and stored at -20°C.

For digestion of proteins, samples were placed on ice and rehydrated with 25 µL of trypsin (Pierce) at 40 ng/µL, for a total of 1µg of trypsin per sample. Gel fragments were incubated on ice for 10 min to allow them to rehydrate, and then incubated overnight at 37°C. Peptides were eluted by incubating in 50 µL of 1% formic acid in 70% acetonitrile with shaking at 1400 rpm for 30 min at room temperature. Eluates were removed, and the wash step was repeated with fresh solution. Eluates were pooled together and samples were vacuum centrifuged to dryness. Samples were desalted by solid phase extraction using C18 MicroSpin columns (Nest Group).

Samples were resuspended in 5 µL of 0.1% formic acid for concentrated samples. Diluted samples were prepared using a 1:4 dilution, and 3 µL of both concentrated and dilute samples were used for mass spectrometry analysis. The liquid chromatography system consisted of a vented trap-elute setup on an EASY-nLC 1200 (Thermo Fisher Scientific), using a 150 mm x 100 µm analytical column packed with 3µm ReproSil-Pur 120 C18-AQ (Dr. Maisch). This was coupled to an Orbitrap Fusion Lumos mass

spectrometer (Thermo Fisher Scientific). A 90-minute gradient was used (5-40% acetonitrile). A voltage of 1800 V was applied to a pulled tip emitter for nanoelectrospray in positive mode. Precursor ions in the range of 375-1500 m/z were isolated using the quadrupole, and MS1 scans were recorded every 3 s using the Orbitrap detector at 60,000 resolution (with 445.12003 m/z used as lock mass), with an automatic gain control target set at 4×10^5 ions and a maximum injection time of 50 ms. Charge states 2-7 were selected for fragmentation by data-dependent acquisition with a 60 s dynamic exclusion time and a 10 ppm mass tolerance. Selected ions were isolated for fragmentation using the quadrupole (Q1 isolation window of 1.6 Th) and fragmented using HCD (normalized collision energy of 30%). MS2 scans were detected using the Orbitrap at 15,000 resolution), with an automatic gain control target set at 5×10^4 ions and a maximum injection time of 30 ms.

Raw MS files were initially analyzed with MaxQuant (version 1.6.0.16). Spectra were searched against the human UniProt database (as of May 2019), supplemented with contaminant proteins from the cRAP database and the EWS-FLI1 fusion protein sequence with FDR < 0.01. After m/z recalibration, mass tolerances were set at 4.5 and 20 ppm for precursor and fragment ions, respectively. MS1 error was calibrated by examining uncalibrated MS1 errors of peaks corresponding to the trypsin enzyme. Raw MS files were then re-analyzed using PEAKS Studio (version 10.5) which incorporates de novo sequencing into the database search tool (294), using the calibrated MS1 mass tolerance of 4 ppm. Cysteine carbamidomethylation was set as a fixed chemical modification, while methionine oxidation, asparagine and glutamine deamidation, and protein N-terminus acetylation were set as variable modifications. Protease specificity was set to trypsin, with up to three missed cleavages allowed. Quantification was performed using the LFQ algorithm. FLI1 and IgG immunoprecipitation samples were analyzed together (3 replicates per condition, 2 concentrations injected into the mass spectrometer each for

FLI1 and IgG samples; 12 samples total). A comparison of protein identifications showed noticeable improvement using the PEAKS algorithm compared to MaxQuant.

Dependency and network analysis

CERES gene dependency data for Ewing and non-Ewing cell lines was downloaded from the DepMap Consortium (20Q2 release). For each protein detected in the IP-MS data, I calculated a Ewing-specific dependency score using the formula:

$$\Delta DepScore = \frac{\sum_1^{n_{ES}} ES\ Dep\ Score}{n_{ES}} - \frac{\sum_1^{n_{NES}} nonES\ Dep\ Score}{n_{NES}}$$

Where n_{ES} is the number of EwS cell lines within the DepMap project containing EWS-FLI1 or EWS-ERG fusions, n_{NES} is the number of non-Ewing cell lines, and EwS Dep Score and nonES Dep Score refers to the gene-specific CRISPR dependency score in the sets of Ewing cell lines and non-Ewing cell lines, respectively. The list of Ewing cell lines used here and their aliases in the DepMap cell line list is in **Table 3.1**.

Cell line	DepMap Name
A673	ACH-000052
COGE352	ACH-001038
EW8	ACH-000499
EWS502	ACH-000279
RDES	ACH-000041
SKES1	ACH-000087
SKNEP1	ACH-001192
SKNMC	ACH-000039
SKPNDW	ACH-001193
TC106	ACH-001283

TC138	ACH-001430
TC32	ACH-001205
TC71	ACH-000424

Table 3.1: EwS cell lines used for dependency analysis

Network analysis was performed using Cytoscape (v3.8.2). Detected proteins were searched against the STRING protein interaction database with the stringApp plugin (v1.6.0) using a confidence score of 0.99 and a maximum additional interactor setting of 0. Nodes were colored based on ΔDepScore and node size was determined by percent protein coverage. Edge size in Figure 3.2 was adjusted manually to highlight grouping of proteins after initially determining edge size using the prefuse force-directed layout setting.

Screening Affimer-scaffolded peptides

TC-32 and HEK293T cells were transduced with lentivirus encoding each Affimer-scaffolded construct at an MOI ~ 0.3. Cells were plated in 96-well plates on Day -1, and doxycycline was added on Day 0 at 1 µg/mL. Separate plates were analyzed by flow cytometry using the BD Accuri C6 instrument on Days 0 and 5, with normalization performed to the Day 0 plate.

RNA-sequencing

TC32 cells were plated on Day -1 in 6-well plates at 25,000 cells/well. Dox was added on Day 0 at 1 µg/mL. Cells were harvested on Day 6 and RNA was isolated using RNeasy Mini kit, according to manufacturer's instructions (Qiagen). After RiboGreen quantification and quality control by Agilent BioAnalyzer, 500 ng of total RNA with RIN values of 8.1-10 plus ERCC spike-in underwent polyA selection and TruSeq library preparation according to instructions provided by Illumina (TruSeq Stranded mRNA LT

Kit, catalog # RS-122-2102), with 8 cycles of PCR. Samples were barcoded and run on a NovaSeq 6000 in a PE100 run, using the NovaSeq 6000 S4 Reagent Kit (200 Cycles) (Illumina). An average of 64 million paired reads was generated per sample. Ribosomal reads represented 0.2-3.4% of the total reads generated and the percent of mRNA bases averaged 92%.

For analysis, adaptors were trimmed and quality filtered using 'trim_galore' and mapped to GRCh38/hg19 reference genome using STAR v2.7.9 with default parameters (258). Read count tables were generated using HTSeq v0.11.3 (259). Bam files were sorted by name using 'samtools' and alignment quality was assessed using 'qualimap' v2.2.2. Normalization and principal component analysis was performed using DESeq2 v1.34.0 using default parameters (260). For GSEA analysis using a custom TC-32 specific EWS-FLI1-regulated gene set, I selected all genes with $\log_2$(fold-change) was less than or equal to -1.5 upon danoprevir treatment of EWS-FLI1-SMASh cells. GSEA Preranked was run using v4.0.3 against all Hallmark and C2 gene sets.

Immunofluorescence Microscopy

Immunofluorescence for the HA tag was performed on cells plated on Millicell EZ Slide glass slides (EMD Millipore), coated for 45 minutes with bovine plasma fibronectin (Millipore Sigma). After drug treatment, cells were washed once with PBS and fixed in 4% formaldehyde for 10 minutes at room temperature. Slides were then washed three times in PBS for 5 minutes, permeabilized for 15 minutes in 0.3% Triton X-100, washed again in PBS three times, and blocked with 5% goat serum (Millipore Sigma, G9023) in PBS for 1 hour at room temperature. Slides were incubated with rabbit anti-HA primary antibody (Cell Signaling Technology, 3724S) at 1:600 in blocking buffer for 1 hour, washed three times in PBS, and incubated with goat anti-rabbit secondary antibody conjugated to AlexaFluor555 (Invitrogen, A-21422) at 1:1,000 and Phalloidin conjugated to

AlexaFluor488 (ThermoFisher, A12379) at 1:40. Cells were then counterstained with DAPI at 1:1,000 for 10 minutes and treated with ProLong Diamond Antifade Mountant with DAPI (Invitrogen, P36962) for 48 hours. Images were acquired on a Zeiss LSM-880 confocal microscope at 63x magnification. Images in Figure 3.12 were prepared using Fiji (262).

CHAPTER IV

Conclusions and future directions

In Chapter 1 of this work, I introduced several themes that have emerged from the study of cancers that affect children and young people. This included a discussion of two general classes of tumor mutations, along with two prototypical cancer types corresponding to each class. In Chapter 2, I focused on pediatric tumors driven by loss of the epigenetic regulator *SMARCB1*. I studied the mechanisms of response and resistance to EZH2 inhibition, an epigenetic therapy that works in part by indirectly reversing the epigenetic dysregulation caused by dysfunction of the BAF complex. I also described two potential combination therapies that overcome resistance and improve response, approaches that either target gaps in the mechanism of action of EZH2 inhibition or that exploit specific vulnerabilities conferred by EZH2 inhibition. In Chapter 3, I focused on Ewing sarcoma, a tumor type caused by a dominant oncogenic fusion. I defined the protein interactome of this fusion with the aim of describing how this single protein dysregulates the biochemistry of the cell. I also designed and tested interference peptides to both probe and eventually interfere with the aberrant oncogenic assembly formed by the fusion. In this chapter, I will discuss future directions for both of these areas of study. I will also attempt to extend the themes I discussed in Chapter 1, with the aim of envisioning future approaches to reverse the profound effects conferred by a small number of oncogenic mutations in pediatric tumors.

4.1 Effective EZH2 therapy

In Chapter 2, I proposed a model for effective EZH2 inhibitor therapy which posits that the upregulation of specific EZH2 targets converging on the CDK4/6/RB1/E2F

axis is necessary for therapeutic response. However, many questions remain about the details of this model.

Based on genomic studies of patient tumors and cell lines, I have nominated *CDKN1A* and *CDKN2A* as key therapeutic targets of EZH2. Confirming this will require currently ongoing genetic knockout studies, in which I hope to demonstrate that CRISPR-mediated knockout of *CDKN1A*, *CDKN2A*, as well as the putative resistance gene and *CDKN1A* regulator *ANKRD11* confers TAZ resistance similarly to $RB1^{del}$. It is also possible, however, that there is some functional redundancy between these two CDK inhibitors and that knockout of both is required to confer TAZ resistance. This would itself be an interesting finding regarding cell cycle control in MRT.

More broadly, however, it is unclear whether these two genes are the only targets necessary for response to TAZ. Even though $RB1^{del}$ significantly reduces response to TAZ, it does not completely abolish it, suggesting that other response mechanisms play a role. In addition, TAZ treatment of G401 cells causes upregulation of hundreds of genes. How many of these have a therapeutic effect? Conversely, how many might lead to deleterious side effects? Although TAZ is reasonably well-tolerated by patients (139), it does carry warnings for secondary malignancies that include T-ALL and AML (www.fda.gov), and it is possible that EZH2 targets in MRT and ES might include potential oncogenes. In addition, our finding that TAZ induces PGBD5-dependent DNA damage in G401 cells suggests a potential mutagenic effect of this drug.

A recent near genome-wide CRISPR screen identified NSD1 as another TAZ resistance gene (199). In principle, the subset of EZH2 target genes that mediate TAZ therapeutic effect should also confer resistance in such a screen. As a follow-up study, I therefore propose to define the genomic targets of EZH2 in MRT and ES cell lines using ChIP-seq for EZH2 and H3K27me3. These targets, presumably several hundred in

number, could then be tested in a more focused CRISPR screen for TAZ resistance genes. As there may be redundant genes mediating the TAZ therapeutic effect (for example, *CDKN1A* and *CDKN2A*), the significance cutoffs for such a screen would need to be relatively permissive, and further studies testing combined knockout of the top-scoring hits would be needed to establish sufficiency and redundancy of different EZH2 target genes for TAZ response.

In addition, further work is needed to define the mechanism by which TAZ induces DNA damage. In Chapter 2, I have proposed that this DNA damage is a result of PGBD5 induction. I am currently generating PGBD5 knockdown cell lines which I will test for susceptibility to both TAZ monotherapy and the TAZ + elimusertib combination therapy. The possible outcomes will either confirm PGDB5 as the mechanism of synergy or will reveal a previously unknown effect of EZH2 inhibition.

4.2 Beyond PRC2 inhibition

Despite their therapeutic promise, current approaches towards targeted therapy for *SMARCB1*-deficient cancers ultimately suffer from the same drawback. Two such approaches are currently being developed- inhibition of PRC2, and inhibition of the ncBAF subunit BRD9. Both approaches target synthetic lethal dependencies- in the former case by inhibiting a complex that is disinhibited by *SMARCB1* loss (89), and in the latter case by blocking a complex that compensates for lost BAF activity (72). However, neither approach truly fixes the fundamental defect at work in these tumor cells, that is, the loss of canonical BAF function. As discussed in the previous section, while I have proposed that *CDKN2A* upregulation is a necessary mediator of response to EZH2 inhibition, it is clear that loss of *CDKN2A* expression is not the sole oncogenic effect of *SMARCB1* loss. Indeed, loss of *CDKN2A* alone in mice does not cause the

rapid and highly penetrant induction of rhabdoid tumors seen with *SMARCB1* loss (89, 295, 296). The effect of *SMARCB1* loss must therefore cause a far more broad and profound defect in the epigenetic state of these cells.

Such a defect is difficult to correct pharmacologically; rather than the inhibition of a dominant oncogene, one must essentially recapitulate the functions of a lost tumor suppressor. However, if achieved, this would mimic the results of *SMARCB1*-rexpression in MRT cells, which reduces the assembly of BRD9-containing ncBAF complexes (72), increases cBAF occupancy at enhancers and bivalent promoters while antagonizing PRC2 occupancy, and reverses the oncogenic transcriptional program (70), thus correcting the primary aberrant feature of these cells.

One can speculate as to how this may be pharmacologically accomplished. Recently published structural models of nucleosome-bound BAF (69, 297) reveal that SMARCB1 forms a central scaffold within the complex. Together with the ATPase subunits SMARCA2/4, SMARCB1 forms one of two contacts between BAF and the nucleosome, enabling the complex to bind chromatin. This is mediated through a C-terminal α-helix on SMARCB1 (aa 351-385), and four Arg residues in particular that contact the nucleosome acidic patch. SMARCB1 also contacts the DPF2 reader subunit via the Repeat 2 (RPT2) domain (indeed DPF2 incorporation requires a fully intact BAF complex) (298). Finally, SMARCB1 interacts with the SWIRM domains of SMARCC1 and SMARCC2 via the two RPT domains, and with ARID1A via the N-terminal winged helix domain. While the nucleosome-contacting helix is almost certainly necessary for SMARCB1 to reconstitute BAF function, a complete structure-function analysis identifying the minimal regions of SMARCB1 necessary to evict PRC2 and allow cBAF to re-occupy lineage-specific loci is a crucial gap in knowledge. Once these minimal regions are identified, one can envision how a heterobifunctional, peptidomimetic compound could be engineered to bridge the nucleosome, via a minimal helix-type motif

that mimics the SMARCB1 C-terminal helix, with key BAF subunits such as ARID1A or DPF2. Such a “BAF prosthetic” would ideally occupy the place of SMARCB1 within the chromatin-bound BAF structure and allow it to recapitulate the complex’s normal functions.

4.2 Defining the EWS-FLI1 assembly and its regulators

In Chapter 3, I assembled a comprehensive list of interactors and ranked them by their Ewing-specific genetic dependencies. The next logical step is to select top candidates for further validation and exploration. I am currently pursuing several avenues to determining direct candidate interactors of EWS-FLI1 and to more fully define the range of EWS-FLI1-containing complexes in EwS cells.

First, I am taking a proteomic approach using cross-linking mass spectrometry (XL-MS) (299). The power of this approach lies in the ability to directly map protein-protein interactions, either in situ or in natively purified complexes, with a residue-level resolution. Recent work from our lab has defined optimized MS strategies for cross-linked samples (300). I am currently optimizing a native pulldown protocol for the isolation and crosslinking of native EWS-FLI1 complexes. I plan to use this strategy to determine direct EWS-FLI1 interactors. I predict that these direct interactors will include a subset of the EwS-specific dependencies discussed in Chapter 3 which can then be further tested for their specific functions at the EWS-FLI1 complex.

One potential obstacle to this strategy lies in the sequence composition of EWSR1, the LCD of which contains few lysine residues amenable to tryptic cleavage and few primary amines reactive with commonly used crosslinkers (299). To circumvent this obstacle, I plan to use MS-cleavable crosslinkers that react with hydroxyl side

chains, such as CDI (301), together with multi-protease digestion that does not depend on tryptic cleavage sites.

Another obstacle lies in sufficient enrichment and fractionation of samples in order to obtain detectable peptides from the proteins of interest. This stems from the relatively low abundance of cross-linked peptides in complex samples. While cross-linking followed by immunoprecipitation is an appealing strategy, I have found that crosslinking with MS-cleavable crosslinkers renders EWS-FLI1 unamenable to recognition by FLI1 antibodies, likely due to epitope masking. To circumvent this, I have developed an ex-situ crosslinking strategy, in which the EWS-FLI1 complex is affinity purified by desthiobiotoin-conjugated antibodies, eluted from streptavidin beads under native conditions, and crosslinked ex situ. I am currently scaling up this approach, to be followed soon by MS analysis.

Second, it should be noted that the IP-MS approach I used in Chapter 3 does not distinguish between different EWS-FLI1-containing complexes. It is almost certain that EWS-FLI1 exists within at least two complex subtypes, given its occupancy at both ETS target genes and GGAA repeats. Therefore, I next propose to further fractionate the immunoprecipitated EWS-FLI1 complex using density gradient centrifugation, as has recently been done to define different BAF subtypes (71). I predict that this will yield at least two distinct subtypes, one containing transcriptional repressors (such as the NuRD complex) that occupy ETS target sites and one containing primarily activators such as the TAF-containing complex discussed in Chapter 3, which will occupy GGAA microsatellites.

Finally, I plan to leverage the improved interference peptides I have designed to probe EWS-FLI1 complex assembly. I plan to immunoprecipitate EWS-FLI1 in the presence and absence of the Breakpoint_L peptide to define the changes that occur in the EWS-FLI1 complex upon peptide expression. I will also reciprocally

immunoprecipitate the HA-tagged peptide to confirm which protein cofactors interact with it directly. This will be done in tandem with FLI1 and HA chromatin immunoprecipitation (ChIP), in order to define the locations of both EWS-FLI1 and Breakpoint_L on chromatin. I predict that these experiments will reveal that the effect of Breakpoint_L is mediated by two potential mechanisms: 1) Breakpoint_L localizes to the EWS-FLI1 complex and evicts a subset of interactors from the complex. Evidence of this mechanism will be co-localization of the peptide and the fusion on chromatin by ChIP, and a reciprocal interaction detected by FLI-IP and HA-IP. 2) Breakpoint_L does not localize to the EWS-FLI1 complex, but instead sequesters a subset of interactors away from the complex. Evidence of this will be distinct locations of the peptide and fusion on chromatin and an absence of direct interactions detected by IP-MS. Instead, expression of the peptide will lead to loss of interactors from the EWS-FLI1 complex as the interactors instead bind to the peptide.

Finally, I plan to take a similar approach with the EWS_12 peptide to probe the molecular determinants of EWS-FLI1 stability. The observation of reduced EWS-FLI1 levels upon EWS_12 expression is compelling but requires both validation with additional clones and the use of a more highly-expressed probe to maximize the fusion-destabilizing effect, using the RadA_3xNLS scaffold discussed in Chapter 3. Using similar IP-MS and ChIP-Seq experiments as those proposed for Breakpoint_L, I plan to determine the mechanism by which EWS_12 reduces fusion protein levels. One possible mechanism is that EWS_12 localizes to the EWS-FLI1 complex to evict EWS-FLI1 and allow its degradation. This would be followed by experiments with EWS peptides containing fewer [G/S]Y[G/S] repeats, in order to determine the threshold number of repeats needed for interaction with the fusion complex and eviction of the fusion. This would be a starting point for defining an additional therapeutic avenue.

4.4 Towards a molecular understanding of EWS-FLI1

A truly targeted therapy against EwS would interfere with the single molecule that dysregulates the biochemistry of the EwS cell of origin- the EWS-FLI1 fusion. This requires an understanding of what makes EWS-FLI1 a molecularly aberrant protein. Work over the past decade and a half suggests that EWS-FLI1 possesses two neomorphic functions that distinguish it from wild-type EWSR1 or FLI1: 1) The ability to bind GGAA microsatellite repeats throughout the genome, and 2) the ability to convert them into neomorphic enhancers.

While FLI1 recognizes an ETS consensus sequence that contains a core GGAA motif, the canonical ETS binding site also includes three bases 5' and two bases 3' to this core which enhance binding specificity and affinity (302). Yet although GGAA repeats do not form a complete ETS consensus site, in vitro experiments with oligonucleotide probes have revealed that the normal FLI1 ETS domain can, in fact, bind a limited number of GGAA repeats (169, 303). However, this ability to bind is reduced as the GGAA repeat number approaches the "sweet spot," the 18-26 repeats typically found at EWS-FLI1-bound loci in EwS cells. Conversely, the EWS-FLI1 fusion protein, while binding lower numbers of GGAA repeats less strongly than FLI1, binds more strongly to "sweet spot" repeat numbers. This ability requires at least part of the EWS domain, in addition to the FLI1 ETS domain (303), and mutation of the tyrosines of the EWS domain abolishes this binding (161). More recent work has supported these results, indicating that a threshold number of GGAA repeats is necessary to form DNA-associated EWS-FLI1 condensates in vitro (304).

What are the unique molecular features of EWS-FLI1 that permit fusion-specific binding to microsatellite repeats? The observations above indicate two aspects of this binding: 1) The EWS portion of the fusion protein hinders binding of EWS-FLI1 monomers to closely-spaced repeats, perhaps due to steric hindrance, and 2) a

sufficiently high GGAA repeat number results in increased affinity through an emergent property of the fusion, overcoming this hindrance to binding. This emergent property is almost certainly the tyrosine-dependent oligomerization of the fusion protein, mediated at least in part through its PrLD. Thus, the oligomerized EWS-FLI1 may create a multivalent ETS-binding assembly that can cooperatively bind to GGAA repeats, as long as there is a threshold number of available, albeit sub-optimal ETS binding sites.

The next question, then, is whether oligomerization of EWS-FLI1 requires similar molecular interactions as oligomerization of wild-type EWSR1. Similarly to EWS-FLI1, the self-assembly of FET proteins requires the tyrosines of the PrLD domain (189). However, in vitro work indicates that the FLI1 moiety actually enhances oligomerization of EWS-FLI1 compared to the PrLD domain of EWSR1 alone (304). This matches studies showing that self-assembly of the FUS PrLD requires higher protein concentrations than either full-length FUS or FUS joined to a DNA-binding domain (160). This is also supported by more recent work in EwS cells, which found that exogenous expression of the EWSR1 PrLD does not readily form small, discrete puncta, as compared to expression of EWS-FLI1 at endogenous levels (305). In addition, assembly of normal FET proteins is promoted by RNA via the FET RNA-recognition motif (RRM) and RGG-rich domains (155, 160). These domains are lost in the fusion, thus abolishing the RNA-dependence of fusion self-assembly (161). These observations together suggest that different sets of intermolecular forces participate in assembly of FET PrLDs compared to FET-containing fusion proteins. More specifically, while full-length FET proteins assemble via forces that may include RNA-dependent interactions, aromatic stacking interactions of their tyrosines (306), and pi-cation interactions between RGG domains and PrLDs, fusions like EWS-FLI1 are reliant on tyrosine-stacking and fusion-specific interactions between the PrLD and FLI1. Such specific interactions may explain my observation that a breakpoint-spanning peptide interferes with EWS-FLI1 function,

although as discussed in the last section, significant work remains to define this effect. Alternatively, there may be additional regions within the FLI1 C-terminal domain of the fusion protein that play a role in assembly through interactions with the PrLD.

Once bound to these microsatellites, EWS-FLI1 must then convert them into active enhancers. The contributions of EWS-FLI1 itself and the cellular environment of the cell of origin are still unclear. On one hand, studies using MSCs transduced with EWS-FLI1 show that expression of the fusion causes an increase in chromatin accessibility and active enhancer marks at GGAA repeats (170), a process that appears to depend on BAF recruitment (161). However, the ability of EWS-FLI1 to activate transcription of target genes is not universal to all cell types (307), and this process may be dependent on the preexisting chromatin landscape around GGAA repeats in the cell of origin (180), or as I propose in Chapter 3, a unique protein interactome that facilitates chromatin remodeling by EWS-FLI1, or indeed, a combination of both.

Finally, how might the unique aberrant molecular features of EWS-FLI1 be targeted therapeutically? Disruption of EWS-FLI1 assembly would ideally interfere with intermolecular interactions specific to the fusion. In this work, I have nominated a breakpoint-spanning peptide as a specific disruptor of EWS-FLI1 function. This peptide might disrupt interactions with a EwS cell-of-origin-specific protein that mediates the conversion of GGAA microsatellites into active enhancers. It may also function by disrupting EwS-specific homotypic interactions between and within fusion protein molecules that mediate self-assembly. However, other regions of the fusion almost certainly play important roles in its aberrant function. A more fine-grained peptide interference approach would nominate such regions. This would require expressing scaffold-stabilized, overlapping peptides spanning the full length of the fusion protein. Ideally, this approach would identify a peptide that can profoundly impair EWS-FLI1 complex assembly with little effect on other protein complexes.

Other potential approaches can draw inspiration from the FET protein field. For example, work on the FUS PrLD domain has shown that just a single amino acid substitution, replacing a glycine with a glutamate, is sufficient to alter the oligomerization properties of FUS, driving it to aggregate instead of forming dynamic assemblies (308). It is tempting to speculate that such an effect may work in reverse. Could the modification of the net charge of EWS-FLI1 abolish the ability of EWS-FLI1 to oligomerize, instead of promoting it? This would in principle cause the disassembly of the oncogenic fusion complex and would represent a true disruption of the driver oncogenic event in EwS cells. One can imagine at least two avenues to achieve this. The first would be through a therapeutic ligand that shares sufficient similarity with the EWSR1 PrLD to interact with it, but which carries distinct electrostatic features that might alter its assembly properties and that outcompete its assembly with other EWS-FLI1 molecules. An ideal starting point here would be the PrLD of TAF15, a member of the FET family distinguished by its increased number of SYD repeats (155) that impart a greater negative charge and distinct self-assembly properties. TAF15 interacts with EWSR1 in cells and induces a redistribution of EWS-FLI1 puncta (305), demonstrating the feasibility of modulating EWS-FLI1 assembly. The second avenue might take advantage of the cell's evolved mechanisms to regulate EWSR1 assembly. As discussed in Chapter 1, EWSR1 is known to be subject to PTMs that affect its interactions with other proteins. The complete set of PTMs of EWS-FLI1 is not known and could be defined through a comprehensive proteomics approach that makes use of multiple proteases to achieve complete sequence coverage of EWS-FLI1. This would be followed by targeted mutation of each modified residue combined with a readout of EWS-FLI1 complex assembly, such as microscopy. If a PTM site is found that promotes self-assembly by the action of its depositing enzyme, then the inhibition of this enzyme would be a potential therapeutic approach to disassemble the EWS-FLI1 complex.

4.5 Conclusion

In conclusion, I have described two prototypical examples of pediatric sarcomas. I examined both direct and indirect approaches to therapeutically target the singular, oncogenic events that transform cells into these devastating tumors. The indirect approach, described in Chapter 2, relies on an epigenetic synthetic lethality that partially corrects the epigenetic dysfunction resulting from loss of a tumor suppressor. While limited as a monotherapy, this indirect approach can be enhanced through rational combination epigenetic therapies. The direct approach, described in Chapter 3, seeks to target a dominant oncogenic fusion by interfering with its tumor-specific protein-protein interactions. Ultimately, future approaches to treating these tumors must seek to take advantage of the relative genomic stability of pediatric sarcomas, leveraging it by directly targeting the few oncogenic drivers that dysregulate cellular biochemistry and restoring the normal transcriptional and epigenetic programs of their respective cells of origin.

APPENDIX

Supplementary Tables for Chapter 2:

Supplementary Table S1: List of patient tumor specimens used for RNA-seq and MSK-IMPACT analysis. *We note that two primary tumors in patients who responded to TAZ harbored deletions of *RB1* (patient 2, sample ES_02_T_02) in one tumor and *CDKN2A/B* in another tumor (patient 5, sample ES_05_T_01). However, these primary tumors were fully resected prior to the initiation of TAZ treatment and did not recur at the primary sites. In the case of patient 2, a later TAZ-responsive metastasis (ES_2_T_03) did not harbor the *RB1* loss. In the case of patient 5, a later TAZ-responsive metastasis (ES_05_T_09) did not harbor the *CDKN2A/B* loss. This suggests that these mutations were subclonal and were not present in tumors exposed to TAZ treatment. Thus, the mutations in these tumors were unlikely to have impacted their response to TAZ.

Supplementary Table S2: List of mutations found in all patient tumor specimens in Supplementary table 1 for which MSK-IMPACT data is available.

Supplementary Table S3: List of mutations found in all MRT and ES cell lines used in this study as determined by targeted MSK-IMPACT sequencing (related to Figure 3B).

Supplementary Table S4: List of PDX models used in this study, with clinical characteristics of the original tumor specimens, followed by a list of mutations found in all PDX models, as determined by targeted MSK-IMPACT sequencing.

Supplementary Tables for Chapter 3:

Supplementary Table S5: Filtered list of EWS-FLI1-interacting proteins detected by IP-MS. Proteins are ordered by ΔDepScore and are filtered based on $\log_2$(fold-change), ΔDepScore, and a STRING nuclear compartment score of 4 or greater.

Supplementary Table S6: Amino acid sequences of anti-EwS peptides

Supplementary Table S7: List of all EwS plasmids used in Chapter 3 and their respective insert sequences. EwS interference peptides are in red, NLSs are in blue, and HA tag is in gold. Flexible linkers are underlined.

Supplementary Table S1:

Patient ID	Sample ID	Site	Sample	TAZ	RNAseq	IMPACT	Pre/Post-Tx	Figure 2.1
2	ES_02_T_0	Soft tissue trunk, right flank	Primary	Response*	No	Yes	Pre	No
2	ES_02_T_0	Soft tissue trunk, right flank	Primary	Response*	Yes	Yes	Pre	No
2	ES_02_T_0	Left mediastinal	Metastasis	Response	No	Yes	Pre	Yes
3	ES_03_T_0	Pelvis	Local	Response	Yes	Yes	Pre	Yes
3	ES_03_T_0	Stomach	Local	Response	Yes	Yes	Pre	No
3	ES_03_T_0	Gastric mass with wedge excision of	Local	Response	No	Yes	Pre	Yes
4	ES_04_T_0	Fine needle aspirate lymph node 4R	Unknown	Response	No	Yes	Pre	Yes
5	ES_05_T_0	Soft tissue pelvis right	Primary	Response*	No	Yes	Pre	No
5	ES_05_T_0	Soft tissue pelvis right	Primary	Response*	Yes	No	Pre	No
6	ES_06_T_0	Right thumb	Primary	Progression	No	Yes	Pre	Yes
15	ES_15_T_1	Left kidney	Primary	Response	No	Yes	Pre	Yes
15	ES_15_T_0	Left retroperitoneal soft tissue	Local	Response	Yes	No	Pre	No
16	ES_16_T_0	Right posterior chest wall	Metastasis	Progression	No	Yes	Pre	Yes
17	ES_17_T_0	Soft tissue, perineal mass	Primary	Progression	No	Yes	Pre	Yes
17	ES_17_T_0	Left thigh	Metastasis	Progression	No	Yes	Pre	Yes
18	ES_18_T_0	Right arm lesion	Primary	Response	No	Yes	Pre	Yes
19	ES_19_T_0	Left breast	Primary	Response	No	Yes	Pre	No
19	ES_19_T_0	Left breast	Primary	Response	Yes	No	Pre	No
21	ES_21_T_0	Right axillary lymph node	Metastasis	Progression	No	Yes	Pre	Yes
22	ES_22_T_0	Left thigh	Primary	Progression	No	Yes	Pre	Yes
23	ES_23_T_0	Right groin	Primary	Progression	Yes	Yes	Pre	Yes
23	ES_23_T_0	Right inguinal lymph node	Metastasis	Progression	No	Yes	Pre	Yes
24	ES_24_T_0	Left posterior thigh	Primary	Progression	Yes	Yes	Pre	Yes
25	ES_25_T_0	Right ovary	Primary	Progression	No	Yes	Pre	Yes
25	ES_25_T_0	Abdomen Upper Quadrant Left	Metastasis	Progression	Yes	No	Pre	No
25	ES_25_T_0	Abdomen Diaphragm Right	Metastasis	Progression	Yes	No	Pre	No
26	ES_26_T_0	Bone and mass in left distal humerus	Unknown	Progression	No	Yes	Pre	Yes

Supplementary Table S2

Sample	Gene	Gene Panel	Protein Change	Mutation Type	Variant Type	Allele Freq
ES_01_T_01	GATA1	IMPACT505	H232D	Missense_Mutation	SNP	0.23
ES_02_T_02	PTPRT	IMPACT505	R461*	Nonsense_Mutation	SNP	0.26
ES_02_T_02	TP63	IMPACT505	R97C	Missense_Mutation	SNP	0.40
ES_02_T_02	SMYD3	IMPACT505	R224*	Nonsense_Mutation	SNP	0.12
ES_02_T_02	PREX2	IMPACT505	R263W	Missense_Mutation	SNP	0.35
ES_02_T_02	CDHR5	IMPACT505	A607_E637del	In_Frame_Del	DEL	0.05
ES_02_T_02	GLI2	IMPACT505	S272A	Missense_Mutation	SNP	0.22
ES_02_T_02	GLI2	IMPACT505	Y273D	Missense_Mutation	SNP	0.25
ES_02_T_02	SMARCB1	IMPACT505		DeepDel		
ES_02_T_02	RB1	IMPACT505		DeepDel		
ES_02_T_02	RYBP	IMPACT505		DeepDel		
ES_02_T_02	SHQ1	IMPACT505		DeepDel		
ES_02_T_02	FOXP1	IMPACT505		DeepDel		
ES_02_T_02	PPP4R2	IMPACT505		DeepDel		
ES_02_T_02	MAPK1	IMPACT505		DeepDel		
ES_02_T_03	MGA	IMPACT410	D582Efs*6	Frame_Shift_Del	DEL	0.09
ES_02_T_03	TP63	IMPACT410	R97C	Missense_Mutation	SNP	0.46
ES_02_T_03	SMARCB1	IMPACT410		DeepDel		
ES_03_T_02	SMARCB1	IMPACT505	A240Lfs*28	Frame_Shift_Ins	INS	0.51
ES_03_T_02	ZNF735	IMPACT505	S91F	Missense_Mutation	SNP	0.23
ES_03_T_02	CCDC92	IMPACT505	T63P	Missense_Mutation	SNP	0.17
ES_03_T_03	SMARCB1	IMPACT505	A240Lfs*28	Frame_Shift_Ins	INS	0.45
ES_03_T_03	ZNF735	IMPACT505	S91F	Missense_Mutation	SNP	0.26
ES_03_T_03	SMARCB1	IMPACT505		DeepDel		
ES_03_T_03	BARD1	IMPACT505		DeepDel		
ES_03_T_03	CHEK2	IMPACT505		DeepDel		
ES_03_T_03	CCNE1	IMPACT505		AMP		
ES_03_T_03	CCND3	IMPACT505		AMP		
ES_03_T_03	CDK4	IMPACT505		AMP		
ES_03_T_03	MDM2	IMPACT505		AMP		
ES_03_T_03	RAC1	IMPACT505		AMP		
ES_03_T_03	CDK6	IMPACT505		AMP		
ES_03_T_03	BRAF	IMPACT505		AMP		
ES_03_T_03	RUNX1	IMPACT505		DeepDel		
ES_03_T_03	GATA3	IMPACT505		AMP		
ES_03_T_03	ETV1	IMPACT505		AMP		
ES_03_T_03	FAT1	IMPACT505		DeepDel		
ES_03_T_03	PTPRD	IMPACT505		DeepDel		
ES_03_T_03	PTPRT	IMPACT505		DeepDel		

ES_03_T_03	SDHA	IMPACT505		DeepDel		
ES_03_T_03	VEGFA	IMPACT505		AMP		
ES_03_T_03	CARD11	IMPACT505		AMP		
ES_03_T_03	EZH2	IMPACT505		AMP		
ES_03_T_03	RHEB	IMPACT505		AMP		
ES_03_T_03	GLI1	IMPACT505		AMP		
ES_03_T_03	BRD4	IMPACT505		AMP		
ES_03_T_03	PIK3R2	IMPACT505		AMP		
ES_03_T_03	MEF2B	IMPACT505		AMP		
ES_03_T_03	LZTR1	IMPACT505		DeepDel		
ES_03_T_03	NF2	IMPACT505		DeepDel		
ES_03_T_03	ESR1	IMPACT505		AMP		
ES_03_T_03	ROS1	IMPACT505		DeepDel		
ES_03_T_03	CD274	IMPACT505		DeepDel		
ES_03_T_03	JAK2	IMPACT505		DeepDel		
ES_03_T_03	TP53	IMPACT505		AMP		
ES_03_T_03	RET	IMPACT505		DeepDel		
ES_03_T_03	ERBB4	IMPACT505		DeepDel		
ES_03_T_03	PDGFRA	IMPACT505		DeepDel		
ES_03_T_03	KIT	IMPACT505		DeepDel		
ES_03_T_03	SMO	IMPACT505		AMP		
ES_03_T_03	DNAJB1	IMPACT505		AMP		
ES_03_T_03	CEBPA	IMPACT505		AMP		
ES_03_T_03	U2AF1	IMPACT505		DeepDel		
ES_03_T_03	FGFR2	IMPACT505		DeepDel		
ES_03_T_03	DAXX	IMPACT505		AMP		
ES_03_T_03	EP300	IMPACT505		AMP		
ES_03_T_03	TENT5C	IMPACT505		DeepDel		
ES_03_T_03	NOTCH2	IMPACT505		DeepDel		
ES_03_T_03	VTCN1	IMPACT505		DeepDel		
ES_03_T_03	ALOX12B	IMPACT505		AMP		
ES_03_T_03	AURKB	IMPACT505		AMP		
ES_03_T_03	E2F3	IMPACT505		AMP		
ES_03_T_03	FLT4	IMPACT505		DeepDel		
ES_03_T_03	PRDM1	IMPACT505		AMP		
ES_03_T_03	KDR	IMPACT505		DeepDel		
ES_03_T_03	TRIP13	IMPACT505		DeepDel		
ES_03_T_03	TERT	IMPACT505		DeepDel		
ES_03_T_03	IRF4	IMPACT505		AMP		
ES_03_T_03	HLA-A	IMPACT505		AMP		
ES_03_T_03	MDC1	IMPACT505		AMP		

ES_03_T_03	HLA-B	IMPACT505		AMP		
ES_03_T_03	HLA-C	IMPACT505		AMP		
ES_03_T_03	NOTCH4	IMPACT505		AMP		
ES_03_T_03	STK19	IMPACT505		AMP		
ES_03_T_03	TAP1	IMPACT505		AMP		
ES_03_T_03	TAP2	IMPACT505		AMP		
ES_03_T_03	CDKN1A	IMPACT505		AMP		
ES_03_T_03	PTP4A1	IMPACT505		AMP		
ES_03_T_03	PNRC1	IMPACT505		AMP		
ES_03_T_03	SESN1	IMPACT505		AMP		
ES_03_T_03	FYN	IMPACT505		AMP		
ES_03_T_03	IFNGR1	IMPACT505		AMP		
ES_03_T_03	TNFAIP3	IMPACT505		AMP		
ES_03_T_03	LATS1	IMPACT505		AMP		
ES_03_T_03	ARID1B	IMPACT505		AMP		
ES_03_T_03	PRKN	IMPACT505		AMP		
ES_03_T_03	PMS2	IMPACT505		AMP		
ES_03_T_03	INHBA	IMPACT505		AMP		
ES_03_T_03	IKZF1	IMPACT505		AMP		
ES_03_T_03	HGF	IMPACT505		DeepDel		
ES_03_T_03	PIK3CG	IMPACT505		AMP		
ES_03_T_03	POT1	IMPACT505		AMP		
ES_03_T_03	KMT2C	IMPACT505		AMP		
ES_03_T_03	XRCC2	IMPACT505		AMP		
ES_03_T_03	PREX2	IMPACT505		DeepDel		
ES_03_T_03	SMARCA2	IMPACT505		DeepDel		
ES_03_T_03	PDCD1LG2	IMPACT505		DeepDel		
ES_03_T_03	IGF1	IMPACT505		AMP		
ES_03_T_03	SCG5	IMPACT505		DeepDel		
ES_03_T_03	GREM1	IMPACT505		DeepDel		
ES_03_T_03	PALB2	IMPACT505		AMP		
ES_03_T_03	MAPK3	IMPACT505		AMP		
ES_03_T_03	PLCG2	IMPACT505		DeepDel		
ES_03_T_03	GPS2	IMPACT505		AMP		
ES_03_T_03	CALR	IMPACT505		AMP		
ES_03_T_03	NOTCH3	IMPACT505		AMP		
ES_03_T_03	BABAM1	IMPACT505		AMP		
ES_03_T_03	JAK3	IMPACT505		AMP		
ES_03_T_03	UPF1	IMPACT505		AMP		
ES_03_T_03	ERG	IMPACT505		DeepDel		
ES_03_T_03	TMPRSS2	IMPACT505		DeepDel		

ES_03_T_03	ICOSLG	IMPACT505		DeepDel		
ES_03_T_03	CRKL	IMPACT505		DeepDel		
ES_03_T_03	MAPK1	IMPACT505		DeepDel		
ES_03_T_03	ZNRF3	IMPACT505		DeepDel		
ES_03_T_03	RAC2	IMPACT505		AMP		
ES_03_T_03	PIM1	IMPACT505		AMP		
ES_03_T_03	EPHA7	IMPACT505		AMP		
ES_03_T_03	NTRK3	IMPACT505		DeepDel		
ES_03_T_03	IGF1R	IMPACT505		DeepDel		
ES_03_T_03	KMT2B	IMPACT505		AMP		
ES_03_T_05	SMARCB1	IMPACT468	A240Lfs*28	Frame_Shift_Ins	INS	0.29
ES_03_T_05	ATRX	IMPACT468	K1936R	Missense_Mutation	SNP	0.02
ES_03_T_07	SMARCB1	IMPACT468	A240Lfs*28	Frame_Shift_Ins	INS	0.59
ES_03_T_07	EZH2	IMPACT468	Y666N	Missense_Mutation	SNP	0.28
ES_03_T_07	SMARCB1	IMPACT468		DeepDel		
ES_03_T_07	CHEK2	IMPACT468		DeepDel		
ES_03_T_07	NF2	IMPACT468		DeepDel		
ES_03_T_07	EP300	IMPACT468		AMP		
ES_03_T_07	CRKL	IMPACT468		DeepDel		
ES_03_T_07	MAPK1	IMPACT468		DeepDel		
ES_03_T_07	RAC2	IMPACT468		AMP		
ES_04_T_06	TGFBR2	IMPACT410	T255M	Missense_Mutation	SNP	0.39
ES_04_T_06	SMARCB1	IMPACT410		DeepDel		
ES_05_T_01	SOS1	IMPACT505	D123H	Missense_Mutation	SNP	0.22
ES_05_T_01	NOTCH4	IMPACT505	N1811T	Missense_Mutation	SNP	0.22
ES_05_T_01	FLT3	IMPACT505		DeepDel		
ES_05_T_01	CD274	IMPACT505		DeepDel		
ES_05_T_01	JAK2	IMPACT505		DeepDel		
ES_05_T_01	TP53	IMPACT505		AMP		
ES_05_T_01	CRKL	IMPACT505		AMP		
ES_05_T_01	PDGFRA	IMPACT505		DeepDel		
ES_05_T_01	KIT	IMPACT505		DeepDel		
ES_05_T_01	CDKN2A	IMPACT505		DeepDel		
ES_05_T_01	MAPK1	IMPACT505		AMP		
ES_05_T_01	SMARCB1	IMPACT505		DeepDel		
ES_05_T_01	U2AF1	IMPACT505		DeepDel		
ES_05_T_01	RUNX1	IMPACT505		DeepDel		
ES_05_T_01	FLT1	IMPACT505		DeepDel		
ES_05_T_01	TENT5C	IMPACT505		DeepDel		
ES_05_T_01	NOTCH2	IMPACT505		DeepDel		
ES_05_T_01	VTCN1	IMPACT505		DeepDel		

ES_05_T_01	ALOX12B	IMPACT505		AMP		
ES_05_T_01	AURKB	IMPACT505		AMP		
ES_05_T_01	CDKN2B	IMPACT505		DeepDel		
ES_05_T_01	PAX5	IMPACT505		DeepDel		
ES_05_T_01	PTPRD	IMPACT505		DeepDel		
ES_05_T_01	PTPRT	IMPACT505		DeepDel		
ES_05_T_01	KDR	IMPACT505		DeepDel		
ES_05_T_01	PREX2	IMPACT505		DeepDel		
ES_05_T_01	PRDM14	IMPACT505		DeepDel		
ES_05_T_01	SMARCA2	IMPACT505		DeepDel		
ES_05_T_01	PDCD1LG2	IMPACT505		DeepDel		
ES_05_T_01	MTAP	IMPACT505		DeepDel		
ES_05_T_01	TEK	IMPACT505		DeepDel		
ES_05_T_01	GNAQ	IMPACT505		DeepDel		
ES_05_T_01	NTRK2	IMPACT505		DeepDel		
ES_05_T_01	PIK3C2G	IMPACT505		DeepDel		
ES_05_T_01	ERG	IMPACT505		DeepDel		
ES_05_T_01	TMPRSS2	IMPACT505		DeepDel		
ES_05_T_01	ICOSLG	IMPACT505		DeepDel		
ES_05_T_01	LZTR1	IMPACT505		AMP		
ES_05_T_01	SYK	IMPACT505		DeepDel		
ES_05_T_01	EPHB1	IMPACT505		DeepDel		
ES_05_T_09	BCL6	IMPACT468	S554Y	Missense_Mutation	SNP	0.28
ES_05_T_09	FAT1	IMPACT468	D2849H	Missense_Mutation	SNP	0.28
ES_05_T_09	SMARCB1	IMPACT468		DeepDel		
ES_06_T_01	HNF1A	IMPACT410	E329*	Nonsense_Mutation	SNP	0.07
ES_06_T_01	SMARCB1	IMPACT410		DeepDel		
ES_08_T_01	SMARCB1	IMPACT410		DeepDel		
ES_08_T_01	MAPK1	IMPACT410		AMP		
ES_08_T_01	CRKL	IMPACT410		AMP		
ES_09_T_02	SMARCB1	IMPACT468		DeepDel		
ES_09_T_03	ANKRD11	IMPACT468	D1730N	Missense_Mutation	SNP	0.18
ES_09_T_03	SMARCB1	IMPACT468		DeepDel		
ES_09_T_03	PLCG2	IMPACT468		DeepDel		
ES_15_T_11	ARID1B	IMPACT468	F1798Lfs*52	Frame_Shift_Del	DEL	0.44
ES_15_T_11	SMARCB1	IMPACT468		DeepDel		
ES_15_T_05	RB1	IMPACT468	I124Rfs*6	Frame_Shift_Del	DEL	0.78
ES_15_T_05	ARID1B	IMPACT468	F1798Lfs*52	Frame_Shift_Del	DEL	0.41
ES_15_T_05	SMARCB1	IMPACT468		DeepDel		
ES_15_T_05	CHEK2	IMPACT468		DeepDel		
ES_15_T_05	RB1	IMPACT468		DeepDel		

ES_15_T_05	NF2	IMPACT468		DeepDel		
ES_15_T_05	CYSLTR2	IMPACT468		DeepDel		
ES_15_T_05	MAPK1	IMPACT468		DeepDel		
ES_16_T_01	ANKRD11	IMPACT468	Y1114H	Missense_Mutation	SNP	0.21
ES_16_T_02	ANKRD11	IMPACT468	Y1114H	Missense_Mutation	SNP	0.09
ES_17_T_03	ROS1	IMPACT468	D725N	Missense_Mutation	SNP	0.10
ES_17_T_03	SMARCB1	IMPACT468		DeepDel		
ES_17_T_01	SMARCB1	IMPACT468		DeepDel		
ES_18_T_01	CDKN2C	IMPACT468	Y147H	Missense_Mutation	SNP	0.11
ES_18_T_01	CD274	IMPACT468		DeepDel		
ES_19_T_01	BRCA2	IMPACT505	S205G	Missense_Mutation	SNP	0.25
ES_19_T_01	SMARCB1	IMPACT505		DeepDel		
ES_19_T_01	MET	IMPACT505		AMP		
ES_19_T_01	CDK6	IMPACT505		AMP		
ES_19_T_01	BRAF	IMPACT505		AMP		
ES_19_T_01	REST	IMPACT505		DeepDel		
ES_19_T_01	ESR1	IMPACT505		AMP		
ES_19_T_01	PDGFRA	IMPACT505		DeepDel		
ES_19_T_01	KIT	IMPACT505		DeepDel		
ES_19_T_01	SMO	IMPACT505		AMP		
ES_19_T_01	CREBBP	IMPACT505		AMP		
ES_19_T_01	EP300	IMPACT505		AMP		
ES_19_T_01	GRIN2A	IMPACT505		AMP		
ES_19_T_01	SOCS1	IMPACT505		AMP		
ES_19_T_01	KDR	IMPACT505		DeepDel		
ES_19_T_01	EPHA5	IMPACT505		DeepDel		
ES_19_T_01	ALB	IMPACT505		DeepDel		
ES_19_T_01	IFNGR1	IMPACT505		AMP		
ES_19_T_01	TNFAIP3	IMPACT505		AMP		
ES_19_T_01	LATS1	IMPACT505		AMP		
ES_19_T_01	ARID1B	IMPACT505		AMP		
ES_19_T_01	PIK3CG	IMPACT505		AMP		
ES_19_T_01	POT1	IMPACT505		AMP		
ES_19_T_01	SLX4	IMPACT505		AMP		
ES_19_T_01	ERCC4	IMPACT505		AMP		
ES_19_T_01	PALB2	IMPACT505		AMP		
ES_19_T_01	MAPK3	IMPACT505		AMP		
ES_19_T_01	RAC2	IMPACT505		AMP		
ES_19_T_03	BRCA2	IMPACT505	S205G	Missense_Mutation	SNP	0.12
ES_19_T_03	SMARCB1	IMPACT505		DeepDel		
ES_21_T_01	CDKN2A	IMPACT468		DeepDel		

ES_21_T_01	SMARCB1	IMPACT468		DeepDel		
ES_21_T_01	CDKN2B	IMPACT468		DeepDel		
ES_21_T_01	CDKN2AP14ARF	IMPACT468		DeepDel		
ES_21_T_01	CDKN2AP16INK4A	IMPACT468		DeepDel		
ES_22_T_01	SMARCB1	IMPACT468	X32_splice	Splice_Site	SNP	0.55
ES_22_T_01	IGF1R	IMPACT468		DeepDel		
ES_22_T_03	SMARCB1	IMPACT468	X32_splice	Splice_Site	SNP	0.53
ES_22_T_03	ID3	IMPACT468	Q100*	Nonsense_Mutation	SNP	0.08
ES_22_T_03	IGF1R	IMPACT468		DeepDel		
ES_23_T_02	PIK3CG	IMPACT468	M728I	Missense_Mutation	SNP	0.38
ES_23_T_02	SMARCB1	IMPACT468		DeepDel		
ES_23_T_02	BABAM1/ATP6V1E1	IMPACT468		Fusion		
ES_23_T_03	PIK3CG	IMPACT468	M728I	Missense_Mutation	SNP	0.26
ES_23_T_03	SMARCB1	IMPACT468		DeepDel		
ES_23_T_03	PRKN	IMPACT468		DeepDel		
ES_23_T_03	BABAM1/ATP6V1E1	IMPACT468		Fusion		
ES_24_T_02	NCOR1	IMPACT468	M1417L	Missense_Mutation	SNP	0.10
ES_24_T_02	SMARCB1	IMPACT468		DELETION		
ES_25_T_06	SMARCB1	IMPACT468		DeepDel		
ES_26_T_01	SMARCB1	IMPACT468		DeepDel		
ES_26_T_01	ARID2	IMPACT468	V190F	Missense_Mutation		

Supplementary Table S3:

Cell Line	Gene	Protein Change	Mutation Type	Variant Type	Allele Freq
A204	TP53	G245S	Missense_Mutation	SNP	0.20
A204	SMARCB1	Q182Afs*28	Frame_Shift_Del	DEL	0.99
A204	APC	R653=	Splice_Region	SNP	0.46
A204	NAB2	P211S	Missense_Mutation	SNP	0.52
A204	PIK3CA	I391M	Missense_Mutation	SNP	0.51
A204	BARD1	L359_P365del	In_Frame_Del	DEL	0.48
A204	KMT2D	P2557L	Missense_Mutation	SNP	0.50
A204	FOXA1	E269V	Missense_Mutation	SNP	0.51
A204	PARP1	S383Y	Missense_Mutation	SNP	0.50
A204	DOT1L	A1053T	Missense_Mutation	SNP	0.49
A204	NTRK1	R780Q	Missense_Mutation	SNP	0.52
A204	PIK3R2	V54M	Missense_Mutation	SNP	0.54
A204	MGA	N1982S	Missense_Mutation	SNP	0.47
A204	NSD1	M2261T	Missense_Mutation	SNP	0.49
A204	POT1	Q301H	Missense_Mutation	SNP	0.50
A204	NF1	L1274F	Missense_Mutation	SNP	0.50

A204	FLT4	S430A	Missense_Mutation	SNP	0.47
A204	EP300	S106G	Missense_Mutation	SNP	0.49
A204	NTRK3	N714S	Missense_Mutation	SNP	0.49
A204	NUP93	R486C	Missense_Mutation	SNP	0.53
A204	NSD1	M2250I	Missense_Mutation	SNP	0.50
A204	NSD1	A1036P	Missense_Mutation	SNP	0.50
A204	CUL3	V567I	Missense_Mutation	SNP	0.49
A204	NSD1	A691T	Missense_Mutation	SNP	0.51
A204	PDGFRB	E485K	Missense_Mutation	SNP	0.50
A204	ETAA1	M221T	Missense_Mutation	SNP	0.50
A204	MGA	C1270R	Missense_Mutation	SNP	0.48
A204	ETAA1	G439R	Missense_Mutation	SNP	0.49
A204	NSD3	I40T	Missense_Mutation	SNP	0.51
A204	EPAS1	A698P	Missense_Mutation	SNP	0.48
A204	PPARG	D92Y	Missense_Mutation	SNP	0.48
A204	PIK3CB	Y176C	Missense_Mutation	SNP	0.48
A204	SETD2	D1211H	Missense_Mutation	SNP	0.51
A204	ZNRF3	H327Q	Missense_Mutation	SNP	0.50
A204	GBP3	R290C	Missense_Mutation	SNP	0.47
A204	NSFL1C	D292N	Missense_Mutation	SNP	0.50
A204	ZNF474	R173H	Missense_Mutation	SNP	0.55
A204	ZNF474	L318*	Frame_Shift_Del	DEL	0.49
A204	AGAP4	R484C	Missense_Mutation	SNP	0.52
A204	FSTL4	E353D	Missense_Mutation	SNP	0.50
A204	H6PD	L616V	Missense_Mutation	SNP	0.49
A204	SMYD3		DeepDel		
A204	NFE2L2		DeepDel		
A204	SMARCA2		DeepDel		
EPI544	KMT2C	A1685S	Missense_Mutation	SNP	0.10
EPI544	TCF7L2	P483T	Missense_Mutation	SNP	0.49
EPI544	ANKRD11	P2059H	Missense_Mutation	SNP	1.00
EPI544	EPHA7	P278S	Missense_Mutation	SNP	0.49
EPI544	EPHA7	I138V	Missense_Mutation	SNP	0.50
EPI544	ANKRD11	P1638A	Missense_Mutation	SNP	1.00
EPI544	FAT1	S2353A	Missense_Mutation	SNP	0.48
EPI544	PDCD1	A215V	Missense_Mutation	SNP	0.48
EPI544	PHOX2B	A256_A260del	In_Frame_Del	DEL	0.15
EPI544	KIT	T304A	Missense_Mutation	SNP	0.69
EPI544	ANKRD11	P2290S	Missense_Mutation	SNP	0.58
EPI544	PIK3CG	A30G	Missense_Mutation	SNP	0.50
EPI544	RECQL4	E711K	Missense_Mutation	SNP	0.49

EPI544	KMT2D	P2382S	Missense_Mutation	SNP	0.54
EPI544	HLA-C	V272M	Missense_Mutation	SNP	0.54
EPI544	PREX2	V678L	Missense_Mutation	SNP	0.49
EPI544	DNAJB1	D250N	Missense_Mutation	SNP	0.51
EPI544	DNMT1	V120L	Missense_Mutation	SNP	0.49
EPI544	SESN2	T320A	Missense_Mutation	SNP	0.67
EPI544	HLA-C	V76M	Missense_Mutation	SNP	0.13
EPI544	SETDB1	D1044=	Splice_Region	SNP	0.34
EPI544	DICER1	A318T	Missense_Mutation	SNP	0.48
EPI544	EPCAM	Q262R	Missense_Mutation	SNP	0.50
EPI544	NSD3	R815G	Missense_Mutation	SNP	0.33
EPI544	GBP3	R290C	Missense_Mutation	SNP	0.64
EPI544	MTTP	E98D	Missense_Mutation	SNP	0.55
EPI544	NSFL1C	D292N	Missense_Mutation	SNP	0.47
EPI544	AGAP4	R484C	Missense_Mutation	SNP	1.00
EPI544	CWC22	R794Q	Missense_Mutation	SNP	0.52
EPI544	AGAP7P	M442T	Missense_Mutation	SNP	0.50
EPI544	FAM86C1	N117K	Missense_Mutation	SNP	0.52
EPI544	OR11H2	L235I	Missense_Mutation	SNP	0.06
EPI544	GPNMB	A97V	Missense_Mutation	SNP	0.49
EPI544	ALG1L	D170N	Missense_Mutation	SNP	0.47
EPI544	SDCCAG8	E367K	Missense_Mutation	SNP	0.61
EPI544	EPHA5		DeepDel		
EPI544	SDHA		AMP		
EPI544	TRIP13		AMP		
EPI544	TERT		AMP		
EPI544	DROSHA		AMP		
EPI544	IL7R		AMP		
EPI544	RICTOR		AMP		
EPI544	WHSC1L1		AMP		
EPI544	FGFR1		AMP		
EPI544	CDKN2A		DeepDel		
EPI544	H3F3C		DeepDel		
EPI544	AXIN1		AMP		
EPI544	NTHL1		AMP		
EPI544	TSC2		AMP		
EPI544	TRAF7		AMP		
EPI544	PDPK1		AMP		
EPI544	SLX4		AMP		
EPI544	CREBBP		AMP		
EPI544	GRIN2A		AMP		

EPI544	SOCS1		AMP		
EPI544	ERCC4		AMP		
EPI544	SMARCB1		DeepDel		
ES1	INPP4B	S673=	Splice_Region	SNP	0.49
ES1	PIK3CA	I391M	Missense_Mutation	SNP	0.33
ES1	GRIN2A	N1436S	Missense_Mutation	SNP	0.51
ES1	USP8	L776P	Missense_Mutation	SNP	0.05
ES1	KMT2D	M3398V	Missense_Mutation	SNP	0.49
ES1	ANKRD11	A1780T	Missense_Mutation	SNP	0.50
ES1	NCOR1	A2182T	Missense_Mutation	SNP	0.50
ES1	NCOR1	H2252Y	Missense_Mutation	SNP	0.48
ES1	FAT1	V3147G	Missense_Mutation	SNP	0.49
ES1	KLF4	T114N	Missense_Mutation	SNP	0.48
ES1	PALB2	G998E	Missense_Mutation	SNP	0.49
ES1	MTOR	V1885I	Missense_Mutation	SNP	0.33
ES1	ALOX12B	I65T	Missense_Mutation	SNP	0.50
ES1	ZFHX3	G3525_G3527del	In_Frame_Del	DEL	0.32
ES1	KDR	R57T	Missense_Mutation	SNP	0.48
ES1	HIST3H3	R54H	Missense_Mutation	SNP	0.60
ES1	PIK3C2G	A261E	Missense_Mutation	SNP	0.48
ES1	CUL3	V567I	Missense_Mutation	SNP	1.00
ES1	RAD50	I94L	Missense_Mutation	SNP	0.48
ES1	BRCA2	I3412V	Missense_Mutation	SNP	0.50
ES1	EPAS1	P785T	Missense_Mutation	SNP	0.50
ES1	MSH2	D459N	Missense_Mutation	SNP	0.51
ES1	SLX4	T500M	Missense_Mutation	SNP	0.52
ES1	ESR1	A571V	Missense_Mutation	NA	0.30
ES1	ARID2	S479P	Missense_Mutation	SNP	0.50
ES1	ERCC4	A235T	Missense_Mutation	SNP	0.50
ES1	EPCAM	S159N	Missense_Mutation	SNP	0.51
ES1	KMT2D	Q3938_Q3954del	In_Frame_Del	DEL	0.32
ES1	MGA	P893L	Missense_Mutation	SNP	0.17
ES1	SUZ12	S59_V68delinsAA	In_Frame_Del	DEL	0.18
ES1	PPM1D	R429S	Missense_Mutation	SNP	0.50
ES1	AGAP4	R484C	Missense_Mutation	SNP	0.67
ES1	PPP2R3A	A171S	Missense_Mutation	SNP	0.68
ES1	OR11H1	S268G	Missense_Mutation	SNP	0.07
ES1	AIMP2	A72G	Missense_Mutation	SNP	0.46
ES1	SDHA		DeepDel		
ES1	HGF		DeepDel		
ES1	CDK6		DeepDel		

ES1	SOX17		AMP		
ES1	LYN		AMP		
ES1	PREX2		AMP		
ES1	PRDM14		AMP		
ES1	TCEB1		AMP		
ES1	NBN		AMP		
ES1	RAD21		AMP		
ES1	MYC		AMP		
ES1	AGO2		AMP		
ES1	RECQL4		AMP		
ES1	CDKN2A		DeepDel		
ES1	SMARCB1		DeepDel		
ES2	HLA-C	A235T	Missense_Mutation	SNP	0.40
ES2	HLA-B	Y91C	Missense_Mutation	SNP	0.99
ES2	ATRX	H865Q	Missense_Mutation	SNP	1.00
ES2	PDCD1LG2	Q79E	Missense_Mutation	SNP	1.00
ES2	KMT2C	P2412T	Missense_Mutation	SNP	1.00
ES2	PIK3CD	F146I	Missense_Mutation	SNP	0.35
ES2	ERBB4	H374Q	Missense_Mutation	SNP	0.52
ES2	ATR	Y2132D	Missense_Mutation	SNP	0.49
ES2	SESN2	R36W	Missense_Mutation	SNP	0.62
ES2	ZFHX3	V777_A780del	In_Frame_Del	DEL	0.52
ES2	TRAF2	S11Y	Missense_Mutation	SNP	0.32
ES2	SPRTN	T439S	Missense_Mutation	SNP	0.66
ES2	PREX2	G1522D	Missense_Mutation	SNP	0.66
ES2	HLA-C	L180D	Missense_Mutation	ONP	0.13
ES2	EP300	I196V	Missense_Mutation	SNP	0.48
ES2	TET1	K15R	Missense_Mutation	SNP	0.51
ES2	DNAJB1	I175F	Missense_Mutation	SNP	0.35
ES2	FAT1	I4462N	Missense_Mutation	SNP	0.50
ES2	APC	D227E	Missense_Mutation	SNP	0.49
ES2	NSFL1C	D292N	Missense_Mutation	SNP	0.49
ES2	PPP2R3A	A171S	Missense_Mutation	SNP	1.00
ES2	ZNF737	Y369C	Missense_Mutation	SNP	0.42
ES2	OR4C46	L235H	Missense_Mutation	SNP	0.44
ES2	LARGE2	L575*	Nonsense_Mutation	SNP	0.41
ES2	JAK1		DeepDel		
ES2	MYC		AMP		
ES2	AGO2		AMP		
ES2	RECQL4		AMP		
ES2	SMARCB1		DeepDel		

G401	MST1	G673S	Missense_Mutation	SNP	0.07
G401	KDR	C482R	Missense_Mutation	SNP	0.49
G401	INPP4B	S673=	Splice_Region	SNP	0.46
G401	SMO	A68G	Missense_Mutation	SNP	0.22
G401	NSD1	R1188S	Missense_Mutation	SNP	0.46
G401	ABL1	G706S	Missense_Mutation	SNP	0.52
G401	ESR1	S137R	Missense_Mutation	SNP	0.49
G401	KMT2D	R1388L	Missense_Mutation	SNP	0.48
G401	ALOX12B	P127S	Missense_Mutation	SNP	0.49
G401	BIRC3	R401K	Missense_Mutation	SNP	0.49
G401	POT1	G404V	Missense_Mutation	SNP	0.75
G401	ARID1B	P508S	Missense_Mutation	SNP	0.45
G401	PALB2	G998E	Missense_Mutation	SNP	0.48
G401	MLH1	I655V	Missense_Mutation	SNP	0.52
G401	CBL	L620F	Missense_Mutation	SNP	0.49
G401	IRS1	G123E	Missense_Mutation	SNP	0.49
G401	SLFN11	V881I	Missense_Mutation	SNP	1.00
G401	NSD2	Y1006H	Missense_Mutation	SNP	0.51
G401	AXL	A572T	Missense_Mutation	SNP	0.52
G401	RAD50	I94L	Missense_Mutation	SNP	0.47
G401	BRD4	R1097H	Missense_Mutation	SNP	0.48
G401	HLA-C	L180D	Missense_Mutation	ONP	0.31
G401	CYLD	Q729H	Missense_Mutation	SNP	0.50
G401	MDM4	MUTATED	Splice_Region	DEL	0.53
G401	MDM4	MUTATED	Splice_Region	SNP	0.12
G401	GRID2	T68M	Missense_Mutation	SNP	0.48
G401	PPP2R3A	A171S	Missense_Mutation	SNP	0.50
G401	FSTL4	E353D	Missense_Mutation	SNP	0.52
G401	CDHR5	G546E	Missense_Mutation	SNP	0.48
G401	AMPD3	F532L	Missense_Mutation	SNP	0.49
G401	HGF		AMP		
G401	CDK6		AMP		
G401	PIK3CG		AMP		
G401	MET		AMP		
G401	POT1		AMP		
G401	SMO		AMP		
G401	BRAF		AMP		
G401	EZH2		AMP		
G401	RHEB		AMP		
G401	KMT2C		AMP		
G401	XRCC2		AMP		

G401	SMARCB1		DeepDel		
MP-MRT-AN	SDHA	V637=	Splice_Region	SNP	0.60
MP-MRT-AN	CDKN1A	MUTATED	Splice_Region	SNP	0.48
MP-MRT-AN	NAB2	E490*	Nonsense_Mutation	SNP	0.50
MP-MRT-AN	SERPINB4	E353K	Missense_Mutation	SNP	0.49
MP-MRT-AN	BRCA2	N289H	Missense_Mutation	SNP	0.49
MP-MRT-AN	BRCA2	N991D	Missense_Mutation	SNP	0.49
MP-MRT-AN	ANKRD11	P2263S	Missense_Mutation	SNP	0.53
MP-MRT-AN	EPHA7	P278S	Missense_Mutation	SNP	0.47
MP-MRT-AN	EPHA7	I138V	Missense_Mutation	SNP	0.48
MP-MRT-AN	ANKRD11	A2023P	Missense_Mutation	SNP	0.47
MP-MRT-AN	FOXO1	D82N	Missense_Mutation	SNP	0.54
MP-MRT-AN	FANCA	R350Q	Missense_Mutation	SNP	0.49
MP-MRT-AN	RAD51	R150Q	Missense_Mutation	SNP	0.48
MP-MRT-AN	NOTCH1	D1185N	Missense_Mutation	SNP	0.47
MP-MRT-AN	PTCH1	R1442Q	Missense_Mutation	SNP	0.51
MP-MRT-AN	PDCD1	A215V	Missense_Mutation	SNP	0.53
MP-MRT-AN	ARID2	G936C	Missense_Mutation	SNP	0.49
MP-MRT-AN	AXIN1	V600M	Missense_Mutation	SNP	0.50
MP-MRT-AN	NOTCH4	P204L	Missense_Mutation	SNP	0.48
MP-MRT-AN	TSC1	T899S	Missense_Mutation	SNP	0.49
MP-MRT-AN	PIK3C2G	E1260D	Missense_Mutation	SNP	0.47
MP-MRT-AN	SH2B3	A536T	Missense_Mutation	SNP	0.53
MP-MRT-AN	DNMT1	H97R	Missense_Mutation	SNP	0.52
MP-MRT-AN	PLCG2	E721K	Missense_Mutation	SNP	0.47
MP-MRT-AN	PIK3CG	P401L	Missense_Mutation	SNP	0.47
MP-MRT-AN	GATA2	P250A	Missense_Mutation	SNP	0.51
MP-MRT-AN	RPTOR	P227L	Missense_Mutation	SNP	0.52
MP-MRT-AN	INPPL1	K303N	Missense_Mutation	SNP	0.49
MP-MRT-AN	HLA-C	V272M	Missense_Mutation	SNP	0.49
MP-MRT-AN	HLA-C	A176T	Missense_Mutation	SNP	0.31
MP-MRT-AN	ERF	A415V	Missense_Mutation	SNP	0.54
MP-MRT-AN	CDH1	P126L	Missense_Mutation	SNP	0.50
MP-MRT-AN	KMT2A	P3610L	Missense_Mutation	SNP	0.49
MP-MRT-AN	SLX4	R481G	Missense_Mutation	SNP	0.50
MP-MRT-AN	EP300	G2218S	Missense_Mutation	SNP	1.00
MP-MRT-AN	NOTCH1	R1296H	Missense_Mutation	SNP	0.52
MP-MRT-AN	GAB1	L270S	Missense_Mutation	SNP	0.51
MP-MRT-AN	TFE3	A223T	Missense_Mutation	SNP	0.60
MP-MRT-AN	NTHL1	R33K	Missense_Mutation	SNP	0.50
MP-MRT-AN	HLA-B	E176K	Missense_Mutation	SNP	0.13

MP-MRT-AN	PPP4R2	P174L	Missense_Mutation	SNP	0.52
MP-MRT-AN	ETAA1	P715L	Missense_Mutation	SNP	0.49
MP-MRT-AN	GAB2	V475I	Missense_Mutation	SNP	0.47
MP-MRT-AN	NSFL1C	D292N	Missense_Mutation	SNP	0.49
MP-MRT-AN	OR5D14	R236H	Missense_Mutation	SNP	0.53
MP-MRT-AN	ZNF474	L318*	Frame_Shift_Del	DEL	0.30
MP-MRT-AN	OR5D14	G191S	Missense_Mutation	SNP	0.53
MP-MRT-AN	PPP2R3A	A171S	Missense_Mutation	SNP	0.50
MP-MRT-AN	NOTCH2NLA	T50M	Missense_Mutation	SNP	0.14
MP-MRT-AN	FAM86C1	N117K	Missense_Mutation	SNP	1.00
MP-MRT-AN	IGKV3OR2-268	A29T	Missense_Mutation	SNP	0.40
MP-MRT-AN	C17ORF80	X541_splice	Splice_Site	SNP	0.48
MP-MRT-AN	RAB11FIP1	G700R	Missense_Mutation	SNP	0.47
MP-MRT-AN	SCNN1B	H2Q	Missense_Mutation	SNP	0.46
MP-MRT-AN	HSCB	R11Q	Missense_Mutation	SNP	1.00
MP-MRT-AN	MET		AMP		
MP-MRT-AN	MTAP		DeepDel		
MP-MRT-AN	CDKN2A		DeepDel		
MP-MRT-AN	CDKN2B		DeepDel		
MP-MRT-AN	SMARCB1		DeepDel		
KP-MRT-NS	TP53	R273C	Missense_Mutation	SNP	1.00
KP-MRT-NS	EIF1AX	G8R	Missense_Mutation	SNP	0.45
KP-MRT-NS	LATS1	R670=	Splice_Region	SNP	0.42
KP-MRT-NS	ERCC4	R670Q	Missense_Mutation	SNP	0.51
KP-MRT-NS	USP8	L776P	Missense_Mutation	SNP	0.06
KP-MRT-NS	PDCD1	A215V	Missense_Mutation	SNP	0.49
KP-MRT-NS	INPP4B	G554S	Missense_Mutation	SNP	0.58
KP-MRT-NS	CBL	L620F	Missense_Mutation	SNP	0.49
KP-MRT-NS	BIRC3	V386M	Missense_Mutation	SNP	0.46
KP-MRT-NS	CUL3	V567I	Missense_Mutation	SNP	1.00
KP-MRT-NS	SMO	V129I	Missense_Mutation	SNP	0.68
KP-MRT-NS	EPHA5	D20N	Missense_Mutation	SNP	0.63
KP-MRT-NS	ROS1	P1539L	Missense_Mutation	SNP	0.23
KP-MRT-NS	BRCA2	I3412V	Missense_Mutation	SNP	1.00
KP-MRT-NS	FAT1	A3739V	Missense_Mutation	SNP	0.40
KP-MRT-NS	GATA2	P250A	Missense_Mutation	SNP	0.47
KP-MRT-NS	WT1	Q155H	Missense_Mutation	SNP	0.62
KP-MRT-NS	PREX2	T797N	Missense_Mutation	SNP	0.45
KP-MRT-NS	SLFN11	R489C	Missense_Mutation	SNP	0.34
KP-MRT-NS	ARID2	S587G	Missense_Mutation	SNP	0.49
KP-MRT-NS	KMT2B	P587R	Missense_Mutation	SNP	0.50

KP-MRT-NS	MSH2	L811F	Missense_Mutation	SNP	0.50
KP-MRT-NS	IRS1	D1137N	Missense_Mutation	SNP	0.49
KP-MRT-NS	PLK2	P52L	Missense_Mutation	SNP	0.49
KP-MRT-NS	TRAF2	A168S	Missense_Mutation	SNP	0.54
KP-MRT-NS	AMER1	A29T	Missense_Mutation	SNP	0.43
KP-MRT-NS	HLA-B	N104I	Missense_Mutation	SNP	0.94
KP-MRT-NS	RBM10	V456M	Missense_Mutation	SNP	0.42
KP-MRT-NS	GTF2I	T707I	Missense_Mutation	SNP	0.20
KP-MRT-NS	CMTR2	I523V	Missense_Mutation	SNP	0.51
KP-MRT-NS	SLFN11	K507E	Missense_Mutation	SNP	0.28
KP-MRT-NS	SLFN11	F492L	Missense_Mutation	SNP	0.31
KP-MRT-NS	MTTP	E98D	Missense_Mutation	SNP	0.60
KP-MRT-NS	NSFL1C	D292N	Missense_Mutation	SNP	1.00
KP-MRT-NS	CWC22	R794Q	Missense_Mutation	SNP	1.00
KP-MRT-NS	FAM86B1	N252H	Missense_Mutation	SNP	0.17
KP-MRT-NS	RAB11FIP1	V576A	Missense_Mutation	SNP	0.47
KP-MRT-NS	SLFN13	R489C	Missense_Mutation	SNP	0.12
KP-MRT-NS	OR11H1	S268G	Missense_Mutation	SNP	0.08
KP-MRT-NS	NOTCH2NLA	E226Q	Missense_Mutation	SNP	0.07
KP-MRT-NS	ZWINT	R245Q	Missense_Mutation	SNP	0.49
KP-MRT-NS	SLFN13	K507E	Missense_Mutation	SNP	0.08
KP-MRT-NS	OR11H2	Y233*	Nonsense_Mutation	SNP	0.06
KP-MRT-NS	OR11H2	L235I	Missense_Mutation	SNP	0.08
KP-MRT-NS	OR11H2	M243T	Missense_Mutation	SNP	0.08
KP-MRT-NS	BORCS8-MEF2B	R307S	Missense_Mutation	SNP	0.46
KP-MRT-NS	TUBBP5	I169V	Missense_Mutation	SNP	0.12
KP-MRT-NS	TUBBP5	R262W	Missense_Mutation	SNP	0.25
KP-MRT-NS	SMARCB1		DeepDel		
KP-MRT-RY	SMARCB1	R53*	Nonsense_Mutation	SNP	1.00
KP-MRT-RY	KMT2C	A1685S	Missense_Mutation	SNP	0.10
KP-MRT-RY	HLA-A	R45H	Missense_Mutation	SNP	0.10
KP-MRT-RY	KMT2C	G908C	Missense_Mutation	SNP	0.05
KP-MRT-RY	TCF7L2	P483T	Missense_Mutation	SNP	0.52
KP-MRT-RY	ASXL1	G652S	Missense_Mutation	SNP	0.50
KP-MRT-RY	TET2	P29R	Missense_Mutation	SNP	0.48
KP-MRT-RY	EPHA7	P278S	Missense_Mutation	SNP	0.52
KP-MRT-RY	EPHA7	I138V	Missense_Mutation	SNP	0.50
KP-MRT-RY	PDCD1	A215V	Missense_Mutation	SNP	0.65
KP-MRT-RY	ARID2	G936C	Missense_Mutation	SNP	0.50
KP-MRT-RY	STAT5B	A130V	Missense_Mutation	SNP	0.51
KP-MRT-RY	SLFN11	V881I	Missense_Mutation	SNP	0.48

KP-MRT-RY	TSC1	Q654E	Missense_Mutation	SNP	0.51
KP-MRT-RY	KMT2A	G3131S	Missense_Mutation	SNP	0.51
KP-MRT-RY	CUL3	V567I	Missense_Mutation	SNP	1.00
KP-MRT-RY	NOTCH1	T1573A	Missense_Mutation	SNP	0.48
KP-MRT-RY	DNMT1	H97R	Missense_Mutation	SNP	0.53
KP-MRT-RY	BRCA2	V2109I	Missense_Mutation	SNP	0.50
KP-MRT-RY	EPCAM	T172M	Missense_Mutation	SNP	0.62
KP-MRT-RY	PRKCI	R327=	Splice_Region	SNP	0.52
KP-MRT-RY	ARID2	A1434S	Missense_Mutation	SNP	0.49
KP-MRT-RY	ATXN7	A546T	Missense_Mutation	SNP	0.48
KP-MRT-RY	RAB35	V155I	Missense_Mutation	SNP	0.52
KP-MRT-RY	TAP2	M577V	Missense_Mutation	SNP	0.52
KP-MRT-RY	HLA-A	W191R	Missense_Mutation	SNP	0.11
KP-MRT-RY	MUTYH	V201M	Missense_Mutation	SNP	0.49
KP-MRT-RY	TBX3	A491E	Missense_Mutation	SNP	0.58
KP-MRT-RY	FANCA	E630V	Missense_Mutation	SNP	0.50
KP-MRT-RY	POLD1	D893G	Missense_Mutation	SNP	0.47
KP-MRT-RY	MSH6	I710N	Missense_Mutation	SNP	0.37
KP-MRT-RY	RAD50	R725Q	Missense_Mutation	SNP	0.50
KP-MRT-RY	E2F3	C390F	Missense_Mutation	SNP	0.49
KP-MRT-RY	STK19	Q195E	Missense_Mutation	SNP	0.49
KP-MRT-RY	SLFN11	A523T	Missense_Mutation	SNP	0.53
KP-MRT-RY	CYP19A1	W39R	Missense_Mutation	SNP	0.50
KP-MRT-RY	HIST1H2BC	E3*	Nonsense_Mutation	SNP	0.52
KP-MRT-RY	STAT5B	Q636=	Splice_Region	SNP	0.49
KP-MRT-RY	FAM86B2	R270W	Missense_Mutation	SNP	0.86
KP-MRT-RY	SPOCD1	P189L	Missense_Mutation	SNP	1.00
KP-MRT-RY	GBP3	R290C	Missense_Mutation	SNP	0.48
KP-MRT-RY	MTTP	E98D	Missense_Mutation	SNP	0.55
KP-MRT-RY	NSFL1C	D292N	Missense_Mutation	SNP	0.48
KP-MRT-RY	ZNF474	L318*	Frame_Shift_Del	DEL	0.47
KP-MRT-RY	CWC22	R794Q	Missense_Mutation	SNP	0.34
KP-MRT-RY	RAB6C	S214Y	Missense_Mutation	SNP	0.67
KP-MRT-RY	SLFN13	K507E	Missense_Mutation	SNP	0.31
KP-MRT-RY	TUBBP5	I169V	Missense_Mutation	SNP	0.07
KP-MRT-RY	DAB2	T565I	Missense_Mutation	SNP	0.52
KP-MRT-RY	RAB11FIP1	G700R	Missense_Mutation	SNP	0.50
KP-MRT-RY	TUBBP5	R262W	Missense_Mutation	SNP	0.11
KP-MRT-RY	SPOCD1	A45P	Missense_Mutation	SNP	0.53
KP-MRT-RY	ERBB3		AMP		
KP-MRT-RY	GLI1		AMP		

KP-MRT-RY	CDK4		AMP		
KP-MRT-RY	FOXO1		DeepDel		
KP-MRT-RY	RB1		DeepDel		
KP-MRT-RY	CYSLTR2		DeepDel		
KP-MRT-RY	DIS3		DeepDel		
KP-MRT-RY	KLF5		DeepDel		
KP-MRT-RY	ERCC5		DeepDel		
KP-MRT-RY	IRS2		DeepDel		
KP-MRT-RY	RAD51B		DeepDel		
TM8716	CIC	P1279Lfs*29	Frame_Shift_Ins	INS	0.36
TM8716	ICOSLG	A270V	Missense_Mutation	SNP	0.50
TM8716	JAK2	L393V	Missense_Mutation	SNP	0.49
TM8716	POT1	G404V	Missense_Mutation	SNP	0.50
TM8716	NOTCH2	D1327G	Missense_Mutation	SNP	0.51
TM8716	TERT	H412Y	Missense_Mutation	SNP	0.49
TM8716	ABL1	A861T	Missense_Mutation	SNP	0.51
TM8716	APC	N1118D	Missense_Mutation	SNP	0.49
TM8716	FAT1	M2845I	Missense_Mutation	SNP	0.51
TM8716	FAT1	Y1250C	Missense_Mutation	SNP	0.50
TM8716	RNF43	R337Q	Missense_Mutation	SNP	0.49
TM8716	POLE	R2165H	Missense_Mutation	SNP	0.50
TM8716	CIC	G525S	Missense_Mutation	SNP	0.49
TM8716	MST1R	R75S	Missense_Mutation	SNP	0.49
TM8716	CRLF2	E66K	Missense_Mutation	SNP	0.52
TM8716	ABRAXAS1	D373N	Missense_Mutation	SNP	0.52
TM8716	ZFHX3	V577I	Missense_Mutation	SNP	0.52
TM8716	GLIPR1L2	V51I	Missense_Mutation	SNP	0.47
TM8716	GRID2	T68M	Missense_Mutation	SNP	0.54
TM8716	NSFL1C	D292N	Missense_Mutation	SNP	0.52
TM8716	SPATA31A3	K1090N	Missense_Mutation	SNP	0.14
TM8716	CWC22	R794Q	Missense_Mutation	SNP	0.49
TM8716	ALG1	A431E	Missense_Mutation	SNP	0.07
TM8716	PIWIL4	R329Q	Missense_Mutation	SNP	0.48
TM8716	ARID1B		DeepDel		
TM8716	SMARCB1		DeepDel		
VAESBJ	TERT	Promoter	5'Flank	SNP	0.31
VAESBJ	NF2	S87*	Nonsense_Mutation	SNP	1.00
VAESBJ	PIK3CA	I391M	Missense_Mutation	SNP	0.33
VAESBJ	SLX4	A1221V	Missense_Mutation	SNP	0.66
VAESBJ	USP8	T785A	Missense_Mutation	SNP	0.06
VAESBJ	FANCC	C10Y	Missense_Mutation	SNP	1.00

VAESBJ	TCF7L2	P483T	Missense_Mutation	SNP	0.48
VAESBJ	SLX4	N457K	Missense_Mutation	SNP	0.61
VAESBJ	KMT2D	P813L	Missense_Mutation	SNP	0.99
VAESBJ	SPEN	N1856S	Missense_Mutation	SNP	1.00
VAESBJ	CSF3R	E149D	Missense_Mutation	SNP	1.00
VAESBJ	PRDM1	S354N	Missense_Mutation	SNP	0.54
VAESBJ	KMT2D	R1759H	Missense_Mutation	SNP	0.34
VAESBJ	ZFHX3	Q2759H	Missense_Mutation	SNP	0.65
VAESBJ	FYN	S70L	Missense_Mutation	SNP	0.42
VAESBJ	TERT	A1062T	Missense_Mutation	SNP	0.34
VAESBJ	SLX4	M386V	Missense_Mutation	SNP	0.65
VAESBJ	PALB2	L337S	Missense_Mutation	SNP	0.34
VAESBJ	SLX4	L671S	Missense_Mutation	SNP	0.67
VAESBJ	SLX4	R204C	Missense_Mutation	SNP	0.62
VAESBJ	BLM	E1035G	Missense_Mutation	SNP	0.06
VAESBJ	SLX4	A952M	Missense_Mutation	DNP	0.69
VAESBJ	RTEL1	P1058H	Missense_Mutation	SNP	0.46
VAESBJ	YES1	T60A	Missense_Mutation	SNP	0.44
VAESBJ	TNFAIP3	T668N	Missense_Mutation	SNP	0.56
VAESBJ	IRS2	P872L	Missense_Mutation	SNP	0.64
VAESBJ	DAB2	V544I	Missense_Mutation	SNP	0.33
VAESBJ	MTTP	E98D	Missense_Mutation	SNP	1.00
VAESBJ	NSFL1C	D292N	Missense_Mutation	SNP	0.44
VAESBJ	PPP2R3A	A171S	Missense_Mutation	SNP	0.74
VAESBJ	ZNF737	Y369C	Missense_Mutation	SNP	0.33
VAESBJ	NOTCH2NLA	E226Q	Missense_Mutation	SNP	0.05
VAESBJ	SLC16A9	V54I	Missense_Mutation	SNP	0.53
VAESBJ	OR11H2	L235I	Missense_Mutation	SNP	0.12
VAESBJ	NEGR1		DeepDel		
VAESBJ	MTAP		DeepDel		
VAESBJ	CDKN2A		DeepDel		
VAESBJ	CDKN2B		DeepDel		
VAESBJ	SRSF2		AMP		
VAESBJ	RPTOR		AMP		
VAESBJ	DNMT1		DeepDel		
VAESBJ	SMARCB1		DeepDel		
TTC642	TP53	G245S	Missense_Mutation	SNP	0.07
TTC642	SMARCB1	Q182Afs*28	Frame_Shift_Del	DEL	0.98
TTC642	APC	R653=	Splice_Region	SNP	0.49
TTC642	PIK3CA	I391M	Missense_Mutation	SNP	0.50
TTC642	BARD1	L359_P365del	In_Frame_Del	DEL	0.47

TTC642	KMT2D	P2557L	Missense_Mutation	SNP	0.48
TTC642	FOXA1	E269V	Missense_Mutation	SNP	0.50
TTC642	PARP1	S383Y	Missense_Mutation	SNP	0.48
TTC642	DOT1L	A1053T	Missense_Mutation	SNP	0.48
TTC642	NTRK1	R780Q	Missense_Mutation	SNP	0.48
TTC642	PIK3R2	V54M	Missense_Mutation	SNP	0.57
TTC642	MGA	N1982S	Missense_Mutation	SNP	0.48
TTC642	NSD1	M2261T	Missense_Mutation	SNP	0.49
TTC642	POT1	Q301H	Missense_Mutation	SNP	0.47
TTC642	NF1	L1274F	Missense_Mutation	SNP	0.48
TTC642	FLT4	S430A	Missense_Mutation	SNP	0.49
TTC642	EP300	S106G	Missense_Mutation	SNP	0.50
TTC642	NTRK3	N714S	Missense_Mutation	SNP	0.49
TTC642	NUP93	R486C	Missense_Mutation	SNP	0.52
TTC642	NSD1	M2250I	Missense_Mutation	SNP	0.49
TTC642	NSD1	A1036P	Missense_Mutation	SNP	0.50
TTC642	CUL3	V567I	Missense_Mutation	SNP	0.52
TTC642	NSD1	A691T	Missense_Mutation	SNP	0.49
TTC642	PDGFRB	E485K	Missense_Mutation	SNP	0.50
TTC642	ETAA1	M221T	Missense_Mutation	SNP	0.49
TTC642	MGA	C1270R	Missense_Mutation	SNP	0.49
TTC642	ETAA1	G439R	Missense_Mutation	SNP	0.46
TTC642	NSD3	I40T	Missense_Mutation	SNP	0.50
TTC642	EPAS1	A698P	Missense_Mutation	SNP	0.50
TTC642	PPARG	D92Y	Missense_Mutation	SNP	0.48
TTC642	PIK3CB	Y176C	Missense_Mutation	SNP	0.51
TTC642	SETD2	D1211H	Missense_Mutation	SNP	0.49
TTC642	ZNRF3	H327Q	Missense_Mutation	SNP	0.49
TTC642	CARM1	M400I	Missense_Mutation	SNP	0.14
TTC642	GBP3	R290C	Missense_Mutation	SNP	0.55
TTC642	NSFL1C	D292N	Missense_Mutation	SNP	0.47
TTC642	ZNF474	R173H	Missense_Mutation	SNP	0.64
TTC642	ZNF474	L318*	Frame_Shift_Del	DEL	0.51
TTC642	AGAP4	R484C	Missense_Mutation	SNP	0.65
TTC642	FSTL4	E353D	Missense_Mutation	SNP	0.44
TTC642	CDHR5	A607P	Missense_Mutation	SNP	0.23
TTC642	H6PD	L616V	Missense_Mutation	SNP	0.54
TTC642	CDHR5	S585G	Missense_Mutation	SNP	0.24

Supplementary Table S4:

Model	Tumor type	Tumor site	Disease status	TAZ treatment status	Patient ID	Passage re-implanted
HYMAD_EPIS_X0003aS1	Epithelioid sarcoma	Left thigh	Metastasis	Pre	22	P2
HYMAD_EPIS_X0004aS1	Epithelioid sarcoma	Right lung	Metastasis	Post	20	P2
KUNGA_MRT_X0002aS1	Malignant rhabdoid tumor	Left upper quadrant	Metastasis	Pre	25	P2
KUNGA_EPIS_X0002aS1	Epithelioid sarcoma	Right perineal mass	Metastasis	N/A	N/A	P3
SOMWR_EPIS_X00013aS1	Epithelioid sarcoma	Right femoral head	Metastasis	N/A	N/A	P2

Supplementary Table S5

Name	log2FC	DepScore
EWSR1	3.04439	0.43119
IGF2BP1	3.79442	0.39906
ZEB2	4.24793	0.38936
CHMP4B	3.58496	0.34656
THAP11	5.39232	0.33129
EPC2	1.58496	0.3157
BCL11B	1.926	0.29174
H2AFZ	3.2854	0.27754
CTNNBL1	2.10434	0.24023
CFAP20	3.58496	0.22017
TUBB	1.54649	0.20943
UBB	1.66297	0.20943
XRCC5	5.73471	0.20406
ACTL6A	4.70044	0.18647
NAT10	2.45943	0.18411
IPO5	1	0.18251
YBX1	3.87447	0.18173
PUM1	2.58496	0.1716
NUP93	2.65344	0.16954
LARP1	4.39232	0.16636
TRA2B	2.91648	0.16636
TRIM28	3.58496	0.16475
POU3F2	3.58496	0.16042
SRRM2	4.77007	0.15899
SHMT2	2	0.15693
EIF4G1	3.39232	0.1566
LSM8	5.16993	0.1529
POU3F1	3.32193	0.15106

RPS23	6.20945	0.1504
THOC7	5	0.14857
ZBTB2	6.88264	0.14836
RPL22	5.85798	0.14785
NOP56	3.90689	0.14516
HOXC12	2.80735	0.14173
SPTY2D1	2	0.14049
CUL3	3.70044	0.13967
RBM10	4.78136	0.13707
FUS	2.06609	0.13704
CDC40	5.61471	0.13516
JPH1	3.9542	0.13185
CDC23	2	0.13031
LSM7	2	0.12921
LIG3	6.70044	0.12882
CHTOP	6.83289	0.12772
MX2	1.80735	0.12763
RFC1	2.80735	0.12757
HNRNPH3	4.88264	0.12649
SUB1	1	0.12539
YBX3	4.32193	0.1206
RUVBL2	4.14296	0.11889
TOP2A	2	0.11725
PRPF19	3.92376	0.11686
OTX2	6.39232	0.11604
NUDT21	5.64386	0.11591
RBM4	3.90689	0.11577
METTL14	2.58496	0.11304
FNBP4	2.32193	0.11261
BANF1	5.32193	0.11227
HIST1H1D	6.16993	0.11205
CWC22	3.49185	0.11118
PCID2	4.80735	0.10705
EPB41L5	2	0.10633
DYNLL1	3.54432	0.10437
IGF2BP2	6.24793	0.10425
TMPO	4.52356	0.10351
PABPC1	4.76553	0.10349
SEH1L	4.32193	0.10278
KMT2C	1	0.10228
ACIN1	3.79494	0.10224

TRRAP	2.77259	0.10223
WDR33	6.70044	0.10203
AEBP2	1.58496	0.10202
DHX15	4.152	0.10126
ZNF629	1.22239	0.10056
FIP1L1	5.45943	0.09995
SRSF7	2.02237	0.09963
PDHA2	5.45943	0.09881
PNKP	5.52356	0.09854
BANP	3	0.09852
HDAC2	6.04439	0.09811
HIST2H2BE	3.09192	0.09715
WRAP53	3	0.09589
RPL4	3.65344	0.09575
RPL3	4.81378	0.09507
AHDC1	2.58496	0.09465
HMGA2	2.58496	0.09333
SSBP4	4.16993	0.09315
RBM8A	3.02237	0.09312
TFCP2L1	2.58496	0.09119
PSPC1	3	0.09092
DHX9	1.68684	0.09089
VDAC2	2	0.09088
PPIG	7.02237	0.09015
EDC4	2.58496	0.08998
HNRNPH1	2.12383	0.08974
HOXD13	4	0.08895
G3BP1	4.16993	0.08801
SENP1	5	0.08724
TAF8	4.80735	0.08701
EBF3	2.32193	0.08618
RPS25	5	0.08612
ELL	3	0.08551
PELP1	4.97728	0.08516
WDR5	5.08746	0.0848
PPWD1	3.32193	0.08439
RBM14	3.98706	0.08316
PHF3	2.58496	0.08203
HNRNPUL2	2.558	0.08176
TRMT10C	2.58496	0.0813
STK3	1.80735	0.08092

NPM1	3.20043	0.08068
HIST1H2BN	2.98272	0.07869
KPNA1	3.58496	0.07828
WIZ	2	0.07823
SCAF4	4.32193	0.07737
TFCP2	7.06609	0.07724
ISY1	4.90689	0.07647
ERH	2.66985	0.07437
RPL7A	5.79442	0.07374
CAV2	3.32193	0.07269
TAF1	3.52356	0.07237
HNRNPC	1.87294	0.07149
ZMYM3	1.80735	0.06972
CLASRP	2.32193	0.06961
PABPC3	3.71882	0.06929
CDC5L	5.29278	0.06929
IGF2BP3	7.06609	0.06925
TERF2	2	0.06894
THOC3	5.80735	0.0674
CENPV	3.80735	0.06595
SNRNP70	3.88264	0.06552
RRP12	6.70044	0.06406
SNW1	4.41785	0.06398
CPSF2	4.75489	0.06382
XPO1	2.58496	0.06376
RPS24	4.70044	0.06331
EIF4A3	3.99247	0.06299
MED1	2	0.06289
ZNF639	3	0.06262
RPS29	3.58496	0.06226
PTPN14	3	0.06179
YWHAZ	2	0.06157
DDX46	2	0.061
HIST1H1C	6.2854	0.05982
SRSF11	3.12928	0.05981
PPIH	3.58496	0.05948
TUBA1A	1.29399	0.05944
LSM5	3.58496	0.05944
RBM5	4.45943	0.05943
EEF2	4.90689	0.0591
POLDIP3	6.67243	0.05832

JARID2	4	0.05827
HNRNPA3	4.00643	0.05793
RPS14	3.16993	0.05754
CSTF3	2.5025	0.05702
RPS26	6	0.05699
RPL36	5.58496	0.05697
SNRPC	3.58496	0.05651
SALL1	4.58496	0.05642
POLR2H	2.58496	0.05633
PCBP1	3.67243	0.05556
RBBP4	6.37504	0.05477
IK	4.05889	0.0547
HIST1H2BD	2.98272	0.05461
PLRG1	5.59991	0.05455
ZMYND8	1	0.0545
CHD4	4.2854	0.05435
RAVER1	4	0.05406
DDX39B	6.85798	0.05364
HNRNPM	2.13034	0.05342
PPHLN1	3.39232	0.05302
CPSF3	5.64386	0.05243
H2AFV	3.2854	0.05174
TAF7	5.32193	0.05137
SRSF5	3.14684	0.05097
GAPDH	1.66297	0.0509
PRDM10	1	0.05075
SREK1	4.45943	0.05057
POLR2B	1	0.05054
NOL11	2.58496	0.05025
RPS10	2	0.04973
DKC1	5.52356	0.04882
CBLL1	6.97728	0.04873
RBM11	2	0.04864
SF3B3	2.89224	0.04808
DDX1	3.32193	0.04702
EED	2.58496	0.04665
TERF2IP	1	0.04484
ZIC2	4.70044	0.04419
CEBPG	5.08746	0.04387
KIF14	2	0.04317
ZNF768	3	0.04306

NIP7	3	0.04266
PRPF40B	2.58496	0.04265
GPATCH4	3.24793	0.04251
RUVBL1	5.64386	0.04223
AK9	2	0.04162
LSM3	5.24793	0.04152
NR2F1	2.90689	0.04118
TBPL2	3.32193	0.04076
TFAP2B	3.32193	0.04042
HIST1H1B	5.35755	0.03912
PHF5A	4.45943	0.03884
INTS5	4	0.03817
ZNF384	3.32193	0.0381
TEX10	6.12928	0.03792
METTL3	2.58496	0.03773
NOLC1	2.38466	0.03769
RIF1	2.52356	0.03765
MTA1	6.55459	0.03756
ILF3	3.16168	0.03744
LSM4	5.16993	0.03709
RSBN1	1.32193	0.03618
LUC7L3	3.08746	0.03607
SRSF6	3.34147	0.03589
COIL	2	0.03584
DDX6	3.43539	0.03563
KIF2A	1	0.03488
GPATCH8	3.22239	0.03476
TP53BP1	2.58496	0.03472
TOP1	3	0.03444
U2SURP	4.53605	0.03424
GTF3C2	5.45943	0.03382
POGZ	3	0.03337
SNRPN	2.32193	0.03282
DHX30	4.98868	0.03242
ATF6	4.16993	0.03221
GTF2I	3.28011	0.03157
DNAJA3	3.64386	0.03146
VDAC1	2.58496	0.03139
PATZ1	2.58496	0.0313
TIMM50	4.32193	0.0312
HIST1H2BO	3.09192	0.03117

TRA2A	7.65821	0.03098
NXF1	4.02237	0.03085
THOC2	4.89077	0.03053
RPL23	2.65208	0.03028
RBBP5	3.80735	0.02895
SAFB	3.26679	0.02854
PRPF38A	4.45943	0.02847
SEC13	5.39232	0.02779
CLK3	4	0.02751
NKX2-1	3	0.02739
TBL1XR1	2.58496	0.02735
NUP62	4.36457	0.02701
ZKSCAN2	2.58496	0.02659
BEND3	2	0.02652
ARNT	1	0.0265
CDK13	3.70044	0.02633
SUPT16H	2.90689	0.02585
NUP85	2.96963	0.02581
HCFC1	1.38702	0.02566
RPS27A	1.66297	0.02549
H2AFY2	6.49185	0.02533
THOC6	4.88264	0.02512
ARID1B	1.58496	0.02508
NUP160	3.47393	0.02502
ZNF326	6	0.02468
RPS3A	5.44294	0.02467
NUP155	4.17792	0.02461
CREM	4.16993	0.02436
H2AFX	2.26303	0.02385
NOP16	3.32193	0.02368
XRCC1	5.12928	0.02357
RPS5	3.04439	0.02352
MRPS18B	4	0.02347
MYEF2	5.02975	0.02346
RPL36AL	5.24793	0.02316
LUC7L	5.08746	0.02289
ING1	1	0.0227
ZFC3H1	1	0.02269
TIMM44	3.32193	0.02243
MARS	1	0.02202
AFF4	2.18763	0.02149

ATF7	4	0.02132
RBM27	5.57289	0.02109
UBAP2L	3.32193	0.02104
RALYL	1.26303	0.02057
CCT4	2	0.01999
LYAR	5.18982	0.01975
SLC25A11	2.77259	0.01975
NKTR	5.16993	0.01969
H1FX	6.67243	0.0194
SRSF10	3.80735	0.0193
DHCR7	4.70044	0.0184
RPS6	1.62803	0.01793
MTA3	5.64386	0.01785
ILF2	3.5025	0.0175
SRSF9	7.89482	0.01745
PNN	4.19265	0.0172
LRPPRC	2.65208	0.01718
RPS17	5.64386	0.01712
EEF1G	1.58496	0.01661
CLK2	3.70044	0.0165
HIST1H2BM	2.98272	0.01642
SNRNP40	4.36457	0.01626
MAZ	4.16993	0.01601
MLLT1	4.32193	0.01573
RFC5	1.80735	0.01567
SF3A2	3.60486	0.01535
CHD5	2.45943	0.01535
CDK9	2	0.01528
CDC73	5.24793	0.01491
HNRNPK	2.14359	0.01457
RPS12	3.85798	0.01457
PKP4	1.152	0.01449
DHX35	2.58496	0.01444
SNRPB	2.32193	0.01399
NUP54	3.76717	0.01391
TAF9B	3	0.01379
PCF11	4.87447	0.01352
RPS8	5.90689	0.01328
DHX16	2.58496	0.01308
LBR	2.39232	0.01303
GPATCH1	2	0.0128

DDX55	2	0.01278
HNRNPLL	1.848	0.01273
XRCC6	7.90689	0.01269
SCAF8	3.24793	0.01236
AHCTF1	2.58496	0.01216
MFAP1	4.14296	0.01192
PSIP1	3.32193	0.01159
RSL1D1	6.14975	0.01136
FUBP3	1.70044	0.01132
PHB2	2.25987	0.0113
EEF1A1	1.19068	0.01082
SHROOM4	2.41504	0.01038
CHMP2A	3	0.01037
ARL6IP4	1	0.01026
RBM26	6.72792	0.01015
WDR18	5.9542	0.01003
NCBP2	5.32193	0.00986
PDS5B	3.56071	0.00976
HIST1H2BL	2.98272	0.00953
SRPK1	3.58496	0.00897
TUBB4A	1.87447	0.00875
HIST1H2BK	2.98272	0.00858
NOL9	5.16993	0.00847
TUBB2A	1.47294	0.00825
NFIB	6.12928	0.00804
VDAC3	1.58496	0.00793
ZMYM2	2.58496	0.00782
TRERF1	2	0.00777
PRMT1	4.32193	0.00769
CDK12	2.58496	0.00753
ZFHX3	2.87447	0.00749
SYNCRIP	3.36457	0.00747
GTF3C1	2.70044	0.00732
HNRNPL	1.78499	0.00728
HIST1H2BC	2.98272	0.00727
APTX	3.58496	0.00685
OSBPL8	3.32193	0.00668
RPS2	7.06609	0.00665
NDUFS2	1	0.00657
RBM15B	4.41504	0.00654
SAP30BP	1.58496	0.00653

NUP214	4.28951	0.00618
RBBP6	4.24793	0.00576
YTHDF2	2	0.00563
UTP15	1	0.00557
TAF6	4.16993	0.00551
SRSF12	3.55459	0.00539
RPL26	5.55459	0.00535
RBMX	2	0.00531
HIST1H2AD	1.87447	0.00529
SNRPA	3.60881	0.00523
BCKDHB	3.58496	0.00449
STRBP	4.96963	0.00442
TBP	3.32193	0.00437
UBL5	3.58496	0.00425
KANK1	2.45943	0.00421
RING1	1	0.00404
HIST2H2AB	2.03242	0.00402
MECP2	1	0.00396
HIST1H4A	3.39232	0.00353
HSPA6	1.54057	0.00307
ELAVL1	4.24793	0.00254
GTF3C4	3.39232	0.00251
SLC25A6	1.1635	0.00219
SNRPB2	1.48543	0.00205
HMG20A	2	0.00199
NDC1	5.18982	0.00192
RPL15	3.88753	0.00185
RBM22	6.37504	0.00173
MTA2	6.17991	0.00169
NOP58	6.39232	0.00164
CHMP2B	1	0.00126
ZFR	4.23266	9.76E-04
TUBB6	1.22239	8.93E-04
KHDRBS3	3.4021	8.50E-04
UTP20	3.32193	6.67E-04
KPNB1	3.35755	6.07E-04
CDC27	2.80735	3.27E-04
SNRPD2	2.35548	3.11E-04

Supplementary Table S6: List of EwS interference peptides

Peptide	Sequence
Breakpoint_S	SSYGQQNPSYDSVRR
Breakpoint_M	QAPSQYSQQSSSYGQQNPSYDSVRRGAWGNNMNSG
Breakpoint_L	QPPTSYPPQTGSYSQAPSQYSQQSSSYGQQNPSYDSVRRGAWGNNMNSGLNKSPPLGGAQ
Breakpoint_WT	QPPTSYPPQTGSYSQAPSQYSQQSSSYGQQSSFRQDHPSSMGVYGQESGGFSGPGENRSMSGPDNRGRGRGGFDRGGMSRGGRGGGRGGMGAGERGG
EWS_5	SYGQQSSYGQQSSYGQQPPTSYPPQTGSYSQAPSQYSQQSSSYGQQ
EWS_7	YPQVPGSYPMQPVTAPPSYPPTSYSSTQPTSYDQSSYSQQNTYGQPSSYGQQSSYGQQSSYGQQPPTSYPPQTGSYSQAPSQYSQQSSSYGQQ
EWS_10	SYAAQSAYGTQPAYPAYGQQPAATAPTRPQDGNKPTETSQPQSSTGGYNQPSLGYGQSNYSYPQVPGSYPMQPVTAPPSYPPTSYSSTQPTSYDQSSYSQQNTYGQPSSYGQQSSSYGQQSSYGQQPPTSYPPQTGSYSQAPSQYSQQSSSYGQQ
EWS_12	TYGQTAYATSYGQPPTVEGTSTGYTTPTAPQAYSQPVQGYGTGAYDTTTATVTTTQASYAAQSAYGTQPAYPAYGQQPAATAPTRPQDGNKPTETSQPQSSTGGYNQPSLGYGQSNYSYPQVPGSYPMQPVTAPPSYPPTSYSSTQPTSYDQSSYSQQNTYGQPSSYGQQSSSYGQQSSYGQQPPTSYPPQTGSYSQAPSQYSQQSSSYGQQ
EWS_14	MASTDYSTYSQAAAQQGYSAYTAQPTQGYAQTTQAYGQQSYGTYGQPTDVSYTQAQTTATYGQTAYATSYGQPPTVEGTSTGYTTPTAPQAYSQPVQGYGTGAYDTTTATVTTTQASYAAQSAYGTQPAYPAYGQQPAATAPTRPQDGNKPTETSQPQSSTGGYNQPSLGYGQSNYSYPQVPGSYPMQPVTAPPSYPPTSYSSTQPTSYDQSSYSQQNTYGQPSSYGQQSSSYGQQSSYGQQPPTSYPPQTGSYSQAPSQYSQQSSSYGQQ

Supplementary Table S7: List of EwS peptide interference plasmids

Plasmid	Insert
Affimer Empty_scaffold_N-term	MIPPKKKRKVGLSEAKPATPEIQEIVDKVKPQLEEKTNETYGKLEAVQYKTQVDAGTNYYIKVRAGDNKYMHLKVFKSLPGQNEDLVLTGYQVDKNKDDELTGFFEYPYDVPDYA
Affimer Empty_scaffold_Intra	MIPWGLSEAKPATPEIQEIVDKVKPQLEEKTNETYGKLEAVQYKTQVDAGTNYYIKVRAGDNKYMHLKVFPKKKRKVPGQNEDLVLTGYQVDKNKDDELTGFFEYPYDVPDYA
Affimer Breakpoint_S_N-term	MIPSSYGQQNPSYDSVRRPKKKRKVGLSEAKPATPEIQEIVDKVKPQLEEKTNETYGKLEAVQYKTQVDAGTNYYIKVRAGDNKYMHLKVFKSLPGQNEDLVLTGYQVDKNKDDELTGFFEYPYDVPDYA
Affimer Breakpoint_S_Intra	MIPWGLSEAKPATPEIQEIVDKVKPQLEEKTNETYGKLEAVQYKTQVDAGTNYYIKVRAGDNKYMHLKVFSSYGQQNPSYDSVRRPKKKRKVPGQNEDLVLTGYQVDKNKDDELTGFFEYPYDVPDYA
Affimer Breakpoint_M_N-term	MIPQAPSQYSQQSSSYGQQNPSYDSVRRGAWGNNMNSGPKKKRKVGLSEAKPATPEIQEIVDKVKPQLEEKTNETYGKLEAVQYKTQVDAGTNYYIKVRAGDNKYMHLKVFKSLPGQNEDLVLTGYQVDKNKDDELTGFFEYPYDVPDYA
Affimer Breakpoint_M_Intra	MIPWGLSEAKPATPEIQEIVDKVKPQLEEKTNETYGKLEAVQYKTQVDAGTNYYIKVRAGDNKYMHLKVFQAPSQYSQQSSSYGQQNPSYDSVRRGAWGNNMNSGPKKKRKVPGQNEDLVLTGYQVDKNKDDELTGFFEYPYDVPDYA
Affimer Breakpoint_L_N-term	MIPQPPTSYPPQTGSYSQAPSQYSQQSSSYGQQNPSYDSVRRGAWGNNMNSGLNKSPPLGGAQPKKKRKVGLSEAKPATPEIQEIVDKVKPQLEEKTNETYGKLEAVQYKTQVDAGTNYYIKVRAGDNKYMHLKVFKSLPGQNEDLVLTGYQVDKNKDDELTGFFEYPYDVPDYA
Affimer Breakpoint_WT_N-term	MIPQPPTSYPPQTGSYSQAPSQYSQQSSSYGQQSSFRQDHPSSMGVYGQESGGFSGPGENRSMSGPDNRGRGRGGFDRGGMSRGGRGGGRGGMGAGERGGPKKKRKVGLSEAKPATPEIQEIVDKVKPQLEEKTNETYGKLEAVQYKTQVDAGTNYYIKVRAGDNKYMHLKVFKSLPGQNEDLVLTGYQVDKNKDDELTGFFEYPYDVPD
Affimer Breakpoint_WT_Intra	MIPWGLSEAKPATPEIQEIVDKVKPQLEEKTNETYGKLEAVQYKTQVDAGTNYYIKVRAGDNKYMHLKVFQPPTSYPPQTGSYSQAPSQYSQQSSSYGQQSSFRQDHPSSMGVYGQESGGFSGPGENRSMSGPDNRGRGRGGFDRGGMSRGGRGGGRGGMGAGERGGPKKKRKVPGQNEDLVLTGYQVDKNKDDELTGFFEYPYDVPD
Affimer EWS_5_N-term	MIPSYGQQSSYGQQSSYGQQPPTSYPPQTGSYSQAPSQYSQQSSSYGQQPKKKRKVGLSEAKPATPEIQEIVDKVKPQLEEKTNETYGKLEAVQYKTQVDAGTNYYIKVRAGDNKYMHLKVFKSLPGQNEDLVLTGYQVDKNKDDELTGFFEYPYDVPDYA

Affimer EWS_5_Intra	MIPWGLSEAKPATPEIQEIVDKVKPQLEEKTNETYGKLEAVQYKTQVDAGTNYYIKVRAGDNKYMHLKVFSYGQQSSYGQQSSYGQQPPTSYPPQTGSYSQAPSQYSQQSSSYGQQPKKKRKVPGQNEDLVLTGYQVDKNKDDELTGFFEYPYDVPDY
Affimer EWS_7_N-term	MIPYPQVPGSYPMQPVTAPPSYPPTSYSSTQPTSYDQSSYSQQNTYGQPSSYGQQSSYGQQSSYGQQPPTSYPPQTGSYSQAPSQYSQQSSSYGQQPKKKRKVGLSEAKPATPEIQEIVDKVKPQLEEKTNETYGKLEAVQYKTQVDAGTNYYIKVRAGDNKYMHLKVFKSLPGQNEDLVLTGYQVDKNKDDELTGFFEYPYDVPD
Affimer EWS_7_Intra	MIPWGLSEAKPATPEIQEIVDKVKPQLEEKTNETYGKLEAVQYKTQVDAGTNYYIKVRAGDNKYMHLKVFYPQVPGSYPMQPVTAPPSYPPTSYSSTQPTSYDQSSYSQQNTYGQPSSYGQQSSYGQQSSYGQQPPTSYPPQTGSYSQAPSQYSQQSSSYGQQPKKKRKVPGQNEDLVLTGYQVDKNKDDELTGFFEYPYDVPDYA
Affimer EWS_10_N-term	MIPSYAAQSAYGTQPAYPAYGQQPAATAPTRPQDGNKPTETSQPQSSTGGYNQPSLGYGQSNYSYPQVPGSYPMQPVTAPPSYPPTSYSSTQPTSYDQSSYSQQNTYGQPSSYGQQSSYGQQSSYGQQPPTSYPPQTGSYSQAPSQYSQQSSSYGQQPKKKRKVGLSEAKPATPEIQEIVDKVKPQLEEKTNETYGKLEAVQYKTQVDAGTNYYIKVRAGDNKYMHLKVFKSLPGQNEDLVLTGYQVDKNKDDELTGFFEYPYDVPDYA
Affimer EWS_10_Intra	MIPWGLSEAKPATPEIQEIVDKVKPQLEEKTNETYGKLEAVQYKTQVDAGTNYYIKVRAGDNKYMHLKVFSYAAQSAYGTQPAYPAYGQQPAATAPTRPQDGNKPTETSQPQSSTGGYNQPSLGYGQSNYSYPQVPGSYPMQPVTAPPSYPPTSYSSTQPTSYDQSSYSQQNTYGQPSSYGQQSSYGQQSSYGQQPPTSYPPQTGSYSQAPSQYSQQSSSYGQQPKKKRKVPGQNEDLVLTGYQVDKNKDDELTGFFEYPYDVP
Affimer EWS_12_N-term	MIPTYGQTAYATSYGQPPTVEGTSTGYTTPTAPQAYSQPVQGYGTGAYDTTTATVTTTQASYAAQSAYGTQPAYPAYGQQPAATAPTRPQDGNKPTETSQPQSSTGGYNQPSLGYGQSNYSYPQVPGSYPMQPVTAPPSYPPTSYSSTQPTSYDQSSYSQQNTYGQPSSYGQQSSYGQQSSYGQQPPTSYPPQTGSYSQAPSQYSQQSSSYGQQPKKKRKVGLSEAKPATPEIQEIVDKVKPQLEEKTNETYGKLEAVQYKTQVDAGTNYYIKVRAGDNKYMHLKVFKSLPGQNEDLVLTGYQVDKNKDDELTGFFEYPYDVPDYA
Affimer EWS_12_Intra	MIPWGLSEAKPATPEIQEIVDKVKPQLEEKTNETYGKLEAVQYKTQVDAGTNYYIKVRAGDNKYMHLKVFTYGQTAYATSYGQPPTVEGTSTGYTTPTAPQAYSQPVQGYGTGAYDTTTATVTTTQASYAAQSAYGTQPAYPAYGQQPAATAPTRPQDGNKPTETSQPQSSTGGYNQPSLGYGQSNYSYPQVPGSYPMQPVTAPPSYPPTSYSSTQPTSYDQSSYSQQNTYGQPSSYGQQSSYGQQSSYGQQPPTSYPPQTGSYSQAPSQYSQQSSSYGQQPKKKRKVPGQNEDLVLTGYQVDKNKDDELTGFFEYPYDVPDYA
Affimer EWS_14_N-term	MIPMASTDYSTYSQAAAQQGYSAYTAQPTQGYAQTTQAYGQQSYGTYGQPTDVSYTQAQTTATYGQTAYATSYGQPPTVEGTSTGYTTPTAPQAYSQPVQGYGTGAYDTTTATVTTTQASYAAQSAYGTQPAYPAYGQQPAATAPTRPQDGNKPTETSQPQSSTGGYNQPSLGYGQSNYSYPQVPGSYPMQPVTAPPSYPPTSYSSTQPTSYDQSSYSQQNTYGQPSSYGQQSSYGQQSSYGQQPPTSYPPQTGSYSQAPSQYSQQSSSYGQQPKKKRKVGLSEAKPATPEIQEIVDKVKPQLEEKTNETYGKLEAVQYKTQVDAGTNYYIKVRAGDNKYMHLKVFKSLPGQNEDLVLTGYQVDKNKDDELTGFFEYPYDVPDYA
Affimer EWS_14_Intra	MIPWGLSEAKPATPEIQEIVDKVKPQLEEKTNETYGKLEAVQYKTQVDAGTNYYIKVRAGDNKYMHLKVFMASTDYSTYSQAAAQQGYSAYTAQPTQGYAQTTQAYGQQSYGTYGQPTDVSYTQAQTTATYGQTAYATSYGQPPTVEGTSTGYTTPTAPQAYSQPVQGYGTGAYDTTTATVTTTQASYAAQSAYGTQPAYPAYGQQPAATAPTRPQDGNKPTETSQPQSSTGGYNQPSLGYGQSNYSYPQVPGSYPMQPVTAPPSYPPTSYSSTQPTSYDQSSYSQQNTYGQPSSYGQQSSYGQQSSYGQQPPTSYPPQTGSYSQAPSQYSQQSSSYGQQPKKKRKVPGQNEDLVLTGYQVDKNKDDELTGFFEYPYDVPD
EWS_FL	MASTDYSTYSQAAAQQGYSAYTAQPTQGYAQTTQAYGQQSYGTYGQPTDVSYTQAQTTATYGQTAYATSYGQPPTVEGTSTGYTTPTAPQAYSQPVQGYGTGAYDTTTATVTTTQASYAAQSAYGTQPAYPAYGQQPAATAPTRPQDGNKPTETSQPQSSTGGYNQPSLGYGQSNYSYPQVPGSYPMQPVTAPPSYPPTSYSSTQPTSYDQSSYSQQNTYGQPSSYGQQSSYGQQSSYGQQPPTSYPPQTGSYSQAPSQYSQQSSSYGQQSSFRQDHPSSMGVYGQESGGFSGPGENRSMSGPDNRGRGRGGFDRGGMSRGGRGGGRGGMGAGERGGFNKPGGPMDEGPDLDLGPPVDPDEDSDNSAIYVQGLNDSVTLDDLADFFKQCGVVKMNKRTGQPMIHIYLDKETGKPKGDATVSYEDPPTAKAAVEWFDGKDFQGSKLKVSLARKKPPMNSMRGGLPPREGRGMPPPLRGGPGGPGGPGGPMGRMGGRGGDRGGFPPRGPRGSRGNPSGGGNVQHRAGDWQCPNPGCGNQNFAWRTECNQCKAPKPEGFLPPPFPPPGGDRGRGGPGGMRGGRGGLMDRGGPGGMFRGGRGGDRGGFRGGRGMDRGGFGGGRRGGPGGPPGPLMEQMGGRRGGRGGPGKMDKGEHRQERRDRPYPKKKRKVFEYPYDVPDYA
SS18	MSVAFAAPRQRGKGEITPAAIQKMLDDNNHLIQCIMDSQNKGKTSECSQYQQMLHTNLVYLATIADSNQNMQSLLPAPPTQNMPMGPGGMNQSGPPPPPRSHNMPSDGMVGGGPPAPHMQNQMNGQMPGPNHMPMQGPGPNQLNMTNSSMNMPSSSHGSMGGYNHSVPSSQSMPVQNQMTMSQGQPMGNYGPRPNMSMQPNQGPMMHQQPPSQQYNMPQGGGQHYQGQQPPMGMMGQVNQGNHMMGQRQIPPYRPPQQGPPQQYSGQEDYYGDQYSHGGQGPPEGMNQQYYPDGHNDYGYQQPSYPEQGYDRPYEDSSQHYYEGGNSQYGQQQDAYQGPPPQQGYPPQQQQYPGQQGYPGQQQGYGPSQGGPGPQYPNYPQGQGQQYGGYRPTQPGPPQPPQQRPYGYDQGQYGNYQQPKKKRKVFEYPYDVPDYA

SS18-SSX	MSVAFAAPRQRGKGEITPAAIQKMLDDNNHLIQCIMDSQNKGKTSECSQYQQMLHTNL VYLATIADSNQNMQSLLPAPPTQNMPMGPGGMNQSGPPPPPRSHNMPSDGMVGGG PPAPHMQNQMNGQMPGPNHMPMQGPGPNQLNMTNSSMNMPSSSHGSMGGYNHS VPSSQSMPVQNQMTMSQGQPMGNYGPRPNMSMQPNQGPMMHQQPPSQQYNMPQ GGGQHYQGQQPPMGMMGQVNQGNHMMGQRQIPPYRPPQQGPPQQYSGQEDYYG DQYSHGGQGPPEGMNQQYYPDGHNDYGYQQPSYPEQGYDRPYEDSSQHYYEGGN SQYGQQQDAYQGPPPQQGYPPQQQQYPGQQGYPGQQQGYGPSQGGPGPQYPNY PQGQGQQYGGYRPTQPGPPQPPQQRPYGYDQIMPKKPAEDENDSKGVSEASGPQN DGKQLHPPGKANISEKINKRSGPKRGKHAWTHRLRERKQLVIYEEISDPEEDDEPKKK RKVFEYPYDVPDYA
RadA_Breakpoint_L	MATIGRISTGSKSLDKLLGGGIETQAITEVFGEFGSGATQLAHTLAVMVQLPPEEGGLN GSVIWIDTENTFRPERIREIAQNRGLDPDEVLKHIYVARAFNSNHQMLLVQQAEDKIKEL LNTDRPVKLLIVDSLTSHFRSEYIGRGALAERQQKLAKHLADLHRLANLYDIAVFVTNQV QASGGGGSQPPTSYPPQTGSYSQAPSQYSQQSSSYGQQNPSYDSVRRGAWGNNM NSGLNKSPPLGGAQSGGGGSGHILAHSATLRVYLRKGKGGKRIARLIDAPHLPEGEAV FSITEKGIEDPKKKRKVFEYPYDVPDYA
RadA_3xNLS_linker	MAPAAKKKKLDGSMATIGRISTGSKSLDKLLGGGIETQAITEVFGEFGSGATQLAHTLA VMVQLPPEEGGLNGSVIWIDTENTFRPERIREIAQNRGLDPDEVLKHIYVARAFNSNHQ MLLVQQAEDKIKELLNTDRPVKLLIVDSLTSHFRSEYIGRGALAERQQKLAKHLADLHRL ANLYDIAVFVTNQVQASGGGGSSGGGGSGHILAHSATLRVYLRKGKGGKRIARLIDAP HLPEGEAVFSITEKGIEDGSPKKKRKVGSGSKRPAATKKAGQAKKKKFEYPYDVPDYA FEYPYDVPDYA
RadA_3xNLS_Breakpoint_ L_C-term	MAPAAKKKKLDGSMATIGRISTGSKSLDKLLGGGIETQAITEVFGEFGSGATQLAHTLA VMVQLPPEEGGLNGSVIWIDTENTFRPERIREIAQNRGLDPDEVLKHIYVARAFNSNHQ MLLVQQAEDKIKELLNTDRPVKLLIVDSLTSHFRSEYIGRGALAERQQKLAKHLADLHRL ANLYDIAVFVTNQVQASGGGGSSGGGGSGHILAHSATLRVYLRKGKGGKRIARLIDAP HLPEGEAVFSITEKGIEDQPPTSYPPQTGSYSQAPSQYSQQSSSYGQQNPSYDSVRR GAWGNNMNSGLNKSPPLGGAQGSPKKKRKVGSGSKRPAATKKAGQAKKKKFEYPYD VPDYAFEYPYDVPDYA
RadA_3xNLS_Breakpoint_ L_Intra	MAPAAKKKKLDGSMATIGRISTGSKSLDKLLGGGIETQAITEVFGEFGSGATQLAHTLA VMVQLPPEEGGLNGSVIWIDTENTFRPERIREIAQNRGLDPDEVLKHIYVARAFNSNHQ MLLVQQAEDKIKELLNTDRPVKLLIVDSLTSHFRSEYIGRGALAERQQKLAKHLADLHRL ANLYDIAVFVTNQVQASGGGGSQPPTSYPPQTGSYSQAPSQYSQQSSSYGQQNPSY DSVRRGAWGNNMNSGLNKSPPLGGAQSGGGGSGHILAHSATLRVYLRKGKGGKRIA RLIDAPHLPEGEAVFSITEKGIEDGSPKKKRKVGSGSKRPAATKKAGQAKKKKFEYPYD VPDYAFEYPYDVPDYA
RadA_3xNLS_Breakpoint_ WT_C-term	MAPAAKKKKLDGSMATIGRISTGSKSLDKLLGGGIETQAITEVFGEFGSGATQLAHTLA VMVQLPPEEGGLNGSVIWIDTENTFRPERIREIAQNRGLDPDEVLKHIYVARAFNSNHQ MLLVQQAEDKIKELLNTDRPVKLLIVDSLTSHFRSEYIGRGALAERQQKLAKHLADLHRL ANLYDIAVFVTNQVQASGGGGSSGGGGSGHILAHSATLRVYLRKGKGGKRIARLIDAP HLPEGEAVFSITEKGIEDQPPTSYPPQTGSYSQAPSQYSQQSSSYGQQSSFRQDHPS SMGVYGQESGGFSGPGENRSMSGPDNRGRGRGGFDRGGMSRGGRGGGRGGMGA GERGGGSPKKKRKVGSGSKRPAATKKAGQAKKKKFEYPYDVPDYAFEYPYDVPDYA
RadA_3xNLS_Breakpoint_ WT_Intra	MAPAAKKKKLDGSMATIGRISTGSKSLDKLLGGGIETQAITEVFGEFGSGATQLAHTLA VMVQLPPEEGGLNGSVIWIDTENTFRPERIREIAQNRGLDPDEVLKHIYVARAFNSNHQ MLLVQQAEDKIKELLNTDRPVKLLIVDSLTSHFRSEYIGRGALAERQQKLAKHLADLHRL ANLYDIAVFVTNQVQASGGGGSQPPTSYPPQTGSYSQAPSQYSQQSSSYGQQSSFR QDHPSSMGVYGQESGGFSGPGENRSMSGPDNRGRGRGGFDRGGMSRGGRGGGR GGMGAGERGGSGGGGSGHILAHSATLRVYLRKGKGGKRIARLIDAPHLPEGEAVFSIT EKGIEDGSPKKKRKVGSGSKRPAATKKAGQAKKKKFEYPYDVPDYAFEYPYDVPDYA

BIBLIOGRAPHY

1. Armitage P, Doll R. The age distribution of cancer and a multi-stage theory of carcinogenesis. British Journal of Cancer. 2004;91(12):1983-9.
2. Steliarova-Foucher E, Colombet M, Ries LAG, Moreno F, Dolya A, Bray F, et al. International incidence of childhood cancer, 2001-10: a population-based registry study. Lancet Oncol. 2017;18(6):719-31.
3. Sweet-Cordero EA, Biegel JA. The genomic landscape of pediatric cancers: Implications for diagnosis and treatment. Science. 2019;363(6432):1170-5.
4. Mody RJ, Wu YM, Lonigro RJ, Cao X, Roychowdhury S, Vats P, et al. Integrative Clinical Sequencing in the Management of Refractory or Relapsed Cancer in Youth. Jama. 2015;314(9):913-25.
5. Parsons DW, Roy A, Yang Y, Wang T, Scollon S, Bergstrom K, et al. Diagnostic Yield of Clinical Tumor and Germline Whole-Exome Sequencing for Children With Solid Tumors. JAMA Oncol. 2016;2(5):616-24.
6. Ripperger T, Bielack SS, Borkhardt A, Brecht IB, Burkhardt B, Calaminus G, et al. Childhood cancer predisposition syndromes-A concise review and recommendations by the Cancer Predisposition Working Group of the Society for Pediatric Oncology and Hematology. Am J Med Genet A. 2017;173(4):1017-37.
7. Kentsis A. Why do young people get cancer? Pediatr Blood Cancer. 2020;67(7):e28335.
8. Lawrence MS, Stojanov P, Polak P, Kryukov GV, Cibulskis K, Sivachenko A, et al. Mutational heterogeneity in cancer and the search for new cancer-associated genes. Nature. 2013;499(7457):214-8.
9. Campbell BB, Light N, Fabrizio D, Zatzman M, Fuligni F, de Borja R, et al. Comprehensive Analysis of Hypermutation in Human Cancer. Cell. 2017;171(5):1042-56.e10.
10. DuBois SG, Corson LB, Stegmaier K, Janeway KA. Ushering in the next generation of precision trials for pediatric cancer. Science. 2019;363(6432):1175-81.
11. Gröbner SN, Worst BC, Weischenfeldt J, Buchhalter I, Kleinheinz K, Rudneva VA, et al. The landscape of genomic alterations across childhood cancers. Nature. 2018;555(7696):321-7.
12. Mertens F, Johansson B, Fioretos T, Mitelman F. The emerging complexity of gene fusions in cancer. Nat Rev Cancer. 2015;15(6):371-81.
13. Burdach SEG, Westhoff MA, Steinhauser MF, Debatin KM. Precision medicine in pediatric oncology. Mol Cell Pediatr. 2018;5(1):6.
14. Hanahan D, Weinberg Robert A. Hallmarks of Cancer: The Next Generation. Cell. 2011;144(5):646-74.
15. Spreafico F, Fernandez CV, Brok J, Nakata K, Vujanic G, Geller JI, et al. Wilms tumour. Nat Rev Dis Primers. 2021;7(1):75.
16. Beckwith JB, Palmer NF. Histopathology and prognosis of Wilms tumors: results from the First National Wilms' Tumor Study. Cancer. 1978;41(5):1937-48.
17. Haas JE, Palmer NF, Weinberg AG, Beckwith JB. Ultrastructure of malignant rhabdoid tumor of the kidney. A distinctive renal tumor of children. Hum Pathol. 1981;12(7):646-57.
18. Palmer NF, Sutow W. Clinical aspects of the rhabdoid tumor of the kidney: a report of the National Wilms' Tumor Study Group. Med Pediatr Oncol. 1983;11(4):242-5.
19. Weeks DA, Beckwith JB, Mierau GW, Luckey DW. Rhabdoid tumor of kidney. A report of 111 cases from the National Wilms' Tumor Study Pathology Center. Am J Surg Pathol. 1989;13(6):439-58.

20. Parham DM, Peiper SC, Robicheaux G, Ribeiro RC, Douglass EC. Malignant rhabdoid tumor of the liver. Evidence for epithelial differentiation. Arch Pathol Lab Med. 1988;112(1):61-4.
21. Lynch HT, Shurin SB, Dahms BB, Izant RJ, Jr., Lynch J, Danes BS. Paravertebral malignant rhabdoid tumor in infancy. In vitro studies of a familial tumor. Cancer. 1983;52(2):290-6.
22. Tsuneyoshi M, Daimaru Y, Hashimoto H, Enjoji M. Malignant soft tissue neoplasms with the histologic features of renal rhabdoid tumors: an ultrastructural and immunohistochemical study. Hum Pathol. 1985;16(12):1235-42.
23. Biggs PJ, Garen PD, Powers JM, Garvin AJ. Malignant rhabdoid tumor of the central nervous system. Hum Pathol. 1987;18(4):332-7.
24. Fort DW, Tonk VS, Tomlinson GE, Timmons CF, Schneider NR. Rhabdoid tumor of the kidney with primitive neuroectodermal tumor of the central nervous system: Associated tumors with different histologic, cytogenetic, and molecular findings. Genes, Chromosomes and Cancer. 1994;11(3):146-52.
25. Tang M, Verhaak RG. A Molecular Take on Malignant Rhabdoid Tumors. Trends Cancer. 2016;2(5):217-8.
26. Douglass EC, Valentine M, Rowe ST, Parham DM, Wilimas JA, Sanders JM, et al. Malignant rhabdoid tumor: A highly malignant childhood tumor with minimal karyotypic changes. Genes, Chromosomes and Cancer. 1990;2(3):210-6.
27. Shashi V, Lovell MA, Von Kap-Herr C, Waldron P, Golden WL. Malignant rhabdoid tumor of the kidney: Involvement of chromosome 22. Genes, Chromosomes and Cancer. 1994;10(1):49-54.
28. Schofield DE, Beckwith JB, Sklar J. Loss of heterozygosity at chromosome regions 22q11–12 and 11p15.5 in renal rhabdoid tumors. Genes, Chromosomes and Cancer. 1996;15(1):10-7.
29. Biegel JA, Rorke LB, Packer RJ, Emanuel BS. Monosomy 22 in rhabdoid or atypical tumors of the brain. J Neurosurg. 1990;73(5):710-4.
30. Karnes PS, Tran TN, Cui MY, Bogenmann E, Shimada H, Ying KL. Establishment of a rhabdoid tumor cell line with a specific chromosomal abnormality, 46,XY,t(11;22)(p15.5;q11.23). Cancer Genet Cytogenet. 1991;56(1):31-8.
31. Biegel JA, Allen CS, Kawasaki K, Shimizu N, Budarf ML, Bell CJ. Narrowing the critical region for a rhabdoid tumor locus in 22q11. Genes, Chromosomes and Cancer. 1996;16(2):94-105.
32. Rosty C, Peter M, Zucman J, Validire P, Delattre O, Aurias A. Cytogenetic and molecular analysis of a t(1;22)(p36;q11.2) in a rhabdoid tumor with a putative homozygous deletion of chromosome 22. Genes, Chromosomes and Cancer. 1998;21(2):82-9.
33. Versteege I, Sévenet N, Lange J, Rousseau-Merck MF, Ambros P, Handgretinger R, et al. Truncating mutations of hSNF5/INI1 in aggressive paediatric cancer. Nature. 1998;394(6689):203-6.
34. Biegel JA, Zhou JY, Rorke LB, Stenstrom C, Wainwright LM, Fogelgren B. Germ-line and acquired mutations of INI1 in atypical teratoid and rhabdoid tumors. Cancer Res. 1999;59(1):74-9.
35. Sévenet N, Sheridan E, Amram D, Schneider P, Handgretinger R, Delattre O. Constitutional mutations of the hSNF5/INI1 gene predispose to a variety of cancers. Am J Hum Genet. 1999;65(5):1342-8.
36. Knudson AG, Jr. Mutation and cancer: statistical study of retinoblastoma. Proc Natl Acad Sci U S A. 1971;68(4):820-3.

37. Roberts CWM, Leroux MM, Fleming MD, Orkin SH. Highly penetrant, rapid tumorigenesis through conditional inversion of the tumor suppressor gene Snf5. Cancer Cell. 2002;2(5):415-25.
38. Han ZY, Richer W, Fréneaux P, Chauvin C, Lucchesi C, Guillemot D, et al. The occurrence of intracranial rhabdoid tumours in mice depends on temporal control of Smarcb1 inactivation. Nat Commun. 2016;7:10421.
39. Kalpana GV, Marmon S, Wang W, Crabtree GR, Goff SP. Binding and stimulation of HIV-1 integrase by a human homolog of yeast transcription factor SNF5. Science. 1994;266(5193):2002-6.
40. Muchardt C, Sardet C, Bourachot B, Onufryk C, Yaniv M. A human protein with homology to Saccharomyces cerevisiae SNF5 interacts with the potential helicase hbrm. Nucleic Acids Res. 1995;23(7):1127-32.
41. Stern M, Jensen R, Herskowitz I. Five SWI genes are required for expression of the HO gene in yeast. Journal of Molecular Biology. 1984;178(4):853-68.
42. Neigeborn L, Carlson M. GENES AFFECTING THE REGULATION OF SUC2 GENE EXPRESSION BY GLUCOSE REPRESSION IN SACCHAROMYCES CEREVISIAE. Genetics. 1984;108(4):845-58.
43. Peterson CL, Herskowitz I. Characterization of the yeast SWI1, SWI2, and SWI3 genes, which encode a global activator of transcription. Cell. 1992;68(3):573-83.
44. Peterson CL, Tamkun JW. The SWI-SNF complex: a chromatin remodeling machine? Trends Biochem Sci. 1995;20(4):143-6.
45. Hirschhorn JN, Brown SA, Clark CD, Winston F. Evidence that SNF2/SWI2 and SNF5 activate transcription in yeast by altering chromatin structure. Genes Dev. 1992;6(12a):2288-98.
46. Winston F, Carlson M. Yeast SNF/SWI transcriptional activators and the SPT/SIN chromatin connection. Trends in Genetics. 1992;8(11):387-91.
47. Kruger W, Peterson CL, Sil A, Coburn C, Arents G, Moudrianakis EN, et al. Amino acid substitutions in the structured domains of histones H3 and H4 partially relieve the requirement of the yeast SWI/SNF complex for transcription. Genes Dev. 1995;9(22):2770-9.
48. Kruger W, Herskowitz I. A negative regulator of HO transcription, SIN1 (SPT2), is a nonspecific DNA-binding protein related to HMG1. Mol Cell Biol. 1991;11(8):4135-46.
49. Kwon H, Imbalzano AN, Khavari PA, Kingston RE, Green MR. Nucleosome disruption and enhancement of activator binding by a human SW1/SNF complex. Nature. 1994;370(6489):477-81.
50. Muchardt C, Yaniv M. A human homologue of Saccharomyces cerevisiae SNF2/SWI2 and Drosophila brm genes potentiates transcriptional activation by the glucocorticoid receptor. Embo j. 1993;12(11):4279-90.
51. Khavari PA, Peterson CL, Tamkun JW, Mendel DB, Crabtree GR. BRG1 contains a conserved domain of the SWI2/SNF2 family necessary for normal mitotic growth and transcription. Nature. 1993;366(6451):170-4.
52. Kennison JA, Tamkun JW. Dosage-dependent modifiers of polycomb and antennapedia mutations in Drosophila. Proc Natl Acad Sci U S A. 1988;85(21):8136-40.
53. Tamkun JW, Deuring R, Scott MP, Kissinger M, Pattatucci AM, Kaufman TC, et al. brahma: A regulator of Drosophila homeotic genes structurally related to the yeast transcriptional activator SNF2SWI2. Cell. 1992;68(3):561-72.
54. Cairns BR, Kim YJ, Sayre MH, Laurent BC, Kornberg RD. A multisubunit complex containing the SWI1/ADR6, SWI2/SNF2, SWI3, SNF5, and SNF6 gene products isolated from yeast. Proc Natl Acad Sci U S A. 1994;91(5):1950-4.

55. Côté J, Quinn J, Workman JL, Peterson CL. Stimulation of GAL4 derivative binding to nucleosomal DNA by the yeast SWI/SNF complex. Science. 1994;265(5168):53-60.
56. Peterson CL, Dingwall A, Scott MP. Five SWI/SNF gene products are components of a large multisubunit complex required for transcriptional enhancement. Proc Natl Acad Sci U S A. 1994;91(8):2905-8.
57. Imbalzano AN, Kwon H, Green MR, Kingston RE. Facilitated binding of TATA-binding protein to nucleosomal DNA. Nature. 1994;370(6489):481-5.
58. Laurent BC, Treich I, Carlson M. The yeast SNF2/SWI2 protein has DNA-stimulated ATPase activity required for transcriptional activation. Genes Dev. 1993;7(4):583-91.
59. Kadoch C, Crabtree GR. Mammalian SWI/SNF chromatin remodeling complexes and cancer: Mechanistic insights gained from human genomics. Sci Adv. 2015;1(5):e1500447.
60. Centore RC, Sandoval GJ, Soares LMM, Kadoch C, Chan HM. Mammalian SWI/SNF Chromatin Remodeling Complexes: Emerging Mechanisms and Therapeutic Strategies. Trends Genet. 2020;36(12):936-50.
61. Dunaief JL, Strober BE, Guha S, Khavari PA, Alin K, Luban J, et al. The retinoblastoma protein and BRG1 form a complex and cooperate to induce cell cycle arrest. Cell. 1994;79(1):119-30.
62. Trouche D, Le Chalony C, Muchardt C, Yaniv M, Kouzarides T. RB and hbrm cooperate to repress the activation functions of E2F1. Proc Natl Acad Sci U S A. 1997;94(21):11268-73.
63. Braun SMG, Petrova R, Tang J, Krokhotin A, Miller EL, Tang Y, et al. BAF subunit switching regulates chromatin accessibility to control cell cycle exit in the developing mammalian cortex. Genes Dev. 2021;35(5-6):335-53.
64. Ho L, Crabtree GR. Chromatin remodelling during development. Nature. 2010;463(7280):474-84.
65. Kadoch C, Hargreaves DC, Hodges C, Elias L, Ho L, Ranish J, et al. Proteomic and bioinformatic analysis of mammalian SWI/SNF complexes identifies extensive roles in human malignancy. Nat Genet. 2013;45(6):592-601.
66. Sullivan LM, Folpe AL, Pawel BR, Judkins AR, Biegel JA. Epithelioid sarcoma is associated with a high percentage of SMARCB1 deletions. Modern Pathology. 2013;26(3):385-92.
67. Chbani L, Guillou L, Terrier P, Decouvelaere AV, Grégoire F, Terrier-Lacombe MJ, et al. Epithelioid sarcoma: a clinicopathologic and immunohistochemical analysis of 106 cases from the French sarcoma group. Am J Clin Pathol. 2009;131(2):222-7.
68. Valencia AM, Collings CK, Dao HT, St. Pierre R, Cheng Y-C, Huang J, et al. Recurrent SMARCB1 Mutations Reveal a Nucleosome Acidic Patch Interaction Site That Potentiates mSWI/SNF Complex Chromatin Remodeling. Cell. 2019;179(6):1342-56.e23.
69. Mashtalir N, Suzuki H, Farrell DP, Sankar A, Luo J, Filipovski M, et al. A Structural Model of the Endogenous Human BAF Complex Informs Disease Mechanisms. Cell. 2020;183(3):802-17.e24.
70. Nakayama RT, Pulice JL, Valencia AM, McBride MJ, McKenzie ZM, Gillespie MA, et al. SMARCB1 is required for widespread BAF complex-mediated activation of enhancers and bivalent promoters. Nat Genet. 2017;49(11):1613-23.
71. Michel BC, D'Avino AR, Cassel SH, Mashtalir N, McKenzie ZM, McBride MJ, et al. A non-canonical SWI/SNF complex is a synthetic lethal target in cancers driven by BAF complex perturbation. Nat Cell Biol. 2018;20(12):1410-20.

72. Wang X, Wang S, Troisi EC, Howard TP, Haswell JR, Wolf BK, et al. BRD9 defines a SWI/SNF sub-complex and constitutes a specific vulnerability in malignant rhabdoid tumors. Nat Commun. 2019;10(1):1881.
73. Kassis JA, Kennison JA, Tamkun JW. Polycomb and Trithorax Group Genes in Drosophila. Genetics. 2017;206(4):1699-725.
74. Lewis EB. A gene complex controlling segmentation in Drosophila. Nature. 1978;276(5688):565-70.
75. Schuettengruber B, Bourbon HM, Di Croce L, Cavalli G. Genome Regulation by Polycomb and Trithorax: 70 Years and Counting. Cell. 2017;171(1):34-57.
76. Blackledge NP, Rose NR, Klose RJ. Targeting Polycomb systems to regulate gene expression: modifications to a complex story. Nature Reviews Molecular Cell Biology. 2015;16(11):643-9.
77. Copeland RA, Solomon ME, Richon VM. Protein methyltransferases as a target class for drug discovery. Nat Rev Drug Discov. 2009;8(9):724-32.
78. Rea S, Eisenhaber F, O'Carroll D, Strahl BD, Sun Z-W, Schmid M, et al. Regulation of chromatin structure by site-specific histone H3 methyltransferases. Nature. 2000;406(6796):593-9.
79. Grossniklaus U, Paro R. Transcriptional silencing by polycomb-group proteins. Cold Spring Harb Perspect Biol. 2014;6(11):a019331.
80. Blackledge NP, Klose RJ. The molecular principles of gene regulation by Polycomb repressive complexes. Nat Rev Mol Cell Biol. 2021;22(12):815-33.
81. Bracken AP, Dietrich N, Pasini D, Hansen KH, Helin K. Genome-wide mapping of Polycomb target genes unravels their roles in cell fate transitions. Genes Dev. 2006;20(9):1123-36.
82. Ku M, Koche RP, Rheinbay E, Mendenhall EM, Endoh M, Mikkelsen TS, et al. Genomewide analysis of PRC1 and PRC2 occupancy identifies two classes of bivalent domains. PLoS Genet. 2008;4(10):e1000242.
83. Fursova NA, Blackledge NP, Nakayama M, Ito S, Koseki Y, Farcas AM, et al. Synergy between Variant PRC1 Complexes Defines Polycomb-Mediated Gene Repression. Mol Cell. 2019;74(5):1020-36.e8.
84. Fan H, Guo Y, Tsai YH, Storey AJ, Kim A, Gong W, et al. A conserved BAH module within mammalian BAHD1 connects H3K27me3 to Polycomb gene silencing. Nucleic Acids Res. 2021;49(8):4441-55.
85. Shao Z, Raible F, Mollaaghababa R, Guyon JR, Wu CT, Bender W, et al. Stabilization of chromatin structure by PRC1, a Polycomb complex. Cell. 1999;98(1):37-46.
86. Francis NJ, Saurin AJ, Shao Z, Kingston RE. Reconstitution of a functional core polycomb repressive complex. Mol Cell. 2001;8(3):545-56.
87. Kia SK, Gorski MM, Giannakopoulos S, Verrijzer CP. SWI/SNF mediates polycomb eviction and epigenetic reprogramming of the INK4b-ARF-INK4a locus. Mol Cell Biol. 2008;28(10):3457-64.
88. Oruetxebarria I, Venturini F, Kekarainen T, Houweling A, Zuijderduijn LM, Mohd-Sarip A, et al. P16INK4a is required for hSNF5 chromatin remodeler-induced cellular senescence in malignant rhabdoid tumor cells. J Biol Chem. 2004;279(5):3807-16.
89. Wilson BG, Wang X, Shen X, McKenna ES, Lemieux ME, Cho YJ, et al. Epigenetic antagonism between polycomb and SWI/SNF complexes during oncogenic transformation. Cancer Cell. 2010;18(4):316-28.
90. Visser HP, Gunster MJ, Kluin-Nelemans HC, Manders EM, Raaphorst FM, Meijer CJ, et al. The Polycomb group protein EZH2 is upregulated in proliferating, cultured human mantle cell lymphoma. Br J Haematol. 2001;112(4):950-8.

91. Varambally S, Dhanasekaran SM, Zhou M, Barrette TR, Kumar-Sinha C, Sanda MG, et al. The polycomb group protein EZH2 is involved in progression of prostate cancer. Nature. 2002;419(6907):624-9.
92. Bracken AP, Pasini D, Capra M, Prosperini E, Colli E, Helin K. EZH2 is downstream of the pRB-E2F pathway, essential for proliferation and amplified in cancer. Embo j. 2003;22(20):5323-35.
93. Kim KH, Roberts CW. Targeting EZH2 in cancer. Nat Med. 2016;22(2):128-34.
94. Morin RD, Johnson NA, Severson TM, Mungall AJ, An J, Goya R, et al. Somatic mutations altering EZH2 (Tyr641) in follicular and diffuse large B-cell lymphomas of germinal-center origin. Nat Genet. 2010;42(2):181-5.
95. Bödör C, Grossmann V, Popov N, Okosun J, O'Riain C, Tan K, et al. EZH2 mutations are frequent and represent an early event in follicular lymphoma. Blood. 2013;122(18):3165-8.
96. Yap DB, Chu J, Berg T, Schapira M, Cheng SW, Moradian A, et al. Somatic mutations at EZH2 Y641 act dominantly through a mechanism of selectively altered PRC2 catalytic activity, to increase H3K27 trimethylation. Blood. 2011;117(8):2451-9.
97. McCabe MT, Graves AP, Ganji G, Diaz E, Halsey WS, Jiang Y, et al. Mutation of A677 in histone methyltransferase EZH2 in human B-cell lymphoma promotes hypertrimethylation of histone H3 on lysine 27 (H3K27). Proc Natl Acad Sci U S A. 2012;109(8):2989-94.
98. Majer CR, Jin L, Scott MP, Knutson SK, Kuntz KW, Keilhack H, et al. A687V EZH2 is a gain-of-function mutation found in lymphoma patients. FEBS Lett. 2012;586(19):3448-51.
99. Kim KH, Kim W, Howard TP, Vazquez F, Tsherniak A, Wu JN, et al. SWI/SNF-mutant cancers depend on catalytic and non-catalytic activity of EZH2. Nat Med. 2015;21(12):1491-6.
100. Wang Y, Chen SY, Karnezis AN, Colborne S, Santos ND, Lang JD, et al. The histone methyltransferase EZH2 is a therapeutic target in small cell carcinoma of the ovary, hypercalcaemic type. J Pathol. 2017;242(3):371-83.
101. Pugh TJ, Weeraratne SD, Archer TC, Pomeranz Krummel DA, Auclair D, Bochicchio J, et al. Medulloblastoma exome sequencing uncovers subtype-specific somatic mutations. Nature. 2012;488(7409):106-10.
102. Gui Y, Guo G, Huang Y, Hu X, Tang A, Gao S, et al. Frequent mutations of chromatin remodeling genes in transitional cell carcinoma of the bladder. Nat Genet. 2011;43(9):875-8.
103. Waddell N, Pajic M, Patch AM, Chang DK, Kassahn KS, Bailey P, et al. Whole genomes redefine the mutational landscape of pancreatic cancer. Nature. 2015;518(7540):495-501.
104. van Haaften G, Dalgliesh GL, Davies H, Chen L, Bignell G, Greenman C, et al. Somatic mutations of the histone H3K27 demethylase gene UTX in human cancer. Nat Genet. 2009;41(5):521-3.
105. Ler LD, Ghosh S, Chai X, Thike AA, Heng HL, Siew EY, et al. Loss of tumor suppressor KDM6A amplifies PRC2-regulated transcriptional repression in bladder cancer and can be targeted through inhibition of EZH2. Science Translational Medicine. 2017;9(378):eaai8312.
106. Panditharatna E, Marques JG, Wang T, Trissal MC, Liu I, Jiang L, et al. BAF Complex Maintains Glioma Stem Cells in Pediatric H3K27M Glioma. Cancer Discov. 12. United States: ©2022 The Authors; Published by the American Association for Cancer Research.; 2022. p. 2880-905.

107. Boyer LA, Plath K, Zeitlinger J, Brambrink T, Medeiros LA, Lee TI, et al. Polycomb complexes repress developmental regulators in murine embryonic stem cells. Nature. 2006;441(7091):349-53.
108. Pasini D, Bracken AP, Hansen JB, Capillo M, Helin K. The polycomb group protein Suz12 is required for embryonic stem cell differentiation. Mol Cell Biol. 2007;27(10):3769-79.
109. Chou RH, Yu YL, Hung MC. The roles of EZH2 in cell lineage commitment. Am J Transl Res. 2011;3(3):243-50.
110. Béguelin W, Rivas MA, Calvo Fernández MT, Teater M, Purwada A, Redmond D, et al. EZH2 enables germinal centre formation through epigenetic silencing of CDKN1A and an Rb-E2F1 feedback loop. Nat Commun. 2017;8(1):877.
111. Béguelin W, Popovic R, Teater M, Jiang Y, Bunting KL, Rosen M, et al. EZH2 is required for germinal center formation and somatic EZH2 mutations promote lymphoid transformation. Cancer Cell. 2013;23(5):677-92.
112. Chang CJ, Yang JY, Xia W, Chen CT, Xie X, Chao CH, et al. EZH2 promotes expansion of breast tumor initiating cells through activation of RAF1-β-catenin signaling. Cancer Cell. 2011;19(1):86-100.
113. Du J, Li L, Ou Z, Kong C, Zhang Y, Dong Z, et al. FOXC1, a target of polycomb, inhibits metastasis of breast cancer cells. Breast Cancer Res Treat. 2012;131(1):65-73.
114. Cao Q, Yu J, Dhanasekaran SM, Kim JH, Mani RS, Tomlins SA, et al. Repression of E-cadherin by the polycomb group protein EZH2 in cancer. Oncogene. 2008;27(58):7274-84.
115. Ernst T, Chase AJ, Score J, Hidalgo-Curtis CE, Bryant C, Jones AV, et al. Inactivating mutations of the histone methyltransferase gene EZH2 in myeloid disorders. Nat Genet. 2010;42(8):722-6.
116. Ntziachristos P, Tsirigos A, Van Vlierberghe P, Nedjic J, Trimarchi T, Flaherty MS, et al. Genetic inactivation of the polycomb repressive complex 2 in T cell acute lymphoblastic leukemia. Nat Med. 2012;18(2):298-301.
117. Lee W, Teckie S, Wiesner T, Ran L, Prieto Granada CN, Lin M, et al. PRC2 is recurrently inactivated through EED or SUZ12 loss in malignant peripheral nerve sheath tumors. Nat Genet. 2014;46(11):1227-32.
118. Glazer RI, Hartman KD, Knode MC, Richard MM, Chiang PK, Tseng CK, et al. 3-Deazaneplanocin: a new and potent inhibitor of S-adenosylhomocysteine hydrolase and its effects on human promyelocytic leukemia cell line HL-60. Biochem Biophys Res Commun. 1986;135(2):688-94.
119. Tan J, Yang X, Zhuang L, Jiang X, Chen W, Lee PL, et al. Pharmacologic disruption of Polycomb-repressive complex 2-mediated gene repression selectively induces apoptosis in cancer cells. Genes Dev. 2007;21(9):1050-63.
120. Knutson SK, Wigle TJ, Warholic NM, Sneeringer CJ, Allain CJ, Klaus CR, et al. A selective inhibitor of EZH2 blocks H3K27 methylation and kills mutant lymphoma cells. Nature Chemical Biology. 2012;8(11):890-6.
121. McCabe MT, Ott HM, Ganji G, Korenchuk S, Thompson C, Van Aller GS, et al. EZH2 inhibition as a therapeutic strategy for lymphoma with EZH2-activating mutations. Nature. 2012;492(7427):108-12.
122. Yap TA, Winter JN, Giulino-Roth L, Longley J, Lopez J, Michot JM, et al. Phase I Study of the Novel Enhancer of Zeste Homolog 2 (EZH2) Inhibitor GSK2816126 in Patients with Advanced Hematologic and Solid Tumors. Clin Cancer Res. 2019;25(24):7331-9.
123. Qi W, Chan H, Teng L, Li L, Chuai S, Zhang R, et al. Selective inhibition of Ezh2 by a small molecule inhibitor blocks tumor cells proliferation. Proc Natl Acad Sci U S A. 2012;109(52):21360-5.

124. Konze KD, Ma A, Li F, Barsyte-Lovejoy D, Parton T, Macnevin CJ, et al. An orally bioavailable chemical probe of the Lysine Methyltransferases EZH2 and EZH1. ACS Chem Biol. 2013;8(6):1324-34.
125. Xu B, On DM, Ma A, Parton T, Konze KD, Pattenden SG, et al. Selective inhibition of EZH2 and EZH1 enzymatic activity by a small molecule suppresses MLL-rearranged leukemia. Blood. 2015;125(2):346-57.
126. Knutson SK, Warholic NM, Wigle TJ, Klaus CR, Allain CJ, Raimondi A, et al. Durable tumor regression in genetically altered malignant rhabdoid tumors by inhibition of methyltransferase EZH2. Proc Natl Acad Sci U S A. 2013;110(19):7922-7.
127. Verma SK, Tian X, LaFrance LV, Duquenne C, Suarez DP, Newlander KA, et al. Identification of Potent, Selective, Cell-Active Inhibitors of the Histone Lysine Methyltransferase EZH2. ACS Med Chem Lett. 2012;3(12):1091-6.
128. Vaswani RG, Gehling VS, Dakin LA, Cook AS, Nasveschuk CG, Duplessis M, et al. Identification of (R)-N-((4-Methoxy-6-methyl-2-oxo-1,2-dihydropyridin-3-yl)methyl)-2-methyl-1-(1-(1-(2,2,2-trifluoroethyl)piperidin-4-yl)ethyl)-1H-indole-3-carboxamide (CPI-1205), a Potent and Selective Inhibitor of Histone Methyltransferase EZH2, Suitable for Phase I Clinical Trials for B-Cell Lymphomas. J Med Chem. 2016;59(21):9928-41.
129. Kung PP, Bingham P, Brooun A, Collins M, Deng YL, Dinh D, et al. Optimization of Orally Bioavailable Enhancer of Zeste Homolog 2 (EZH2) Inhibitors Using Ligand and Property-Based Design Strategies: Identification of Development Candidate (R)-5,8-Dichloro-7-(methoxy(oxetan-3-yl)methyl)-2-((4-methoxy-6-methyl-2-oxo-1,2-dihydropyridin-3-yl)methyl)-3,4-dihydroisoquinolin-1(2H)-one (PF-06821497). J Med Chem. 2018;61(3):650-65.
130. Song Y, Liu Y, Li ZM, Li L, Su H, Jin Z, et al. SHR2554, an EZH2 inhibitor, in relapsed or refractory mature lymphoid neoplasms: a first-in-human, dose-escalation, dose-expansion, and clinical expansion phase 1 trial. Lancet Haematol. 2022;9(7):e493-e503.
131. Keam SJ. Valemetostat Tosilate: First Approval. Drugs. 2022;82(16):1621-7.
132. Brooun A, Gajiwala KS, Deng Y-L, Liu W, Bolaños B, Bingham P, et al. Polycomb repressive complex 2 structure with inhibitor reveals a mechanism of activation and drug resistance.
133. Li C, Wang Y, Gong Y, Zhang T, Huang J, Tan Z, et al. Finding an easy way to harmonize: a review of advances in clinical research and combination strategies of EZH2 inhibitors. Clin Epigenetics. 2021;13(1):62.
134. Tomassi S, Romanelli A, Zwergel C, Valente S, Mai A. Polycomb Repressive Complex 2 Modulation through the Development of EZH2–EED Interaction Inhibitors and EED Binders. Journal of Medicinal Chemistry. 2021;64(16):11774-97.
135. Huang Y, Sendzik M, Zhang J, Gao Z, Sun Y, Wang L, et al. Discovery of the Clinical Candidate MAK683: An EED-Directed, Allosteric, and Selective PRC2 Inhibitor for the Treatment of Advanced Malignancies. J Med Chem. 2022;65(7):5317-33.
136. Geller JI, Roth JJ, Biegel JA. Biology and Treatment of Rhabdoid Tumor. Crit Rev Oncog. 2015;20(3-4):199-216.
137. de Visscher SA, van Ginkel RJ, Wobbes T, Veth RP, Ten Heuvel SE, Suurmeijer AJ, et al. Epithelioid sarcoma: Still an only surgically curable disease. Cancer. 2006;107(3):606-12.
138. Gounder MM, Merriam P, Ratan R, Patel SR, Chugh R, Villalobos VM, et al. Real-world outcomes of patients with locally advanced or metastatic epithelioid sarcoma. Cancer. 2021;127(8):1311-7.
139. Gounder M, Schöffski P, Jones RL, Agulnik M, Cote GM, Villalobos VM, et al. Tazemetostat in advanced epithelioid sarcoma with loss of INI1/SMARCB1: an international, open-label, phase 2 basket study. Lancet Oncol. 2020;21(11):1423-32.

140. Grünewald TGP, Cidre-Aranaz F, Surdez D, Tomazou EM, de Álava E, Kovar H, et al. Ewing sarcoma. Nat Rev Dis Primers. 2018;4(1):5.
141. Sankar S, Lessnick SL. Promiscuous partnerships in Ewing's sarcoma. Cancer Genet. 2011;204(7):351-65.
142. Jawad MU, Cheung MC, Min ES, Schneiderbauer MM, Koniaris LG, Scully SP. Ewing sarcoma demonstrates racial disparities in incidence-related and sex-related differences in outcome: an analysis of 1631 cases from the SEER database, 1973-2005. Cancer. 2009;115(15):3526-36.
143. Worch J, Cyrus J, Goldsby R, Matthay KK, Neuhaus J, DuBois SG. Racial Differences in the Incidence of Mesenchymal Tumors Associated with EWSR1 Translocation. Cancer Epidemiology, Biomarkers & Prevention. 2011;20(3):449-53.
144. Ewing J. Classics in oncology. Diffuse endothelioma of bone. James Ewing. Proceedings of the New York Pathological Society, 1921. CA Cancer J Clin. 1972;22(2):95-8.
145. Turc-Carel C, Philip I, Berger MP, Philip T, Lenoir G. [Chromosomal translocation (11; 22) in cell lines of Ewing's sarcoma]. C R Seances Acad Sci III. 1983;296(23):1101-3.
146. Aurias A, Rimbaut C, Buffe D, Dubousset J, Mazabraud A. [Translocation of chromosome 22 in Ewing's sarcoma]. C R Seances Acad Sci III. 1983;296(23):1105-7.
147. Delattre O, Zucman J, Plougastel B, Desmaze C, Melot T, Peter M, et al. Gene fusion with an ETS DNA-binding domain caused by chromosome translocation in human tumours. Nature. 1992;359(6391):162-5.
148. Sorensen PH, Lessnick SL, Lopez-Terrada D, Liu XF, Triche TJ, Denny CT. A second Ewing's sarcoma translocation, t(21;22), fuses the EWS gene to another ETS-family transcription factor, ERG. Nat Genet. 1994;6(2):146-51.
149. Gaspar N, Hawkins DS, Dirksen U, Lewis IJ, Ferrari S, Le Deley MC, et al. Ewing Sarcoma: Current Management and Future Approaches Through Collaboration. J Clin Oncol. 2015;33(27):3036-46.
150. Crozat A, Aman P, Mandahl N, Ron D. Fusion of CHOP to a novel RNA-binding protein in human myxoid liposarcoma. Nature. 1993;363(6430):640-4.
151. Riggi N, Cironi L, Suvà M-L, Stamenkovic I. Sarcomas: genetics, signalling, and cellular origins. Part 1: The fellowship of TET. The Journal of Pathology. 2007;213(1):4-20.
152. Sandberg AA. Genetics of chondrosarcoma and related tumors. Curr Opin Oncol. 2004;16(4):342-54.
153. Ladanyi M, Gerald W. Fusion of the EWS and WT1 genes in the desmoplastic small round cell tumor. Cancer Res. 1994;54(11):2837-40.
154. Maki RG, Grohar PJ, Antonescu CR. Ewing sarcoma and related FET family translocation-associated round cell tumors: A century of clinical and scientific progress. Genes Chromosomes Cancer. 2022;61(8):509-17.
155. Schwartz JC, Cech TR, Parker RR. Biochemical Properties and Biological Functions of FET Proteins. Annu Rev Biochem. 2015;84:355-79.
156. March ZM, King OD, Shorter J. Prion-like domains as epigenetic regulators, scaffolds for subcellular organization, and drivers of neurodegenerative disease. Brain Res. 2016;1647:9-18.
157. Ross ED, Edskes HK, Terry MJ, Wickner RB. Primary sequence independence for prion formation. Proc Natl Acad Sci U S A. 2005;102(36):12825-30.
158. Kato M, Han Tina W, Xie S, Shi K, Du X, Wu Leeju C, et al. Cell-free Formation of RNA Granules: Low Complexity Sequence Domains Form Dynamic Fibers within Hydrogels. Cell. 2012;149(4):753-67.

159. Lin Y, Protter David SW, Rosen Michael K, Parker R. Formation and Maturation of Phase-Separated Liquid Droplets by RNA-Binding Proteins. Molecular Cell. 2015;60(2):208-19.
160. Burke Kathleen A, Janke Abigail M, Rhine Christy L, Fawzi Nicolas L. Residue-by-Residue View of In Vitro FUS Granules that Bind the C-Terminal Domain of RNA Polymerase II. Molecular Cell. 2015;60(2):231-41.
161. Boulay G, Sandoval GJ, Riggi N, Iyer S, Buisson R, Naigles B, et al. Cancer-Specific Retargeting of BAF Complexes by a Prion-like Domain. Cell. 2017;171(1):163-78.e19.
162. Kwon I, Kato M, Xiang S, Wu L, Theodoropoulos P, Mirzaei H, et al. Phosphorylation-regulated binding of RNA polymerase II to fibrous polymers of low-complexity domains. Cell. 2013;155(5):1049-60.
163. McSwiggen DT, Mir M, Darzacq X, Tjian R. Evaluating phase separation in live cells: diagnosis, caveats, and functional consequences. Genes Dev. 2019;33(23-24):1619-34.
164. Boija A, Klein IA, Sabari BR, Dall'Agnese A, Coffey EL, Zamudio AV, et al. Transcription Factors Activate Genes through the Phase-Separation Capacity of Their Activation Domains. Cell. 2018;175(7):1842-55.e16.
165. May WA, Gishizky ML, Lessnick SL, Lunsford LB, Lewis BC, Delattre O, et al. Ewing sarcoma 11;22 translocation produces a chimeric transcription factor that requires the DNA-binding domain encoded by FLI1 for transformation. Proc Natl Acad Sci U S A. 1993;90(12):5752-6.
166. Lessnick SL, Braun BS, Denny CT, May WA. Multiple domains mediate transformation by the Ewing's sarcoma EWS/FLI-1 fusion gene. Oncogene. 1995;10(3):423-31.
167. Ohno T, Rao VN, Reddy ES. EWS/Fli-1 chimeric protein is a transcriptional activator. Cancer Res. 1993;53(24):5859-63.
168. Cidre-Aranaz F, Alonso J. EWS/FLI1 Target Genes and Therapeutic Opportunities in Ewing Sarcoma. Front Oncol. 2015;5:162.
169. Gangwal K, Sankar S, Hollenhorst PC, Kinsey M, Haroldsen SC, Shah AA, et al. Microsatellites as EWS/FLI response elements in Ewing's sarcoma. Proc Natl Acad Sci U S A. 2008;105(29):10149-54.
170. Riggi N, Knoechel B, Gillespie SM, Rheinbay E, Boulay G, Suva ML, et al. EWS-FLI1 utilizes divergent chromatin remodeling mechanisms to directly activate or repress enhancer elements in Ewing sarcoma. Cancer Cell. 2014;26(5):668-81.
171. Monument MJ, Johnson KM, McIlvaine E, Abegglen L, Watkins WS, Jorde LB, et al. Clinical and biochemical function of polymorphic NR0B1 GGAA-microsatellites in Ewing sarcoma: a report from the Children's Oncology Group. PLoS One. 2014;9(8):e104378.
172. Petermann R, Mossier BM, Aryee DN, Khazak V, Golemis EA, Kovar H. Oncogenic EWS-Fli1 interacts with hsRPB7, a subunit of human RNA polymerase II. Oncogene. 1998;17(5):603-10.
173. Selvanathan SP, Graham GT, Erkizan HV, Dirksen U, Natarajan TG, Dakic A, et al. Oncogenic fusion protein EWS-FLI1 is a network hub that regulates alternative splicing. Proc Natl Acad Sci U S A. 2015;112(11):E1307-16.
174. Sankar S, Bell R, Stephens B, Zhuo R, Sharma S, Bearss DJ, et al. Mechanism and relevance of EWS/FLI-mediated transcriptional repression in Ewing sarcoma. Oncogene. 2013;32(42):5089-100.
175. Takao S, Forbes L, Uni M, Cheng S, Pineda JMB, Tarumoto Y, et al. Convergent organization of aberrant MYB complex controls oncogenic gene expression in acute myeloid leukemia. eLife. 2021;10:e65905.

176. Sole A, Grossetête S, Heintzé M, Babin L, Zaïdi S, Revy P, et al. Unraveling Ewing Sarcoma Tumorigenesis Originating from Patient-Derived Mesenchymal Stem Cells. Cancer Res. 2021;81(19):4994-5006.
177. Lessnick SL, Dacwag CS, Golub TR. The Ewing's sarcoma oncoprotein EWS/FLI induces a p53-dependent growth arrest in primary human fibroblasts. Cancer Cell. 2002;1(4):393-401.
178. Sohn EJ, Li H, Reidy K, Beers LF, Christensen BL, Lee SB. EWS/FLI1 oncogene activates caspase 3 transcription and triggers apoptosis in vivo. Cancer Res. 2010;70(3):1154-63.
179. Minas TZ, Surdez D, Javaheri T, Tanaka M, Howarth M, Kang HJ, et al. Combined experience of six independent laboratories attempting to create an Ewing sarcoma mouse model. Oncotarget. 2017;8(21):34141-63.
180. Gomez NC, Hepperla AJ, Dumitru R, Simon JM, Fang F, Davis IJ. Widespread Chromatin Accessibility at Repetitive Elements Links Stem Cells with Human Cancer. Cell Rep. 2016;17(6):1607-20.
181. Seong BKA, Dharia NV, Lin S, Donovan KA, Chong S, Robichaud A, et al. TRIM8 modulates the EWS/FLI oncoprotein to promote survival in Ewing sarcoma. Cancer Cell. 2021;39(9):1262-78.e7.
182. Kovar H, Aryee DN, Jug G, Henöckl C, Schemper M, Delattre O, et al. EWS/FLI-1 antagonists induce growth inhibition of Ewing tumor cells in vitro. Cell Growth Differ. 1996;7(4):429-37.
183. Franzetti GA, Laud-Duval K, van der Ent W, Brisac A, Irondelle M, Aubert S, et al. Cell-to-cell heterogeneity of EWSR1-FLI1 activity determines proliferation/migration choices in Ewing sarcoma cells. Oncogene. 2017;36(25):3505-14.
184. Apfelbaum AA, Wu F, Hawkins AG, Magnuson B, Jiménez JA, Taylor SD, et al. EWS::FLI1 and HOXD13 Control Tumor Cell Plasticity in Ewing Sarcoma. Clin Cancer Res. 2022;28(20):4466-78.
185. Gao Y, He X-Y, Wu XS, Huang Y-H, Toneyan S, Ha T, et al. ETV6 dependency in Ewing sarcoma by antagonism of EWS-FLI1-mediated enhancer activation. Nature Cell Biology. 2023;25(2):298-308.
186. Lu DY, Ellegast JM, Ross KN, Malone CF, Lin S, Mabe NW, et al. The ETS transcription factor ETV6 constrains the transcriptional activity of EWS–FLI to promote Ewing sarcoma. Nature Cell Biology. 2023;25(2):285-97.
187. Klevernic IV, Morton S, Davis RJ, Cohen P. Phosphorylation of Ewing's sarcoma protein (EWS) and EWS-Fli1 in response to DNA damage. Biochem J. 2009;418(3):625-34.
188. Bachmaier R, Aryee DN, Jug G, Kauer M, Kreppel M, Lee KA, et al. O-GlcNAcylation is involved in the transcriptional activity of EWS-FLI1 in Ewing's sarcoma. Oncogene. 2009;28(9):1280-4.
189. Kato M, Han TW, Xie S, Shi K, Du X, Wu LC, et al. Cell-free formation of RNA granules: low complexity sequence domains form dynamic fibers within hydrogels. Cell. 2012;149(4):753-67.
190. Yang L, Chansky HA, Hickstein DD. EWS.Fli-1 fusion protein interacts with hyperphosphorylated RNA polymerase II and interferes with serine-arginine protein-mediated RNA splicing. J Biol Chem. 2000;275(48):37612-8.
191. Ramaswamy K, Forbes L, Minuesa G, Gindin T, Brown F, Kharas MG, et al. Peptidomimetic blockade of MYB in acute myeloid leukemia. Nat Commun. 2018;9(1):110.
192. Sorolla A, Wang E, Golden E, Duffy C, Henriques ST, Redfern AD, et al. Precision medicine by designer interference peptides: applications in oncology and molecular therapeutics. Oncogene. 2020;39(6):1167-84.

193. Versteege I, Sevenet N, Lange J, Rousseau-Merck MF, Ambros P, Handgretinger R, et al. Truncating mutations of hSNF5/INI1 in aggressive paediatric cancer. Nature. 1998;394(6689):203-6.
194. McKenna ES, Sansam CG, Cho YJ, Greulich H, Evans JA, Thom CS, et al. Loss of the epigenetic tumor suppressor SNF5 leads to cancer without genomic instability. Mol Cell Biol. 2008;28(20):6223-33.
195. Kadoch C, Williams RT, Calarco JP, Miller EL, Weber CM, Braun SM, et al. Dynamics of BAF-Polycomb complex opposition on heterochromatin in normal and oncogenic states. Nat Genet. 2017;49(2):213-22.
196. Guerra S, Cichowski K. Targeting Cancer at the Intersection of Signaling and Epigenetics. Annual Review of Cancer Biology. 2019;3(1):365-84.
197. Baylin SB, Jones PA. Epigenetic Determinants of Cancer. Cold Spring Harb Perspect Biol. 2016;8(9).
198. Chi SN, Bourdeaut F, Casanova M, Kilburn LB, Hargrave DR, McCowage GB, et al. Update on phase 1 study of tazemetostat, an enhancer of zeste homolog 2 inhibitor, in pediatric patients with relapsed or refractory integrase interactor 1–negative tumors. Journal of Clinical Oncology. 2022;40(16_suppl):10040-.
199. Drosos Y, Myers JA, Xu B, Mathias KM, Beane EC, Radko-Juettner S, et al. NSD1 mediates antagonism between SWI/SNF and polycomb complexes and is required for transcriptional activation upon EZH2 inhibition. Mol Cell. 2022;82(13):2472-89.e8.
200. Cheng DT, Mitchell TN, Zehir A, Shah RH, Benayed R, Syed A, et al. Memorial Sloan Kettering-Integrated Mutation Profiling of Actionable Cancer Targets (MSK-IMPACT): A Hybridization Capture-Based Next-Generation Sequencing Clinical Assay for Solid Tumor Molecular Oncology. J Mol Diagn. 2015;17(3):251-64.
201. Gibaja V, Shen F, Harari J, Korn J, Ruddy D, Saenz-Vash V, et al. Development of secondary mutations in wild-type and mutant EZH2 alleles cooperates to confer resistance to EZH2 inhibitors. Oncogene. 2016;35(5):558-66.
202. Bisserier M, Wajapeyee N. Mechanisms of resistance to EZH2 inhibitors in diffuse large B-cell lymphomas. Blood. 2018;131(19):2125-37.
203. Honma D, Kanno O, Watanabe J, Kinoshita J, Hirasawa M, Nosaka E, et al. Novel orally bioavailable EZH1/2 dual inhibitors with greater antitumor efficacy than an EZH2 selective inhibitor. Cancer Sci. 2017;108(10):2069-78.
204. He Y, Selvaraju S, Curtin ML, Jakob CG, Zhu H, Comess KM, et al. The EED protein–protein interaction inhibitor A-395 inactivates the PRC2 complex. Nature Chemical Biology. 2017;13(4):389-95.
205. Qi W, Zhao K, Gu J, Huang Y, Wang Y, Zhang H, et al. An allosteric PRC2 inhibitor targeting the H3K27me3 binding pocket of EED. Nat Chem Biol. 2017;13(4):381-8.
206. Coe BP, Thu KL, Aviel-Ronen S, Vucic EA, Gazdar AF, Lam S, et al. Genomic deregulation of the E2F/Rb pathway leads to activation of the oncogene EZH2 in small cell lung cancer. PLoS One. 2013;8(8):e71670.
207. Custers L, Khabirova E, Coorens THH, Oliver TRW, Calandrini C, Young MD, et al. Somatic mutations and single-cell transcriptomes reveal the root of malignant rhabdoid tumours. Nat Commun. 2021;12(1):1407.
208. Kenny C, O'Meara E, Ulaş M, Hokamp K, O'Sullivan MJ. Global Chromatin Changes Resulting from Single-Gene Inactivation-The Role of SMARCB1 in Malignant Rhabdoid Tumor. Cancers (Basel). 2021;13(11).
209. Kotake Y, Cao R, Viatour P, Sage J, Zhang Y, Xiong Y. pRB family proteins are required for H3K27 trimethylation and Polycomb repression complexes binding to and silencing p16INK4alpha tumor suppressor gene. Genes Dev. 2007;21(1):49-54.

210. Gallagher D, Voronova A, Zander MA, Cancino GI, Bramall A, Krause MP, et al. Ankrd11 is a chromatin regulator involved in autism that is essential for neural development. Dev Cell. 2015;32(1):31-42.
211. Neilsen PM, Cheney KM, Li CW, Chen JD, Cawrse JE, Schulz RB, et al. Identification of ANKRD11 as a p53 coactivator. J Cell Sci. 2008;121(Pt 21):3541-52.
212. Noll JE, Jeffery J, Al-Ejeh F, Kumar R, Khanna KK, Callen DF, et al. Mutant p53 drives multinucleation and invasion through a process that is suppressed by ANKRD11. Oncogene. 2012;31(23):2836-48.
213. Fan T, Jiang S, Chung N, Alikhan A, Ni C, Lee CC, et al. EZH2-dependent suppression of a cellular senescence phenotype in melanoma cells by inhibition of p21/CDKN1A expression. Mol Cancer Res. 2011;9(4):418-29.
214. Negishi M, Wongpalee SP, Sarkar S, Park J, Lee KY, Shibata Y, et al. A new lncRNA, APTR, associates with and represses the CDKN1A/p21 promoter by recruiting polycomb proteins. PLoS One. 2014;9(4):e95216.
215. Daulat AM, Finetti P, Revinski D, Silveira Wagner M, Camoin L, Audebert S, et al. ECT2 associated to PRICKLE1 are poor-prognosis markers in triple-negative breast cancer. Br J Cancer. 2019;120(9):931-40.
216. Daulat AM, Bertucci F, Audebert S, Sergé A, Finetti P, Josselin E, et al. PRICKLE1 Contributes to Cancer Cell Dissemination through Its Interaction with mTORC2. Dev Cell. 2016;37(4):311-25.
217. Jiang D, He Y, Mo Q, Liu E, Li X, Huang L, et al. PRICKLE1, a Wnt/PCP signaling component, is overexpressed and associated with inferior prognosis in acute myeloid leukemia. J Transl Med. 2021;19(1):211.
218. Zhou R, Tang Z, Li H, Wang X, Sun Y. PRICKLE1 promotes gastric cancer metastasis by activating mTOR signaling. Am J Transl Res. 2021;13(5):4266-80.
219. Hu J, Yang Y, Ma Y, Ning Y, Chen G, Liu Y. Proliferation Cycle Transcriptomic Signatures are Strongly associated With Gastric Cancer Patient Survival. Front Cell Dev Biol. 2021;9:770994.
220. Chen X, Johns DC, Geiman DE, Marban E, Dang DT, Hamlin G, et al. Krüppel-like factor 4 (gut-enriched Krüppel-like factor) inhibits cell proliferation by blocking G1/S progression of the cell cycle. J Biol Chem. 2001;276(32):30423-8.
221. Chen X, Whitney EM, Gao SY, Yang VW. Transcriptional profiling of Krüppel-like factor 4 reveals a function in cell cycle regulation and epithelial differentiation. J Mol Biol. 2003;326(3):665-77.
222. De Azevedo WF, Leclerc S, Meijer L, Havlicek L, Strnad M, Kim SH. Inhibition of cyclin-dependent kinases by purine analogues: crystal structure of human cdk2 complexed with roscovitine. Eur J Biochem. 1997;243(1-2):518-26.
223. Manfredi MG, Ecsedy JA, Chakravarty A, Silverman L, Zhang M, Hoar KM, et al. Characterization of Alisertib (MLN8237), an investigational small-molecule inhibitor of aurora A kinase using novel in vivo pharmacodynamic assays. Clin Cancer Res. 2011;17(24):7614-24.
224. Wilkinson RW, Odedra R, Heaton SP, Wedge SR, Keen NJ, Crafter C, et al. AZD1152, a selective inhibitor of Aurora B kinase, inhibits human tumor xenograft growth by inducing apoptosis. Clin Cancer Res. 2007;13(12):3682-8.
225. Yang J, Ikezoe T, Nishioka C, Tasaka T, Taniguchi A, Kuwayama Y, et al. AZD1152, a novel and selective aurora B kinase inhibitor, induces growth arrest, apoptosis, and sensitization for tubulin depolymerizing agent or topoisomerase II inhibitor in human acute leukemia cells in vitro and in vivo. Blood. 2007;110(6):2034-40.
226. Vardi Y, Ying Z, Zhang CH. Two-sample tests for growth curves under dependent right censoring. Biometrika. 2001;88(4):949-60.

227. Henssen AG, Koche R, Zhuang J, Jiang E, Reed C, Eisenberg A, et al. PGBD5 promotes site-specific oncogenic mutations in human tumors. Nat Genet. 2017;49(7):1005-14.
228. Henssen AG, Reed C, Jiang E, Garcia HD, von Stebut J, MacArthur IC, et al. Therapeutic targeting of PGBD5-induced DNA repair dependency in pediatric solid tumors. Science translational medicine. 2017;9(414).
229. Henssen AG, Henaff E, Jiang E, Eisenberg AR, Carson JR, Villasante CM, et al. Genomic DNA transposition induced by human PGBD5. Elife. 2015;4.
230. Mah LJ, El-Osta A, Karagiannis TC. gammaH2AX: a sensitive molecular marker of DNA damage and repair. Leukemia. 2010;24(4):679-86.
231. León TE, Rapoz-D'Silva T, Bertoli C, Rahman S, Magnussen M, Philip B, et al. EZH2-Deficient T-cell Acute Lymphoblastic Leukemia Is Sensitized to CHK1 Inhibition through Enhanced Replication Stress. Cancer Discov. 2020;10(7):998-1017.
232. Januario T, Ye X, Bainer R, Alicke B, Smith T, Haley B, et al. PRC2-mediated repression of SMARCA2 predicts EZH2 inhibitor activity in SWI/SNF mutant tumors. Proc Natl Acad Sci U S A. 2017;114(46):12249-54.
233. Powell JA, Gardner AE, Bais AJ, Hinze SJ, Baker E, Whitmore S, et al. Sequencing, transcript identification, and quantitative gene expression profiling in the breast cancer loss of heterozygosity region 16q24.3 reveal three potential tumor-suppressor genes. Genomics. 2002;80(3):303-10.
234. Vasmatzis G, Johnson SH, Knudson RA, Ketterling RP, Braggio E, Fonseca R, et al. Genome-wide analysis reveals recurrent structural abnormalities of TP63 and other p53-related genes in peripheral T-cell lymphomas. Blood. 2012;120(11):2280-9.
235. Gebauer N, Künstner A, Ketzer J, Witte HM, Rausch T, Benes V, et al. Genomic insights into the pathogenesis of Epstein-Barr virus-associated diffuse large B-cell lymphoma by whole-genome and targeted amplicon sequencing. Blood Cancer J. 2021;11(5):102.
236. Isrie M, Hendriks Y, Gielissen N, Sistermans EA, Willemsen MH, Peeters H, et al. Haploinsufficiency of ANKRD11 causes mild cognitive impairment, short stature and minor dysmorphisms. Eur J Hum Genet. 20. England2012. p. 131-3.
237. Behnert A, Auber B, Steinemann D, Frühwald MC, Huisinga C, Hussein K, et al. KBG syndrome patient due to 16q24.3 microdeletion presenting with a paratesticular rhabdoid tumor: Coincidence or cancer predisposition? Am J Med Genet A. 2018;176(6):1449-54.
238. Zhang W, Geiman DE, Shields JM, Dang DT, Mahatan CS, Kaestner KH, et al. The gut-enriched Kruppel-like factor (Kruppel-like factor 4) mediates the transactivating effect of p53 on the p21WAF1/Cip1 promoter. J Biol Chem. 2000;275(24):18391-8.
239. Moonen JR, Chappell J, Shi M, Shinohara T, Li D, Mumbach MR, et al. KLF4 recruits SWI/SNF to increase chromatin accessibility and reprogram the endothelial enhancer landscape under laminar shear stress. Nat Commun. 2022;13(1):4941.
240. Schoninger SF, Blain SW. The Ongoing Search for Biomarkers of CDK4/6 Inhibitor Responsiveness in Breast Cancer. Mol Cancer Ther. 2020;19(1):3-12.
241. Finn RS, Dering J, Conklin D, Kalous O, Cohen DJ, Desai AJ, et al. PD 0332991, a selective cyclin D kinase 4/6 inhibitor, preferentially inhibits proliferation of luminal estrogen receptor-positive human breast cancer cell lines in vitro. Breast Cancer Res. 2009;11(5):R77.
242. Dean JL, Thangavel C, McClendon AK, Reed CA, Knudsen ES. Therapeutic CDK4/6 inhibition in breast cancer: key mechanisms of response and failure. Oncogene. 2010;29(28):4018-32.

243. Noatynska A, Tavernier N, Gotta M, Pintard L. Coordinating cell polarity and cell cycle progression: what can we learn from flies and worms? Open Biol. 2013;3(8):130083.
244. Shrestha R, Little KA, Tamayo JV, Li W, Perlman DH, Devenport D. Mitotic Control of Planar Cell Polarity by Polo-like Kinase 1. Dev Cell. 2015;33(5):522-34.
245. Payankaulam S, Yeung K, McNeill H, Henry RW, Arnosti DN. Regulation of cell polarity determinants by the Retinoblastoma tumor suppressor protein. Sci Rep. 2016;6:22879.
246. Gong X, Du J, Parsons SH, Merzoug FF, Webster Y, Iversen PW, et al. Aurora A Kinase Inhibition Is Synthetic Lethal with Loss of the RB1 Tumor Suppressor Gene. Cancer Discov. 2019;9(2):248-63.
247. Palmer AC, Sorger PK. Combination Cancer Therapy Can Confer Benefit via Patient-to-Patient Variability without Drug Additivity or Synergy. Cell. 2017;171(7):1678-91.e13.
248. Law LW. Effects of combinations of antileukemic agents on an acute lymphocytic leukemia of mice. Cancer Res. 1952;12(12):871-8.
249. Frei E, 3rd, Karon M, Levin RH, Freireich EJ, Taylor RJ, Hananian J, et al. The effectiveness of combinations of antileukemic agents in inducing and maintaining remission in children with acute leukemia. Blood. 1965;26(5):642-56.
250. Tsuda Y, Iimori M, Nakashima Y, Nakanishi R, Ando K, Ohgaki K, et al. Mitotic slippage and the subsequent cell fates after inhibition of Aurora B during tubulin-binding agent-induced mitotic arrest. Sci Rep. 2017;7(1):16762.
251. Hauf S, Cole RW, LaTerra S, Zimmer C, Schnapp G, Walter R, et al. The small molecule Hesperadin reveals a role for Aurora B in correcting kinetochore-microtubule attachment and in maintaining the spindle assembly checkpoint. J Cell Biol. 2003;161(2):281-94.
252. Kentsis A, Reed C, Rice KL, Sanda T, Rodig SJ, Tholouli E, et al. Autocrine activation of the MET receptor tyrosine kinase in acute myeloid leukemia. Nat Med. 2012;18(7):1118-22.
253. Ianevski A, Giri AK, Aittokallio T. SynergyFinder 2.0: visual analytics of multi-drug combination synergies. Nucleic Acids Res. 2020;48(W1):W488-w93.
254. Eisenhauer EA, Therasse P, Bogaerts J, Schwartz LH, Sargent D, Ford R, et al. New response evaluation criteria in solid tumours: revised RECIST guideline (version 1.1). Eur J Cancer. 2009;45(2):228-47.
255. Cerami E, Gao J, Dogrusoz U, Gross BE, Sumer SO, Aksoy BA, et al. The cBio cancer genomics portal: an open platform for exploring multidimensional cancer genomics data. Cancer Discov. 2012;2(5):401-4.
256. Gao J, Aksoy BA, Dogrusoz U, Dresdner G, Gross B, Sumer SO, et al. Integrative analysis of complex cancer genomics and clinical profiles using the cBioPortal. Sci Signal. 2013;6(269):pl1.
257. Olshen AB, Venkatraman ES, Lucito R, Wigler M. Circular binary segmentation for the analysis of array-based DNA copy number data. Biostatistics. 2004;5(4):557-72.
258. Dobin A, Davis CA, Schlesinger F, Drenkow J, Zaleski C, Jha S, et al. STAR: ultrafast universal RNA-seq aligner. Bioinformatics. 2013;29(1):15-21.
259. Anders S, Pyl PT, Huber W. HTSeq--a Python framework to work with high-throughput sequencing data. Bioinformatics. 2015;31(2):166-9.
260. Love MI, Huber W, Anders S. Moderated estimation of fold change and dispersion for RNA-seq data with DESeq2. Genome Biol. 2014;15(12):550.
261. Stirling DR, Swain-Bowden MJ, Lucas AM, Carpenter AE, Cimini BA, Goodman A. CellProfiler 4: improvements in speed, utility and usability. BMC Bioinformatics. 2021;22(1):433.

262. Schindelin J, Arganda-Carreras I, Frise E, Kaynig V, Longair M, Pietzsch T, et al. Fiji: an open-source platform for biological-image analysis. Nat Methods. 2012;9(7):676-82.
263. Mattar M, McCarthy CR, Kulick AR, Qeriqi B, Guzman S, de Stanchina E. Establishing and Maintaining an Extensive Library of Patient-Derived Xenograft Models. Front Oncol. 2018;8:19.
264. Meerbrey KL, Hu G, Kessler JD, Roarty K, Li MZ, Fang JE, et al. The pINDUCER lentiviral toolkit for inducible RNA interference in vitro and in vivo. Proc Natl Acad Sci U S A. 2011;108(9):3665-70.
265. Zucman J, Delattre O, Desmaze C, Plougastel B, Joubert I, Melot T, et al. Cloning and characterization of the Ewing's sarcoma and peripheral neuroepithelioma t(11;22) translocation breakpoints. Genes Chromosomes Cancer. 1992;5(4):271-7.
266. Smith R, Owen LA, Trem DJ, Wong JS, Whangbo JS, Golub TR, et al. Expression profiling of EWS/FLI identifies NKX2.2 as a critical target gene in Ewing's sarcoma. Cancer Cell. 2006;9(5):405-16.
267. Bailly RA, Bosselut R, Zucman J, Cormier F, Delattre O, Roussel M, et al. DNA-binding and transcriptional activation properties of the EWS-FLI-1 fusion protein resulting from the t(11;22) translocation in Ewing sarcoma. Mol Cell Biol. 1994;14(5):3230-41.
268. Szklarczyk D, Gable AL, Lyon D, Junge A, Wyder S, Huerta-Cepas J, et al. STRING v11: protein-protein association networks with increased coverage, supporting functional discovery in genome-wide experimental datasets. Nucleic Acids Res. 2019;47(D1):D607-d13.
269. Ford KM, Panwala R, Chen DH, Portell A, Palmer N, Mali P. Peptide-tiling screens of cancer drivers reveal oncogenic protein domains and associated peptide inhibitors. Cell Syst. 2021;12(7):716-32.e7.
270. Kadoch C, Crabtree GR. Reversible disruption of mSWI/SNF (BAF) complexes by the SS18-SSX oncogenic fusion in synovial sarcoma. Cell. 2013;153(1):71-85.
271. Colas P, Cohen B, Jessen T, Grishina I, McCoy J, Brent R. Genetic selection of peptide aptamers that recognize and inhibit cyclin-dependent kinase 2. Nature. 1996;380(6574):548-50.
272. Reverdatto S, Burz DS, Shekhtman A. Peptide aptamers: development and applications. Curr Top Med Chem. 2015;15(12):1082-101.
273. Hoffmann T, Stadler LK, Busby M, Song Q, Buxton AT, Wagner SD, et al. Structure-function studies of an engineered scaffold protein derived from stefin A. I: Development of the SQM variant. Protein Eng Des Sel. 2010;23(5):403-13.
274. Woodman R, Yeh JT, Laurenson S, Ko Ferrigno P. Design and validation of a neutral protein scaffold for the presentation of peptide aptamers. J Mol Biol. 2005;352(5):1118-33.
275. Rossmann M, S JG, Moschetti T, Dinan M, Hyvönen M. Development of a multipurpose scaffold for the display of peptide loops. Protein Eng Des Sel. 2017;30(6):419-30.
276. Chung HK, Jacobs CL, Huo Y, Yang J, Krumm SA, Plemper RK, et al. Tunable and reversible drug control of protein production via a self-excising degron. Nat Chem Biol. 2015;11(9):713-20.
277. Fadul J, Bell R, Hoffman LM, Beckerle MC, Engel ME, Lessnick SL. EWS/FLI utilizes NKX2-2 to repress mesenchymal features of Ewing sarcoma. Genes Cancer. 2015;6(3-4):129-43.
278. Deng Q, Natesan R, Cidre-Aranaz F, Arif S, Liu Y, Rasool RU, et al. Oncofusion-driven de novo enhancer assembly promotes malignancy in Ewing sarcoma via aberrant expression of the stereociliary protein LOXHD1. Cell Rep. 2022;39(11):110971.

279. Kinsey M, Smith R, Lessnick SL. NR0B1 is required for the oncogenic phenotype mediated by EWS/FLI in Ewing's sarcoma. Mol Cancer Res. 2006;4(11):851-9.
280. Kinsey M, Smith R, Iyer AK, McCabe ER, Lessnick SL. EWS/FLI and its downstream target NR0B1 interact directly to modulate transcription and oncogenesis in Ewing's sarcoma. Cancer Res. 2009;69(23):9047-55.
281. Matsumoto Y, Tanaka K, Nakatani F, Matsunobu T, Matsuda S, Iwamoto Y. Downregulation and forced expression of EWS-Fli1 fusion gene results in changes in the expression of G(1)regulatory genes. Br J Cancer. 2001;84(6):768-75.
282. Palombo R, Frisone P, Fidaleo M, Mercatelli N, Sette C, Paronetto MP. The Promoter-Associated Noncoding RNA pncCCND1_B Assembles a Protein-RNA Complex to Regulate Cyclin D1 Transcription in Ewing Sarcoma. Cancer Res. 2019;79(14):3570-82.
283. Hancock JD, Lessnick SL. A transcriptional profiling meta-analysis reveals a core EWS-FLI gene expression signature. Cell Cycle. 2008;7(2):250-6.
284. Bao X, Tang J, Lopez-Pajares V, Tao S, Qu K, Crabtree Gerald R, et al. ACTL6a Enforces the Epidermal Progenitor State by Suppressing SWI/SNF-Dependent Induction of KLF4. Cell Stem Cell. 2013;12(2):193-203.
285. Chang C-Y, Shipony Z, Lin SG, Kuo A, Xiong X, Loh KM, et al. Increased ACTL6A occupancy within mSWI/SNF chromatin remodelers drives human squamous cell carcinoma. Molecular Cell. 2021;81(24):4964-78.e8.
286. Giaimo BD, Ferrante F, Herchenröther A, Hake SB, Borggrefe T. The histone variant H2A.Z in gene regulation. Epigenetics & Chromatin. 2019;12(1):37.
287. Yang HD, Kim PJ, Eun JW, Shen Q, Kim HS, Shin WC, et al. Oncogenic potential of histone-variant H2A.Z.1 and its regulatory role in cell cycle and epithelial-mesenchymal transition in liver cancer. Oncotarget. 2016;7(10):11412-23.
288. Thiery JP, Acloque H, Huang RY, Nieto MA. Epithelial-mesenchymal transitions in development and disease. Cell. 2009;139(5):871-90.
289. Wiles ET, Bell R, Thomas D, Beckerle M, Lessnick SL. ZEB2 Represses the Epithelial Phenotype and Facilitates Metastasis in Ewing Sarcoma. Genes Cancer. 2013;4(11-12):486-500.
290. Huang X, Zhang H, Guo X, Zhu Z, Cai H, Kong X. Insulin-like growth factor 2 mRNA-binding protein 1 (IGF2BP1) in cancer. J Hematol Oncol. 2018;11(1):88.
291. Schilling J, Schöppe J, Plückthun A. From DARPins to LoopDARPins: novel LoopDARPin design allows the selection of low picomolar binders in a single round of ribosome display. J Mol Biol. 2014;426(3):691-721.
292. Wu Y, Zeng J, Roscoe BP, Liu P, Yao Q, Lazzarotto CR, et al. Highly efficient therapeutic gene editing of human hematopoietic stem cells. Nat Med. 2019;25(5):776-83.
293. Boone MA, Taslim C, Crow JC, Selich-Anderson J, Byrum AK, Showpnil IA, et al. The FLI portion of EWS/FLI contributes a transcriptional regulatory function that is distinct and separable from its DNA-binding function in Ewing sarcoma. Oncogene. 2021;40(29):4759-69.
294. Zhang J, Xin L, Shan B, Chen W, Xie M, Yuen D, et al. PEAKS DB: de novo sequencing assisted database search for sensitive and accurate peptide identification. Mol Cell Proteomics. 2012;11(4):M111.010587.
295. Sharpless NE, Bardeesy N, Lee K-H, Carrasco D, Castrillon DH, Aguirre AJ, et al. Loss of p16Ink4a with retention of p19Arf predisposes mice to tumorigenesis. Nature. 2001;413(6851):86-91.
296. Krimpenfort P, Quon KC, Mooi WJ, Loonstra A, Berns A. Loss of p16Ink4a confers susceptibility to metastatic melanoma in mice. Nature. 2001;413(6851):83-6.

297. He S, Wu Z, Tian Y, Yu Z, Yu J, Wang X, et al. Structure of nucleosome-bound human BAF complex. Science. 2020;367(6480):875-81.
298. Mashtalir N, D'Avino AR, Michel BC, Luo J, Pan J, Otto JE, et al. Modular Organization and Assembly of SWI/SNF Family Chromatin Remodeling Complexes. Cell. 2018;175(5):1272-88.e20.
299. Liu F, Rijkers DT, Post H, Heck AJ. Proteome-wide profiling of protein assemblies by cross-linking mass spectrometry. Nat Methods. 2015;12(12):1179-84.
300. Ser Z, Cifani P, Kentsis A. Optimized Cross-Linking Mass Spectrometry for in Situ Interaction Proteomics. J Proteome Res. 2019;18(6):2545-58.
301. Hage C, Iacobucci C, Rehkamp A, Arlt C, Sinz A. The First Zero-Length Mass Spectrometry-Cleavable Cross-Linker for Protein Structure Analysis. Angew Chem Int Ed Engl. 2017;56(46):14551-5.
302. Mao X, Miesfeldt S, Yang H, Leiden JM, Thompson CB. The FLI-1 and chimeric EWS-FLI-1 oncoproteins display similar DNA binding specificities. J Biol Chem. 1994;269(27):18216-22.
303. Johnson KM, Mahler NR, Saund RS, Theisen ER, Taslim C, Callender NW, et al. Role for the EWS domain of EWS/FLI in binding GGAA-microsatellites required for Ewing sarcoma anchorage independent growth. Proc Natl Acad Sci U S A. 2017;114(37):9870-5.
304. Zuo L, Zhang G, Massett M, Cheng J, Guo Z, Wang L, et al. Loci-specific phase separation of FET fusion oncoproteins promotes gene transcription. Nature Communications. 2021;12(1):1491.
305. Chong S, Graham TGW, Dugast-Darzacq C, Dailey GM, Darzacq X, Tjian R. Tuning levels of low-complexity domain interactions to modulate endogenous oncogenic transcription. Molecular Cell. 2022;82(11):2084-97.e5.
306. Ng KP, Potikyan G, Savene RO, Denny CT, Uversky VN, Lee KA. Multiple aromatic side chains within a disordered structure are critical for transcription and transforming activity of EWS family oncoproteins. Proc Natl Acad Sci U S A. 2007;104(2):479-84.
307. Patel M, Simon JM, Iglesia MD, Wu SB, McFadden AW, Lieb JD, et al. Tumor-specific retargeting of an oncogenic transcription factor chimera results in dysregulation of chromatin and transcription. Genome Res. 2012;22(2):259-70.
308. Nomura T, Watanabe S, Kaneko K, Yamanaka K, Nukina N, Furukawa Y. Intranuclear aggregation of mutant FUS/TLS as a molecular pathomechanism of amyotrophic lateral sclerosis. J Biol Chem. 2014;289(2):1192-202.